



**UNIVERSITY *of the*
WESTERN CAPE**

**Impact of different chemical synthesis techniques on the structural and
photoluminescence properties of $\text{Zn}_4\text{B}_6\text{O}_{13}:\text{RE}^{3+}$ (where $\text{RE}^{3+} = \text{Sm}^{3+}, \text{Eu}^{3+}, \text{and Dy}^{3+}$)
nanophosphors**

Athenkosi Siyalo

Dissertation in fulfilment of the requirements for the degree

Masters in Nanoscience

Department of Physics and Astronomy,

University of the Western Cape.

Supervisor: Prof. Sylvain Halinditwali, University of the Western Cape

**Co-Supervisors: Prof. Leelakrishna Reddy and Dr Balakrishna Avula, University of
Johannesburg**

November 2023

Declaration

I declare that *Impact of various chemical techniques on the structural and photoluminescence properties of $Zn_4B_6O_{13}: RE^{3+}$ (where $RE^{3+} = Sm^{3+}, Eu^{3+},$ and Dy^{3+}) nanophosphors* is my work, that it has not been submitted for any degree or examination in any other university, and that all the sources I have used or quoted have been indicated and acknowledged by complete references.



On this _____ day of _____ Nov-2023

Signature of the student



UNIVERSITY *of the*
WESTERN CAPE

Dedication

This dissertation is dedicated to Almighty God, my father Mr
T Siyalo and my entire family.



Acknowledgements

- I would like to express my sincere gratitude to God Almighty for protecting me throughout the year and for letting this research to come to this point.
- I would like to thank my supervisor Prof. S Halindintwali for his guidance, support and patience throughout this study.
- Special thanks to my co-supervisor Prof. L Reddy for the support and guidance throughout the entire research.
- Many thanks to Dr A Balakishna for his assistance in the reports write ups.
- I extend special thanks to Dr S Kumhar for his infinite laboratory assistance and advice.
- I would like to thank the Nanoscience program and Prof R Lindsay for giving me the opportunity to participate in this research and their financial support.
- Special appreciation to the University of Johannesburg for allowing me to use their facility to conduct my experiments.
- I am grateful to Professor H.C. Swart and his team for permitting me to carry out characterizations at the University of Free State.
- I want to express my heartfelt thanks to my family for their everlasting support and belief in my endeavours and everyone else who has been part of my journey.
- I would like to thank my siblings Sinovuyo Siyalo, Simangele Siyalo, and Saphokazi Siyalo for all the spiritual and physical support.
- Special thanks to Faith Tsebe for all the support.
- I would like to thank Mr S and Mr V Siyalo for all the spiritual support.
- Lastly, I extend my gratitude to my friends for their constant support.

Abstract

Different chemical synthesizing techniques, such as sol-gel, combustion, and solid-state reaction routes, offer the unique possibility of generating high-purity nanophosphors with different morphologies. In this project, we intend to do a comparative study on the structural and photoluminescence properties of $\text{Zn}_4\text{B}_6\text{O}_{13}:\text{RE}^{3+}$ (where $\text{RE}^{3+} = \text{Sm}^{3+}, \text{Eu}^{3+}, \text{and Dy}^{3+}$) nanophosphors using the above-mentioned techniques. Up to now, the comparative study based on the synthesis techniques has not yet been reported. As it will be shown in the literature survey's section, these methods were found to drastically affect the structural and photoluminescence characteristics of phosphor materials, which directs us to implement such studies on highly crystalline $\text{Zn}_4\text{B}_6\text{O}_{13}:\text{RE}^{3+}$ (where $\text{RE}^{3+} = \text{Sm}^{3+}, \text{Eu}^{3+}, \text{and Dy}^{3+}$) nanophosphors. In this work, we intend to use different characterization techniques such as X-ray diffraction (XRD), field emission scanning electron microscopy (FE-SEM), Fourier transform infrared spectroscopy (FT-IR), ultraviolet visible spectroscopy (UV-Vis), and photoluminescence (PL) spectroscopy. In this study, we aim to justify the appropriate technique that will produce the best PL properties for $\text{Zn}_4\text{B}_6\text{O}_{13}:\text{RE}^{3+}$ (where $\text{RE}^{3+} = \text{Sm}^{3+}, \text{Eu}^{3+}, \text{and Dy}^{3+}$) nanophosphors, which could be used as a benchmark for future researchers in solid-state lighting systems. The incorporation of the $\text{Sm}^{3+}, \text{Eu}^{3+}, \text{and Dy}^{3+}$ dopants did not change the cubic crystal structure of the $\text{Zn}_4\text{B}_6\text{O}_{13}$ host material, as confirmed by the XRD results. However, they caused a slight deviation to higher 2θ values, which confirms the charge exchange between the dopants and the host.

The lowest crystallite size was obtained through the sol-gel method on the $\text{Zn}_4\text{B}_6\text{O}_{13}:\text{Sm}^{3+}$ phosphor. Whereas the largest crystallite size was obtained through solid-state method. The SEM showed dominance of the hexagonal and some irregular morphologies of the prepared samples. The histograms obtained from the SEM data revealed that the average particle size of the prepared phosphors ranged from 500 to 2200 nm. The largest average particle sizes of 2200 nm were obtained from $\text{Zn}_4\text{B}_6\text{O}_{13}:\text{Dy}^{3+}$ prepared with the combustion method. However, this method also produced the smallest average particle size of 500 nm for the $\text{Zn}_4\text{B}_6\text{O}_{13}:\text{Eu}^{3+}$ phosphors. The UV-Vis showed an increase in bandgap on the $\text{Zn}_4\text{B}_6\text{O}_{13}:\text{Sm}^{3+}$ and $\text{Zn}_4\text{B}_6\text{O}_{13}:\text{Eu}^{3+}$ phosphors prepared by the solid-state method, respectively. Whereas it decreased on the $\text{Zn}_4\text{B}_6\text{O}_{13}:\text{Dy}^{3+}$ phosphor. The $\text{Zn}_4\text{B}_6\text{O}_{13}:\text{Sm}^{3+}$ phosphor prepared with the combustion method exhibited the highest photoluminescence emission intensity at 618 nm

upon excitation energies at 228 nm and 352 nm wavelengths, respectively. In addition, the $\text{Zn}_4\text{B}_6\text{O}_{13}$ prepared by the combustion method exhibited orange-red colour emission at 618 nm, which is attributed to the ${}^4\text{G}_{5/2} \rightarrow {}^6\text{H}_{9/2}$ transition with the shortest lifetime decay of 244 ms when compared to results obtained from other methods. Moreover, intense photoluminescence emissions were also observed on the $\text{Zn}_4\text{B}_6\text{O}_{13}:\text{Eu}^{3+}$ and $\text{Zn}_4\text{B}_6\text{O}_{13}:\text{Dy}^{3+}$ phosphors prepared with the solid-state method, respectively. Whereas the $\text{Zn}_4\text{B}_6\text{O}_{13}:\text{Sm}^{3+}$ phosphor prepared with the sol-gel method showed the poorest photoluminescence emission. The average lifetime decay of $\text{Zn}_4\text{B}_6\text{O}_{13}:\text{Eu}^{3+}$ phosphors in all methods decreased by approximately 99% when excited at 395 nm, compared to an excitation at 246 nm. This change is observed to reduce from 244, 323, and 463 ms to 5.47, 2.94, and 3.16 ms for combustion, sol-gel, and solid-state methods, respectively. The prepared phosphors could be potential candidates for various LED applications, depending on their respective colour emissions.

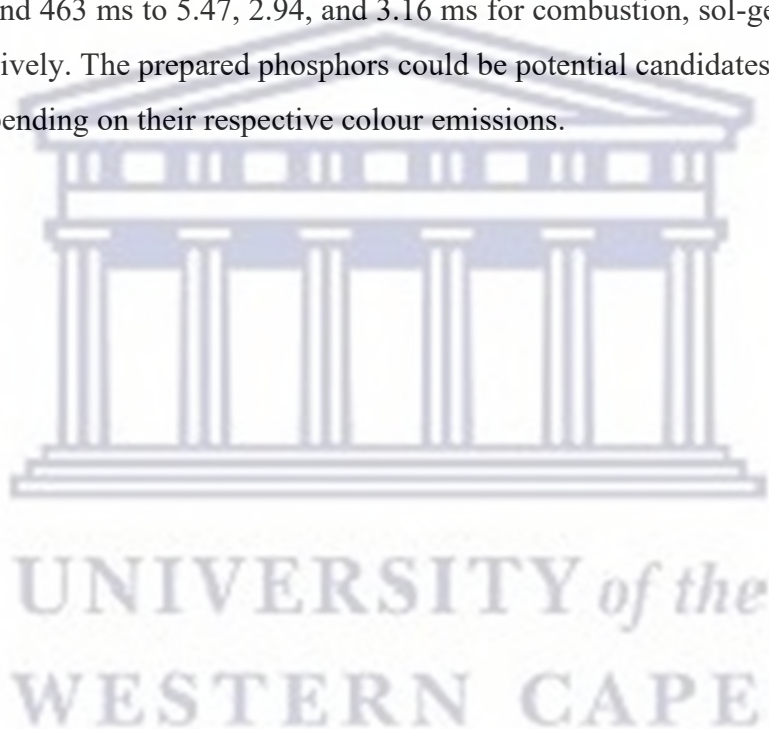


Table of Contents

Declaration.....	ii
Dedication.....	iii
Acknowledgements.....	iv
Abstract.....	v
Table of Contents.....	vii
List of Figures.....	x
List of Tables.....	xiv
List of abbreviations.....	xv
Chapter I.....	1
Introduction.....	1
1.1 Materials and their Classification.....	1
1.2 Materials in the nano range.....	4
1.3 Introduction to phosphors materials.....	5
1.4 Classification of phosphors and their structures.....	6
1.4.1 Organic phosphors.....	6
1.4.2 Inorganic phosphors.....	6
1.5 Introduction of different synthesis methods for phosphor preparation.....	8
1.5.1 Combustion.....	8
1.5.2 Sol-gel.....	9
1.5.3 Co-precipitation.....	10
1.5.4 Hydrothermal method.....	11
1.6 Impact of different synthesis methods on structural properties of phosphors.....	12
1.6.1 Crystalline properties.....	12
1.7 Impact of different synthesis methods on morphological properties of phosphors.....	13
1.8 Impact of different synthesis methods on the photoluminescence properties of phosphors.....	14
1.9 ZnO material-based anionic group systems.....	15
1.10 Formation of Zn ₄ B ₆ O ₁₃ compounds and their structural properties.....	16
1.11 Rare earth ions and their properties.....	18
1.12 Colour emission properties of Eu ³⁺ , Dy ³⁺ and Sm ³⁺ ions.....	20
1.13 Problem statement.....	22
1.14 Research aims and objectives.....	22
1.14.1 Aim.....	22

1.14.2 Objectives	23
1.15 Dissertation layout.....	23
Chapter II	25
Literature review	25
2.1 Emission properties of ZnO based phosphors.....	25
2.2 Various synthesis methods for emission properties of ZnO based phosphors.....	27
2.2.1 Emission properties of ZnO based phosphors prepared via combustion reaction method	28
2.2.2 Emission properties of ZnO based phosphors prepared via sol-gel reaction method	30
2.2.3 Emission properties of ZnO based phosphors prepared via solid state reaction method	32
2.3 Luminescence properties due to dopants	34
2.3.1 Luminescence properties of Sm ³⁺ ions.....	34
2.3.1 Luminescence properties of Eu ³⁺ ions.....	36
2.3.1 Luminescence properties of Dy ³⁺ ions	38
2.4 Conclusion.....	39
Chapter III.....	42
3.1 Introduction	42
3.2 Synthesis methods.....	42
3.2.1 Sol-gel method.....	42
3.2.2 Combustion Method	44
3.2.3 Solid State Method	45
3.3 Characterization techniques	48
3.3.1 X-Ray Diffraction.....	48
3.4 Microscopy.....	51
3.4.1 Scanning Electron Microscopy (SEM).....	51
3.5 Spectroscopy	55
3.5.1 Ultraviolet visible spectroscopy (UV-Vis).....	55
3.5.1 (a) Determination of optical coefficients.....	56
3.5.1 (b) Kubelka-Munk equation and Tauc plot	57
3.5.2 Fourier Transform Infrared (FT-IR) spectroscopy	59
3.5.3 Photoluminescence (PL).....	63
3.6 Colour chromaticity diagram	67
Chapter IV.....	71
4.1 Introduction	71

4.2 Results and discussions	72
4.2.1 X-ray diffraction studies	72
4.2.2 Surface morphology studies and elemental analysis	76
4.2.3 Fourier Transform Infrared (FT-IR) analysis	81
4.2.4 UV-VIS and band gap measurements	83
4.2.5 Photoluminescence excitation and emission spectra measurements	88
4.2.6 Lifetime decay measurements	90
4.2.7 CIE colour coordinates	92
4.3 Conclusion.....	94
Chapter V	95
5.1 Introduction	95
5.2 Results and discussion.....	96
5.2.1 X-ray diffraction studies	96
5.2.2. Surface morphology studies and elemental analysis	99
5.2.3 Fourier Transform Infrared (FT-IR) analysis.	103
5.2.4 UV-VIS and band gap measurements	104
5.2.5 Photoluminescence excitation and emission spectra measurements	107
5.2.6 Lifetime decay measurements	109
5.2.7 CIE color coordinates	111
5.3 Conclusion.....	113
Chapter VI.....	114
6.1 Introduction	114
6.2 Results and discussion.....	115
6.2.1 X-ray diffraction studies	115
6.2.2 Surface morphology studies and elemental analysis	117
6.2.3 Fourier Transform Infrared (FT-IR) analysis.	120
6.2.4 UV-VIS and band gap measurements	122
6.2.5 Photoluminescence excitation and emission spectra measurements	125
6.2.6 Lifetime decay measurements	127
6.2.7 CIE color coordinates	130
6.3 Conclusion.....	133
Chapter VII	134
Conclusion	134
Bibliography	136

List of Figures

FIGURE 1.1 (A) FLUORESCENCE AND (B) PHOSPHORESCENCE OCCURRENCES OF COLOUR [12], [13].....	3
FIGURE 1.2 NANOMATERIALS AND THEIR DIMENSIONS [20].....	4
FIGURE 1.3 SCHEMATIC REPRESENTATION OF DIFFERENT WLED PHOSPHORS MADE FROM CE^{3+} AND TB^{3+} DOPED ALKALINE-EARTH SILICATE SR_2MGSi_2O CRYSTAL STRUCTURES [45].....	7
FIGURE 1.4 SCHEMATIC PRESENTATION FOR SYNTHESIS OF NANOPHOSPHORS USING COMBUSTION METHOD [48].	8
FIGURE 1.6 SCHEMATIC REPRESENTATION OF SOL-GEL METHOD DEPENDING ON THE DESIRED PHOSPHOR MATERIAL [56].	9
FIGURE 1.7 A FLOW DIAGRAM FOR CO-PRECIPIATION PREPARATION METHOD.....	10
FIGURE 1.8 A SCHEMATIC REPRESENTATION FOR (A) AN AUTOCLAVE (B) HYDROTHERMAL METHOD [63].	11
FIGURE 1.9 THE GRAPHIC REPRESENTATION OF THE $ZN_4B_6O_{13}$ CRYSTAL STRUCTURE [88].	18
FIGURE 1.11 SCHEMATIC REPRESENTATION OF MATRIX-ASSISTED LUMINESCENCE OF RE^{3+} IONS (WHERE S IS A SENSITIZER AND A IS AN ACTIVATOR) [8].	20
FIGURE 2.1 THE HEXAGONAL WURTZITE CRYSTAL STRUCTURE OF ZNO MATERIAL [122].	28
FIGURE 2.2 THE ELECTRONIC ENERGY LEVEL DIAGRAM FOR THE EU^{3+} ION [135].	37
TABLE 2.2 SUMMATIVE LUMINESCENCE EMISSION PROPERTIES DUE TO SM^{3+}, EU^{3+}, AND DY^{3+} IONS [126], [141].....	41
FIGURE 3.1 A FLOW DIAGRAM FOR THE SOL-GEL SYNTHESIS PROCEDURE.....	44
FIGURE 3.2 FLOW DIAGRAM OF THE COMBUSTION METHOD.	45
FIGURE 3.3 A FLOW CHART FOR THE SOLID-STATE SYNTHESIS METHOD.....	47
FIGURE 3.4 (A) THE SCHEMATIC ARRANGEMENT OF THE COMPONENTS OF AN XRD DIFFRACTOMETER [159] AND (B) SCHEMATIC REPRESENTATION OF INCIDENT AND DIFFRACTED X-RAYS ON AND OFF THE SAMPLE [160].....	48
FIGURE 3.5 A SCHEMATIC DIAGRAM FOR SCANNING ELECTRON MICROSCOPY FUNDAMENTAL COMPONENTS [171].	52
FIGURE 3.6 A SCHEMATIC DIAGRAM FOR BEAM-SPECIMEN INTERACTIONS [177].	54
FIGURE 3.7 UV-VIS WORKING PRINCIPLE [185].	55
FIGURE 3.8 A SCHEMATIC DIAGRAM OF THE FT-IR SPECTROMETER [135].....	60
FIGURE 3.9 SCHEMATIC DIAGRAM FOR ROTATIONAL AND VIBRATIONAL ENERGY LEVELS [9]..	61
FIGURE 3.10 SCHEMATIC DIAGRAM OF A DIPOLE MOMENT [9].....	62
FIGURE 3.11 SCHEMATIC DIAGRAMS FOR EXCITATION AND EMISSION PROCESSES IN PHOTOLUMINESCENCE [205].....	65
FIGURE 3.12 SCHEMATIC DIAGRAM FOR THE PHOTOLUMINESCENCE OPERATION PROCEDURE [215].....	66
FIGURE 3.13 A SCHEMATIC DIAGRAM FOR THE COLOUR MATCHING EXPERIMENT [217].	69
FIGURE 3.14 THE EVOLUTION OF THE CIE CHROMATICITY DIAGRAM [219].	70
FIGURE 4.1. THE FULL XRD PATTERNS OF $ZN_4B_6O_{13}:xSM^{3+}$ (WHERE $x = 0, 1\%$) NANOPHOSPHORS PREPARED BY VARIOUS SYNTHESIS TECHNIQUES: (A) COMBUSTION, (B) SOL-GEL, (C) SOLID-STATE REACTION METHOD AND (D) XRD DIFFRACTION BARS FOR $ZN_4B_6O_{13}$ MATRICES (JCPDS No: 01-086-0917).	74

FIGURE 4.2: FIELD-EMISSION SCANNING ELECTRON MICROSCOPY (FE-SEM), IMAGES OF $Zn_4B_6O_{13}:xSm^{3+}$ (WHERE $x = 0, 1\%$) NANOPHOSPHORS PREPARED BY VARIOUS CHEMICAL TECHNIQUES: (A), COMBUSTION (B), SOL-GEL (C) SOLID-STATE REACTION METHODS.	77
FIGURE 4.2: ELEMENTAL DISPERSIVE SPECTROSCOPY (EDS) AND ELEMENTAL MAPPING IMAGES OF $Zn_4B_6O_{13}:xSm^{3+}$ (WHERE $x = 0, 1\%$) NANOPHOSPHORS PREPARED BY VARIOUS CHEMICAL TECHNIQUES: (D) COMBUSTION, (E) SOL-GEL, AND (F) SOLID-STATE REACTION METHODS.	78
FIGURE 4.2 HISTOGRAMS DISPLAYING THE AVERAGE PARTICLE SIZE DISTRIBUTION OF $Zn_4B_6O_{13}:xSm^{3+}$ (WHERE $x = 0.1\text{MOL}\%$) NANOPHOSPHORS PREPARED USING (A) COMBUSTION, (B) SOL-GEL, AND (C) SOLID STATE METHODS.	80
FIGURE 4.4: FT-IR SPECTRA OF $Zn_4B_6O_{13}:xSm^{3+}$ (WHERE $x = 0, 1\%$) NANOPHOSPHORS PREPARED BY VARIOUS CHEMICAL TECHNIQUES: (A) SOL-GEL (B) COMBUSTION (C) SOLID-STATE REACTION METHOD.	82
FIGURE 4.5 UV-VIS DRS SPECTRA OF $Zn_4B_6O_{13}:xSm^{3+}$ (WHERE $x = 0, 1\%$) NANOPHOSPHORS PREPARED BY VARIOUS CHEMICAL TECHNIQUES: (A) SOL-GEL (B) COMBUSTION (C) SOLID-STATE REACTION METHOD.	84
FIGURE 4.6 OPTICAL BANDGAP CALCULATIONS OF $Zn_4B_6O_{13}:xSm^{3+}$ (WHERE $x = 0, 1\%$) NANOPHOSPHORS PREPARED BY VARIOUS CHEMICAL TECHNIQUES: (A) SOL-GEL (B) COMBUSTION (C) SOLID-STATE REACTION METHOD. THE LINE REPRESENTS THE BEST LINEAR FIT TO DETERMINE THE OPTICAL BAND GAP.	85
FIGURE 4.7 (A), (B) PHOTOLUMINESCENCE EXCITATION AND (C), (D) EMISSION SPECTRA OF $Zn_4B_6O_{13}:xSm^{3+}$ (WHERE $x = 0, 1\%$) NANOPHOSPHORS PREPARED BY VARIOUS CHEMICAL TECHNIQUES: (1) SOL-GEL (2) COMBUSTION (3) SOLID-STATE REACTION METHOD USING THE PARAMETERS OF $\lambda_{EMI} = 657 \text{ NM}$ AND $\lambda_{EXC} = 226, 408 \text{ NM}$ WAVELENGTHS.	88
FIGURE 4.8 LIFETIME DECAY PROFILES OF $Zn_4B_6O_{13}:xSm^{3+}$ (WHERE $x = 0, 1\%$) NANOPHOSPHORS PREPARED BY VARIOUS CHEMICAL TECHNIQUES: (A) SOL-GEL (B) COMBUSTION (C) SOLID-STATE REACTION METHOD.	91
FIGURE 4.9 CIE COLOUR DIAGRAM OF $Zn_4B_6O_{13}:xSm^{3+}$ (WHERE $x = 0, 1\%$) NANOPHOSPHORS PREPARED BY VARIOUS CHEMICAL TECHNIQUES: (A) SOL-GEL (B) COMBUSTION (C) SOLID-STATE REACTION METHOD.	93
FIGURE 5.1. THE FULL XRD PATTERNS OF $Zn_4B_6O_{13}:xEu^{3+}$ (WHERE $x = 0, 1\%$) NANOPHOSPHORS PREPARED BY VARIOUS CHEMICAL TECHNIQUES: (A) SOL-GEL (B) COMBUSTION (C) SOLID-STATE REACTION METHODS.	97
FIGURE 5.2: FIELD-EMISSION SCANNING ELECTRON MICROSCOPY (FE-SEM) IMAGES OF $Zn_4B_6O_{13}:xEu^{3+}$ (WHERE $x = 0, 1\%$) NANOPHOSPHORS PREPARED BY VARIOUS CHEMICAL TECHNIQUES: (A) SOL-GEL, (B) COMBUSTION, AND (C) SOLID-STATE REACTION METHODS.	100
FIGURE 5.2: ELEMENTAL DISPERSIVE SPECTROSCOPY (EDS) IMAGES OF $Zn_4B_6O_{13}:xEu^{3+}$ (WHERE $x = 0, 1\%$) NANOPHOSPHORS PREPARED BY VARIOUS CHEMICAL TECHNIQUES: (D) SOL-GEL, (E) COMBUSTION, AND (F) SOLID-STATE REACTION METHODS.	101
FIGURE 5.3 HISTOGRAMS DISPLAYING THE AVERAGE PARTICLE SIZE DISTRIBUTION OF $Zn_4B_6O_{13}:xEu^{3+}$ NANOPHOSPHORS PREPARED WITH (A) SOL-GEL, (B) COMBUSTION, AND (C) SOLID-STATE METHODS.	102

FIGURE 5.4: FT-IR SPECTRA OF $Zn_4B_6O_{13}:xEu^{3+}$ (WHERE $x = 0, 1\%$) NANOPHOSPHORS PREPARED BY VARIOUS CHEMICAL TECHNIQUES: (A) SOL-GEL (B) COMBUSTION (C) SOLID-STATE REACTION METHOD.	103
FIGURE 5.5: UV-VIS DRS SPECTRA OF $Zn_4B_6O_{13}:xEu^{3+}$ (WHERE $x = 0, 1\%$) NANOPHOSPHORS PREPARED BY VARIOUS CHEMICAL TECHNIQUES: SOL-GEL, COMBUSTION, AND SOLID-STATE REACTION METHOD.	105
FIGURE 5.6: OPTICAL BANDGAP CALCULATIONS OF $Zn_4B_6O_{13}:xEu^{3+}$ (WHERE $x = 0, 1\%$) NANOPHOSPHORS PREPARED BY VARIOUS CHEMICAL TECHNIQUES: (A) SOL-GEL (B) COMBUSTION (C) SOLID-STATE REACTION METHOD. THE LINE REPRESENTS THE BEST LINEAR FIT TO DETERMINE THE ENERGY BAND GAP.	106
FIGURE 5.7: (A), (B) PHOTOLUMINESCENCE EXCITATION AND (C), (D) EMISSION SPECTRA OF $Zn_4B_6O_{13}:xEu^{3+}$ (WHERE $x = 0, 1\%$) NANOPHOSPHORS PREPARED BY VARIOUS CHEMICAL TECHNIQUES: (1) SOL-GEL (2) COMBUSTION (3) SOLID-STATE REACTION METHOD USING THE PARAMETERS OF $\lambda_{EMI} = 614$ NM AND $\lambda_{EXC} = 246, 395$ NM WAVELENGTHS.....	108
FIGURE 5.8: LIFETIME DECAY PROFILES OF $Zn_4B_6O_{13}:xEu^{3+}$ (WHERE $x = 0, 1\%$) NANOPHOSPHORS PREPARED BY VARIOUS CHEMICAL TECHNIQUES: (A) SOL-GEL (B) COMBUSTION (C) SOLID-STATE REACTION METHOD USING THE PARAMETERS OF $\lambda_{EMI} = 614$ NM AND $\lambda_{EXC} = 246$ NM WAVELENGTHS.	109
FIGURE 5.9: LIFETIME DECAY PROFILES OF $Zn_4B_6O_{13}:xEu^{3+}$ (WHERE $x = 0, 1\%$) NANOPHOSPHORS PREPARED BY VARIOUS CHEMICAL TECHNIQUES: (A) SOL-GEL (B) COMBUSTION (C) SOLID-STATE REACTION METHOD USING THE PARAMETERS OF $\lambda_{EMI} = 614$ NM AND $\lambda_{EXC} = 395$ NM WAVELENGTHS.	110
FIGURE 5.10: CIE COLOUR DIAGRAM OF $Zn_4B_6O_{13}:xEu^{3+}$ (WHERE $x = 0, 1\%$) NANOPHOSPHORS PREPARED BY VARIOUS CHEMICAL TECHNIQUES: SOL-GEL, COMBUSTION, AND SOLID-STATE REACTION METHOD.	112
FIGURE 6.1: THE FULL XRD PATTERNS OF $Zn_4B_6O_{13}:xDy^{3+}$ (WHERE $x = 0, 1\%$) NANOPHOSPHORS PREPARED BY VARIOUS CHEMICAL TECHNIQUES: (A) SOL-GEL (B) COMBUSTION (C) SOLID-STATE REACTION METHOD.	116
FIGURE 6.2: FIELD-EMISSION SCANNING ELECTRON MICROSCOPY (FE-SEM) IMAGES OF $Zn_4B_6O_{13}:xDy^{3+}$ (WHERE $x = 0, 1\%$) NANOPHOSPHORS PREPARED BY VARIOUS CHEMICAL TECHNIQUES: (A) SOL-GEL (B), COMBUSTION, AND (C) SOLID-STATE REACTION METHODS.	118
FIGURE 6.2: ELEMENTAL DISPERSIVE SPECTROSCOPY (EDS) AND ELEMENTAL MAPPING IMAGES OF $Zn_4B_6O_{13}:xDy^{3+}$ (WHERE $x = 0, 1\%$) NANOPHOSPHORS PREPARED BY VARIOUS CHEMICAL TECHNIQUES: (D) SOL-GEL, (E) COMBUSTION, AND (F) SOLID-STATE REACTION METHOD.....	119
FIGURE 6.3 HISTOGRAMS DISPLAYING THE AVERAGE PARTICLE SIZE DISTRIBUTION OF $Zn_4B_6O_{13}:Dy^{3+}$ NANOPHOSPHORS PREPARED WITH (A) COMBUSTION, (B) SOL-GEL, AND (C) SOLID-STATE METHODS.....	120
FIGURE 6.4: FT-IR SPECTRA OF $Zn_4B_6O_{13}:xDy^{3+}$ (WHERE $x = 0, 1\%$) NANOPHOSPHORS PREPARED BY VARIOUS CHEMICAL TECHNIQUES: (A) SOL-GEL (B) COMBUSTION (C) SOLID-STATE REACTION METHOD.	121
FIGURE 6.5: UV-VIS DRS SPECTRA OF $Zn_4B_6O_{13}:xDy^{3+}$ (WHERE $x = 0, 1\%$) NANOPHOSPHORS PREPARED BY VARIOUS CHEMICAL TECHNIQUES: (A) SOL-GEL (B) COMBUSTION (C) SOLID-STATE REACTION METHOD.	123

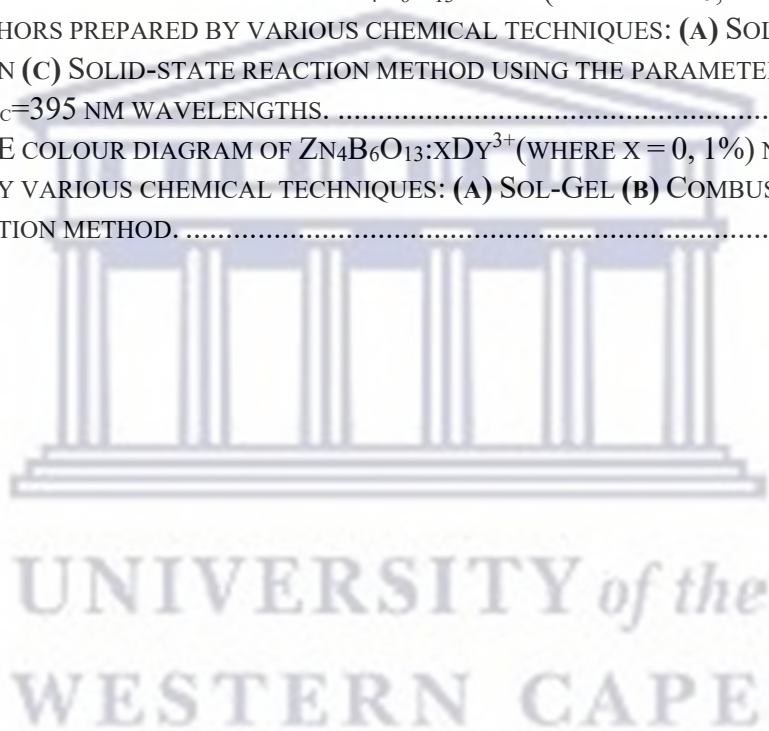
FIGURE 6.6. OPTICAL BANDGAP CALCULATIONS OF $Zn_4B_6O_{13}:xDY^{3+}$ (WHERE $x = 0, 1\%$) NANOPHOSPHORS PREPARED BY VARIOUS CHEMICAL TECHNIQUES: (A) SOL-GEL (B) COMBUSTION (C) SOLID-STATE REACTION METHOD. THE LINE REPRESENTS THE BEST LINEAR FIT TO DETERMINE THE ENERGY BAND GAP. 124

FIGURE 6.7. (A), (B) PHOTOLUMINESCENCE EXCITATION AND (C), (D) EMISSION SPECTRA OF $Zn_4B_6O_{13}:xDY^{3+}$ (WHERE $x = 0, 1\%$) NANOPHOSPHORS PREPARED BY VARIOUS CHEMICAL TECHNIQUES: (1) SOL-GEL (2) COMBUSTION (3) SOLID-STATE REACTION METHOD USING THE PARAMETERS OF $\lambda_{EMI} = 534$ NM AND $\lambda_{EXC} = 228, 356$ NM WAVELENGTHS..... 127

FIGURE 6.8. LIFETIME DECAY PROFILES OF $Zn_4B_6O_{13}:xDY^{3+}$ (WHERE $x = 0, 1\%$) NANOPHOSPHORS PREPARED BY VARIOUS CHEMICAL TECHNIQUES: (A) SOL-GEL (B) COMBUSTION (C) SOLID-STATE REACTION METHOD USING THE PARAMETERS OF $\lambda_{EMI} = 536$ NM AND $\lambda_{EXC} = 228$ NM WAVELENGTHS. 128

FIGURE 6.9. LIFETIME DECAY PROFILES OF $Zn_4B_6O_{13}:xEU^{3+}$ (WHERE $x = 0, 1\%$) NANOPHOSPHORS PREPARED BY VARIOUS CHEMICAL TECHNIQUES: (A) SOL-GEL (B) COMBUSTION (C) SOLID-STATE REACTION METHOD USING THE PARAMETERS OF $\lambda_{EMI} = 614$ NM AND $\lambda_{EXC} = 395$ NM WAVELENGTHS. 129

FIGURE 6.10. CIE COLOUR DIAGRAM OF $Zn_4B_6O_{13}:xDY^{3+}$ (WHERE $x = 0, 1\%$) NANOPHOSPHORS PREPARED BY VARIOUS CHEMICAL TECHNIQUES: (A) SOL-GEL (B) COMBUSTION (C) SOLID-STATE REACTION METHOD. 131



List of Tables

TABLE 1.1 DIFFERENT TYPES OF LUMINESCENCE AND THEIR CORRESPONDING SOURCES OF EXCITATION.	2
TABLE 2.1 SUMMATIVE TABLE FOR THE CHARACTERISTICS OF THE ZnO PHOSPHORS PREPARED VIA SOL-GEL, COMBUSTION, AND SOLID-STATE REACTION METHODS [111], [113].	39
TABLE 4.1. CRYSTALLITE SIZE OF $Zn_4B_6O_{13}:xSm^{3+}$ (WHERE $x = 0, 1\%$) NANOPHOSPHORS PREPARED BY VARIOUS SYNTHESIS TECHNIQUES: (1) SOL-GEL, (2) COMBUSTION, AND (3) SOLID-STATE REACTION METHOD.	75
TABLE 4.2. OPTICAL BANDGAP VALUES OF THE $Zn_4B_6O_{13}:xSm^{3+}$ (WHERE $x = 0, 1\%$) NANOPHOSPHORS PREPARED BY VARIOUS CHEMICAL TECHNIQUES: (1,2) SOL-GEL (3,4) COMBUSTION (5,6) SOLID-STATE REACTION METHOD.	87
TABLE 4.3. AVERAGE LIFETIME DECAY VALUES OF $Zn_4B_6O_{13}:xSm^{3+}$ (WHERE $x = 0, 1\%$) NANOPHOSPHORS PREPARED BY VARIOUS CHEMICAL TECHNIQUES: (1) SOL-GEL (2) COMBUSTION AND (3) SOLID-STATE REACTION METHOD.	92
TABLE 4.4. CIE COLOUR CO-ORDINATES OF $Zn_4B_6O_{13}:xEu^{3+}$ (WHERE $x = 0, 1\%$) NANOPHOSPHORS PREPARED BY VARIOUS CHEMICAL TECHNIQUES: (1) SOL-GEL (2) COMBUSTION AND (3) SOLID-STATE REACTION METHOD.	93
TABLE 5.1. CRYSTALLITE SIZE OF $Zn_4B_6O_{13}:xEu^{3+}$ (WHERE $x = 0, 1\%$) NANOPHOSPHORS PREPARED BY VARIOUS CHEMICAL TECHNIQUES: (1) SOL-GEL (2) COMBUSTION AND (3) SOLID-STATE REACTION METHOD.	98
TABLE 5.2. OPTICAL BANDGAP VALUES OF THE $Zn_4B_6O_{13}:xEu^{3+}$ (WHERE $x = 0, 1\%$) NANOPHOSPHORS PREPARED BY VARIOUS CHEMICAL TECHNIQUES: (1,2) SOL-GEL (3,4) COMBUSTION (5,6) SOLID-STATE REACTION METHOD.	107
TABLE 5.3. AVERAGE LIFETIME DECAY VALUES OF $Zn_4B_6O_{13}:1\%Eu^{3+}$ NANOPHOSPHORS PREPARED BY VARIOUS CHEMICAL TECHNIQUES: (1) SOL-GEL (2) COMBUSTION AND (3) SOLID-STATE REACTION METHOD.	110
TABLE 5.4. CIE COLOUR CO-ORDINATES OF $Zn_4B_6O_{13}:xEu^{3+}$ (WHERE $x = 0, 1\%$) NANOPHOSPHORS PREPARED BY VARIOUS CHEMICAL TECHNIQUES: (1) SOL-GEL (2) COMBUSTION AND (3) SOLID-STATE REACTION METHOD.	112
TABLE 6.1. CRYSTALLITE SIZE OF $Zn_4B_6O_{13}:xDy^{3+}$ (WHERE $x = 0, 1\%$) NANOPHOSPHORS PREPARED BY VARIOUS CHEMICAL TECHNIQUES: (1) SOL-GEL (2) COMBUSTION AND (3) SOLID-STATE REACTION METHOD.	117
TABLE 6.2. OPTICAL BANDGAP VALUES OF THE $Zn_4B_6O_{13}:xDy^{3+}$ (WHERE $x = 0, 1\%$) NANOPHOSPHORS PREPARED BY VARIOUS CHEMICAL TECHNIQUES: (1,2) SOL-GEL (3,4) COMBUSTION (5,6) SOLID-STATE REACTION METHOD.	125
TABLE 6.3. AVERAGE LIFETIME DECAY VALUES OF $Zn_4B_6O_{13}:1\%Dy^{3+}$ NANOPHOSPHORS PREPARED BY VARIOUS CHEMICAL TECHNIQUES: (1) SOL-GEL (2) COMBUSTION AND (3) SOLID-STATE REACTION METHOD.	129
TABLE 6.4. CIE COLOR CO-ORDINATES OF $Zn_4B_6O_{13}:xDy^{3+}$ (WHERE $x = 0, 1\%$) NANOPHOSPHORS PREPARED BY VARIOUS CHEMICAL TECHNIQUES: (1) SOL-GEL (2) COMBUSTION AND (3) SOLID-STATE REACTION METHOD.	132

List of abbreviations

CIE	Commission Internationale de l'Éclairage
DRS	Diffuse Reflection Spectra
EDS	Energy-Dispersive X-ray Spectroscopy
FE-SEM	Field Emission Scanning Electron Microscopy
FTIR	Fourier Transform Infrared
JCPDS	International Centre for Diffraction Data
KM	Kubelka-Munk
LED	Light Emitting Diode
NIR	Near Infrared
PL	Photoluminescence
PLE	Photoluminescence Excitation Spectroscopy
RE	Rare Earth
SEM	Scanning Electron Microscopy
FE-SEM	Field Emission Scanning Electron Microscopy
UV-Vis	Ultraviolet Visible spectroscopy
XRD	X-Ray Diffraction
Sm ³⁺	Samarium
Eu ³⁺	Europium
Dy ³⁺	Dysprosium

Chapter I

Introduction

1.1 Materials and their Classification

Materials are classified into four main groups, namely composites, ceramics, polymers, and metals depending on their chemical and physical characteristics. At standard conditions, they are found in the three phases of matter: solid, liquid, and gas. Whenever monochromatic light is directed towards a sample, it may either be absorbed, reflected, or transmitted through the sample. Only photons of energy greater or equal to the bandgap of solids will be absorbed. The chromaticity colour system detects and interprets the reflected and transmitted light to deduce the emission colour of the sample. [1] Certain materials tend to emit light in response to incident electromagnetic radiation, chemical processes, electron transitions, changes in energy sources, and photoexcitation [2], [3], [4], [5]. The materials mentioned above are referred to as luminescent materials due to their absorption and uncontrolled emission of light. Luminescence is significant in our daily lives, particularly in digital colour technology. Luminescent materials somehow replace the sunlight during the night [2], [3], [6]. The table below displays an overview of the different types of excitation modes for various forms of luminescence.

UNIVERSITY *of the*
WESTERN CAPE

Table 1.1 Different types of luminescence and their corresponding sources of excitation.

Types of luminescence	Excitation mode
Photoluminescence	UV, visible absorption of photons
Electroluminescence	Electric field/current
Thermoluminescence	Radioactive irradiation
Chemiluminescence	Chemical reaction
Bioluminescence	Biochemical reaction
Sonoluminescence	Ultrasound
Triboluminescence	Frictional and electrostatic force
Radioluminescence	Ionizing radiation (X-rays, α, β, γ)
Cathodoluminescence	Cathode rays

Light, being a kind of electromagnetic energy, may exist in two forms, namely incandescence and luminescence [7]. Incandescent light is formed when a substance is heated to a high temperature until it glows, and luminescence light is produced when the same material is activated by high-energy light sources [7], [8]. During the luminescence process, an electron is pushed from the lower energy state (ground state) to a higher energy state (excited state) by absorbing energy from an external light source. When an excited electron returns to its ground state, it releases energy in the form of light. However, certain electrons in the excited state relax non-radioactively without releasing light due to lattice phonon interactions[9], [10], [11].

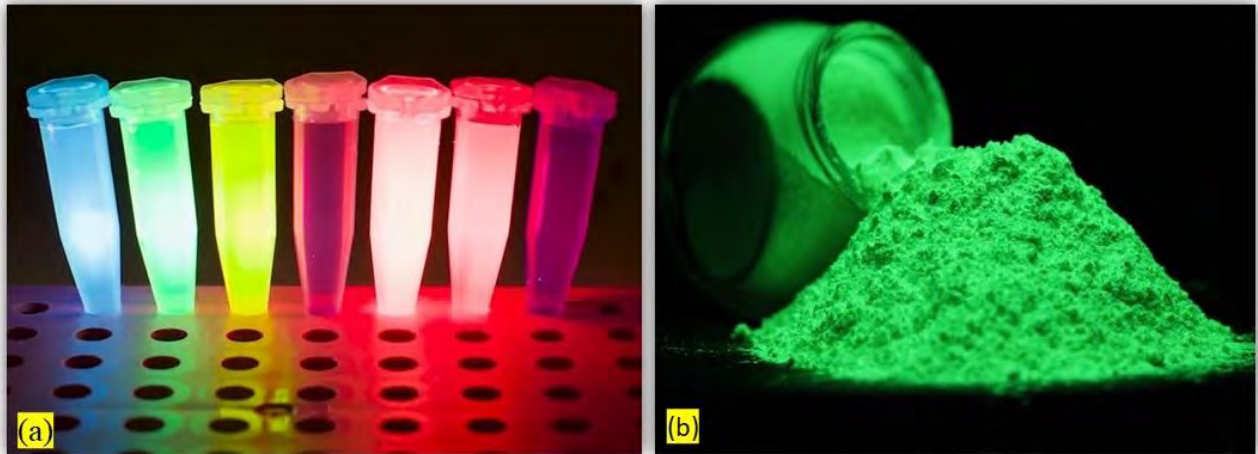


Figure 1.1 (a) Fluorescence and (b) Phosphorescence occurrences of colour [12], [13].

Luminescence can be classified in two processes: fluorescence or phosphorescence, depending on the duration of the remission of light. In fluorescence, emission occurs concurrently with ultraviolet (UV) radiation absorption and stops instantly when the source is removed [7], [14]. The mechanism of this process involves the UV light directed towards the sample, the absorption process occurs, and the electron transits from the ground state to the singlet excited state, whereby its spin does not change. The electron then immediately releases energy in the form of light while falling back to the ground state. This process continuously occurs whenever the material is subjected to a light source; it can typically last between 10^{-10} and 10^{-7} seconds. However, in phosphorescence, the process is vice versa; the emission of light continues for some time after a light source is removed from the material; this is called an afterglow [9], [10]. Conversely, in the phosphorescence process, a material absorbs UV energy, an electron is excited from the ground state to the triplet excited state, and the spin multiplicity of the electron is not maintained. The absorbed energy in the form of light is slowly released when an electron reverses its spin and returns to the ground state. The wavelength of the incident radiation to the material is always shorter than that of the emitted radiation in both processes; this is due to the emitted electron relaxing to its lowest vibrational level in the excited state [7], [8], [15], [15], [16], [17]. The average time for the emission of light after the excitation source is removed from the material is from 10^{-5} to 10^{+3} seconds, and this can occur for hours or even days [18]. **Figure 1.1** shows the manifestation of fluorescence and phosphorescence in materials.

1.2 Materials in the nano range

Nanomaterials are small-sized materials with at least one of their dimensions ranging from 1 to 100 nm. One nanometer is equivalent to a billionth of a meter (10^{-9} m), which is equivalent to the length of 10 hydrogen atoms aligned. These materials are more efficient in numerous applications due to their distinctive optical, chemical, and physical characteristics. Moreover, they have a high surface area and a low melting point compared to bulk materials [18], [19], [20].



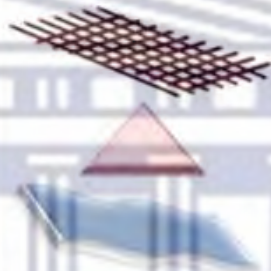

Isotropic nanomaterials	Anisotropic nanomaterials		
			
0D	1D	2D	3D
Spheres, Clusters	Nanorods, wires	Nanofilms, plates	Nanoparticles

Figure 1.2 Nanomaterials and their dimensions [20].

Figure 1.2 shows the classification of nanomaterials in various dimensions: zero-dimensional (0-D), these are in spherical shape and are confined in all directions, e.g., quantum dots, while one-dimensional (1-D) are confined in two directions, for instance, nanorods and nanotubes. The thickness of the two-dimensional (2-D) nanomaterials is less than 100 nm, e.g., nanofilms. There is no quantum confinement in the three-dimensional (3-D) nanoparticles since they extend in all dimensions, e.g., graphite [19], [21]. Nanomaterials can be fabricated through two synthesis approaches: top-down and bottom-up. In the top-down method, a material of large scale is broken down into smaller pieces, which are at the nanoscale level. The following: milling and laser ablation are the physical methods applied to breaking down a material. However, the physical interaction between the tool and the material during the syntheses might affect the surface properties of the product material. Conversely, the bottom-up approach requires the assembling of atoms or molecules together until they form a product on the nanoscale. This approach is made successful by the following synthesis routes, including but not limited to: sol-gel, chemical vapour deposition, and molecular beam epitaxy, depending on

the desired material [21], [22]. Nanomaterials may be synthesized for numerous applications, including those reported by Dreaden et al. [23], 2012, on the use of nanomaterials in bio-imaging. Reports have been made regarding the use of nanomaterials by Luoreiro et al. [24] (2016) in biological sciences, biomedical, and pharmaceutical applications as they played a major role in drug delivery. Other applications include their use in manufacturing solid-state batteries and solar cells for energy. The quantum dots are used in the manufacturing of cell phones [22], [25], [26].

1.3 Introduction to phosphors materials

Phosphors are crystalline substances that emit visible light, they may exist as thin films or powders; they can convert incident energy into visible light. These materials may be classified as luminescent materials, having the capability of emitting light when excited by radiation such as X-rays, high-energy particles, gamma rays, infrared, visible light, ultraviolet light, and matter vibrations (phonons) [27], [27], [28]. There are various forms of phosphors depending on their uses, namely oxyhalides, aluminates, phosphates, and borates. The phosphors in the form of host materials may be incorporated with different rare earth ions dopants to enhance their luminescence emissions. The arrangement of the host material's crystal structure influences the placement and dopant ion energy levels inside the phosphor material. Moreover, it enhances the emission properties of the phosphor material and the effectiveness of the energy transmission for luminescence. The most frequent excitation techniques include X-rays ranging in keV typically used by scintillation detectors, ultraviolet emission, blue excitation in the range of 450–470 nm, and cathode rays due to the feasibility of excitation by radiation and other sources with high energy [29], [30], [31], [32], [33], [34], [35].

1.4 Classification of phosphors and their structures

There are two primary categories of phosphor materials: organic and inorganic phosphors.

1.4.1 Organic phosphors

Organic phosphors are luminous materials that are capable of various light emissions without requiring the addition of a dopant. These phosphors have a weak absorption of visible light. Furthermore, they are mostly synthesized from carbon- and nitrogen-based compounds. Organic phosphors are used in the manufacturing of organic light-emitting diodes (OLED), mostly in optoelectronics, and in fluorescent organic dyes, which are used in dye lasers. The organic phosphors contain stilbene derivatives, which make them more suitable for use in advertising paints and in banknotes as transparent markers [36], [37], [38], [39]. Moreover, they are used as fluorescence tissue in stamps, identity cards, laundry markers, and in microscopy. However, there are some drawbacks regarding organic phosphors, such as insufficient light stability and low water solubility, when they are in their bulk form [1], [38], [39].

1.4.2 Inorganic phosphors

Inorganic phosphors are luminescent materials that are made up of crystalline compounds as host materials that are doped with activator metal ions, such as rare earth ions. Examples of doped materials are nitride, oxyhalide, silicate, oxynitride, selenide, etc. Inorganic phosphors have a wide band gap and are only able to emit a lower colour rendering index (CRI) [40], [41]. When rare earth ions are introduced as dopants into a material, they serve as luminescent centers owing to their following characteristics: high luminescence, adjustable colour emissions, and exceptional chemical stability, especially when combined with various rare earth metals [40], [41], [42].

Rare earth ions can be classified into the weak and the strong interacting groups with the host material. The weak interacting group consists of elements with valence electrons in the d-subshell (lanthanide ions). The emission of light in these ions usually depends on the electron transition between the f-orbitals. These transitions produce a distinctive straight-line emission spectrum due to the protection of the f-orbitals within their coordinate environment [1]. On the

contrary, the strong interacting group of rare-earth ions experiences strong interactions with the host lattice. The observable interactions between the d-orbitals of these ions and the host material led to the generation of broad spectral bands. This interaction increases degeneracy and results in a variety of energy states [38], [39]. The characteristics of inorganic materials are significantly influenced by the choice of activators and also the concentration, charge, and symmetry of the surrounding environment. Historically, alkaline earth ions such as Mg^{2+} , Ca^{2+} , Sr^{2+} , and Ba^{2+} have been highly regarded for their ability to enhance the brightness of specific phosphor materials [43], [44]. **Figure 1.3** below shows the geometric crystal structure of various alkaline earth ions.

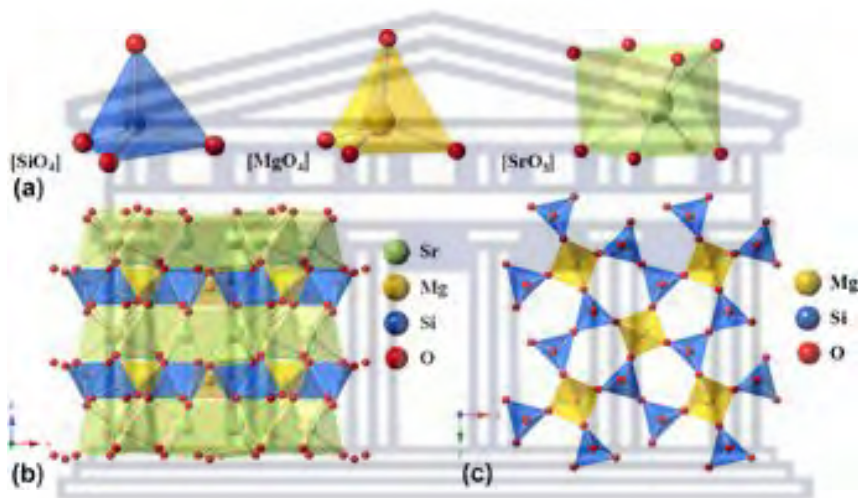


Figure 1.3 Schematic representation of different WLED phosphors made from Ce^{3+} and Tb^{3+} doped alkaline-earth silicate $\text{Sr}_2\text{MgSi}_2\text{O}$ crystal structures [45].

1.5 Introduction of different synthesis methods for phosphor preparation

Numerous synthesis techniques are used in the preparation of nanophosphors. However, each method is implied to meet specific phosphor requirements based on its intended application. Below are some typical synthesizing procedures for nanophosphors.

1.5.1 Combustion

Combustion is a synthesis method that involves a quick exothermic reaction between a fuel and an oxidizer as precursors, such as citric acid and metal nitrate, respectively. The precursors are carefully mixed in deionised water to form an aqueous solution, which is then placed in a furnace where it is heated to high temperatures that could reach up to 1000 °C for a few hours, depending on the desired product. During the combustion process, the metal nitrates are broken down into metal oxides. The heated sample is then removed from the furnace, cooled, and crushed into a fine powder as a product [46], [47]. **Figure 1.4** shows the flow diagram of the combustion synthesis process. This method produces high-purity crystalline oxide powders, which are typically dry. Various studies have been reported on the synthesis of phosphors using the combustion method. This is due to its numerous potential benefits, such as low preparation costs, high production rates, reduced preparation time, and direct crystallization [22], [48], [49], [50], [51].

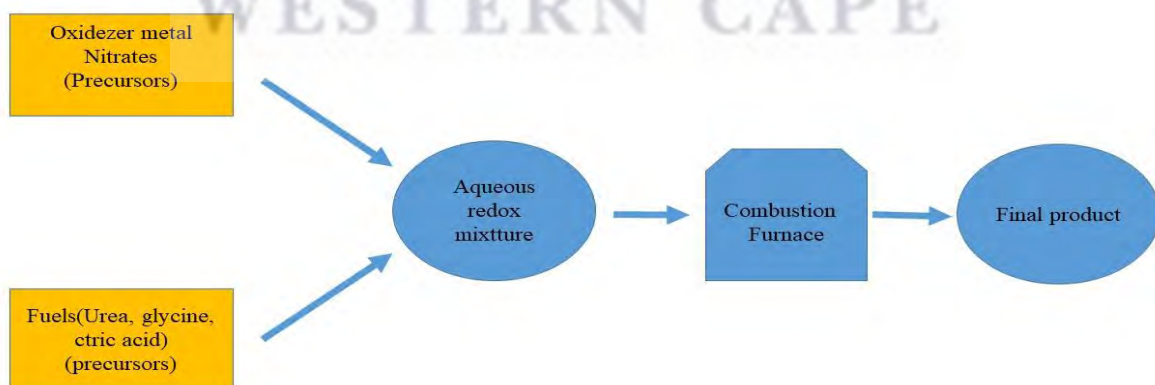


Figure 1.4 Schematic presentation for synthesis of nanophosphors using combustion method [48].

1.5.2 Sol-gel

Sol-gel is a bottom-up method of synthesis that forms a gel-like substance as a product. It is used in the preparation of various nanostructures, specifically nanoparticles of metal oxides. This method is mostly used in the research field because of its capability to attain high homogeneous materials with high purity at a low cost and at a low reaction temperature [52], [53]. The materials obtained through this method are used in various applications, including but not restricted to biosensors, optics, and electronics. This method is classified into two approaches: aqueous and non-aqueous [52], [54], [55]. The aqueous approach involves water as a solvent, while the non-aqueous approach involves organic compounds as solvents. However, the preparation procedure is the same for both approaches. The sol-gel reaction process is as follows: the molecular precursor (usually metal oxide) is dissolved in a solvent, placed on a hot plate, and stirred until there is the formation of a gel. This is an irreversible process. The gel formation is obtained through hydrolysis and condensation processes. Since the gel created is moist, it should undergo a suitable drying process based on its intended purpose and desired characteristics. For example, if the solution is alcoholic, burning alcohol is employed to finalise the drying process. Subsequently, the produced gels undergo calcination after the drying phase. To achieve the desired nanoparticles, the formed gel is ground by special mills to give the final product; refer to **Figure 1.6** [56], [57], [58], [59].

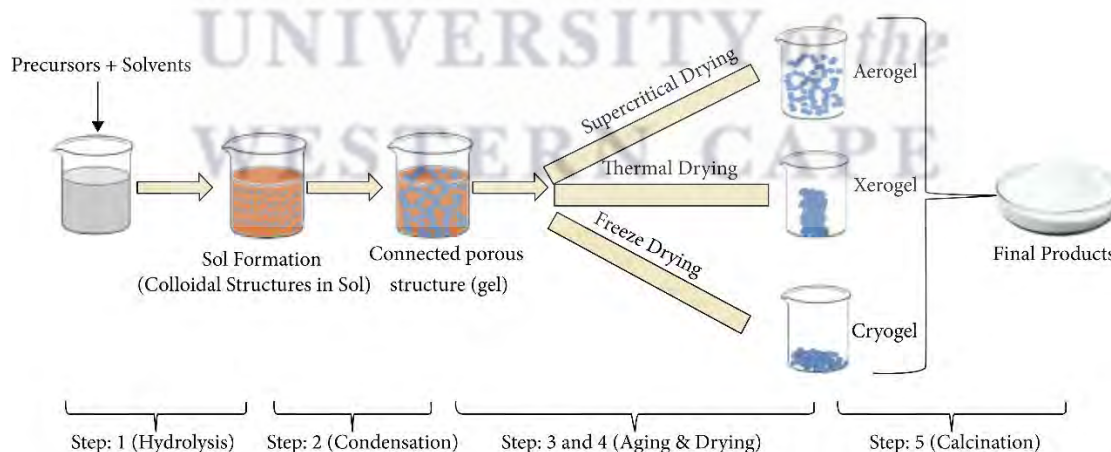


Figure 1.6 Schematic representation of sol-gel method depending on the desired phosphor material [56].

1.5.3 Co-precipitation

Co-precipitation is a synthesis method typically used to prepare phosphors from composite oxide and fluoride precursors. This method does not depend on rare earth ions to produce high-purity phosphors. Moreover, this method is advantageous for obtaining high-crystalline phosphors with improved optical performance [60]. The co-precipitation method is conducted as follows: two precursors are placed in a dissolved Teflon solution, whereby they are evaporated in a concentrated acidic solution until their volume is reduced for the formation of a concentrated solution. A hot, saturated fluoride salt is then added to the solution, leading to precipitate formation [61]. **Figure 1.7** shows the schematic representation of the working principle of the Co-precipitation method. However, this method is time-consuming, and it is more complicated; it requires numerous centrifugations to wash the sample with distilled water to eliminate ions from the precursor's salt solution [56], [57], [59], [62].

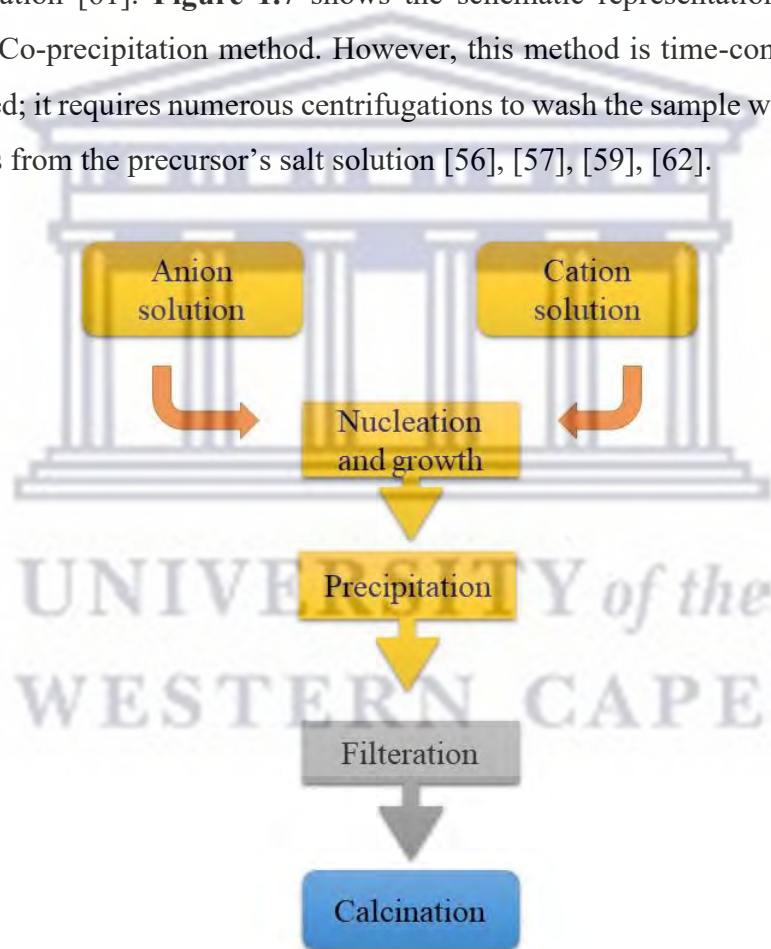


Figure 1.7 A flow diagram for co-precipitation preparation method.

1.5.4 Hydrothermal method

The hydrothermal method, alternatively referred to as the solvothermal method, is a synthesis technique that is mostly used in science to synthesize inorganic compounds, grow crystals, nanoparticles, and other materials. The synthesis method involves the preparation of metal oxides and sulphide precursors solution at room temperature. Their solution is then placed inside a Teflon in an autoclave, a stainless-steel pressure vessel of 101.3 kPa (refer to **Figure 1.8 (a)**), then placed in a microwave, where it is heated to a typical temperature of 373 K; however, the heating temperature may vary depending on the desired product. The solution is then taken out of the microwave for cooling. The cooled solution is then centrifuged with deionised water and filtered to separate the liquid and precipitate. The precipitate is then dried out and calcined; the calcination temperature and period vary based on the desired product, as depicted in **Figure 1.8 (b)** [56]. The hydrothermal process produces crystals or nanoparticles that are challenging to create under ordinary circumstances by taking advantage of the enhanced solubility of many inorganic substances at high temperatures and pressures. It has several applications in nanotechnology, materials science, and other areas, allowing the synthesis of materials with specialized characteristics for different uses [56], [57], [63], [64].

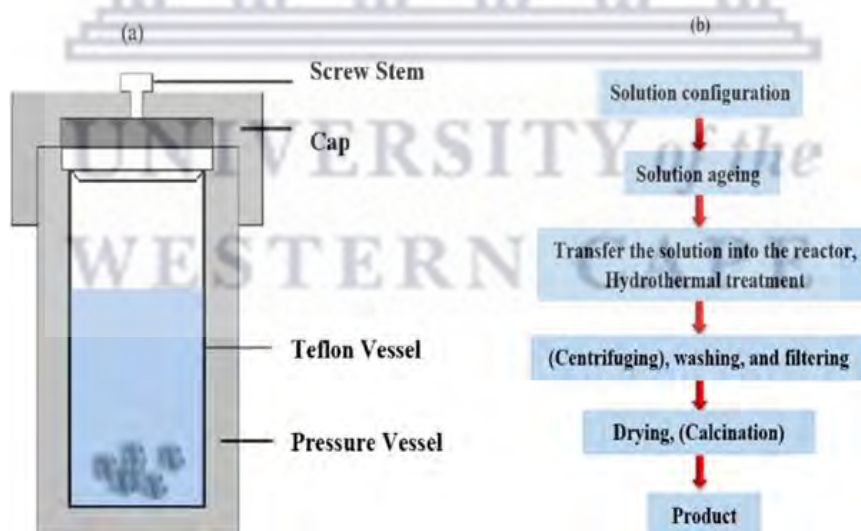


Figure 1.8 A schematic representation for (a) an autoclave (b) hydrothermal method [63].

1.6 Impact of different synthesis methods on structural properties of phosphors

The structural properties of materials: crystallite structure, crystal size, and composition are mainly affected differently by the synthesis method implied. Moreover, the impact on the structural properties affects the general performance of phosphor materials, for instance, luminescence efficiency, emission wavelength, and colour purity. The X-ray diffraction (XRD) method is a characterization technique of choice for structural property studies [61], [65].

1.6.1 Crystalline properties

Various studies have been reported on the impact of a synthesis technique on the crystalline properties of a material. Dwivedi et al. [57] reported on a comparative study for the synthesis of $\text{Ho}^{3+}/\text{Yb}^{3+}$ co-doped YVO_4 phosphor material using combustion, sol-gel, and solid-state methods. According to their XRD investigation, all synthesis methods produced pure-phase crystals; however, the average crystallite sizes of the synthesized particles were different. In addition, they obtained large crystallite sizes at higher temperatures; this is owing to the expansion of the lattice. High temperatures allow more movement of atoms, and as they move, they release energy. However, when the phosphor materials cool down, their lattice strain decreases [58], [61], [66], [67]. The combustion method produced the largest crystallite sizes in comparison to the other two methods. The sol-gel method produced the smallest crystallite size; hence, its photoluminescence spectra showed more prominent luminescence emission than the other two methods. Głuchowski et al. [63] reported a comparative study on the impact of the combustion and sol-gel methods on the structural properties of $\text{Gd}_{3-x}\text{Ce}_x\text{Ga}_3\text{Al}_2\text{O}_{12}$ phosphor material. Their XRD results showed that both methods produced cubic structures. They observed similar luminescence behaviour, as reported by Dwivedi et al. [57]: the combustion method produced a larger crystallite size than the sol-gel method. This arises because in the combustion method, the nitrates act as oxidizing agents; they promote drastic temperature increases, thus causing fast crystal growth that causes expansion in the lattice volume. In sol-gel method, crystal growth is very slow, the slow-paced results from the cross-linking of nitrates in the polymer chains. The addition of the dopant during synthesis also affects the structural properties of a material. Their photoluminescence emission spectra showed more intense emission for the sol-gel method compared to combustion. The low crystallite sizes tend to produce high luminescence intensity, this behaviour results from their

high surface area. For hydrothermal method, it is performed in an autoclave pressure vessel. The high pressure applied by the autoclave vessel compresses the lattice points of the synthesized phosphor material, leading to low crystallite sizes [52], [58], [59].

1.7 Impact of different synthesis methods on morphological properties of phosphors

The morphology of a phosphor material can be influenced differently by various synthesis methods, leading to variations in particle sizes and shapes. Scanning electron microscopy is used for the analysis of the morphology of the prepared phosphors [68].

The morphology of a material mainly depends on the preparation conditions of the raw materials. Depending on the desired applications for the phosphor material, the morphology and particle size can be adjusted [69]. The reaction temperature, preparation time, and pH are the important parameters to note during synthesis, as they influence the morphology of the product material. The increasing pH during synthesis results in high nucleation density and a decrease in particle size [66], [69]. Further studies by Zhang et al. [70] on the synthesis of $\text{Zn}_2\text{SiO}_4:\text{Mn}^{2+}$, reported that an increase in the pH resulted in the increase in rod-length of the particles, this is due to the high nucleation density derived from higher pH [71]. In addition, an increase in pH changes the morphology of particles to uniform size, regular shape, and good dispersion. However, in some materials the decrease in pH causes a decrease in crystallinity [70], [72], [73]. According to Zhang [70] et al upon increasing the reaction temperature, the rod length of the particles increased, rough surfaces became smooth, and particles were in uniform size with good dispersion. Furthermore, an increase in reaction temperature results in the decrease in particle size and reduction of grains. Their studies also indicated that prolonging the reaction time caused a change in the morphology of the prepared particles from olive spherical structure with heavy agglomeration to rod like structures with good dispersion [72], [74], [75]. Das et al. [69] used the conventional hydrothermal method to examine the impact of the synthesis time on $\text{Y}_4\text{Al}_2\text{O}_9$ doped with Eu^{3+} . Their SEM morphology results showed that as the reaction time increased from 2 to 20 hours, the spherical morphology of the sample changed to harad-like structures.

Dwivedi et al. [57] reported on a comparative study for the synthesis of $\text{Ho}^{3+}/\text{Yb}^{3+}$ co-doped YVO_4 phosphor material using combustion, sol-gel, and solid-state methods. Their SEM results revealed that the particles synthesized with sol-gel were more spherical and larger than those from the other two methods. Gluchowski et al. [63] reported on the comparative study of the morphology of $\text{Gd}_{3-x}\text{Ce}_x\text{Ga}_3\text{Al}_2\text{O}_{12}$ phosphor material prepared with combustion and the sol-gel method. The results showed that the combustion method produced irregular grains with a broader crystallite size distribution; the prepared particles were on both the nanometer and micrometer scales. However, the sol-gel method produced particles on the micrometer scale with oval-shaped, smoother grains and a narrower size distribution [57].

1.8 Impact of different synthesis methods on the photoluminescence properties of phosphors

The synthesis method implied may have an impact on the morphology of the phosphor material resulting in the impact on its photoluminescence properties. The change in particle size, band gap, crystal structure, and doping of a host material affects the photoluminescence emission of the synthesized material [69]. The process of photoluminescence involves an electron transition in the energy level diagram, from the ground to the excited state, and from the excited to the ground state, releasing energy in the form of a photon. However, different synthesis methods might affect the energy level diagram, leading to various emissions [76]. The addition of the dopant to the host lattice determines the emission colour and enhances the luminescence emission of the phosphor material. The host transfers the energy to the dopant. Various synthesis methods yield phosphor materials with different particle sizes, which have an impact on their band gap [66]. Larger particles with low crystallite sizes tend to emit high luminescence intensity, this phenomenon arises because larger particles exhibit a lower surface area to volume ratio, resulting in enhanced surface area luminescence [76]. Moreover, low crystallite sizes are known for high luminescence emissions due to their more disordered structure [77].

The temperature used during synthesis plays an important role in the photoluminescence properties of a sample. The quenching process may increase or decrease the photoluminescence properties of a material, as it involves the cooling of a material at a fast rate. Boukerika et al. [78] reported on the synthesis of $\text{Y}_2\text{O}_3:\text{Eu}^{3+}$ phosphor using sol-gel method. Their findings

reported that there were intense luminescence emissions observed after the sample was annealed at higher temperatures. This due to the improved crystallinity due to annealing. Addition of a dopant to the host material also significant in the photoluminescence properties of a material, as the dopants are known as luminescence activators. Zhahedi et al. [79] prepared Ba_2SiO_4 and $\text{Ba}_2\text{SiO}_4:\text{Sm}^{3+}$ phosphors using sol-gel method, they discovered that the doped sample exhibited higher luminescence emissions compared to the undoped. Shinde et al. [66] reported a comparative study on the effect of solid-state and combustion methods on the photoluminescence properties of $\text{Na}_2\text{Sr}_2\text{Al}_2\text{PO}_4\text{Cl}_9$ doped with Ce^{3+} nanophosphor. The samples were excited at 322 nm while monitoring an emission at 376 nm. Their photoluminescence emission spectra showed higher emission in the solid-state method compared to the combustion method. Kang et al. [69] reported that better optical properties such as high luminescence intensity, high colour purity, and high stability are obtained through spherical morphology; this is due to the enhanced packing density and lower scattering.

1.9 ZnO material-based anionic group systems

Anionic groups are chemical compounds with a negative charge, which is due to the excess electrons present in them. These compounds can donate the excess electrons. Moreover, they mostly participate in chemical reactions with positively charged compounds, as they are attracted to the opposite charge through electrostatic forces. The anionic groups also contribute to the stability of some molecules [80], [81]. Depending on the number of excess electrons, they can either be monovalent (-1), divalent (-2), and trivalent (-3). These materials can be substituted in metal oxides to enhance their luminescence properties. These materials can be prepared by various reactions metal hydrides, aryls, and alkyls [82]. Anionic groups can vary widely in their chemical structure. For example, some common anionic groups include sulfate (SO_4^{2-}), nitrate (NO_3^-), carbonate (CO_3^{2-}), and phosphate (PO_4^{3-}). Each of these has a distinct arrangement of atoms. Borate is a π conjugated group which is accepted as one of the most desirable structural groups of non-linear optical materials, it has a trigonal structure [83], [84].

Anionic groups may exhibit different levels of acidity or basicity. For instance, some anions may be part of weak acids, while others may be part of strong bases. Anionic groups can differ in size and molecular weight. Larger anions may have different physical and chemical properties compared to smaller ones. The solubility of compounds containing anionic groups can vary. Some anions are highly soluble in water, while others may not be, depending on factors such as the presence of counterions and the overall chemical structure [80], [81], [85]. Phosphors prepared with ZnO-BO₃, in comparison to pure ZnO phosphors, display superior optical characteristics, such as increased photoluminescence and adjustable emission wavelengths. The crystal structure and thermal stability of the materials can also be affected by the borate groups. The addition of a phosphate group to the zinc oxide material enhances its chemical and thermal stability, as well as its optical and electrical characteristics. Moreover, these phosphors are mostly used in photocatalysis and gas sensing applications. Incorporation of the sulfate groups in the ZnO lattice affects the optical, electrical, and thermal characteristics of the phosphor material. Applications for ZnO-SO₄²⁻ systems in optoelectronics, solar cells, and gas sensing have all been researched [86], [87]. In their study, Letswalo et al. [86] investigated the introduction of sulfate ions (SO₄²⁻) into ZnO: Ce³⁺ nanophosphors to assess their impact on photoluminescence (PL) intensities and the tunability of colour emissions arising from defect states. Zhang et al. [87] reported on the enhancement of luminescence intensities and lifetime in the NaLa(MoO₄)₂:Eu phosphor material resulting from the addition of both SO₄²⁻ and BO₃³⁻ anions.

1.10 Formation of Zn₄B₆O₁₃ compounds and their structural properties

Zinc borate (Zn₄B₆O₁₃) is a cubic crystalline photoluminescent phosphor material that is mainly synthesized from zinc nitrite Zn(NO₂)₂, boric acid H₃BO₃, urea CH₄N₂O and citric acid C₆H₈O₇ as precursors. Moreover, it is isostructural like with sodalite Na₈(Al₆Si₆O₂₄) Cl₂ whereby sodium (Na) atoms are substituted by the zinc (Zn) atoms, while silicon (Si) and aluminium (Al) atoms are replaced by boron (B), and chlorine (Cl) is exchanged for oxygen (O). Within this molecule, all boron atoms coordinate with four oxygen atoms and linked to each other to form a three-dimensional (3-D) (BO₄) tetrahedron structural framework, with a large cavity in which the ZnO₄ tetrahedrons occupy [88]. The crystal structure of this molecule is cubic, whose

lattice parameters are approximately $a = b = c = 7.477 \text{ \AA}$ [89]. **Figure 1.9** shows the sodalite crystal structure of the $\text{Zn}_4\text{B}_6\text{O}_{13}$ phosphor. The reaction equation is as shown below [89], [90]:



$\text{Zn}_4\text{B}_6\text{O}_{13}$ is known as a strong nonlinear optical material with strong absorption coefficients. This molecule has an optical bandgap of 5.8 eV. Its valence and conduction bands are composed of Zn-O anti-bonding characteristics. The valence maximum of this molecule is composed of the hybridized zinc and oxygen d- and p-orbitals, respectively, whereas the conduction maximum is composed of zinc and oxygen s- and p-orbitals, respectively. The d-orbitals represent the localized electronic states, which are responsible for the charge carrier states. This molecule is an indirect semiconductor; its photocatalytic performance comes from its intrinsic electron configuration near the band edge, with efficient photogenerated electrons and holes [89].

This crystalline material, upon UV excitation, shows a strong violet with a strong afterglow. The structural defects of this molecule are responsible for its afterglow [91]. The afterglow is attributed to the presence of thermally unstable, trapped charge carriers at room temperature under UV radiation. The $\text{Zn}_4\text{B}_6\text{O}_{13}$ compound has strongly localized self-trapped excitation states, which are responsible for luminescence properties. Under low-temperature UV radiation, a portion of the generated free charge carriers recombines, resulting in intrinsic violet emission. Whereas another part becomes trapped in electron and hole traps [90]. Its crystal structure reduces the number of possible induced radiation centers. Its bandgap aids in the transition of photogenerated electrons and further improves the absorption of light. The studies conducted by Li et al. [91] for the investigation of the photocatalytic activity of the $\text{Zn}_4\text{B}_6\text{O}_{13}$ phosphor showed that the photocatalytic activity of this phosphor is 5.2 times higher than SnO_2 material, when illuminated with an ultraviolet light source. However, this compound can be doped with various rare earth ions to enhance its characteristics for various applications.

The $\text{Zn}_4\text{B}_6\text{O}_{13}$ phosphor material is dopant-compatible and can be synthesized by various preparation techniques. A large number of researchers have reported on the preparation of $\text{Zn}_4\text{B}_6\text{O}_{13}$ phosphor for various characteristics: Li et al. [91] reported on the synthesis of $\text{Zn}_4\text{B}_6\text{O}_{13}$ doped with Mn^{2+} using solid-state for the investigation of its afterglow effects. Zhao et al. [89] reported on the synthesis of $\text{Zn}_4\text{B}_6\text{O}_{13}:\text{Tb}^{3+}, \text{Yb}^{3+}$ using the solid-state reaction method for the investigation of its multimodal emissions. Lian et al. [90] used the hydrothermal

method to synthesize $Zn_4B_6O_{13}$: Tb/Eu for the investigation of its tunable photoluminescent properties.

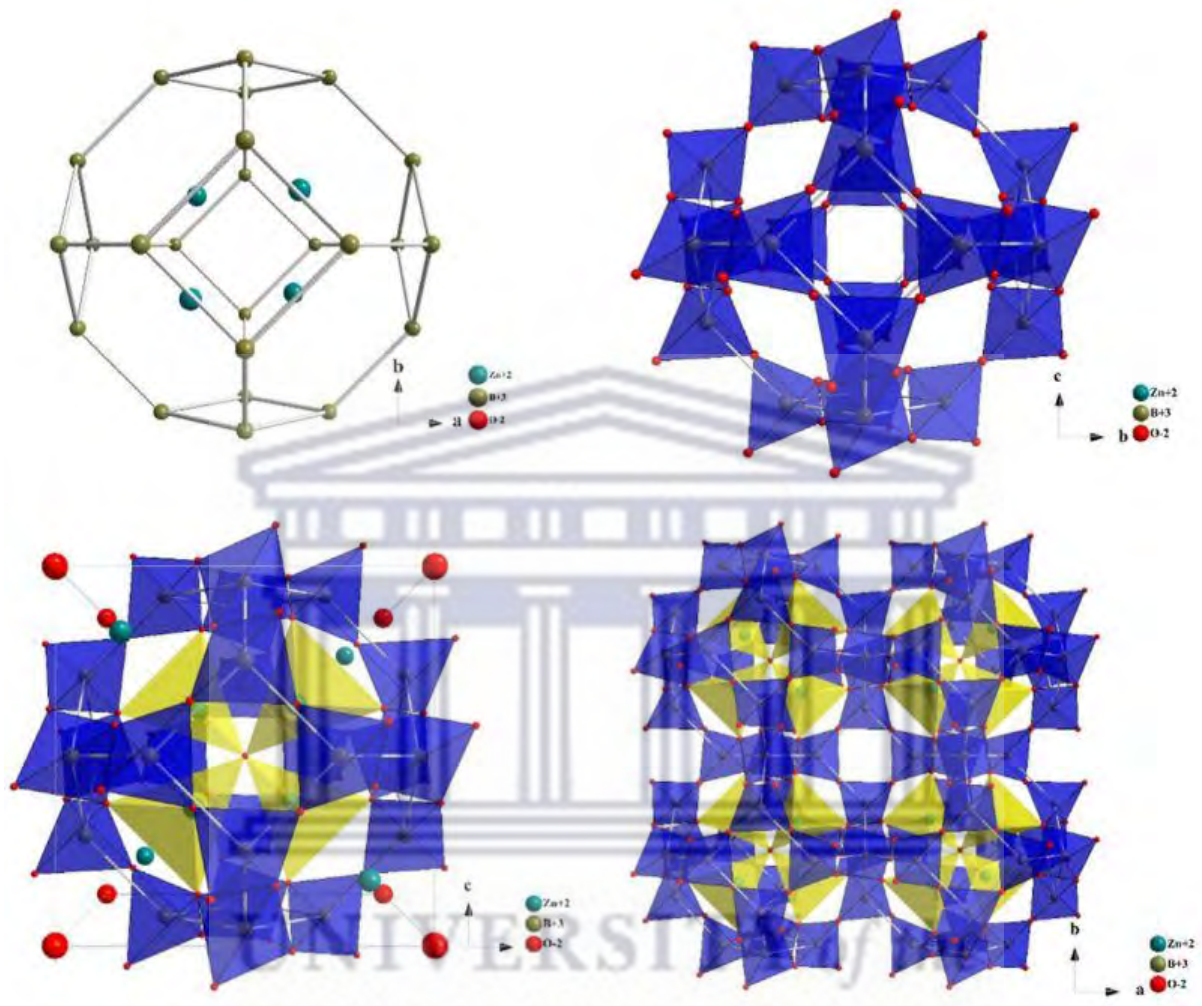


Figure 1.9 The graphic representation of the $Zn_4B_6O_{13}$ crystal structure [88].

1.11 Rare earth ions and their properties

Rare earth (RE) ions consist of a set of 17 closely related elements with atomic numbers ranging from $Sc^{21} \rightarrow Y^{39}$ and $La^{57} \rightarrow Lu^{71}$, where Sc is scandium, Y is yttrium, La is lanthanum, and Lu is lutetium. The superscript is the atomic number of the respective element [92]. RE ions find valuable applications in phosphor materials as sources of colourful emissions. This is due to their ability to produce various emissions when doped in host materials; however, the emission colour depends on the dopant used. These emissions are a result of the discrete energy

levels dictated by the configurations of their 4f electrons. The outer 5p⁶ and 5s² electrons within their electron configuration occupy orbitals that shield and separate the 4f electrons, preventing the latter from participating in bonding interactions and maintaining their distinctive, free ion-like behaviour. The similarity behaviour among the RE ions is due to the nature of their highly localized 4f electrons, as they are nonbonding. These 4f electrons determine the optical behaviour of the phosphor material they are incorporated into [48]. The transitions within the f orbitals are parity-forbidden; hence, they result in a low absorption coefficient. The spectra of rare earth ions in the crystal fields consist of electric dipole transitions; however, there are some fewer magnetic dipole transitions. The theory of magnetic dipole transitions is attributed to intermediate transitions [93], [94].

The behaviour of RE ions is advantageous as they are used in various applications, for instance, in field emission displays, white light-emitting diodes, and photovoltaics [17], [95], [96]. As mentioned above, there are various purposes for which RE³⁺ ions are added to a variety of host materials. When they are incorporated into the host sample, they localise within its forbidden bandgap; as a result, they alter the band structure of the host material and enhance its light emission [7], [95], [97]. When two rare earth ions are incorporated into a host material (co-doping), the other dopant acts as a sensitizer, while the other acts as an activator. The sensitizer absorbs a large amount of excitation energy and transfers it to the activator. They are mostly used to prolong the emission (phosphorescence) of the host material [15], [17], [98]. The following pattern is mostly used in the sensitizer/activator pairings: Dy³⁺/Tb³⁺, Ce³⁺/Tb³⁺, Eu³⁺/Dy³⁺, Dy³⁺/Sm³⁺, and Dy³⁺/Gd³⁺. In this reaction, energy is transferred from one rare earth to another. In order to keep these activator ions apart from one another and ensure high-efficiency emissions, only trace quantities of RE³⁺ ions are introduced into the phosphor material. Concentration quenching is more likely to occur at higher activator ion concentrations [99].

Generating luminescence directly by exciting the rare earth ion is challenging due to the forbidden f-f transition, as previously mentioned [100]. However, this issue can be resolved using indirect methods to excite the ion to a higher energy level. One approach involves incorporating rare earth ions into a matrix or host material made of oxides or glass-forming substances [76], [101]. A specially chosen impurity, known commercially as a sensitizer, absorbs ultraviolet radiation and then transfers this energy to the emitter (activator) via the

crystalline host lattice. Subsequently, the excited rare earth ion returns to its ground state, emitting light quanta corresponding to the energy differences with the ground level [100]. The process of matrix-assisted energy transfer and the resulting luminescence are depicted schematically in **Figure 1.11** below.

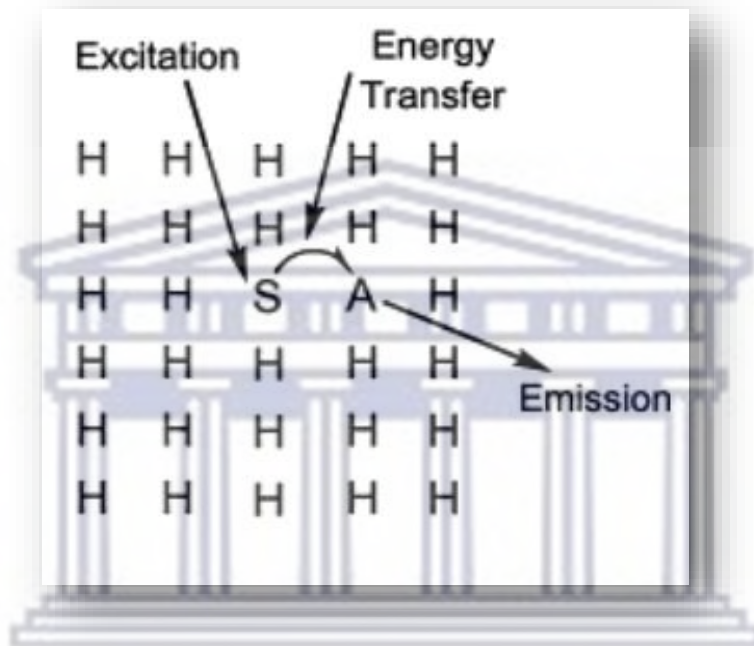


Figure 1.11 schematic representation of matrix-assisted luminescence of RE^{3+} ions (where S is a sensitizer and A is an activator) [8].

1.12 Colour emission properties of Eu^{3+} , Dy^{3+} and Sm^{3+} ions

The following rare earth ions: Eu^{3+} , Dy^{3+} , and Sm^{3+} , namely europium, dysprosium, and samarium, respectively, are classified as trivalent ions due to their 3+ oxidation state. These ions can be substituted in various host materials and are known for their photoluminescent colour emissions, suitable for various applications [102]. Numerous researchers have reported on doping metal oxides with the above trivalent ions.

Neeraj et al. [102] investigated the colour emissions of Eu^{3+} doped $\text{NaM}(\text{WO}_4)_{2x}(\text{MoO}_4)_x$ phosphor material, which they synthesized using the solid-state method. Their photoluminescence emission spectra showed an intense red emission at an excitation of 394 nm. Moreover, they reported that the red emission is associated with the charge transfer band (${}^7\text{F}_0 \rightarrow {}^5\text{L}_6$) due to the incorporation of the Eu^{3+} ions into the host lattice. Boukerika et al. [78] reported on the synthesis of $\text{Y}_2\text{O}_3:\text{Eu}^{3+}$ phosphor material using the sol-gel method. The aim was to investigate luminescence properties. Similar findings to those of Neeraj et al. [102] were observed. Their photoluminescence emission spectra revealed intense red emissions at 610 and 588 nm, which are associated with the Eu^{3+} (${}^5\text{D}_0 \rightarrow {}^7\text{F}_2$) electric and (${}^5\text{D}_0 \rightarrow {}^7\text{F}_0$) magnetic dipole transitions, respectively. Phosphor materials doped with Eu^{3+} have potential for red-light-emitting diode applications. Eu^{3+} is also investigated for enhancing fluorescence lifetime in boron-silicate glasses; this trivalent ion can be homogeneously distributed along the host lattice of the phosphor material. To date, Eu^{3+} doped phosphor materials are known for their long-lasting phosphorescence [103], [104].

Dysprosium Dy^{3+} is widely known for enhancing long-lasting white light emission when incorporated into host materials. Kuang et al. [105] reported on the synthesis of $\text{SrSiO}_3:\text{Dy}^{3+}$ phosphor material. Their results showed an enhancement in the phosphorescence emission of approximately 1 hour after the light source was removed from the sample. The sample was excited at 254 nm with ultra-violet light. Similar behaviour was observed by Liu et al. [103], who investigated white after glow on $\text{CdSiO}_3:\text{Dy}^{3+}$ phosphor. Their results showed long-lasting phosphorescence for approximately 5 hours after the excitation source was removed from the sample. This sample was annealed at 1050 °C. Doping a host material with Dy^{3+} introduces a highly dense trapping level, which is responsible for long-lasting phosphorescence at room temperature; moreover, it is also due to the thermally stipulated recombination of electron and hole traps, which leaves electrons and holes in a long-lived excited state [103], [104], [106], [107]. The white light emission is due to the persistent energy transfer from the host to the Dy^{3+} ions.

Samarium Sm^{3+} is known for tuneable luminescence colour emissions. The luminescence properties of a phosphor material doped with Sm^{3+} arise from the intrinsic 4f – 4f transitions on the dopant ion. Sm^{3+} doped phosphor material has attracted more attention and have been reported by numerous researchers [108]. Xia et al. [107] reported on the investigation of the photoluminescence properties of $\text{BaMoO}_4:\text{Sm}^{3+}$ phosphor; they discovered enhancement of

photoluminescence intensity due to the incorporation of the Sm^{3+} into the host. The emission colours detected were intense reddish orange, which corresponds to the ${}^4\text{G}_{5/2} \rightarrow {}^6\text{H}_{7/2}$ transition [108], [109]. Li et al. [110] reported on the synthesis of $\text{LaAlGe}_2\text{O}_7$ doped with Sm^{3+} to investigate its photoluminescent emissions. Their results showed an increase in emission intensity as they increased the concentration of the Sm^{3+} ion; however, the average decay time of the phosphor material decreased with an increase in the concentration of the dopant. Sm^{3+} .

1.13 Problem statement

Recently, most of the researchers have focused on the photoluminescence properties of singly rare earth ion doped $\text{Zn}_4\text{B}_6\text{O}_{13}$ composites via different synthesis methods. However, a comparative study of various synthesis routes that produced $\text{Zn}_4\text{B}_6\text{O}_{13}$ composites in a single study is lacking. The study aims to find the best synthesis route with efficient emission properties of different rare earth ions in $\text{Zn}_4\text{B}_6\text{O}_{13}$ composites for applications in W-LED technology. As per literature survey, choice of different synthesis routes could impact on structural, morphological, and photoluminescence properties of $\text{Zn}_4\text{B}_6\text{O}_{13}$ composites. The choice of the sol-gel, combustion and solid-state reaction methods could create the possible pathways to identify the best luminescence properties of Sm^{3+} , Eu^{3+} and Dy^{3+} ions in $\text{Zn}_4\text{B}_6\text{O}_{13}$ composites materials. Based on this investigation, the best synthesis method could be modelled for future research.

1.14 Research aims and objectives

1.14.1 Aim

By incorporating different synthesis routes such as sol-gel, combustion and solid-state methods, we aim to investigate their impact of different synthesis routes on the luminescence properties of the rare earth (Eu^{3+} , Dy^{3+} and Sm^{3+}) ions doped $\text{Zn}_4\text{B}_6\text{O}_{13}$ nanophosphors.

1.14.2 Objectives

- To synthesize pure, singly doped ($\text{RE}^{3+} = \text{Eu}^{3+}, \text{Dy}^{3+}, \text{Sm}^{3+}$) $\text{Zn}_4\text{B}_6\text{O}_{13}$ nanophosphors via different synthesis techniques such as sol-gel, chemical combustion, solid-state methods.
- To identify the crystal phase structure of the prepared $\text{Zn}_4\text{B}_6\text{O}_{13}$ nanophosphors and to determine their crystal sizes.
- To examine and analyse the surface morphology and chemical composition of the prepared $\text{Zn}_4\text{B}_6\text{O}_{13}$ materials.
- To investigate the photoluminescence properties of singly doped ($\text{RE}^{3+} = \text{Eu}^{3+}, \text{Dy}^{3+}, \text{Sm}^{3+}$) $\text{Zn}_4\text{B}_6\text{O}_{13}$ nanophosphors via different synthesis routes.
- To determine the chromaticity colour purity and the CIE colour coordinates of the prepared singly doped $\text{Zn}_4\text{B}_6\text{O}_{13}$ nanophosphors.

1.15 Dissertation layout

- Chapter 1: This chapter provides an overview on the types of photoluminescence phosphors, including ZnO and $\text{Zn}_4\text{B}_6\text{O}_{13}$, which is of interest in this study and provides insights about the rare earth ions that are used for doping with Eu^{3+} , Dy^{3+} , and Sm^{3+} .
- Chapter 2: provides a review of the literature on the impact of synthesis methods (sol-gel, combustion, and solid-state) on the photoluminescence properties of ZnO host and $\text{ZnO}:\text{RE}^{3+}$ ions phosphor materials.
- Chapter 3: This chapter discusses the experimental procedures and synthesis methods implied for the preparation of $\text{Zn}_4\text{B}_6\text{O}_{13}:\text{RE}^{3+}$ (where RE^{3+} is Sm^{3+} , Dy^{3+} , and Eu^{3+}), as well as the characterization techniques used for the sample analysis.
- Chapter 4: The photoluminescence properties of $\text{Zn}_4\text{B}_6\text{O}_{13}:\text{Sm}^{3+}$ prepared with three synthesis methods: sol-gel, combustion, and solid-state.
- Chapter 5: Investigates the impact of sol-gel, solid-state, and combustion methods on the photoluminescence properties of $\text{Zn}_4\text{B}_6\text{O}_{13}:\text{Eu}^{3+}$ phosphor material.

- Chapter 6: This chapter investigates the photoluminescence properties of the $\text{Zn}_4\text{B}_6\text{O}_{13}:\text{Dy}^{3+}$ phosphor prepared via sol-gel, combustion, and solid-state synthesis methods.
- Chapter 7: This chapter conveys a summary and conclusion about the findings of this work.



Chapter II

Literature review

2.1 Emission properties of ZnO based phosphors

Emission properties of ZnO-based phosphors have been reported by various researchers, showcasing their potential applications in lighting and in optoelectronics; Ashok et al. [111] investigated the optical properties of ZnO nanostructures doped with various rare earth (RE) ions, including europium Eu. They adopted the sol-gel synthesis method to prepare their ZnO:Eu nanophosphors. The sol-gel method as it is economically efficient for adjusting morphological structure and particle size, providing high yield of nanoparticles (NPS) at the desired temperature. Their UV–Vis results revealed a redshift in the absorption edges of the ZnO:Eu nanopowders and also revealed that the addition of the dopant to the host resulted in a decrease in the optical band gap. The decrease in band gap confirms successful incorporation of the dopant to the host [2], [112]. Moreover, the decrease in bandgap and the redshift after doping are attributed to the presence of defect states below the conduction band, which trap the photogenerated electrons. The photoluminescence (PL) measurements were taken at room temperature at an excitation of 395 nm. The PL emission spectra confirmed an increase in the luminescence intensity of the Eu-doped sample compared to the undoped. According to their results, doping with RE ions improved the emission properties of ZnO, as the RE ions have special electronic structure, small crystal field strength splitting, and partially filled 4f electrons surrounded by full 5s and 5p orbitals, which enabled ZnO to have numerous tunable features, particularly in the optoelectronic domain [2], [111]. Boxu et al. [2] synthesized a series of Er³⁺/Yb³⁺ co-doped Y₂O₃-ZnO ceramic phosphors using the sol-gel method. Their aim was to investigate the photoluminescence properties of the prepared phosphor and the change in its microstructure. The SEM was used to study the morphology of the prepared, porous structure was observed with an increase in Zn²⁺ ions. They reported the presence of two emission bands in their samples: a green band at 535 nm and a red band at 660 nm. These bands are attributed to ²H_{11/2} → ⁴I_{15/2} and ⁴F_{9/2} → ⁴I_{15/2} radiative transitions, respectively. They further reported that these emission peaks were enhanced compared to those of the host material; the increase in

emission is due to the lattice expansion resulting with the changes of the distance between RE ions [2], [12], [113]. Jafaar et al. [112] used the thermal treatment method to synthesise Eu^{3+} -doped $\text{ZnO-Zn}_2\text{SiO}_4$ with dopant concentration ranging from 0, 1, 3, 5, and lastly, 10 mol%. The aim was to study the impact of Eu^{3+} on the photoluminescence properties and morphology of the prepared samples. The samples underwent heat treatment at 700 °C for 3 hours. Their XRD results confirmed that increasing dopant concentration enhances the diffraction peak sharpness. The improvement in the diffraction peaks is ascribed to the enhanced crystal quality of the sample and also due to the increase in calcination temperatures. Due to the absence of significant changes in the morphology when comparing the doped and the host samples, it was concluded that the Eu^{3+} ion concentration did not have an impact on the morphology of the sample. Their photoluminescence (PL) results demonstrated that the doped sample exhibits higher emissions in comparison to the undoped sample. This enhancement is attributed to the electronic transitions of Eu^{3+} present in the sample, contributing to optimal emission performance and the expansion of lattice phenomena [13], [112].

Kaur et al. [4] synthesised ZnO phosphors with different morphologies using solid-state and co-precipitation methods to understand the characteristics of their emission under VUV (vacuum ultraviolet) excitation for potential VUV photodetection development. They discovered that phosphors that possess higher thermal stability and acceptable colour rendering properties are those with sheet-like morphology prepared by solid-state method. They also noticed that in both synthesis methods the increase in temperature caused the emission intensity to decrease, resulting in the CIE coordinates shifting nearer the pure white region. The decrease in emission intensity results from the strong interaction between electron and phonon, which levels up the thermally active non-radiative recombination processes. The violet and blue emissions revealed from the PL emission spectra originate from the radiative transitions of excited electrons from a Zn interstitial defect in a crystal lattice. These phosphors can be used in plasma display devices [4]. Rajkumar et al. [5] synthesised a ternary-type $\text{Ba}_2\text{Y}_2\text{ZnO}_5$ doped with Eu^{3+} deep red phosphor using the solid-state method; their aim was to study the photoluminescence properties of the prepared phosphor. Their XRD results revealed that an increase in Eu^{3+} concentration caused a shift to the lower 2θ values, the red shift is due to the Eu^{3+} ions replacing the Y^{3+} ions in the host lattice. At an excitation of 288 nm, the PL spectra revealed intense red emission, which is attributed to the $^5\text{D}_0 \rightarrow ^7\text{F}_2$ electric dipole transition, implying that the Eu^{3+} ions occupied low symmetry sites of Y^{3+} [5]. They further concluded that $\text{Ba}_2\text{Y}_2\text{ZnO}_5$ doped with Eu^{3+} is a promising phosphor that can be used for latent fingerprint

applications, as a red emitter due to the presence of Eu^{3+} , and for WLED. Shafi et al. [7] investigated the luminescence properties of ZnO and other ternary nanocomposites synthesised via co-precipitation. The hexagonal morphology of the ZnO compound was confirmed in the XRD data. The photoluminescence emission spectra showed green emission, which is attributed to the native defects due to the zinc interstitials and is also associated with the singly ionised oxygen vacancies [7], [114]. Song et al. [8] investigated on the luminescence properties and thermometric performance of $\text{Bi}^{3+}/\text{Sm}^{3+}$ co-doped $\text{BaLa}_2\text{ZnO}_5$ phosphors synthesised using a high-temperature solid-state method. Optical studies revealed an absorption band at 233 nm, which is due to the band-to-band transition of the host, and another weak band within the 290 – 400 nm region that is due to excitonic absorption. They noticed that the increase in temperature caused a decrease in luminescence intensity. This behaviour is attributed to excellent reproducibility observed during repeated heating and cooling processes. The findings suggest that these phosphors have significant potential in the field of biological temperature sensing [8], [113].

2.2 Various synthesis methods for emission properties of ZnO based phosphors

The emission properties of ZnO phosphors prepared through sol-gel, combustion, and solid-state methods have been reported by numerous researchers, investigating the impact of each method on the optical and photoluminescence properties of the ZnO phosphor materials [2], [111], [112]. Due to its large theoretical band gap of 3.37 eV, ZnO is usually excited with ultraviolet light, as this light is more energetic to excite electrons from the valence band to the conduction band, creating electron hole pairs. It turns out that the type and concentration of defects formed in a material depend mainly on the preparation method and directly impact the photoluminescence properties; thus, the summaries of the reports detailing the emission properties of ZnO due to the above-mentioned synthesis method are reported below [115]. The manifestation of the ZnO properties depends on the synthesis method [116].

2.2.1 Emission properties of ZnO based phosphors prepared via combustion reaction method

The combustion method is a fast preparation technique that grows crystallites at a faster rate, requiring an appropriate selection of an organic fuel. This method can be adopted at a low preparation cost and has a high production rate. Moreover, the combustion method usually produces materials that are crystalline with fine grain size, multicomponent, highly pure, and homogeneous ceramics at low temperatures [117], [118], [119], [120], [121]. Furthermore, it involves the preparation of samples at high temperatures and low pressure. This method is advantageous as it is possible to control the crystallite size by adjusting the reaction temperature. Tarwal et al. [117] reported on the investigation of the photoluminescence properties of ZnO prepared using the combustion method. In their study, ZnO nanopowder was synthesized using zinc nitrate with glycine as an organic fuel. Their XRD showed sharp diffraction peaks indicating crystalline nature and hexagonal structure; the absence of secondary peaks and imply that the combustion method has no impact on the crystal structure of the ZnO material. Within the ZnO wurtzite structure, the Zn atom is positioned at the center of the tetrahedral oxygen matrix (refer to **Figure 2.1**) The crystallite sizes obtained through this method are usually less than 100 nm [117], [118], [119], [120], [121]. The low crystallite sizes are responsible for the intense emission in the UV region.

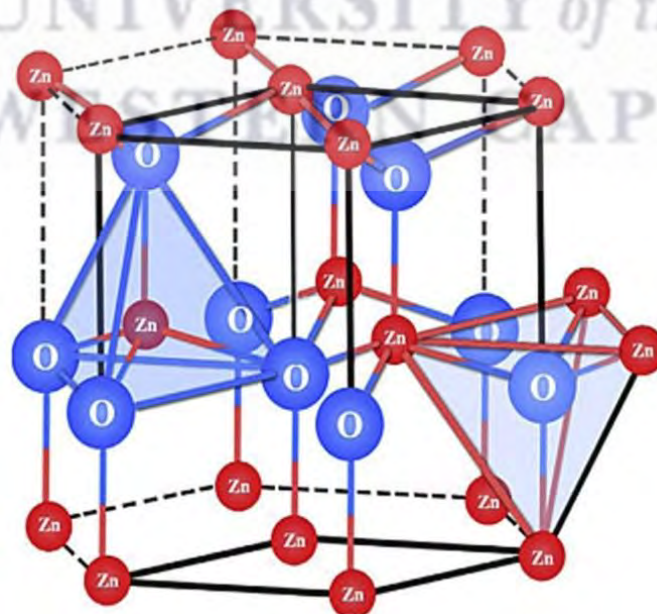


Figure 2.1 The hexagonal wurtzite crystal structure of ZnO material [122].

During the combustion reaction process, there is a rapid release of gaseous byproducts, hence their SEM images revealed the formation of agglomerated and porous morphology, the nitrate bonds are broken, and the oxide bonds are formed. However, there are various morphologies that have previously been reported to be obtained through this method: clusters of tiny particles in a rod-like, shard-like flake with holes [115], [121]. Nanoparticles prepared by this method usually have a large surface area and a wider band gap between the valence and the conduction band. The band gap produced through this method is usually 3.27 eV less than the theoretical bandgap of 3.37 eV [117], [118].

The photoluminescence studies reported by Tarwal et al. [117] revealed an intense UV emission at 398, resulting from ambient air annealing due to enhanced oxidation during combustion method reaction process. The UV emission is ascribed to the near-band edge emission of ZnO with the wide band gap, which is responsible for the free excitonic radiative recombination. In addition, there was a suppressed deep-level green emission at 471 nm, indicating good crystal quality and optical properties. The green band emission is associated to crystal defects such as vacancies and interstitial sites in ZnO, implying fewer structural defects and impurities [117]. In contrast, the green emissions originate from the recombination of the holes with electrons found in singly ionized oxygen vacancies. The mechanism behind the green emission primarily attributed to the concentration of free electrons and the presence of various point defects resulting from heating treatments or oxidation during the process, facilitating the formation of recombination centers. Moreover, the weak green emission is also attributed to the low level of oxygen defect density, the transition of oxygen vacancies and valence band holes, and deep level or trap state emission [117], [118]. Subsequently, the report by Zhao et al. [118] on the study of the photoluminescence properties of ZnO prepared by combustion also coincides with the results reported by Tarwal [117]. Similarly, two peaks were noted in the PL spectra at 412 and 468 nm, which are associated with the transition from the conduction band to a deep acceptor level and the transition from oxygen vacancies' level to the valence band, respectively. ZnO prepared through combustion method is a promising semiconductor for various applications, including blue and ultraviolet light-emitting diodes [117], [118], [119].

2.2.2 Emission properties of ZnO based phosphors prepared via sol-gel reaction method

The sol-gel method is a time-consuming and expensive preparation technique that produces agglomerated ZnO particles with uniform size, improved crystallinity, with low porosity [117], [118], [119]. This method can only be done in small-scale laboratories. However, it requires strict control of the reaction conditions due to its violent hydrolysis reaction in the air during the reaction [120]. The sol-gel method is attractive because of its well-controlled heterogeneous nucleation and growth process, enhancement of the green colour emission, ease of introducing various functional groups, customizable microstructure, and the fact that it can be conducted at room temperature. The ZnO materials prepared through this method usually result in a bandgap that is lower than the theoretical bandgap [115], [121], [123]. Below are summaries of various reports on the emission properties of ZnO-based phosphors prepared with the sol-gel method.

Trwyn et al. [2] used sol-gel method to synthesize silica nanoparticles. They observed that resulting mesoporous silica nanoparticles exhibited chemical and thermal stability, characterized by well-defined, controllable morphology and porosity. Additionally, the researchers demonstrated control over particle size, influencing quantum confinement effects and, consequently, the emission properties of the material [2], [112]. It is acceptable to say that the sol-gel method is advantageous in controlling the morphology of the synthesized particles [117].

Sagar et al. [123] reported on the synthesis of ZnO material using the sol-gel method to investigate its photoluminescence and optical properties. Their SEM images revealed ZnO particles with larger grain size and with a larger distribution, leading to a broader PL band; they overcame the broad emission by annealing the material at higher temperatures. The increase in temperature results in an increase in particle size, however it reduces the bandgap of the material [115]. Their PL spectra show two emission bands: a narrow band in the UV region at 380 nm, which corresponds to the band edge emission due to a free exciton emission, and the other green emission near the 500 nm region related to the defects: non-stoichiometric imperfections and crystal imperfections. The intense emission peak in the UV spectra is also related to the excitonic effect of phonon interactions, strain, and the influence of the optical constant near the band gap. The large exciton-binding energy allows excitonic recombination well beyond room temperature, making excitons a sensitive indicator of material quality [117].

The green PL emission corresponds to the transition from the conduction band to oxide antisite defects. In addition, a Stokes shift was observed between the PL and absorption spectra, associated with various defects, including electron phonon coupling, lattice distortions, interface defects, and point defects, causing a red shift of the emission line absorption edge. The optical properties of the phosphor material show that it exhibits transmittances exceeding 90% in the visible range; this transmittance decrease in the UV range due to the onset of fundamental absorption [123]. Similarly, Bekkari et al. [115] synthesized ZnO nanoparticles with the sol-gel method, and their XRD results showed that the nanoparticles crystallized in a pure ZnO wurtzite structure without any secondary phases. The average crystallite sizes obtained through this method ranged from 20 – 40 nm. According to their PL results, when the ZnO NPS are excited at 280 nm, UV emission at approximately 380 nm is observed. This peak is attributed to the near-band edge transition of ZnO, namely the recombination of free excitons, while the visible luminescence is attributed to various defects in the crystal structure such as oxygen vacancy, zinc vacancy, oxygen interstitial, zinc interstitial, and extrinsic impurities [115]. The defects possess an energy level structure differing from substantial semiconductor atoms, generating one or more energy levels within the forbidden gap of the semiconductor. These defects, known as recombination centres, contribute to the decrease in the radiative lifetime and internal quantum efficiency of the UV emission. A blue emission is observed at 434 nm, which is ascribed to the transition from the zinc interstitial to the valence band. The green emission at 540 to 555 nm is attributed to the transitions from the conduction band to the oxygen interstitial level. The green-yellow peak at around 573 originates from the conduction band transition to the complex of an oxygen vacancy and zinc interstitial [115].

Bera et al. [124] synthesized pure ZnO nanoparticles using the sol-gel method to investigate their photoluminescence properties. A broad, intense visible emission peak centred around 520 nm was observed, with the prepared phosphors exhibiting lifetimes in the range of approximately 14 to 77 ns. Two emission peaks were observed: a sharp and highly intense UV emission band, contrasting with typically broad and weak visible emission. The broad peak is commonly associated with the presence of surface defects. The green emissions are attributed to defects in the ZnO nanoparticles, i.e., neutral, singly, or doubly charged Zn vacancies, and singly or doubly charged oxygen vacancies. The other cause of the green emission is due to the transitions from the conduction band to the deep acceptor levels. The recombination process between the oxygen vacancy and the trapped electron produces green emission [124], [125]. The reduction in the intensity of the 545 nm peak compared to the UV peak is attributed to a

reduced concentration of oxygen vacancies resulting from aging in an oxygen-rich atmosphere [126]. The bandgap obtained through this method is less than the theoretical band gap of 3.37 eV; it is approximately 3.2 eV [125].

2.2.3 Emission properties of ZnO based phosphors prepared via solid state reaction method

Solid-state reaction method is one of the fast, simple, and effective approaches to synthesize ZnO nanoparticles, it can be performed at a low cost and does not require more complex devices; agate mortar and pestle are mainly used as starting apparatus. Moreover, it allows a control of the size of the crystallite by adjusting the synthesis temperatures [127]. The following researchers have reported on the emission properties of ZnO materials prepared through the solid-state method.

Lin et al. [128] reported on the synthesis of ZnO phosphors using solid-state reaction method to investigate their cathodoluminescence properties. The XRD results confirmed the hexagonal wurtzite structure, this implies that solid-state reaction method does not affect the crystal structure of the ZnO material. Their photoluminescence studies revealed green emission bands within the 494 nm region. The green emission band is attributed to the presence of the oxygen vacancies. Pure emission of narrow luminescence band in the blue-violet spectral region. The green emission band originates from the transition of Zn^+ to Zn^{2+} in the excess of Zn ions, involvement of O vacancies, interstitial O, Zn vacancies, and Zn interstitials. The other cause of green emission in the ZnO phosphors is due to the recombination of an electron in singly occupied oxygen vacancies with photoexcited holes in the valence band. A yellow band was observed within the 562 nm region [128]. The ZnO particles synthesized by Pudukudy et al. [127] using solid-state method for the investigation of their photocatalytic activity showed hexagonal wurtzite structure, with high nanocrystallite size confirmed through the XRD technique. The produced crystallite sizes ranged from 19 to 45 nm. Intense diffraction peaks observed indicating high phase purity. The Scanning electron microscopy showed development of porous ZnO nanostructures, which are uniformly distributed, well separated hexagonal morphology with granular shape, and some spherical structures. They observed a small agglomeration with an average particle size of 80 nm. The photoluminescence spectra revealed that the samples exhibited characteristic blue and green emission bands. The photocatalytic activity of the as prepared ZnO phosphors was investigated under UV light. The

photoluminescence emission intensity is affected by crystallinity, porosity, and surface area of the sample [127]. The weak green emission is attributed to the reduction of radiative recombination process in the sample [127]. The blue band centered at 397 nm is attributed to the annihilation of excitons, the visible band at 438 nm is ascribed to the presence of the high density of surface defects; oxygen vacancies, zinc vacancies, oxygen interstitials and zinc interstitials of the sample, and the combination of free excitons [127]. The green emission band is attributed to the electron-hole pair recombination occupying in the singly ionised oxygen vacancies.

Kaur et al. [4] reported on the synthesis of sheet like ZnO nanoparticles using solid-state reaction method. Their aim was to investigate their photoluminescence properties. The prepared phosphors exhibited high thermal stability. Their XRD results confirmed the formation of polycrystalline ZnO with hexagonal wurtzite structures without any additional impurities with an average crystallite size of 36 nm. The SEM images showed that the phosphors exhibited stacked sheet like structures with an average size of 8.24 μm . According to the photoluminescence analysis the phosphors exhibited intense UV emission as well as broader visible luminescence. There were strong UV, green, yellow, and orange emissions. Which are due to excitonic recombination, and the deep level defects within the bandgap. Violet and blue emissions result from radiative transitions of excited electrons from (Zn_i) and (Zn_i) to Zn vacancy, respectively [4]. The red emission band originates from the recombination of photoexcited electrons from the edge of the conduction band to the holes at V_o [4]. The consistent orange band across the temperature range of 10–300 K is due to the radiative transition of an electron from Zn_i to O_i defect levels [4]. The green emission band at 500 nm arises from the electron trapped in singly charged oxygen vacancies which being thermodynamically unstable converts into neutral oxygen vacancies. The electron trapped in neutral oxygen vacancy recombines with a hole present in the VB resulting in green emission. The yellow emission band at 584 nm is attributed to the transition of an electron from the edge of the conduction band to the O_i defect level [4].

2.3 Luminescence properties due to dopants

Zinc oxide (ZnO) material is widely utilized as a host for luminescence applications due to its wide and direct bandgap. However, the ZnO material could be doped with lanthanides to tune its optical properties. Lanthanides ions, with f-f transitions in their partially filled 4f orbitals, exhibit efficient luminescence. In addition, they also enhance the photoluminescence lifetimes of the host material; this can be explained through the energy transfer between the dopant and the host material [116], [129]. The rare earth-doped semiconductors have a wide range of emission wavelengths, from ultraviolet to near infrared [49]. Doping of ZnO, especially with rare earth (RE) ions, introduces surface defects and trapping centres in the band gap, which result in the inhibition of recombination and acceleration of the interfacial charge transfer [130]. Each of the host materials has its own unique colour emission when doped with RE ions. The luminescence properties due to Sm^{3+} , Eu^{3+} , and Dy^{3+} rare earth ions are discussed below.

2.3.1 Luminescence properties of Sm^{3+} ions

Samarium (Sm^{3+}) is one of the trivalent rare earth ions with optical capabilities; it can be incorporated into various host materials for different applications, for instance in colour displays, solid-state lighting, and plasma display panels [116]. When a ZnO material is doped with Sm^{3+} , there is an energy transfer between the dopant and the host. If there are secondary phases and a peak shift in the XRD spectrum, it implies that the charge transfer was not uniform, as there is a change in the inter-planar spacing and lattice micro strain of the host. However, the non-existence of secondary phases implies the uniform substitution of Zn^{2+} ions by Sm^{3+} ions [130]. Moreover, during the substitution process, there is a charge imbalance. The charge imbalance can be corrected by applying a well-designed synthesis mechanism, which will introduce suitable monovalent cations for balancing the charge transfer. The equation below shows the balancing of charge transfer using monovalent cations (MC^+) [130].



There are two other alternative mechanisms for maintaining charge neutrality through the generation of crystal defects without the monovalent charge compensator ion. In the first

mechanism, the charge compensator is carried out by a zinc vacancy (V_{Zn}) defect where two Sm^{3+} ions replace three Zn^{2+} ions along with the zinc vacancy defect (V_{Zn}), leading to the following equation [130].



The second case involves the creation of an oxygen interstitial (O_i) defect during the substitution of two Zn^{2+} ions by two Sm^{3+} ions, leading to the equation below [130].



Numerous reports have been published regarding ZnO doped with Sm^{3+} for the investigation of its luminescence emission. Othmen et al. [116] reported on the synthesis of ZnO: Sm^{3+} nanocrystals using the sol-gel method. Their aim was to investigate the photocatalytic properties of the nanocrystals due to Sm^{3+} ions. Their XRD results confirmed the ZnO wurtzite hexagonal structure, confirming the successful incorporation of Sm^{3+} ions in the ZnO material [116], [129]. Their ultraviolet-visible (UV-Vis) spectroscopy revealed the introduction of a new absorption band on the doped material, which is not present in the spectrum of the ZnO host material. This band is attributed to the f-f transitions from the Sm^{3+} ions. However, there was a slight decrease in the band gap of the ZnO after the introduction of the dopant, which is ascribed to the charge transfer between the ZnO valence band and the Sm^{3+} ion 4f level. Their photoluminescence was obtained at an excitation of 325 nm for both the host and doped material. Emission peaks were observed at 380 nm and 530 nm in both the host and the doped material. However, the emission intensity of the doped material was suppressed compared to the host material. The decrease in intensity is ascribed to the introduction of intrinsic defects from the dopant and the parity-forbidden nature of f-f transitions of Sm^{3+} ions [129], [131]. Furthermore, there was a blue shift in the visible region, meaning the Sm^{3+} dopants affect the nature of the host material. Their results indicated that ZnO-doped Sm^{3+} could be a potential candidate in photocatalysis applications as an orange-red light-emitting material [49], [116], [129]. Similarly, Devi et al. [129] synthesized ZnO: Sm^{3+} nanostructures using the combustion method; their aim was to investigate the photoluminescence properties of the prepared material. Their XRD did not show any additional peaks; all peaks matched the wurtzite structure. At an excitation wavelength of 255 nm, their PL emission spectrum showed an emission at 397 nm, which is attributed to the recombination of free excitons. Other luminescence peaks that originate from defect states such as oxygen vacancies and zinc interstitials were observed within the 420–490 nm (blue) region. The decrease in bandgap was observed after doping ZnO

with Sm^{3+} [129], [132]. However, there are other reported various photoluminescence emissions resulting from the $\text{ZnO}:\text{Sm}^{3+}$ due to Sm^{3+} ; for instance, orange-red emission [49] due to the ${}^4\text{G}_{5/2} \rightarrow {}^6\text{H}_{7/2}$ and ${}^4\text{G}_{5/2} \rightarrow {}^6\text{H}_{9/2}$ transitions, respectively. Green emission due to Sm^{3+} [49] is also reported, resulting from ${}^4\text{G}_{5/2} \rightarrow {}^6\text{H}_{5/2}$ and a yellow emission [130], [133] which is ascribed to ${}^6\text{H}_{5/2} \rightarrow {}^6\text{H}_{9/2}$.

2.3.1 Luminescence properties of Eu^{3+} ions

Europium (Eu^{3+}) ions have been incorporated into various host materials for various luminescence applications, including solid-state lighting, fibre lasers, plasma displays, and field emission displays [86], [134]. In this section, the luminescence properties of $\text{ZnO}:\text{Eu}^{3+}$ will be discussed. Eu^{3+} has been reported to exhibit sharp emissions in both the ultraviolet and the visible. When Eu^{3+} is incorporated into the ZnO material, it provides both stable chemical and physical properties in the ZnO material as there is energy transfer between the dopant and the host material [34]. There are a variety of colour emissions when Eu^{3+} is incorporated into a host material. **Figure 2.2** below shows the Eu^{3+} ion energy level diagram. When a phosphor material is excited by near-UV light, it absorbs energy; the electrons are excited from the valence band to the conduction band. The electron can be excited at various wavelengths, i.e., 361, 382, 395, and 416 nm, which correspond to the following transitions: ${}^7\text{F}_0 \rightarrow {}^5\text{G}_4$, ${}^7\text{F}_0 \rightarrow {}^5\text{G}_2$, ${}^7\text{F}_0 \rightarrow {}^5\text{L}_5$ and ${}^7\text{F}_0 \rightarrow {}^5\text{D}_3$. The electrons tend to emit light in different wavelengths within the following 592, 615, 655, and 702 nm, which correspond to ${}^5\text{D}_0 \rightarrow {}^7\text{F}_1$, ${}^5\text{D}_0 \rightarrow {}^7\text{F}_2$, ${}^5\text{D}_0 \rightarrow {}^7\text{F}_3$ and ${}^5\text{D}_0 \rightarrow {}^7\text{F}_5$ transitions, respectively. The emission results when the electrons are lost non-radiatively to the ${}^5\text{D}_0$ level [134], [135], [136], [137], [138], [139], [140], [141].

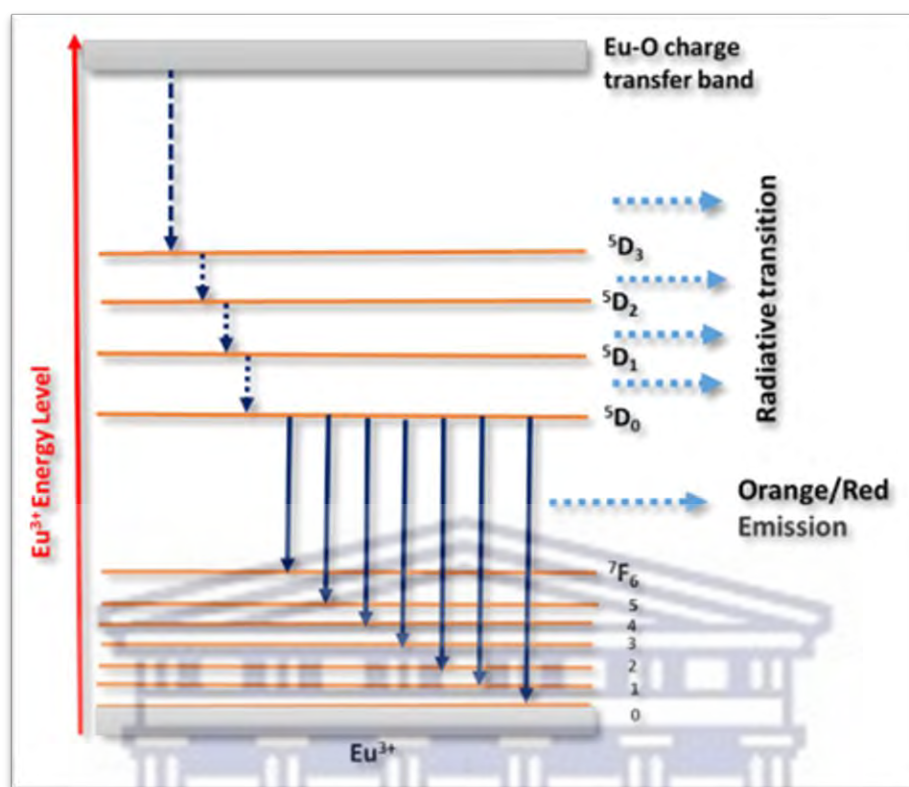


Figure 2.2 The electronic energy level diagram for the Eu^{3+} ion [135].

Zhang et al. [136] reported on the observation of strong white light emission achieved from ZnO:Eu^{3+} . The Eu^{3+} ion is a significant structural probe due to the red visible luminescence that results from ${}^5\text{D}_0 \rightarrow {}^7\text{F}_0$ transitions [138], [139]. The red emission is ascribed to the intense charge transfer band adsorption in the ultraviolet region, which are the f-f transitions of Eu^{3+} at 394 and 465 nm regions. Ntwaeaborwa et al. [134] reported on the synthesis of ZnO doped with Eu^{3+} nanoparticles using the co-precipitation method to investigate the structural, optical, and photoluminescence properties due to Eu^{3+} . Their XRD results revealed secondary phases, which are attributed to the presence of Eu^{3+} ions. Upon increasing the concentration of Eu^{3+} , they observe a change in the crystal structure of the ZnO material as there is a shifting in peak position and an increase in intensity of the diffraction peaks of secondary phases [134], [137]. The shift in diffraction peaks is attributed to the non-uniform charge transfer between the Zn^{2+} and Eu^{3+} ions. They also observed an increase in the crystallite size and a decrease in the bandgap of the material as the concentration of the dopant increased. Upon excitation of 325 nm, the photoluminescence emission spectra revealed intense emission peaks at 593 nm, 618

nm, 646 nm, and 682 nm regions, which are ascribed to the $^5D_0 \rightarrow ^7F_j$ ($j=1, 2, 3,$ and 4) 4f-4f transitions of Eu^{3+} [134], [136].

2.3.1 Luminescence properties of Dy^{3+} ions

Dysprosium (Dy^{3+}) is one of the trivalent rare earth ions; it has been incorporated into the ZnO host material by various researchers for the following applications: white light-emitting diodes, thermoelectric devices, and flat panel displays [142]. Moreover, the Dy^{3+} is considered eco-friendly and useful for enhancing luminescence emissions, i.e., a high-intensity lamp, as it exhibits magnetic strength at very low temperatures [143]. ZnO doped with Dy^{3+} ions is known for exhibiting luminescence in the visible region [144]. Numerous studies for ZnO: Dy^{3+} have been reported. Amira et al. [142] reported on the synthesis of ZnO phosphor doped with Dy^{3+} using the solid-state reaction method to investigate the spectroscopic properties of the prepared phosphor. Their XRD results confirmed the hexagonal wurtzite phase of ZnO and showed a slight shift in the diffraction peaks to the lower 2θ levels, indicating successful incorporation of the Dy^{3+} ions in the ZnO host lattice. The good crystallinity of the ZnO: Dy^{3+} sample was also confirmed, which is due to the successful substitution of the Zn^{2+} by Dy^{3+} [143], [144], [145], [146]. An increase in the band gap was observed after doping with Dy^{3+} . The broadening of the bandgap is attributed to the Burstein-Mos shift, which results from the filling of the conduction band of n-type materials or of the valence band of p-type materials. However, they also reported that further increasing concentrations of the dopant cause the band gap narrowing due to the formation of defects in the band gap. At an excitation wavelength of 325 nm, their PL emission spectra revealed a large emission band at 380 nm, which originates from the recombination of free excitons in ZnO. The broadening of the UV band after Dy^{3+} is due to the creation of Zn vacancies and Zn interstitial defects from Dy^{3+} dopant. The revealed suppression of the visible band is related to excitation transfer from intrinsic defects to Dy^{3+} ions. Moreover, there are other three emission peaks detected at 476 (blue), 567 (yellow), and 658 (red) nm, which are due to $^4F_{9/2} \rightarrow ^6H_{15/2}$, $^4F_{9/2} \rightarrow ^6H_{13/2}$, and $^4F_{9/2} \rightarrow ^6H_{11/2}$ transitions, respectively [147]. Whereby the magnetic dipole transition is given by $^4F_{9/2} \rightarrow ^6H_{15/2}$, while $^4F_{9/2} \rightarrow ^6H_{13/2}$ and $^4F_{9/2} \rightarrow ^6H_{11/2}$ transitions are related to electric dipole transitions. The increase in Dy^{3+} doping concentration resulted in a decrease in the lifetime decay of the ZnO: Dy^{3+} phosphor material. The decrease in decay time is attributed to the excitation energy exchange among the Dy^{3+} ions,

which is due to the reducing distance between these ions, can enhance the energy depletion rate and cause a decrease in decay time [147]. However, their colour chromaticity diagram revealed that the ZnO: Dy³⁺ was in the white region; hence, they concluded that the ZnO: Dy³⁺ phosphor material can be considered a good candidate for white luminescence applications. Similar behaviour of Dy³⁺ ions on ZnO materials was reported by Uma et al. [147].

2.4 Conclusion

The sol-gel method is commonly used for the preparation of excellent phosphors. In comparison to the combustion method, it offers the advantage of good crystallinity and stability. Furthermore, when compared to the solid-state method, it demonstrates the advantage of a higher rate of raw materials synthesis. **Table 2.1** below shows the summative table for the characteristics of the ZnO phosphors prepared via sol-gel, combustion, and solid-state reaction methods.

Table 2.1 summative table for the characteristics of the ZnO phosphors prepared via sol-gel, combustion, and solid-state reaction methods [111], [113].

Characteristic	Combustion Method	Solid-State method	Sol-gel Method
Synthesis Technique	Chemical reaction in a combustion flame using fuel and oxidizer	Solid-state reaction between reactants at elevated temperatures	Formation of a gel precursor followed by heat treatment
Temperature	High temperatures due to combustion flame	High temperatures during reaction and annealing steps	Moderate temperatures during gel formation and annealing
Processing Time	Relatively short processing time	Typically longer processing time due to reaction and annealing steps	Moderate processing time with gel formation and heat treatment

Characteristic	Combustion Method	Solid-State method	Sol-gel Method
Particle Size	Typically smaller particle size	Particle size influenced by reaction and annealing conditions	Controllable particle size through gel formation parameters
Homogeneity	Generally high homogeneity due to rapid combustion	Homogeneity depends on mixing and diffusion during solid-state reaction	Good homogeneity achieved through the gel precursor
Purity	High purity due to rapid reaction	Purity affected by the quality of starting materials and reaction conditions	High purity as the gel can be carefully prepared
Crystal Structure	Crystal structure influenced by combustion conditions	Crystal structure influenced by solid-state reaction conditions	Controlled crystal structure through gel chemistry
Doping Ease	Doping is achievable during combustion	Doping may be more challenging due to solid-state diffusion limitations	Doping can be easily controlled during gel formation
Surface Area	Typically high surface area	Surface area influenced by particle size	Relatively high surface area due to gel precursor
Optical Properties	Can exhibit good optical properties	Optical properties influenced by crystal structure and impurities	Tailorable optical properties through controlled gel chemistry
Applications	Often used in quick, low-cost applications	Widely used in various applications including optoelectronics	Suitable for applications requiring controlled properties

Various luminescence emission properties of ZnO doped with RE³⁺ (where RE³⁺ = Sm³⁺, Eu³⁺, and Dy³⁺) materials have been discussed. The ZnO host material exhibits both similar and distinct behaviours influenced by the mentioned dopants. All the three RE ions dopants have no influence on the crystal structure of the ZnO material. **Table 2.2** below presents the summative luminescence properties attributed to Sm³⁺, Eu³⁺, and Dy³⁺ ions. The observed blue colour emission observed in all RE³⁺ is due to the ZnO host.

Table 2.2 summative luminescence emission properties due to Sm³⁺, Eu³⁺, and Dy³⁺ ions [126], [141].

RE ³⁺	Effect on Particle Size	Effect on Band gap	Emission colours	Effect on Lifetime decay
Sm ³⁺	Increase the particle size of the material	Decreases	Green, orange, and red	Increase with increase in dopant concentration
Eu ³⁺	Increase the particle size of the material	Decreases	Blue, green, yellow and red colour emission	Decrease with increase in dopant concentration
Dy ³⁺	Increase particle size of the host	Increases	blue, yellow, red, and white	Decreases the lifetime decay of the host

Up to now various research on metal oxides such as ZnO have been reported in the literature using various synthesis techniques: sol-gel, solid-state, and combustion reaction methods, but none have reported on a comparative study of all the above metal oxides within a single frame. The main objective of this study is to investigate the impact of the above-mentioned synthesis technique on the structural and photoluminescent properties on the zinc borate Zn₄B₆O₁₃ phosphor material. To identify the best luminescent characteristics of the host material, we decided to introduce the following dopants Eu³⁺, Dy³⁺, and Sm³⁺ for a comparative study.

Chapter III

Experimental Techniques

3.1 Introduction

In this chapter, different synthesis methods and characterisation techniques are used for sample preparation and analysis, respectively. The combustion, sol-gel, and solid-state methods were used to prepare the $Zn_4B_6O_{13}$ host and $Zn_4B_6O_{13}$ doped with rare earth (RE^{3+}) ions where ($RE^{3+} = Sm^{3+}, Eu^{3+},$ and Dy^{3+}) ions elements. All the chemicals used for synthesis were purchased from Sigma-Aldrich. The prepared samples were characterized using various techniques. X-ray diffraction (XRD) was used to study the crystal structure and the crystallite size of the material. The morphology and topology of the samples were studied through field emission scanning electron microscopy (FESEM). Fourier transform infrared (FTIR) spectroscopy was used to examine the chemical composition and functional groups present in the prepared material. Optical properties were examined through ultraviolet-visible spectroscopy (UV-VIS). The photoluminescence emission properties were analysed by photoluminescence spectroscopy (PL).

3.2 Synthesis methods

3.2.1 Sol-gel method

Due to its numerous benefits over other processes, the sol-gel method is one of the most efficient ways to prepare non-metal oxide samples [148]. Moreover, this method is one of the most used, and its variations and adaptations are utilized to synthesize pure thin films and powdered catalysts in high, homogeneous concentrations under stoichiometry control. The sol-gel method has been in existence since the early 1800s [149].

The sol-gel method was used to synthesize the host and doped materials. For host materials, the precursors used are zinc nitrate as an oxidizer, citric acid, and boric acid as fuels. In this study, the doped ($RE^{3+}=Dy^{3+}, Sm^{3+},$ and Eu^{3+}) $Zn_4B_6O_{13}$ materials were synthesized. Zinc

nitrate hexahydrate ($\text{Zn}(\text{NO}_3)_2(6\text{H}_2\text{O})$) (99%) was used as a zinc source; boric acid (H_3BO_3) (99.5%) and citric acid ($\text{C}_6\text{H}_8\text{O}_7$) (99.95%) were used as fuels. The dopants used were samarium III nitrate hexahydrate $\text{Sm}(\text{NO}_3)_3(6\text{H}_2\text{O})$ (99.99%), dysprosium III nitrate pentahydrate $\text{Dy}(\text{NO}_3)_3(5\text{H}_2\text{O})$ (99.9%), and europium III nitrate hydrate $\text{Eu}(\text{NO}_3)_3(\text{H}_2\text{O})$ (99.99%).

To synthesize the host material, zinc nitrate and boric acid were dissolved in 40 ml of hot deionized (DI) water. Citric acid was dissolved in a separate beaker with 40 ml of DI water; this allowed for a homogeneous mixture in the reaction. After citric acid was completely dissolved in deionized water, it was then added to the mixture of zinc nitrate and boric acid while stirring, and they formed a homogeneous mixture. The solution was stirred and heated at 220 °C until it formed a gel-like solution. The gel was allowed to gain more strength by not being removed from the hot plate until it had fully formed. The fully formed gel was then transferred to a crucible, kept in a furnace, and annealed at 800 °C for 2 hours. The final sample was grained to a fine powder, calcined at 900 °C, and finally collected and characterized. The temperatures above 1000 °C were found change the crystal structure of the $\text{Zn}_4\text{B}_6\text{O}_{13}$ material hence the above temperatures 800 and 900 °C were used during sythesis [150], [151], [152].

The balanced chemical equation for the above-mentioned reaction is as follows:



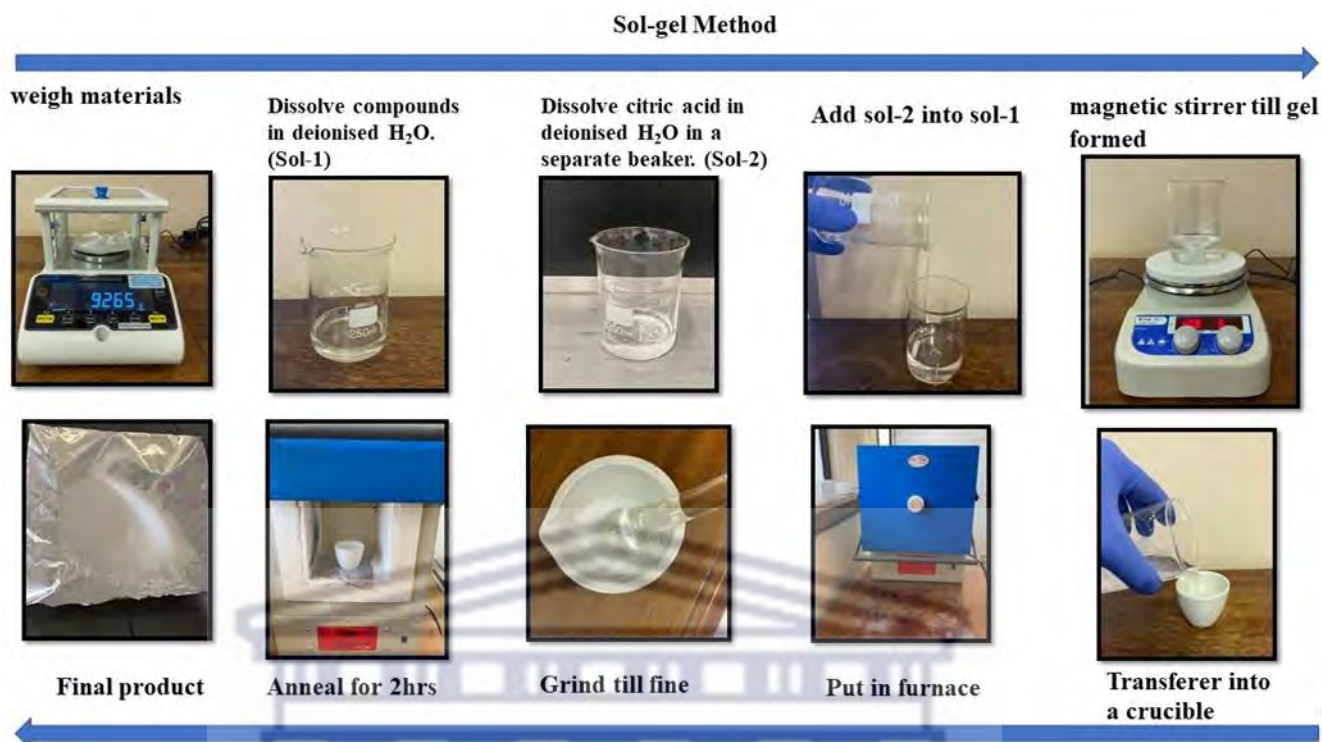


Figure 3.1 A flow diagram for the sol-gel synthesis procedure.

3.2.2 Combustion Method

The majority of companies rely on the combustion method, which is one of the most effective for the preparation of nanophosphor materials [150]. This synthesis method involves simply mixing both organic fuels, such as citric acid, urea, glycerine, and metal nitrates, into enough deionized water, then heating until all the present water evaporates [153]. It involves phases before the explosive reaction, such as blazing (gas phase) and smouldering (heterogeneous phase). The blazing temperature encourages phase formation and crystallization [154].

This is the second method used to synthesize the host and doped nanophosphors. For host material, elements used were zinc nitrate hexahydrate as an oxidizer, urea, and boric acid as fuels. In this study, the doped ($RE^{3+} = Dy^{3+}, Sm^{3+},$ and Eu^{3+}) $Zn_4B_6O_{13}$ materials were prepared. Zinc nitrate hexahydrate ($Zn(NO_3)_2(6H_2O)$) (99%) was used as a zinc source; boric acid (H_3BO_3) (99.5%) was used as a borate; and urea CH_4N_2O (91.05%) for combustion. The dopants used were samarium III nitrate hexahydrate $Sm(NO_3)_3(6H_2O)$ (99.99%), dysprosium III nitrate pentahydrate $Dy(NO_3)_3(5H_2O)$ (99.9%), and europium III nitrate hydrate $Eu(NO_3)_3(H_2O)$ (99.99%).

To synthesize the host material, zinc nitrate and boric acid were dissolved in 40 ml of hot deionised (DI) water. Urea was dissolved in a separate beaker with 40 ml of DI water; this allowed a homogeneous mixture in the reaction. After urea was completely dissolved in deionized water, it was then added to the mixture of zinc nitrate and boric acid while stirring, and they formed a homogeneous mixture. After 30 minutes, a few drops of approximately 10 ml of NH₄OH were added to the solution to reach pH 9. The precipitate was then formed, and the solution was transferred to a ceramic crucible and kept in a furnace at 800 °C for the formation of powder material. The sample was removed from the furnace and ground using a pestle and mortar. The sample was then annealed at 900 °C, and the Zn₄B₆O₁₃ (host) compound was completely formed and characterized.

The balanced chemical equation for the reaction mentioned above is shown below:

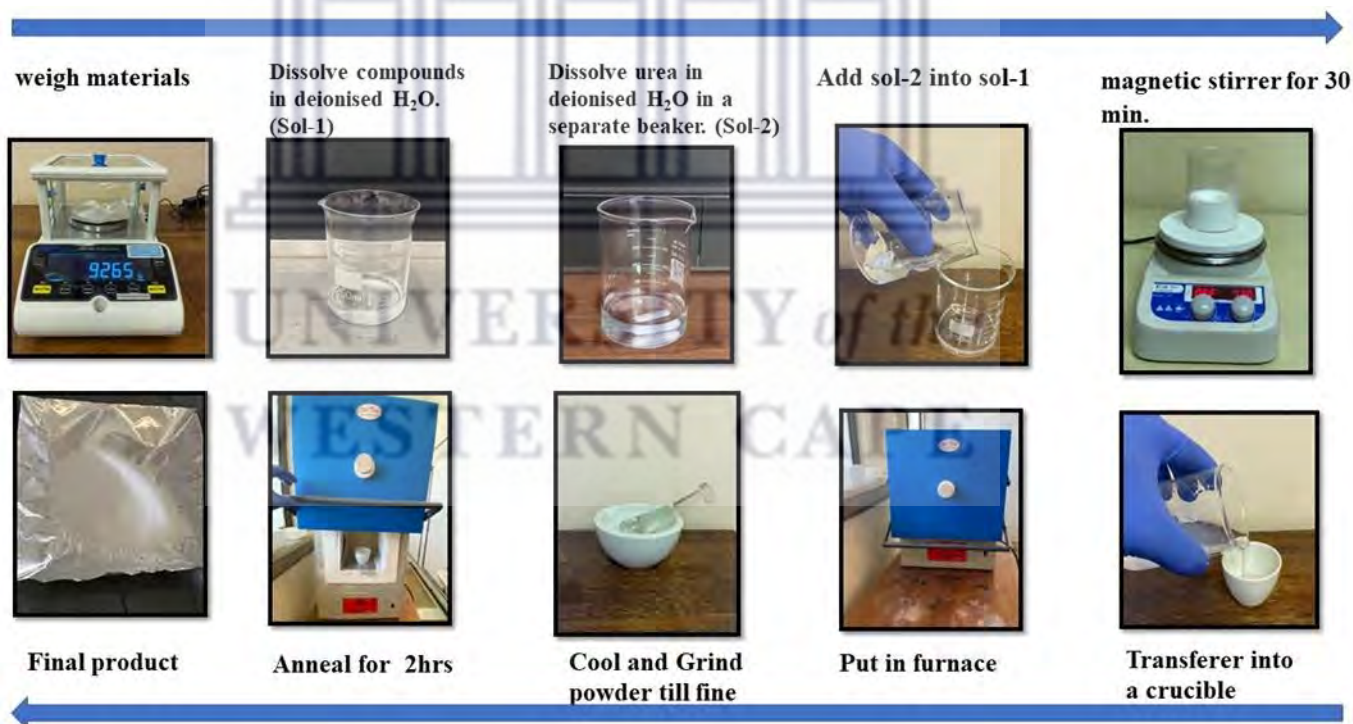
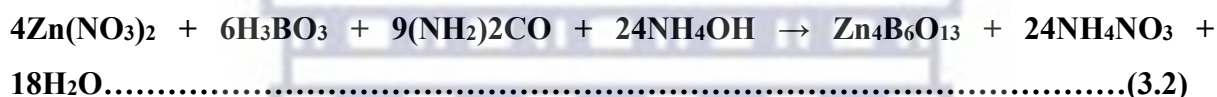


Figure 3.2 Flow diagram of the combustion method.

3.2.3 Solid State Method

The solid-state reaction method is a traditional synthesis technique to produce inorganic compounds due to its simple and economical operation as well as the utilization of inexpensive

and accessible carbonates and oxides as raw materials. However, it is frequently necessary to use a high temperature and/or prolong the processing time for calcination [155].

This is the third used method to synthesize the host and doped nanophosphors. For host materials, elements used were zinc nitrate hexahydrate as an oxidizer, urea, and boric acid as fuels. In this study, the doped ($RE^{3+}=Dy^{3+}$, Sm^{3+} , and Eu^{3+}) $Zn_4B_6O_{13}$ materials were synthesized. Zinc nitrate hexahydrate ($Zn(NO_3)_2(6H_2O)$ (99%) was used as a zinc source; boric acid (H_3BO_3) (99.5%) was used as a borate; and urea (CH_4N_2O) (91.07%). The dopants used were samarium III nitrate hexahydrate $Sm(NO_3)_3(6H_2O)$ (99.99%), dysprosium III nitrate pentahydrate $Dy(NO_3)_3(5H_2O)$ (99.9%), and europium III nitrate hydrate $Eu(NO_3)_3(H_2O)$ (99.99%).

To synthesize the host material, the chemicals mentioned above are the precursors used in this method; they were combined in proper stoichiometric proportions. The precursors with a larger surface area were first ground using an agate pestle and mortar, followed by the ones with smaller surface areas. The grinding process took approximately 20 minutes. Acetone was used during the grinding process to ensure that the sample mixture was uniformly homogeneous. The resulting mixture was transferred to a ceramic crucible and then placed into a furnace for 2 hours at 800 °C. The final product was taken out of a furnace, cooled, ground into a fine powder, and then annealed at 900 °C. The final, prepared sample was then taken for characterization.

The balanced chemical equation for the above-mentioned reaction is as follows:

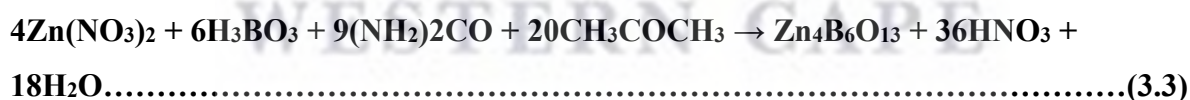




Figure 3.3 A flow chart for the solid-state synthesis method.



3.3 Characterization techniques

3.3.1 X-Ray Diffraction

The prepared samples were examined by XRD before any other characterization technique. This technique is mostly used as the primary step of characterization in the engineering and science fields. XRD is a non-destructive characterization technique that uses X-rays for phase analysis and the crystallinity of materials [156], [157], [158]. The monochromatic X-rays produced by this technique have weak absorption, thus causing no harm to the sample during analysis. Nano-powders, ceramics, polymers, and thin films are forms of materials that can be examined with this technique. The diffraction patterns of X-rays are similar to fingerprints that identify crystalline material by matching the experimental patterns with the JCPDS database. The XRD setup comprises the following main components: the X-ray source, the sample holder, and a detector, as shown in **Figure 3.4 (a)** [159], [160].

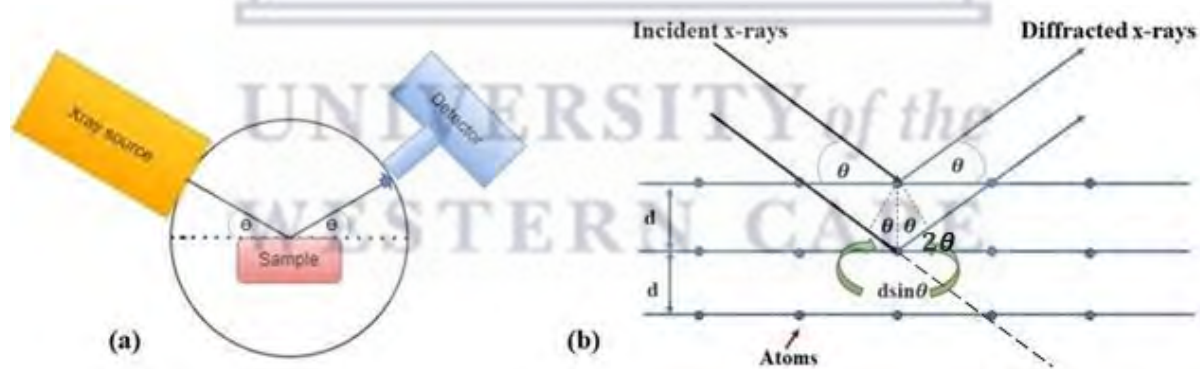


Figure 3.4 (a) The Schematic arrangement of the components of an XRD diffractometer [159] and (b) Schematic representation of incident and diffracted X-rays on and off the sample [160].

The condition of the diffraction of X-rays from the sample is given by Bragg's law. For this law to be successful, there must be a generation of X-rays. The cathode ray tube is the simplest

method applied to generate X-rays. This process occurs under a low-pressure environment. A voltage of 10 to 60 kilovolts (kV) is applied across a hot tungsten filament (cathode), which then accelerates electrons towards an anode, a heavy metal like Cu that was used in this experiment. X-rays are produced through electronic transitions known as $K\alpha$ and $K\beta$, which involve electrons moving from the second innermost K shell to the first innermost L shell (transitioning from $n = 2$ to $n = 1$) and from the third innermost M shell to the first innermost L shell (transitioning from $n = 3$ to $n = 1$), respectively [161], [162]. The produced X-rays are usually Cu $K\alpha$ with a wavelength of 0.5406 nm [159]. A schematic of a $\theta - 2\theta$ experiment is given in **Figure 3.4 (b)**. The sample diffracts the X-ray, which is associated with the interplanar spacing “ d ”, at an angle that obeys Bragg’s law. This law relates the wavelength of the diffracted X-ray with the crystalline sample’s lattice spacing and the angle of diffraction. This relation can be mathematically presented as shown below [159], [163], [164]:

$$n\lambda = 2d\sin\theta \dots \dots \dots (3.4)$$

where θ is the angle of the incident X-ray beam, while 2θ is that of the diffracted beam with respect to the direction of incidence, as shown in **Figure 3.4 (b)**. λ is the x-ray wavelength, d_{hkl} is the path difference between two planes in the periodic atomic lattice, where h, k, and l are Miller indices to characterize the crystal plane from the diffraction patterns, and n is an integer that is regarded as the order of diffraction maxima. For the first order, $n=1$, and for the second order, $n = 2$ etc. although higher orders are not generally observed. Constructive interference occurs when the Bragg’s law is fulfilled [165], [166], [167]. The produced diffraction patterns give distinct information about the material when the conditions satisfy Bragg’s law. The intensity of the produced peaks is plotted as a function of 2θ [157], [165], [166]. The detector records the diffracted X-rays and converts them into an analysable XRD signal, whereby the detected diffraction patterns are used to estimate the crystallite size and deduce other phase properties of the material [159], [168].

Scherer’s equation [165] presented below is used to calculate the crystallite size and peak broadening from the diffraction spectrum. The crystallite size of a particle should never be mistakenly compared to or regarded as a particle size due to the polycrystalline aggregate formation.

$$D = \frac{K\lambda}{\beta_D \cos\theta} \dots \dots \dots (3.5)$$

$$\beta_D = \frac{K\lambda}{D\cos\theta} \dots \dots \dots (3.6)$$

Where \mathbf{K} is the Scherer constant 0.9 for spherical grain, \mathbf{D} is the average crystallite size of a particle, ($\lambda=1.5405 \text{ \AA}$) is the X-ray wavelength utilised by Cu $K\alpha$, (θ is the angle of diffraction), and crystallite size broadening β_D is regarded as full width at half maximum (FWHM) [165]. The intensity of the peaks can be affected by the calcination process. During calcination, the particles become more crystalline, and their intensity peaks increase due to the increase in the average crystallite size [86], [157], [160], [166], [169].

The following equation (3.7) is used to calculate the strain caused by the crystal defects leading to the broadening of peaks, which is then added to equation (3.6) to form the William-Hall equation (3.8) [160].

$$\beta_e = C\varepsilon \tan(\theta) \dots \dots \dots (3.7)$$

Where the strain parameter is denoted as ε , C is a constant, and the strain broadening is given by β_e , which is due to the instrument.

Therefore, equation (3.6) and (3.7) can be combined through convolution, whereby the convolution is assumed to be sum of the two equations, leading to the following equation:

$$\beta_{tot} = \beta_D + \beta_e = C\varepsilon \tan\theta + \frac{k\lambda}{\beta_D \cos\theta} \dots \dots \dots (3.8)$$

where β_{tot} is the full width at half maximum intensity for diffraction peaks. Multiplying equation (3.8) by $\cos\theta$ we obtain the following equation:

$$\beta_{tot} \cos\theta = C\varepsilon_{W-H} \sin\theta + \frac{k\lambda}{D_{W-H}} \dots \dots \dots (3.9)$$

The above equation is known as the uniform deformation model. D_{W-H} is the grain size determined by the Williamson-Hall plot. If we compare equation (3.9) to the standard straight-line $y = mx + c$, therefore from plotting of $\beta_{tot} \cos\theta$ versus $\sin\theta$ we can obtain the strain component $C\varepsilon_{W-H}$ from the slope. The $\frac{k\lambda}{D_{W-H}}$ term is the intercept from the plot, from which the average crystallite size can be estimated [40], [170].

3.4 Microscopy

3.4.1 Scanning Electron Microscopy (SEM)

Scanning electron microscopy (SEM) is an optical characterization technique that allows the observation and analysis of heterogeneous organic and inorganic materials in the micro- to nanoscale range. The significant use of this technique is to acquire high-resolution images of the surface morphology and topography of a material [171], [172]. These images are obtained by examining the surface of a material using a beam of electrons. The electrons are used since they have a shorter wavelength than light and can easily penetrate through the sample, thus producing images with higher resolution and an improved field of depth [135], [160]. It is mandatory to properly prepare and coat samples before microscopy analysis in order to obtain prime results. Coating is significant for ensuring conductivity in samples, as this avoids charging during analysis. Scanning electron microscopy is typically equipped with EDS (energy dispersive X-ray spectroscopy) for chemical composition and elemental mapping. SEM setups comprise the following components: electron source (electron gun), anode, condensor lenses, objective lens, back scattered electron detector, X-ray detector, secondary electron detector, scancoils, amplifier, and scan generator [173], [174], as shown in **Figure 3.5**.



UNIVERSITY *of the*
WESTERN CAPE

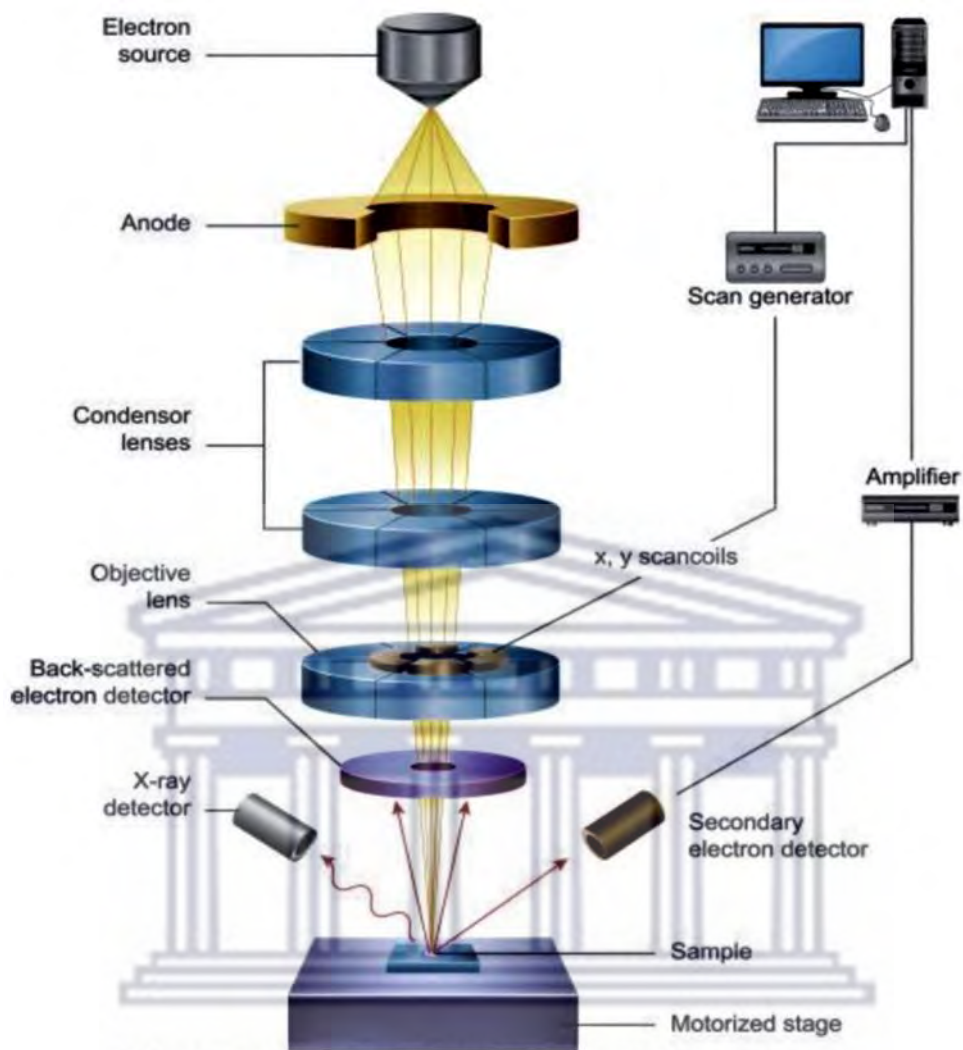


Figure 3.5 A schematic diagram for scanning electron microscopy fundamental components [171].

The electron gun contains tungsten filament, which is heated to a temperature of 2000 – 2700 K to produce electrons from the high negative potential (-20 000 V) to the ground potential (0 V), with an emission current (probe current) of approximately 100 microamperes [175]. The electron beam is focused by the anode towards the electromagnetic lenses, as shown in **Figure 3.5**. The magnetic lenses adjust the diameter of the electron beam passing through and targeting the specimen. These lenses are created by an iron piece soled with copper wire, which causes the magnetic field that controls the direction and magnitude of the beam to the specimen. This is advantageous for the selection of an area or raster to be analysed [174], [176]. A vacuum of (10^{-10} - 10^{-11} torr) in the beam chamber is necessary to avoid beam contamination. There is a path between the magnetic lenses and the specimen, which is known as the working distance.

The working distance affects the focus and the depth of field during sample analysis. Therefore, necessary adjustments to the specimen's height are required for the sample to be in focus. The failure to focus the beam on the sample results in various lens aberrations, which are astigmatism, spherical aberrations, and chromatic aberrations [166], [168], [177].

An electron beam is irradiated onto the surface of the sample in a raster for scanning. The best resolution is obtained through high-energy electrons; however, it varies among the samples being analysed as high-energy electrons might damage other samples. The number of pixels per row and the number of rows affected by the chosen resolution. The scan coils are responsible for creating a rastering pattern on the specimen [177]. When the specimen is bombarded with a beam of electrons, it can release the following: secondary electrons, back-scattered electrons [178], distinctive X-rays, and other photons of varying energies are among the signals produced during the sample-electron beam interaction, as shown in **Figure 3.6** [18]. However, this study focuses on the secondary electrons, back-scattered electrons, and distinctive X-rays as they can be detected by the SEM. The beam interaction with the sample may involve both inelastic and elastic events. Inelastic events occur during the interaction of beam electrons with electric field of an electron in a specimen atom. This interaction causes an energy transfer to the specimen atom, potentially leading to the expulsion of an electron from that atom as a secondary electron, which has energy less than 50 eV. Therefore, their less energy makes them ideal for examining the surface morphology. Elastic events occur during the interaction of the electron beam with the electric field of the nucleus of a specimen atom. This interaction leads to a change in the direction of the beam electron without a significant alteration in the energy of the beam electron (typically < 1 eV). The elastically scattered electron is named the back scattered electron, which is detected in the SEM during specimen analysis [166], [169], [171], [172], [173], [174].

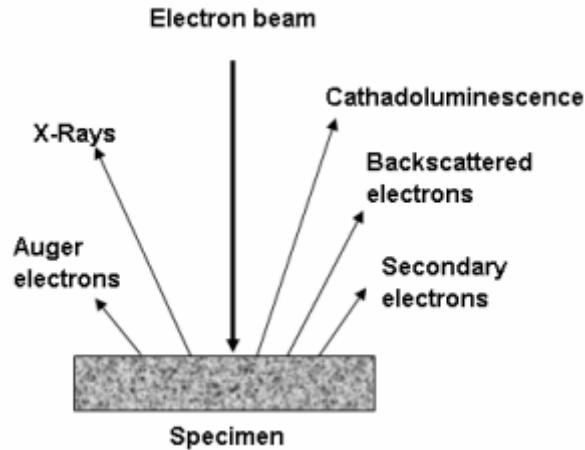


Figure 3.6 A schematic diagram for beam-specimen interactions [177].

When an incident electron beam is travelling through the sample, it scatters, and the electron-hole pairs are formed at all sites but at varied densities. The mean carrier generation rate [166], [179] is given by

$$\langle g \rangle = \frac{E(1-n)I_b}{eh \cdot q} \dots \dots \dots (3.10)$$

where $\langle g \rangle$ represents the average generation rate of electron-hole pairs per unit volume and time. I_b is the incident beam current passing through a thick material, where q is the charge of a hole and e is the elementary charge of an electron [180], both measured in coulombs (C), respectively. The Planks constant is denoted by h , which is measured in J.s. E is the beam energy responsible for electron-hole pair production, which is measured in photons per unit area per unit time, for instance, photon/cm²·s, and n is the bulk scattering coefficient. This equation is significant in providing a quantitative measure of how effectively a material generates charge carriers (electrons and holes) when exposed to beam energy [166]. The beam interaction with the specimen is restricted to areas near the surface at low accelerating voltages, less than 5 kV (refer to **Figure 3.6**). In comparison to images acquired at greater accelerating voltages, this produces images with more surface detail. The detectors, secondary electron detector (SED) and the backscattered electron detector (BSD) [181], collect the respective emitted rays, and these signals are subsequently utilized to generate images [166], [169], [171], [172]. SED images provide a visualization of inelastically scattered electrons near the sample surface, offering topographical information with the highest achievable resolution. However, SED images do not convey material composition information. A backscattered electron

detector (BSD) is designed to capture elastically scattered electrons, which possess higher energy and originate from beneath the sample surface. Consequently, the resolution of a BSD image is typically inferior when compared to an image obtained using a Scanning Electron Diffraction (SED) detector [26], [182].

3.5 Spectroscopy

3.5.1 Ultraviolet visible spectroscopy (UV-Vis)

Ultraviolet-visible (UV-Vis) spectroscopy is a non-destructive characterization technique for analysing the response of a sample to an excitation in the UV-Vis electromagnetic region [183], [184]. In this technique, light in the form of ultraviolet or visible radiation is directed towards the sample, where it is either absorbed, reflected, or transmitted. **Figure 3.7** shows the schematic diagram of the UV-Vis working principle. The intensity of light, encompassing transmission, reflection, and absorption from the sample, is measured across the wavelength range of 200 to 800 nm. This measurement serves as a function of wavelength, providing insights into how the sample interacts with incident light throughout the specified range [185].

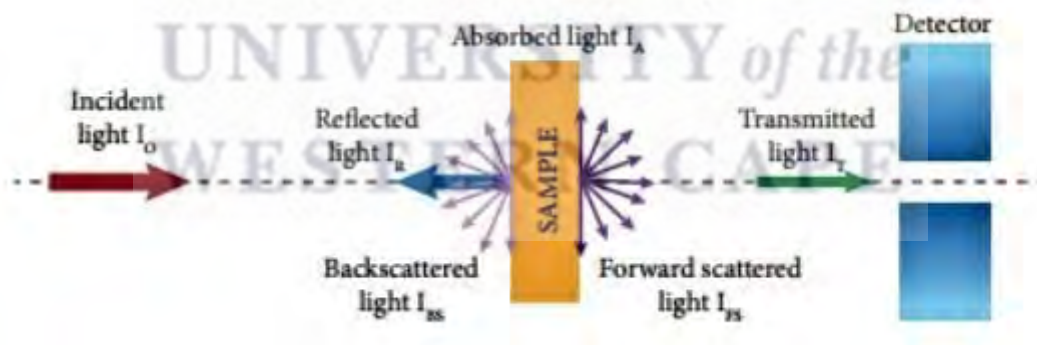


Figure 3.7 UV-Vis working principle [185].

3.5.1 (a) Determination of optical coefficients

The measured reflectivity of light at normal incidence may be used to analyse the sample. The fraction of incident light that is reflected by the sample is known as the reflectivity coefficient $r(\omega)$, as shown in the equation below [166], [186].

$$r(\omega) = \frac{E_r}{E_i} = p(\omega)e^{i\vartheta(\omega)} \dots \dots \dots (3.11)$$

Where E_r is the reflected electric field, E_i is the incidence electric field, $p(\omega)$ is the amplitude, and $\vartheta(\omega)$ is the phase component of the reflectivity coefficient [187].

For better clarification on the behaviour of light when it interacts with a sample at a specific wavelength, the following equation (3.12) is applied, where the extinction coefficient K is regarded as the imaginary part of the refractive index. The refractive index n in a molecule crystal is related to the reflectivity at normal incidence [166].

$$r(\omega) = \frac{n+iK-1}{n+iK+1} \dots \dots \dots (3.12)$$

The acquired information is used to understand the material's electronic transitions. The reflected radiation from the sample does not reveal detailed information about these transitions; hence, the main focus is on absorption. During absorption, there is an electron transition from an occupied orbital to an occupied orbital with higher potential. In this process, an exciton is formed where an electron-hole pair is bound by a coulomb-attractive interaction. The energy difference within these orbitals is usually within 125 to 650 kilojoules per mole (kJ/mol). The lowest energy-occupied molecular orbitals are the sigma (σ) orbitals, corresponding to σ bonds. In materials that absorb in the ultraviolet region, the absorption spectrum typically manifests as sharp lines [166].

The fraction of light that is transmitted through the sample is known as the transmittance coefficient $t(\omega)$, which is given by the following equation [166].

$$t(\omega) = \frac{E_T}{E_i} = \frac{2n}{n+iK+1} \dots \dots \dots (3.13)$$

Where E_T is the reflected electric field. The reflectance (3.12) and transmittance (3.13) equations are related in the Beer-Lambert law equation that will be shown later on for the

determination of absorbance. For a material that absorbs in the ultraviolet region, the absorption spectrum usually consists of sharp lines, as would be expected for a quantized process occurring between two discrete energy levels. The broad band in the UV spectrum is usually a combination of transitions. When the sample comprises a large number of molecules capable of absorbing light, the absorbance increases [188], [189]. The spectrophotometer measures the intensity of the incident light passing through the sample (I_T), comparing it to the intensity of light before passing through the sample (I_0). This measurement is conducted to determine the ratio of transmittance (I_T/I_0); refer to **Figure 3.7**. Transmittance is used to obtain absorbance; the Beer-Lambert law is used as shown below [186]. The equation below is used to obtain the concentration of materials.

The Beer-Lambert law for absorbed waves travelling through the sample may be expressed as [186].

Transmittance:
$$T = \frac{I_T}{I_0} \dots \dots \dots (3.11)$$

The above equation 3.11 can be multiplied by 100 to be in percentage form [190].

$$\%T = \frac{I_T}{I_0} \times 100 \dots \dots \dots (3.12)$$

$$A = -\log (T) \dots \dots \dots (3.13)$$

$$A = -\log \left(\frac{I_T}{I_0} \right) \dots \dots \dots (3.14)$$

To obtain the reflectance measurement **R**, which is the ratio of I_R/I_0 , the intensity of light reflected from the sample (I_R) is measured and compared to the intensity of light reflected from the reference material (I_0) in the reflection spectrum of a perfect silvered mirror for specular reflection [191]. The electronic structure of various molecules in the form of liquids and powder materials is obtained using this technique.

3.5.1 (b) Kubelka-Munk equation and Tauc plot

The Kubelka-Munk equation [192], presented below, is employed for analysing the diffuse reflectance spectra (DRS) in the context of light scattering from samples illuminated with diffuse monochromatic radiation. Furthermore, the equation establishes a relationship between the reflectance of a material and its absorption and scattering properties to estimate the material's optical band gap energy. However, the widely used practice of determining the E_g

of a material directly from the K-M function is found to be inadequate [192]. According to Kubelka and Munk, the scattering and absorption of light are first-order phenomena. The system in this study consists of a substrate coated with a material of interest that is illuminated with a diffuse monochromatic light. The system consists of a cylindrical substance with a flat area A and a thickness L , to neglect boundary effect, corresponding to a medium that reflects light regardless of the substrate reflectance value [192].

$$F(R_{\infty}) = \frac{K}{S} = \frac{(1-R_{\infty})^2}{2R_{\infty}} \dots \dots \dots (3.15)$$

where R_{∞} is the reflectance of a material with semi-infinite thickness ($L \rightarrow \infty$), which is obtained by comparing the reflectance of a material to that of a reference. For this study, a powder material is pressed to a thickness of 2.5 mm to avoid the contribution of the substrate during analysis. Therefore, the semi-infinite thickness is approaching infinity, whereby the substrate does not contribute. E_g is the bandgap energy of the material; it is defined as the energy difference between the bottom of the conduction band and the top of the valence band, S is the scattering factor, K is the molar absorption coefficient [192].

The tauc plot is used to obtain the bandgap of a material from the diffuse reflectance spectra [193]. The Tauc function relates the absorption coefficient and energy bandgap, as it describes the absorption behaviour near the band edge of a material [184], [194].

$$(\alpha h\nu)^n = A(h\nu - E_g) \dots \dots \dots (3.16)$$

The Kubelka-Munk function is related to the absorption coefficient (α), as shown in equation (3.17), which is then substituted in Tauc equation (3.16) to form equation (3.18) to determine the optical bandgap energy of a material, since $\frac{K}{S} = \frac{\alpha}{s}$, whereby S and s are considered constants. In fact, α and s are intrinsic optical properties of the materials and represent the probabilities of light being absorbed and scattered, respectively, per unit path length [192].

$$\alpha \propto F(R_{\infty}) \dots \dots \dots (3.17)$$

$$(F(R_{\infty}) h\nu)^n = A(h\nu - E_g) \dots \dots \dots (3.18)$$

Where α is the absorption coefficient, ν is the vibration frequency, A is the proportionality constant, and n denotes the nature of the electronic transition and depends on the band structure of the material [184], [192],

for dipole allowed transition occurring at direct bandgap $n = \frac{1}{2}$.

for dipole forbidden transition at direct bandgap $n = 3/2$.

for dipole allowed transition near indirect bandgap $n = 2$, requiring participation of phonons.

for dipole forbidden transition at indirect bandgap $n = 3$, the involved orbitals have the same parity, which leads to suppressed dipolar transitions, and are usually called weakly allowed transitions [192].

From the plot of $[F(R_{\infty}) * h\nu]^2$ versus $h\nu$ refer to equation (3.18) where $n = 2$ for a material used in this study, the tangent line is extrapolated by linear fit to $\frac{K}{S} = 0$ to obtain the energy band gap [195], [196]. The E_g of $Zn_4B_6O_{13}:RE^{3+}$ phosphors will be calculated from the diffuse reflectance data analysed according to Eqs. (3.15) and (3.18).

3.5.2 Fourier Transform Infrared (FT-IR) spectroscopy

FT-IR is a non-destructive characterization technique that is used to identify the functional groups present in both organic and inorganic compounds and their concentrations in a typical spectral range between 4000 cm^{-1} and 400 cm^{-1} [66], [197]. This range corresponds to the wavelengths of 2.5 to 25 μm . This technique is able to analyse samples in the form of liquids, solids, and gaseous phases. The operating procedure is to put the sample to be measured in the IR path and measure a transmission spectrum; the resultant absorption bands correspond to the molecular bonds in the probed sample [197].

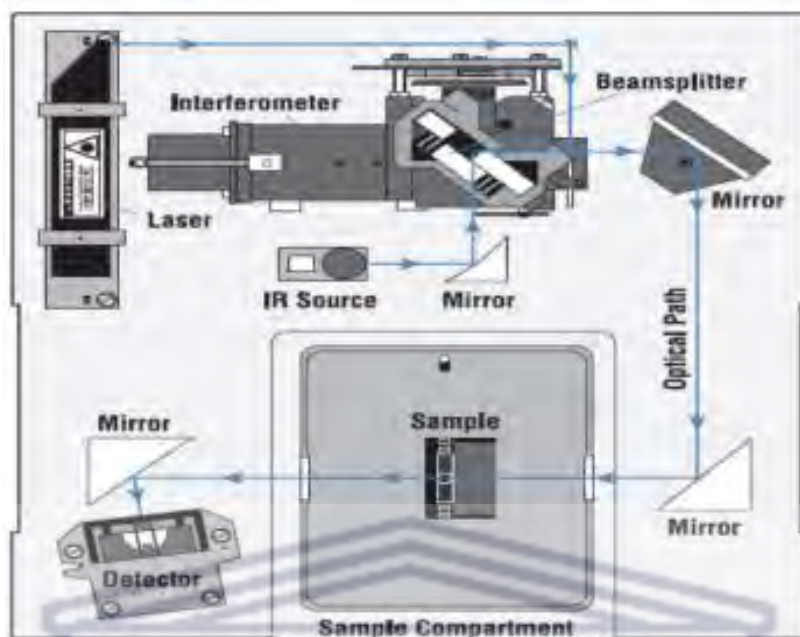


Figure 3.8 A schematic diagram of the FT-IR spectrometer [135].

The FTIR technique comprises the following components: the source, sample holder, interferometer, and detector (refer to **Figure 3.8**). The source produces a beam of infrared radiation, which is divided into two perpendicular beams with equal radiation intensity by the beam splitters. In the interferometer, there is a recombination of two beams with different wavelengths, causing destructive and constructive interference and creating an interferogram. Destructive interference occurs when two waves with the same frequency travelling in the same direction facing in the opposite direction; their sum adds to zero if the peaks and troughs align, resulting in a weak signal [67]. Conversely, constructive interference occurs when two waves with the same frequency travelling in the same direction, their addition forms a new bigger wave which looks like the original wave but has a larger amplitude, resulting in a stronger signal. Moreover, this process occurs when the path length difference (the optical path travelled by light) between two interfering waves. In simple terms, the interference in an interferometer is due to the superposition of light waves during the recombination of light waves. The wave interference manifests as a pattern of alternating bright and dark regions in the interferogram. The beam splitter recombines the two beams, and the interferogram is formed. The mirrors direct the interferogram containing the radiative energy to the sample [198]. When an electric field of a molecule is rotating or vibrating at the same frequency as the incoming radiation,

there is an energy transfer. Several wavelengths that are present in the sample's spectral range are simultaneously absorbed as they pass through it. The sample absorbs only selected frequencies of energy, that match its natural vibrations. **Figure 3.9** shows energy diagram indicating various rotational and vibrational bands [9].

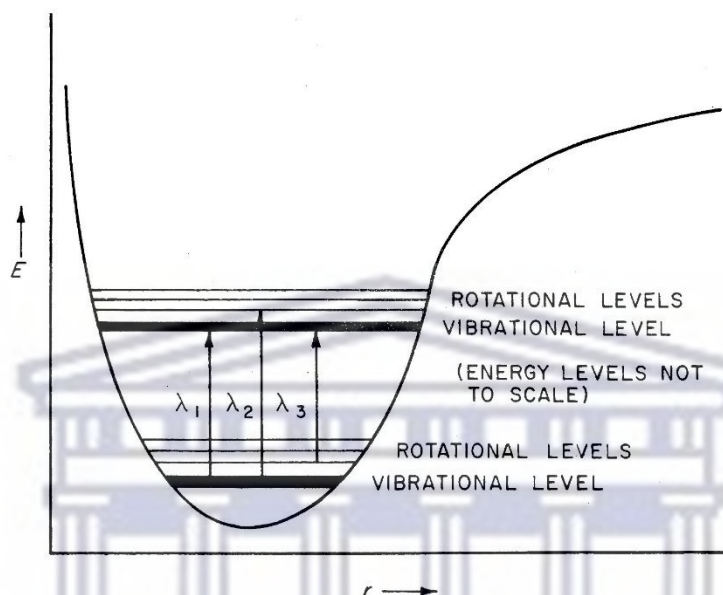


Figure 3.9 Schematic diagram for rotational and vibrational energy levels [9].

The rotational frequencies are of the order of 10^{14} cycles/sec, and the vibrational frequencies are of the order of 10^{11} cycles/sec, which allows them to fall in the infrared region. The rotational spectra have quite sharp absorption bands, while they are broad for the vibrational spectra. The broadening is due to the rotational level associated with each vibrational level. This absorption corresponds to energy changes in the order of 8 to 40 kJ/mol [199]. The absorbed energy serves to increase the amplitude of the molecule's vibrational motions. The frequency of fundamental vibration is given by the following equation [9]

$$\nu = \frac{1}{2\pi} \sqrt{\frac{k}{\mu}} \dots \dots \dots (3.19)$$

The vibration results in the change in molecules dipole moment. For energy transfer to occur, there must be a bond with an electrical dipole that changes the same frequency as incoming radiation [198]. The energy of a vibration of a two-particle system of a reduced mass μ and force constant k in units of dynes/cm is given in (equation 3.20), the k values for different bonds are: 4 to $6 \cdot 10^5$, 8 to $12 \cdot 10^5$, and 12 to $18 \cdot 10^5$ dynes/cm for single, double, and triple

bonds, respectively. The reduced mass of a diatomic molecule is given by $\mu = \frac{M_1 \times M_2}{M_1 + M_2}$ refer to the following equation [9].

$$E_v = \frac{h}{2\pi} \sqrt{\frac{k}{\mu}} \left(v + \frac{1}{2} \right) \dots \dots \dots (3.20)$$

where v is the vibrational quantum number with 0, 1, 2, etc. The vibrational energies are of the order of tenths of electron volts. The stretching and bending modes are due to the vibrational motion in a molecule that gives rise to absorptions. The bending modes occur at lower frequencies than the stretching modes. The higher frequencies of stretching modes are due to the stronger force constants and increased stiffness of bonds during stretching vibrations. Conversely, the bending modes exhibit lower frequencies due to a weaker force constant and less restricted motion compared to the stretching modes. Polar molecules tend to show strong IR absorptions due to their dipole moment, which interacts with the oscillating electric field of the incident infrared radiation. **Figure 3.10** shows the dipole moment (μ). The dipole moment is a vector that is oriented from the centre of gravity of the positive charges to that of the negative charges. It is defined as the product of the size q and the distance r between the charges. It is given by the following equation [9].

$$\mu = q \times r \dots \dots \dots (3.21)$$

Some of these nonpolar molecules may exhibit IR-active vibrations if their dipole moment experiences change as they vibrate [66], [189], [197], [200], [201], [202], [203].

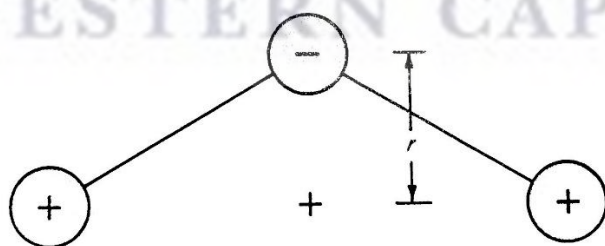


Figure 3.10 schematic diagram of a dipole moment [9].

The detector receives the modified interferogram with the quantity of energy absorbed at each wavelength. The FTIR broadband coverage enables the observation of different molecular vibrations. The range is typically divided into three regions; near infrared (NIR), mid infrared (MIR), and far infrared (FIR) regions associated with particular vibrational modes.

The spectrum is plotted using a mathematical process named a Fourier transform as the modified interferogram, and it is compared to the reference laser beam [189], [200], [201], [202], [203]. It converts unprocessed data into a real spectrum using a mathematical approach; the acquired spectrum serves as a unique fingerprint of the material. The infrared spectrum is obtained by plotting the absorption intensity the wavenumber. There are no two molecules with identical infrared absorption patterns composed of different structures. The infrared spectrum and infrared absorption pattern differ between molecules of various structures [189], [200], [201].

3.5.3 Photoluminescence (PL)

Luminescence refers to the process in which a material absorbs and then emits light. Photoluminescence spectroscopy is a non-destructive characterization method that is used to analyse luminescence properties as well as the dynamic processes of a sample[204]. This technique is highly sensitive and requires no sample preparation [205]. The examined materials are usually nanoparticles, organic molecules, and semiconductors in liquid or powder form for the determination of their applications in lighting technology, for instance, in solid-state and fluorescent lamps. This process involves the excitation of a monochromatic light source in the form of ultraviolet or visible photons directed towards the sample; the incident light can either be absorbed or emitted through photoexcitation in the form of luminescence [206], [207]. When a material absorbs a photon, it promotes an electron to higher energy levels, from the ground state to the excited state. However, the electron in the excited state becomes unstable and returns to the lower energy levels, either radiatively or non-radiatively [208]. The radiative recombination involves the emission of a photon in the form of light during the electron transition from the excited state to the ground state. Conversely, in non-radiative recombination, there is no emission of a photon; the energy lost during the electron transition is released as heat by the emission of phonons; moreover, the lost energy might be transferred to impurities or defects called traps, which consequently results in insufficient light emissions [9].

The excitation conditions must be carefully considered, depending on the nature of the molecule being analysed [209]. The absorption of photons in a material mostly depends on the

energy of the incident light, as different energies have varying penetration depths. Due to their monochromatic nature, high intensity, and ease of focusing, lasers are mostly used for photoluminescence excitation (PLE) [210].

During absorption, there is a creation of a bound electron-hole pair, called an exciton. Electrons in the valence band absorb energy from the photons and elevate to the conduction band. As they elevate, they leave behind a positively charged hole through interband absorption. The electron-hole pair is collectively formed from the hole in the valence band and the electron in the conduction band. The absorption process is usually described as a photon decay mean-free path, which typically yield a broad spectrum. The electron and hole are bound together by a coulomb excitation force, irrespective of the bandgap type [211], [212]. However, in indirect bandgap materials, the separation of electrons and holes may affect the efficiency of exciton formation and recombination processes. This is due to the indirect bandgap. An exciton is usually formed in every analysed insulating material. In materials with an indirect bandgap, excitons near the direct bandgap may become unstable and undergo a final recombination process, resulting in the separation of free electrons and holes. In a direct bandgap, the photons are emitted when electrons at the bottom of the conduction band recombine with holes at the top of the valence band [9], [213]. The absorption of photons is an inverse of the emission of photons. The energy difference between two states can be released depending on the type of transition, whether it is radiative or non-radiative. During the emission process, an ultimate recombination process occurs; an electron transits from a higher energy state to an empty lower energy state. During the electron non-radiative transition, there is an emission of energy in the form of heat as electromagnetic radiation. For the radiative transition, the energy is released in the form of photons [166], [207], [210].

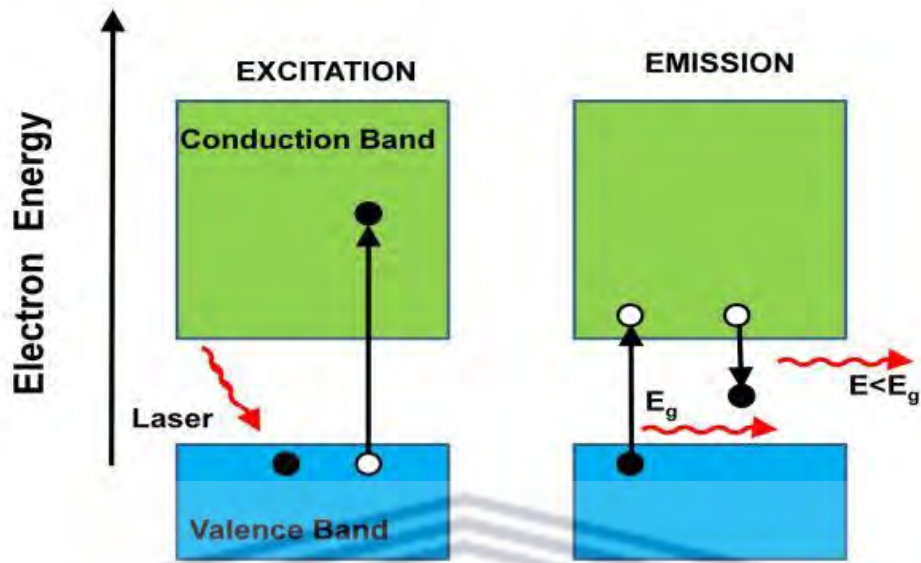


Figure 3.11 Schematic diagrams for excitation and emission processes in photoluminescence [205].

Every semiconductor is uniquely characterized by its band structure. Electrons and holes are the two types of free charge carriers in semiconductors. Electrons are usually scattered within the conduction bands and can merely move between the conduction and valence bands for both intra- and inter-scattering [214]. The PL spectra exhibit various emissions upon excitation at specific wavelength. Emission peaks depend on defects introduced in the material, and the presence of these defects can be clarified by transitions occurring between different sub-levels formed between the conduction and valence bands [111]. The holes can be scattered in the valence band of a semi-conductor (refer to **Figure 3.11**). The behaviour of an electron and a hole is controlled by the excitation intensity. Density, mass, and scattering time are the fundamental components that characterize free carriers. The fundamental energy gap of a semiconducting material is related to the product of the electron (n) and hole (p) densities [207], [210].

$$np = N_c N_v \exp \left[\frac{-E_g}{kT} \right] \dots \dots \dots (3.22)$$

where E_g is the band gap energy, k is the Boltzmann constant, and T is the temperature. N_c and N_v are the conduction and valence band density of states, which are denoted by the equation below [207].

$$N_{c(v)} = \frac{1}{\sqrt{2}} \left[\frac{m_e^* kT}{\pi \hbar^2} \right]^{3/2} \dots \dots \dots (3.23)$$

Where m_e is the mass of an electron and \hbar is the Planck's constant. The PL intensity provides a comparison of the rates of radiative and nonradiative recombination. However, it is difficult to analyse a sample's optical properties with poor surface quality during fast recombination processes. The luminescence emission efficiency η_R can be calculated through the rate equation for the population of the excited state on the possibility of the non-radiative processes [9].

$$\eta_R = \frac{AN}{N(1/\tau_R + 1/\tau_{NR})} = \frac{1}{1 + \tau_R/\tau_{NR}} \dots \dots \dots (3.24)$$

where η_R is given by the ratio of the radiative emission rate to the total de-excitation rate, $\tau_R = A^{-1}$ is the radiative lifetime of the transition, A is the Einstein coefficient, N is the population: the number of photons emitted at a given time. τ_{NR} is the non-radiative lifetime [9].

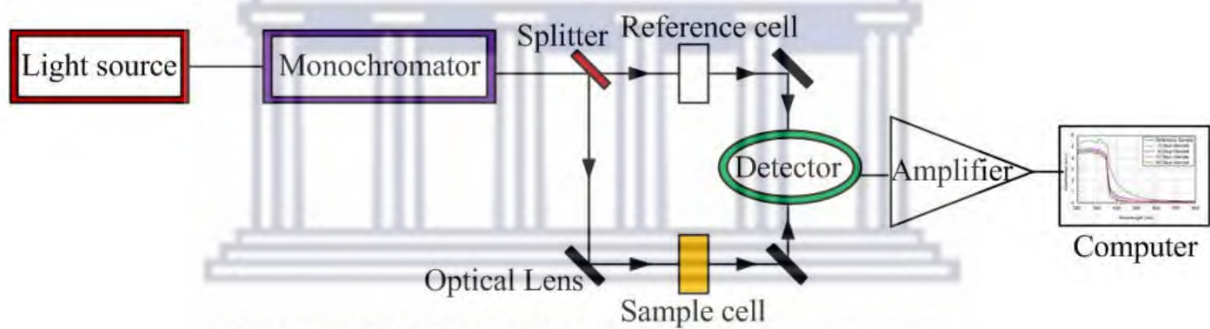


Figure 3.12 Schematic diagram for the photoluminescence operation procedure [215].

Figure 3.12 shows a schematic diagram for the working principle of the photoluminescence spectrophotometer. The photoluminescence spectrophotometer comprises the following; the excitation source, sample holder, monochromator, and detector. The light source, typically a xenon lamp, produces radiation that is directed toward the sample by the optical lenses; this radiation can be emitted by the sample [198]. The radiation emitted from the sample is collected and dispersed with respect to its wavelengths by the excitation monochromator. The detector collects the modified luminescence signal from the monochromator and converts it to an electrical signal that will be analysed by the computer to produce a spectrum [95], [216].

3.6 Colour chromaticity diagram

Colour serves as a powerful tool for display designers, like any other tool it can be counterproductive without skilful application. Simple mistakes, such as overlooking the contrast between a coloured symbol and its background can be avoided with common sense and critical evaluation. However, common sense alone is not enough, it needs basic understanding of the physics, physiology, and perception of colour. This becomes crucial when colours deviate from expected appearances based on their stimulus specification, as seen in phenomena like chromatic induction. Whereby a change in colour is influenced by the nearby surrounding colours. A significant drawback of many colour guidelines in human factors literature is that colour is identified with its physical characteristics. It is important to emphasize that colour stimulus, measured by the spectral power distribution of light entering an eye, differs substantially from the subjective experience or colour response. The colour response involves how the brain interprets and analyse the incoming stimuli. For instance, it is often stated that most vivid or saturated colours are spectrally pure for example a monochromatic light against a black background. However, colours actually appear more saturated against a white background. Unfortunately, colours can manifest in different perceptual modes such as material like paint or as signal light. This leads to variations in colour spaces, making it challenging to determine the most appropriate colour metric for a specific display design. The option often depends on whether the colour-coded information is displayed on a black or white background [217], [218].

An often-overlooked aspect in colour display design is how the achromatic aspect of colours is defined. Terms like intensity, luminance, lightness, and brightness are frequently used without careful consideration and often specified in inappropriate units such as footlamberts and apostilbs. Intensity play an important role in the representation of colours; it contributes to how interpret vividness of colours. Luminance play an important role for specifying the colour stimulus, changes in luminance may drastically upset the lightness scale, and consequently cause achromatic and chromatic colours to change in appearance for instance a yellow colour may turn to brown colour. People often confuse lightness and brightness; however, they are assigned to two different domains of matter and light respectively. Lightness refers the visual sensation where an object appears to either reflect diffusively or transmit a varying proportion of incident light. Brightness is the quality of a visual sensation how much light, whether independently or in response to incident light. In the case of object colours,

brightness is influenced by both incident light and surface reflectance. The latter property for a material is captured in the term lightness [217], [218], [219].

Colour is perceived as a single stimulus attribute; it can be deconstructed to different basic properties or dimensions. Thus, it is possible for colours to be organized along three dimensions. Colour can be seen as a property of light for instance the red light emitted by the traffic light, but also as a property of a surface like the red of the fire engine. Therefore, this implies that colour can either be reflected or emitted. The chromaticity diagram is a technique that is used to represent colours in the two-dimensional Cartesian spectrum in the form of (x, y) coordinates, which can be obtained from the sample that is being characterized. The chromaticity diagram contains three colour channels; two chromatic (x, y) and one achromatic (z) , which is perpendicular to (x, y) . The three variables of CIE colour space are used to define both the chromatic and achromatic aspects of a colour stimulus. Z represents the short visible wavelength response; the Y value, also referred to as luminance, is a mix of the long and medium visible spectrum while the X value represents a mixture of all three regions of the visible spectrum. The diagram is generated though using the relative values of the three tristimulus absolute values defined as following: $x = X/(X+Y+Z)$; $y = Y/(X+Y+Z)$ and $z = Z/(X+Y+Z)$ so that $x+y+z = 1$; it is thus sufficient to specify the stimulus chromaticity with only two coordinates (x, y) in this case and the 3rd can be deduced, as it can be seen on **Figure 3.11**. The chromaticity diagram consists of visual perception characteristics called “hue”, where an area is perceived to resemble one of the primary colours, namely red, blue, and green of monochromatic light at different wavelengths, with the achromatic centre of the tristimulus. The Hue values are arranged around the periphery of the diagram, also known as “spectrum locus”; the saturation is expressed in terms of the radius from the achromatic center ($x = y = 0.33$) to the dominant wavelength λ_d . The farther away from the center, the more vivid colours become and thus less pale. To ensure accuracy, colour matching experiments are conducted under standardized lighting conditions to prevent external light from interacting with the sample. The sample is positioned within a specimen in a way that it aligns with the test stimuli, as depicted in **Figure 3.10**. Monochromatic light is used as the test stimulus, which is directed towards the sample. The light passing through the sample is then directed onto a white screen, which separates transmitted light of various wavelengths, allowing for the precise identification of the colours present in the sample. The intensity of the matching stimuli's light flux is adjusted to achieve a colour match with the sample. This process yields three matching values, including their magnitude and units. Cones, often serving as photoreceptors or matching stimuli, play a

crucial role in colour analysis. They define how light is detected by three hypothetical sensors, and their spectral sensitivities are described by colour matching functions [217], [218], which will be discussed below.

The colour match may be obtained by the following form [218]:

$$[C] \equiv R[R] + G[G] + B[B] \dots \dots \dots (3.25)$$

Where [C] is the unknown stimulus with unknown units, R, G, B the magnitudes of the values of the match. [R],[G], and [B] are the matching stimulus units. The wavelength-dependant amounts are required for the above monochromatic light colour match, which are the colour matching functions $r(\lambda)$, $g(\lambda)$, and $b(\lambda)$, which are also written as $x(\lambda)$, $y(\lambda)$, and $z(\lambda)$.

$$[C] = \int_{380\text{ nm}}^{780\text{ nm}} r(\lambda)P(\lambda)d \cdot [R] \int_{380\text{ nm}}^{780\text{ nm}} g(\lambda)P(\lambda)d \cdot [R] \int_{380\text{ nm}}^{780\text{ nm}} b(\lambda)p(\lambda)d \cdot [R] \dots \dots (3.26)$$

The tri stimulus values are obtained by the integrals which serve as the descriptors of equation (3.6.1) [217]. **Figure 3.11** shows the evolution of the CIE colour chromaticity diagram from 1931 to 1976.

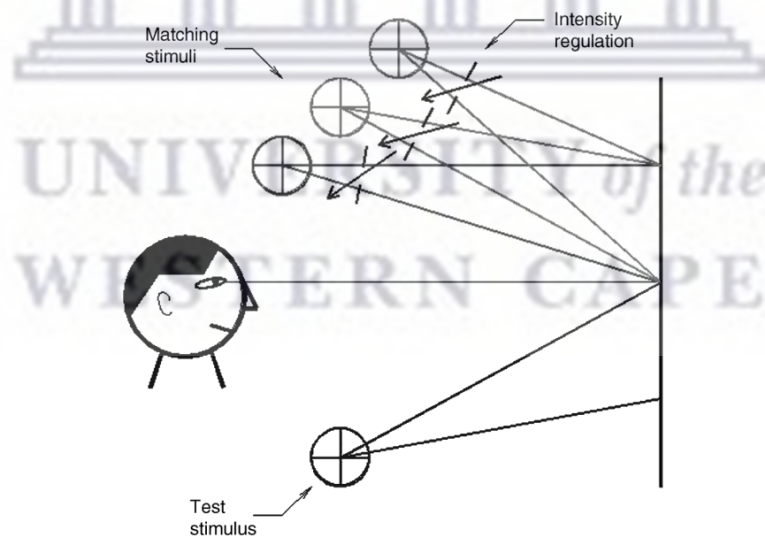


Figure 3.13 A schematic diagram for the colour matching experiment [217].

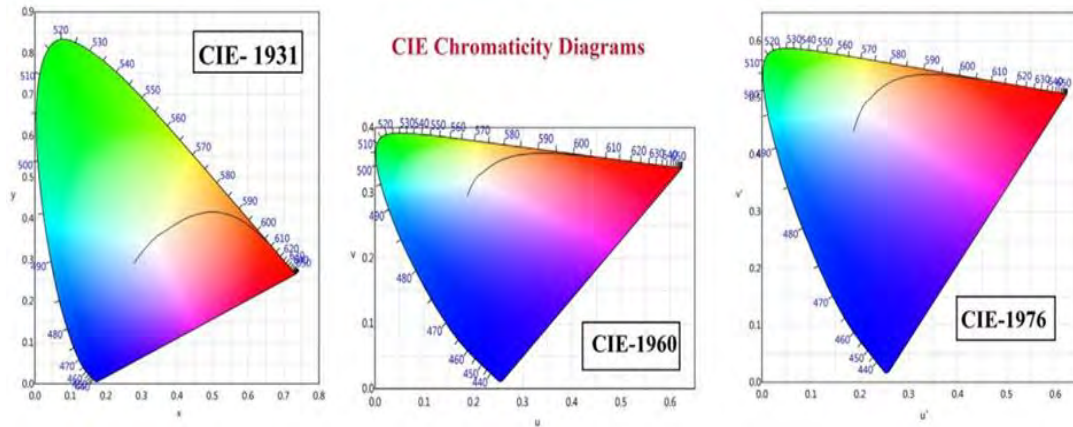


Figure 3.14 The evolution of the CIE chromaticity diagram [219].

Figure 3.14 Shows the evolution of the CIE chromaticity diagram from 1931 to 1976. The latter two diagrams are just the slight modification of the first diagram which is originally proposed CIE 1931. The first diagram has non-uniform and uneven perceptual spacing between colours which led to inaccurate colour presentations. These two versions were introduced with a correction in non-uniformity in the first diagram, this was done by creating a more uniform colour space. However, they were not completely free of misinterpretation of colours, and hence failed to surpass the popularity of the original version [217], [219].

Chapter IV

Impact of different various chemical techniques on the structural and photoluminescence properties of $\text{Zn}_4\text{B}_6\text{O}_{13}:\text{Sm}^{3+}$ nanophosphors

4.1 Introduction

Modern-day technology for solid-state and colour display systems relies heavily on rare-earth ion-doped phosphor materials [220]. This is due to their cheap preparation cost, environmental friendliness, high luminous efficiency, and prolonged lifespan [221]. Solid-state-based LEDs require less energy consumption and are more efficient than traditional lamps; this is one of the reasons why modern research projects are more focused on them. Currently, LEDs have replaced traditional lamps in various colour display technologies, such as computer monitors, signal lighting, televisions, etc. Solid-state lighting (SSL)-based LEDs have unique characteristics as compared to traditional lamps, in such a manner that the former can function in a low-voltage portable lighting as well as in traffic lights [222]. In addition, these SSL-based LEDs could replace the energy efficiency of fluorescent and incandescent lamps [223]. This research aims to justify the appropriate technique that will be used to produce the best photoluminescent properties by choosing an appropriate host with selected dopants. Zinc Borate ($\text{Zn}_4\text{B}_6\text{O}_{13}$) phosphor is an ideal host because of its photoluminescent properties, high thermal stability, high luminescence material with a wide band gap of 5.8 eV, high crystallinity, and the fact that it can be prepared at a low cost [91], [224]. Yuanyuan Li, et al. [91] reported that the electronic structures of $\text{Zn}_4\text{B}_6\text{O}_{13}$ having both the valence and the conduction band being composed of the Zn-O antibonding characteristics.

Different rare earth (RE) ions, particularly the trivalent rare earth ions, have been utilised as phosphor luminescent activators since they often display steady emission due to their f-f electron transitions [89]. Amongst the various RE ions, Sm^{3+} is chosen as a dopant for this study. Furthermore, Sm^{3+} is widely known for its strong orange-red luminescence in the visible region. The above-mentioned dopant is perfect for high-density optical storage due to its ability to store light in small volumes of particles. Moreover, its strong orange-red colour emissions make it perfect for transmitting light signals under water [225]. Madkhli et al. [226] investigated yttrium aluminium borate's photoluminescence when activated by Sm^{3+} ions. They reported that four Sm^{3+} emission peaks are detected at wavelengths of 564, 599, 646, and

707 nm, with corresponding transitions of ${}^4G_{5/2} \rightarrow {}^6H_{5/2}$, ${}^4G_{5/2} \rightarrow {}^6H_{7/2}$, ${}^4G_{5/2} \rightarrow {}^6H_{9/2}$, and ${}^4G_{5/2} \rightarrow {}^6H_{11/2}$, respectively [227], [228]. Further investigation by Ravita et al. [228] on the tuneable photoluminescence studies of potassium zinc aluminium borosilicate (KZABS) doped with Sm^{3+} , had similar samarium transition results to those reported by Madkhli et al. [226]. The visible PL emission spectra of Sm^{3+} ions are obtained after they are excited by monochromatic light at 226 and 408 nm wavelengths. Doping with Sm^{3+} is advantageous as it improves the photoluminescence efficiency of a material. It can either increase or decrease the average lifetime decay of a material, depending on the synthesis method applied. In addition, the dipole-dipole interactions cause concentration quenching during the doping process [226], [227], [228].

4.2 Results and discussions

4.2.1 X-ray diffraction studies

Figure 4.1 (a) – (d) shows the X-ray diffraction (XRD) patterns of the $Zn_4B_6O_{13}:xSm^{3+}$ (where x is 1 mol% concentration) phosphors synthesized with three different methods: combustion, sol-gel, and solid-state, along with the standard background XRD patterns of $Zn_4B_6O_{13}$ (JCPDS No: 01-076-0917) [229], respectively. The XRD patterns show that the diffraction peaks for all samples were detected around 2θ angles of 23° , 28° , 37° , 44° , 48° , 51° , 54° , 57° , 60° , 62° , 70° , 73° , 75° , and 78° . These 2θ correspond to the following lattice crystal phases: (200), (211), (310), (321), (400), (330), (420), (422), (510), (521), (440), (433), (600), and (532), respectively. The obtained XRD results are well matched with the standard PDF data file JCPDS No: 01-076-0917, which corresponds to a cubic crystal structure. The crystalline powders of $Zn_4B_6O_{13}$ compounds form a cubic unit cell structure with a space group of I-43m, for **Figure 4.1 (a)**. The standard reported cell parameters for this cubic model are $a = b = c = 7.4780 \text{ \AA}$, $\alpha = \beta = \gamma = 90^\circ$ including a volume (V) of 418.17 \AA^3 .

Figure 4.1 (b) shows the XRD spectrum of the $Zn_4B_6O_{13}:Sm^{3+}$ phosphor material, prepared by the sol-gel method. The diffraction peaks for the Sol-gel method were determined in a similar way as was previously reported for the combustion method, except for changes in the lattice parameters calculated as follows: $a = b = c = 7.47780 \text{ \AA}$, $\alpha = \beta = \gamma = 90^\circ$ including a volume (V) of 418.14 \AA^3 . The diffraction peaks for the solid-state reaction method were determined in a similar way as was previously reported for the combustion method, except for changes in the

lattice parameters, calculated as follows: $a = b = c = 7.47820 \text{ \AA}$, $\alpha = \beta = \gamma = 90^\circ$ including a volume (V) of 418.21 \AA^3 , respectively.

The XRD results obtained for the synthesized doped phosphors in **Figure 4.1 (a – c)** were overall well matched with the standard background $\text{Zn}_4\text{B}_6\text{O}_{13}$ structure (JCPDS No: 01-076-0917) [229] shown in **Figure 4.1 (d)**. However, there were some slight deviations of the peaks, shifting to the higher 2θ angles as shown in **Figure 4.1 (a-c)** compared to the standard JCPDS data file, which is ascribed to the Sm^{3+} ion dopants. This implies that Sm^{3+} ions were successfully incorporated into the $\text{Zn}_4\text{B}_6\text{O}_{13}$ lattice, resulting in the volume lattice expanding, which is mostly due to the Sm^{3+} substituting at Zn^{2+} ions sites. Therefore, the $\text{Zn}_4\text{B}_6\text{O}_{13}:\text{Sm}^{3+}$ cubic-phase cell parameters increase slightly after doping [60]. The absence of additional Sm^{3+} diffraction peaks in the XRD pattern implies the complete dissolution of the dopant in the respective crystal lattice [132]. All the prepared phosphors show a decrease in the overall intensity peaks. This decrease in the intensity of the diffraction peak is due to the differences in the ionic radii of the Zn^{2+} (0.074 nm) and Sm^{3+} (0.096 nm) cations, whereby Sm^{3+} ions are substituted for Zn^{2+} ions in the host lattice [230]. The combustion and sol-gel methods showed weak XRD peak intensity compared to the solid-state method for the $\text{Zn}_4\text{B}_6\text{O}_{13}:\text{Sm}^{3+}$ phosphor; this is due to their low crystallite sizes, as shown in **Table 4.1**.



UNIVERSITY of the
WESTERN CAPE

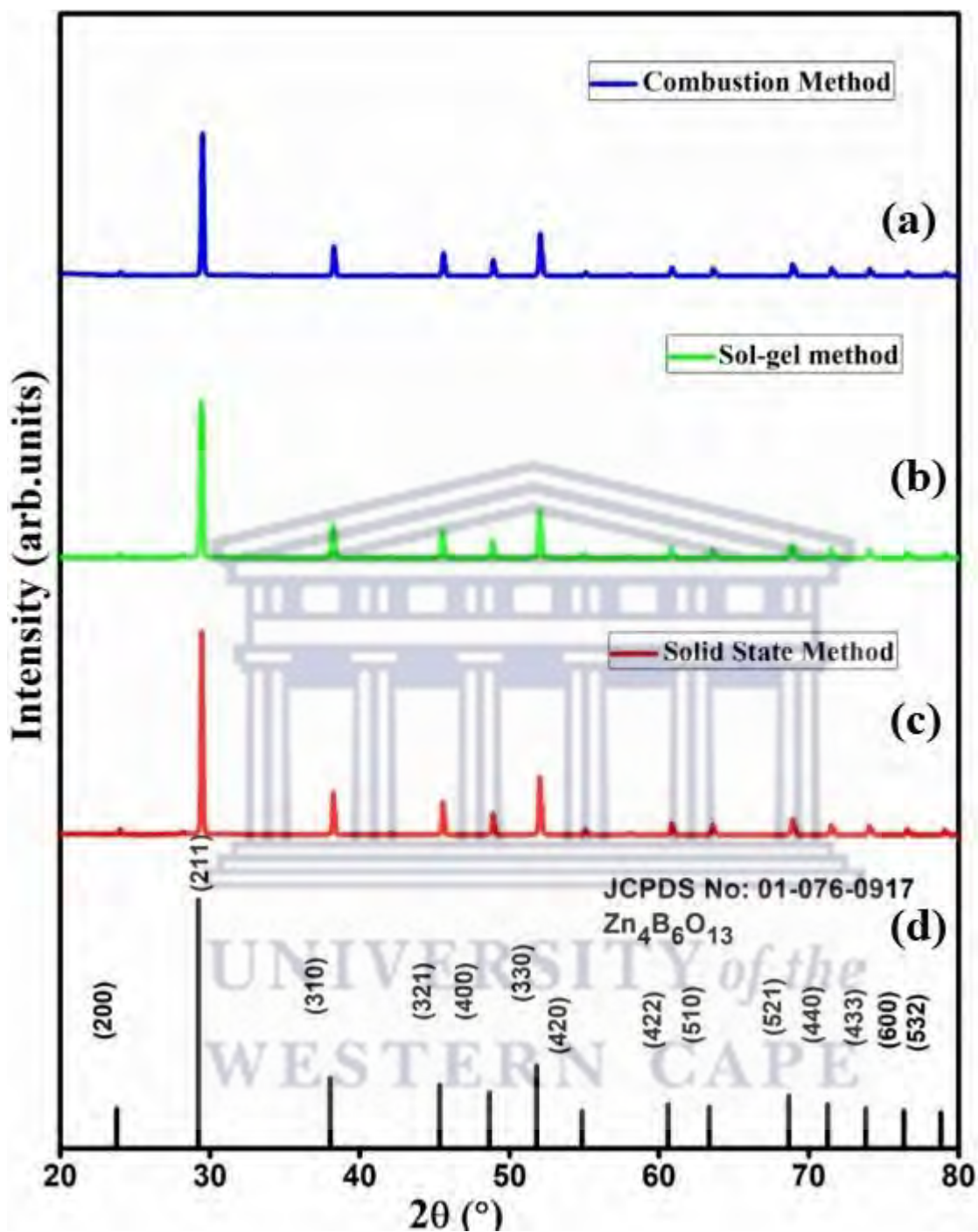


Figure 4.1. The full XRD patterns of $Zn_4B_6O_{13}:xSm^{3+}$ (where $x = 0, 1\%$) nanophosphors prepared by various synthesis techniques: **(a)** Combustion, **(b)** Sol-Gel, **(c)** Solid-state reaction method and **(d)** XRD diffraction bars for $Zn_4B_6O_{13}$ matrices (JCPDS No: 01-086-0917).

The Debye-Scherrer equation shown below was used to calculate the average crystallite sizes of the synthesized nanophosphors from the XRD data [229].

$$D = \frac{k\lambda}{\beta \cos\theta} \dots\dots\dots 4.1$$

Where **D** is the average crystallite size, **k** is the shape constant factor of 0.9, **θ** is the diffraction angle, and **β** is the full width at half maximum (FWHM) for the diffraction peak. The wavelength of the x-ray source (0.15406 nm) is denoted by **λ**. The most intense peak indexed as (211) acts as a fingerprint peak for crystallite estimation of all the Zn₄B₆O₁₃:Sm³⁺ phosphors, which is observed from the XRD spectra (**Figure 4.1**) in all synthesis methods used in this study. This peak resembles good crystallinity [91], [229], [231]. It was used to calculate the average crystallite sizes. **Table 4.1** shows the tabulated crystallite sizes for the synthesized samples. The average crystallite sizes were calculated and found to fall in the 61 – 100 nm range. The average crystalline sizes were found to follow the trend below: solid-state (99.51nm) > combustion (68.93 nm) > sol-gel (61.42 nm) for Zn₄B₆O₁₃:Sm³⁺ phosphor materials.

Table 4.1. Crystallite size of Zn₄B₆O₁₃:xSm³⁺ (where x = 0, 1%) nanophosphors prepared by various synthesis techniques: (1) Sol-Gel, (2) Combustion, and (3) Solid-state reaction method.

S.No	Sample	Crystallite size (nm)
1	Zn ₄ B ₆ O ₁₃ :Sm ³⁺ (Sol-gel)	61.42
2	Zn ₄ B ₆ O ₁₃ :Sm ³⁺ (Combustion)	68.93
3	Zn ₄ B ₆ O ₁₃ :Sm ³⁺ (Solid state)	99.51

4.2.2 Surface morphology studies and elemental analysis

The morphologies of the prepared samples were analysed with field emission scanning electron microscopy (FE-SEM). The elemental analysis was studied through the energy dispersive spectrum (EDS). **Figure 4.2 (a), (b), and (c)** show FE-SEM micrographs of $\text{Zn}_4\text{B}_6\text{O}_{13}:\text{Sm}^{3+}$ and their corresponding EDS spectra are shown in **(d), (e), and (f)**, respectively. The inserted images in **Figure 4.2 (a – c)** also show the magnified FE-SEM images, whereas in **Figure 4.2 (d – f)**, they depict the elemental mapping of the prepared materials, respectively.

Figure 4.2 (a) clearly displays polyhedron-like particles with varying shapes and sizes. These may be due to the addition of Sm^{3+} ion dopants to the host materials. The particles are more agglomerated towards the centre and are surrounded by particles of the same grain size with little or no voids. The average particle size was determined through 'image J' software and was found to be around 1000 nm for the sample prepared via the combustion method, as shown in **Figure 4.3 (a)**. The average particle size was obtained by measuring 62 particles. The voids being pointed out by the blue arrows in this figure are those from the microscope glass slides that were used to hold the specimen during characterization and are not part of the sample [232], [233].

Figure 4.2 (b) shows the SEM image, displaying mostly smooth rods with spherically-like shapes, along with some irregular-shaped particles with different sizes, prepared by the sol-gel method. The smoothness of the particles might be due to the high annealing temperature (900 °C) used during synthesis [232]. The particles are largely agglomerated and more adhered to each other, with small gaps found in the materials, as shown by the yellow arrow lines in the figure. These particles have an average calculated size of 1350 nm, as shown in **Figure 4.3 (b)**. The average particle size was obtained by measuring 45 particles. The large gaps depicted by green arrows are due to the specimen holder and the diffused residual hydrogen during surface analysis [233].

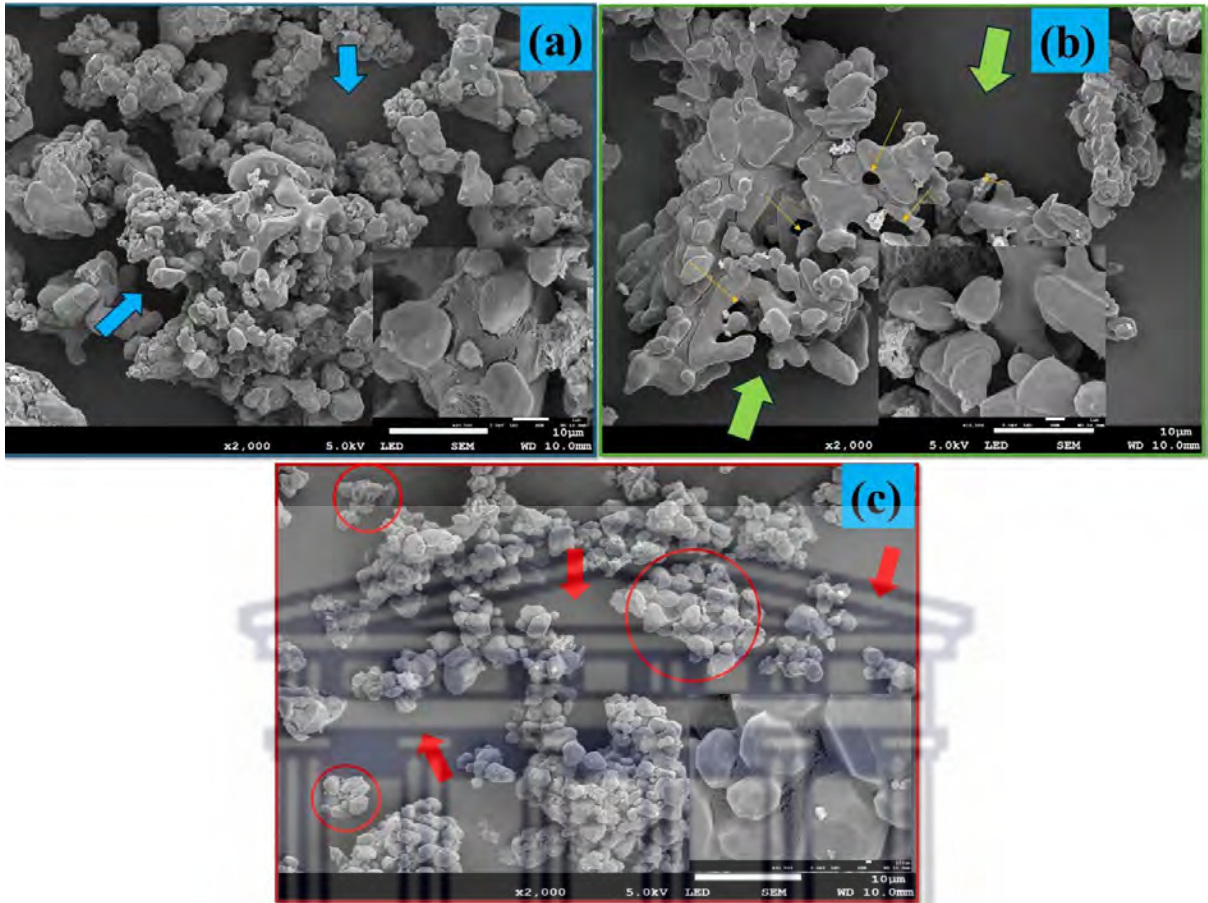


Figure 4.2: Field-emission scanning electron microscopy (FE-SEM), images of $Zn_4B_6O_{13}:xSm^{3+}$ (where $x = 0, 1\%$) nanophosphors prepared by various chemical techniques: (a), Combustion (b), Sol-Gel (c) Solid-state reaction methods.

UNIVERSITY of the
WESTERN CAPE

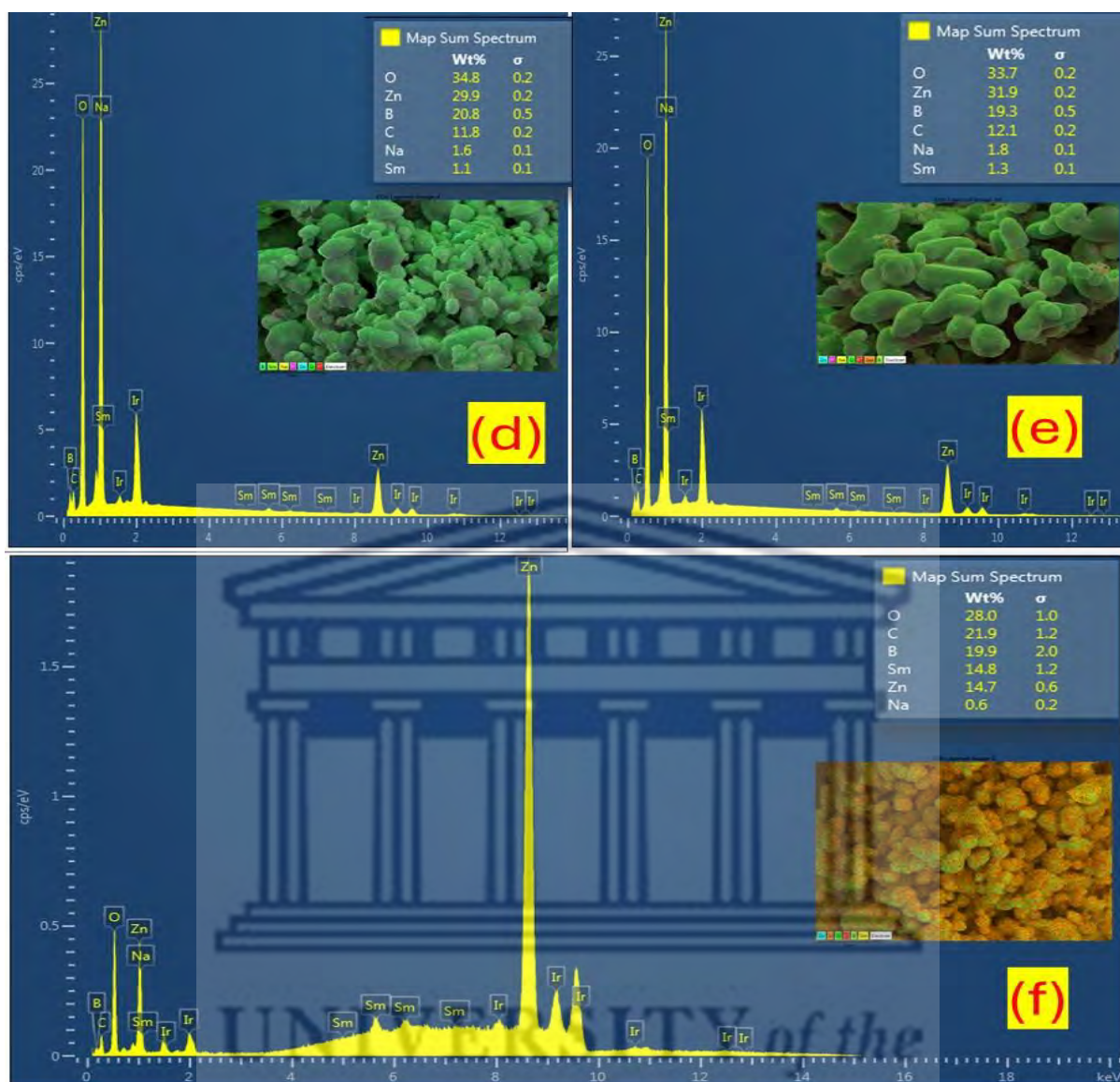


Figure 4.2: Elemental Dispersive Spectroscopy (EDS) and Elemental mapping images of $Zn_4B_6O_{13}:xSm^{3+}$ (where $x = 0, 1\%$) nanophosphors prepared by various chemical techniques: (d) Combustion, (e) Sol-Gel, and (f) Solid-state reaction methods.

Figure 4.2 (c) shows the polyhedron-like particles of samples prepared via solid-state reaction having uniform size and shape. These particles are agglomerated into distinct groups and are largely scattered within the surface area, as shown by the red circles, with little to no voids. The calculated average particle size is 1040 nm for this sample, and it is presented in **Figure 4.3 (c)**. The large spaces depicted by the red arrows are due to the specimen used to hold the sample during surface analysis [232], [233]. The difference in morphologies observed in the prepared samples is due to the Sm^{3+} dopant, which replaces the Zn^{2+} ions in the $Zn_4B_6O_{13}$

material and further introduces the positive charge that affects the shape of the particle [132], [234]. The combustion method produced a particle size of approximately 1000 nm, which is the smallest compared to the other two methods. The average particle size was obtained by measuring 53 particles. In addition, this implies that Sm^{3+} ions successfully reduced the particle size by lowering the grain growth in this method [234]. Moreover, the addition of the dopant affected the morphology of the host material differently, so it can be concluded that the synthesis method applied plays a significant role in the morphology of the prepared samples.

The EDS spectra and elemental mapping images, as shown in **Figure 4.2 (d – f)**, confirm all the precursor elements present in the prepared sample. The detected elements are samarium (Sm), zinc (Zn), oxygen (O), boron (B), sodium (Na), carbon (C), and iridium (Ir). The presence of (Ir) in the EDS spectra was due to the iridium that was used for coating the sample to rectify its conductivity and charging during the surface analysis. The carbon element is due to the carbon tape that was used as a conductive support for the sample during characterization. The average particle size of the prepared sample ranges from 1000 to 1350 nm, which agrees with the report by Chen et al. [224] stating that the $\text{Zn}_4\text{B}_6\text{O}_{13}$ have relatively large particles. The sol-gel method produced the largest particles, with an average size of 1330 nm. The inserts in **Figure 4.2 (d)** and **(e)** show a uniform distribution of the elements used, with a dominance of oxygen and samarium in the $\text{Zn}_4\text{B}_6\text{O}_{13}$ material. The insert in **Figure 4.2 (d)** shows a uniform distribution of elements used, with a dominance of iridium and samarium peaks. The table below for the average distribution sizes was plotted through Image J and 60 particles were measured respectively per sample.

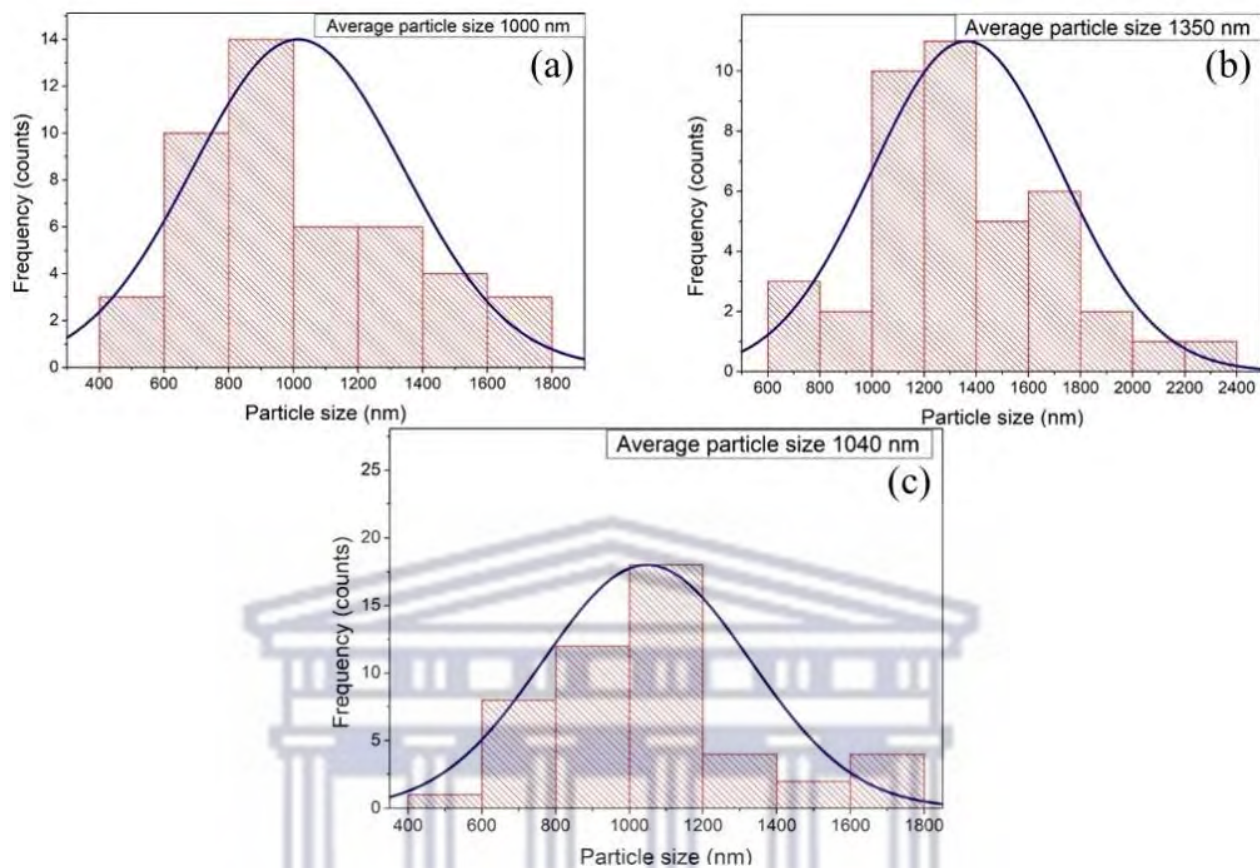


Figure 4.2 Histograms displaying the average particle size distribution of Zn₄B₆O₁₃:xSm³⁺ (where $x = 0.1\text{mol}\%$) nanophosphors prepared using (a) combustion, (b) Sol-gel, and (c) solid state methods.

UNIVERSITY of the
WESTERN CAPE

4.2.3 Fourier Transform Infrared (FT-IR) analysis

The FTIR characterization measurements were done to study and determine the functional groups of the prepared phosphor materials. **Figure 4.4** shows the FT-IR spectra of the $Zn_4B_6O_{13}$ host and doped $Zn_4B_6O_{13}:Sm^{3+}$ phosphor materials synthesized via combustion, solid-state, and sol-gel methods. These results were recorded at room temperature within the wavenumber range of 400 to 4000 cm^{-1} . From the FTIR spectra, a sharp absorption peak within the region of 450 cm^{-1} is observed in both the host and the doped samples for different synthesis methods. Moreover, this sharp peak is ascribed to the vibrational properties of the metal oxide groups (Zn-O) [91]. Sharp peaks within the 600 cm^{-1} regions are attributed to the stretching mode of BO_4 vibrations [91]. The broad peaks observed within the region of 800 cm^{-1} are attributed to the vibrational bands of BO_3^{3-} for both the host and doped phosphors in all synthesis methods. The shoulder peaks found within 600 – 1000 cm^{-1} are due to the bending modes of tetragonal BO_3^{3-} groups [235]. Apart from the bands observed in the low wavenumber region, the bands in the higher wavenumber region are attributed to the impurity structural groups, such as hydroxyl OH groups. Thus, within the 1120 cm^{-1} region, there is a peak that is attributed to the hydroxyl (O-H) bending mode of water (H_2O) molecules used during sample preparation. The O-H bending mode involves bending the bond angle between the hydrogen and oxygen atoms in the H_2O molecule. Furthermore, within the region of 3200 cm^{-1} , hydroxyl transmission broad bands are observed, which are attributed to the stretching modes of water molecules (atmospheric moisture) [91], [236].

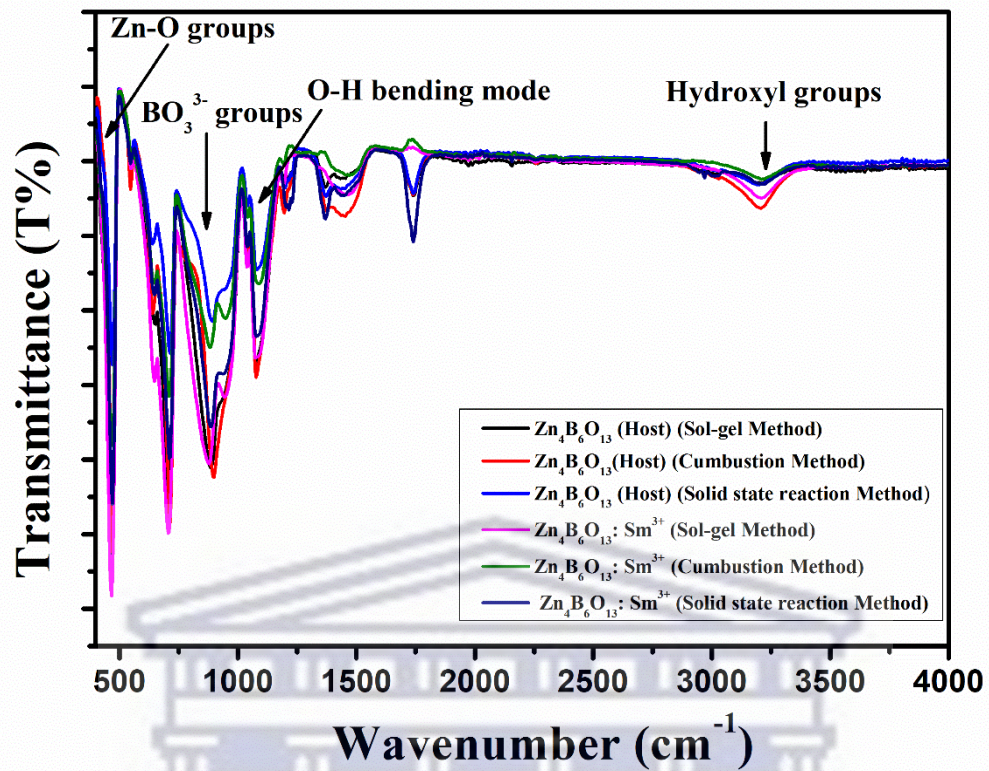


Figure 4.4: FT-IR spectra of $Zn_4B_6O_{13}:xSm^{3+}$ (where $x = 0, 1\%$) nanophosphors prepared by various chemical techniques: (a) Sol-Gel (b) Combustion (c) Solid-state reaction method.

UNIVERSITY of the
WESTERN CAPE

4.2.4 UV-VIS and band gap measurements

The diffuse reflectance spectra (DRS) of UV-Vis for the prepared $\text{Zn}_4\text{B}_6\text{O}_{13}$ host and $\text{Zn}_4\text{B}_6\text{O}_{13}:\text{Sm}^{3+}$ (1 mol%) doped nanophosphors using sol-gel, combustion, and solid-state methods are presented in **Figure 4.5**. These spectra were measured at room temperature in the wavelength range of 200 – 2000 nm. All samples show an intense absorption band edge around the 360 nm region. Moreover, this band is ascribed to the electron transition within the Zn-O bonds of the $\text{Zn}_4\text{B}_6\text{O}_{13}$ materials [49], [237]. There is an observed linear increase in reflectance from the ultraviolet (UV) to the infrared (IR) region for both the host and doped samples prepared by the sol-gel method. The different optical behaviour observed in sol-gel compared to other methods is due to the high agglomeration of large particles, low annealing temperature which resulted in not removing all impurities, and low photo luminescence emission compared to other methods [238]. The mentioned factors result in inability to react to light compared to other methods in the ultraviolet and visible regions. From the spectra, it is noticed that the presence of absorption bands for doped samples prepared by the solid-state and combustion methods at 680, 1100, 1250, and 1600 nm is attributed to Sm^{3+} *f-f* transitions, which form in between meta-stable energy levels of Sm^{3+} ions within valence and conduction bands of the host [195]. The $^4f_5 \rightarrow ^4f_5$ intra-configuration transitions from the ground state ($^6\text{H}_{5/2}$) level of Sm^{3+} to the excited states of $^3\text{H}_{7/2}$ (345 nm), $^4\text{F}_{9/2}$ (363 nm), $^4\text{D}_{5/2}$ (376 nm), $^6\text{F}_{7/2}$ (403 nm), $^4\text{I}_{13/2}$ (365 nm), and $^4\text{I}_{11/2}$ (478 nm) [219], are responsible for the absorption bands in the UV region for the doped samples. Furthermore, the absorption bands in the UV region are attributed to the excitonic transitions in the optical properties of a material. The excitonic transitions suggest that the atomic character of the Sm^{3+} ion is preserved and is not influenced by the host environment; this is due to the effective shielding of 4f_5 electrons from the 5s- and 5p-filled shells [219], [239], [240].

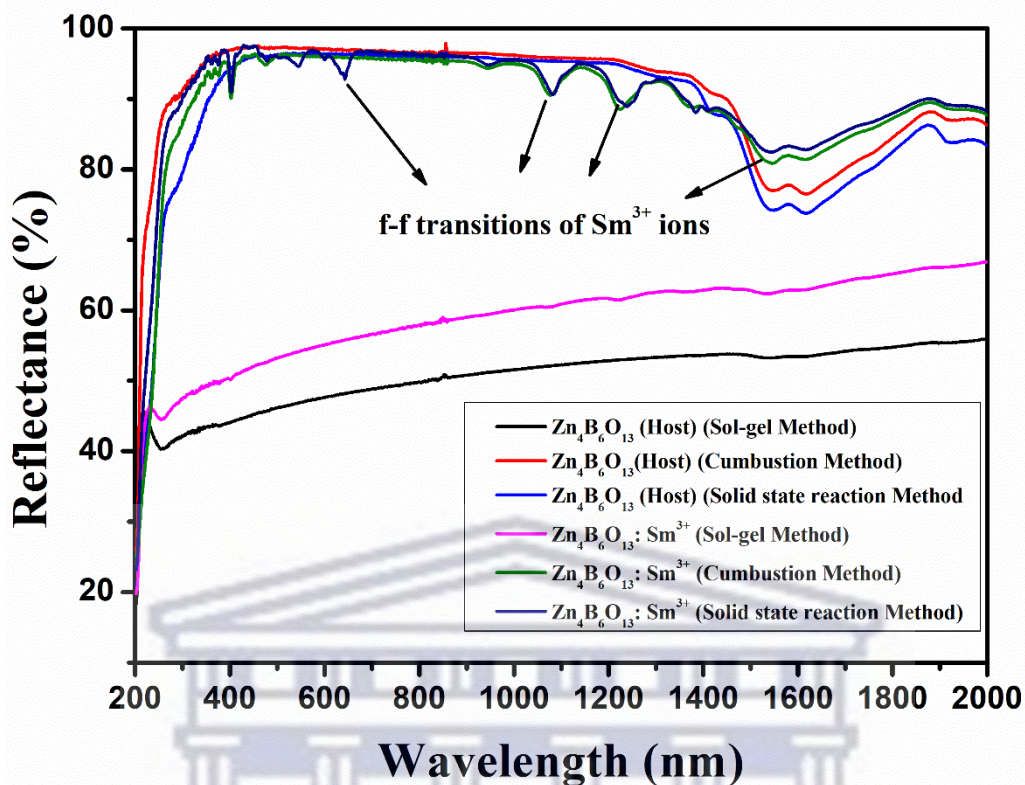


Figure 4.5 UV-Vis DRS spectra of $Zn_4B_6O_{13}:xSm^{3+}$ (where $x = 0, 1\%$) nanophosphors prepared by various chemical techniques: (a) Sol-Gel (b) Combustion (c) Solid-state reaction method.

The band gap energy values of the prepared host and doped samples were estimated from the optical data in **Figure 4.6** prepared by (a) sol-gel, (b) combustion, and (c) solid-state reaction methods.

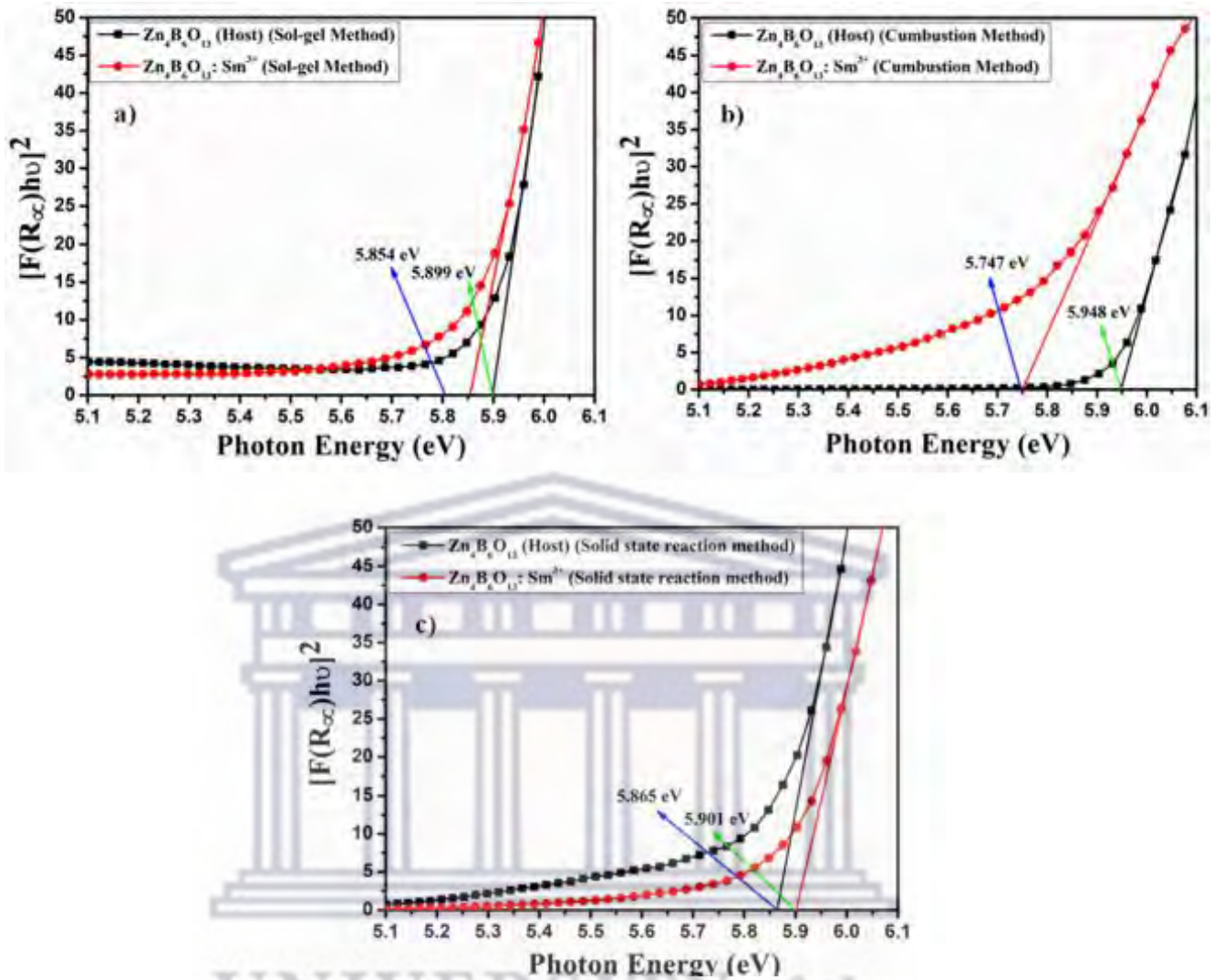


Figure 4.6 Optical bandgap calculations of $Zn_4B_6O_{13}:xSm^{3+}$ (where $x = 0, 1\%$) nanophosphors prepared by various chemical techniques: (a) Sol-Gel (b) Combustion (c) Solid-state reaction method. The line represents the best linear fit to determine the optical band gap.

Figure 4.6 shows the plots for $[F(R_\infty)hv]^2$ versus photon energy ($h\nu$) for the direct transitions. The Kubelka-Munk (K-M) function theory and Tauc plot were used for the analysis. The linear part of the curve is extrapolated to intersect with the x-axis ($h\nu$) at zero absorption to give the energy band gap values [240], [241]. The K-M function is denoted as follows:

$$F(R_\infty) = \frac{(1-R_\infty)^2}{2R_\infty} = \frac{K}{S} \dots \dots \dots (4.2)$$

The scattering and absorption coefficients are given by S and K, respectively. The diffuse reflectance parameter of the material is R_∞ . The Tauc equation is given by:

$$(\alpha h\nu) = C_0(h\nu - E_g) \dots\dots\dots(4.3)$$

is used for the calculation of the optical band gap E_g , where C_0 is the energy in-dependant value. This equation relates the bang gap energy value to the absorption coefficients near the absorption band edge [195]. The extrapolated band gap values from the plots in **Figure 4.6** are presented in **Table 4.2**. Doping with Sm^{3+} caused a change in the energy band gap values of the prepared samples in all synthesis methods. The E_g value for the host was found to be 5.899 eV, and 5.854 eV for the doped phosphor prepared by the sol-gel method. The E_g values for the host and doped samples are 5.948 eV and 5.747 eV, respectively, for the combustion method. From these results, it implies that the band gap values of $Zn_4B_6O_{13}$ prepared by combustion and the sol-gel methods decrease with Sm^{3+} doping. Moreover, this is due to the formation of Sm^{3+} metastable states within the bandgap of host materials. The other cause of the decrease in the energy band gap values might be due to bond deformations and local defects in the $Zn_4B_6O_{13}$ matrix during calcination. Furthermore, the decrease in the energy bandgap on the mentioned methods is attributed to the charge transfer between the $Zn_4B_6O_{13}$ valence band and the 4f level of the Sm^{3+} ions; moreover, it is also attributed to the surface defects [116]. Solid-state is the only method that showed an increase in energy band gap after Sm^{3+} doping; this might be due to the dopant behaving differently in this method, which is explained by the Moss-Burstein effect [242], [243]. In addition, an increase in the band gap indicates that the addition of the dopant (Sm^{3+}) to the host lattice blocked low energy transitions, which resulted in an upward shift of the Fermi level within the conduction bands [116].

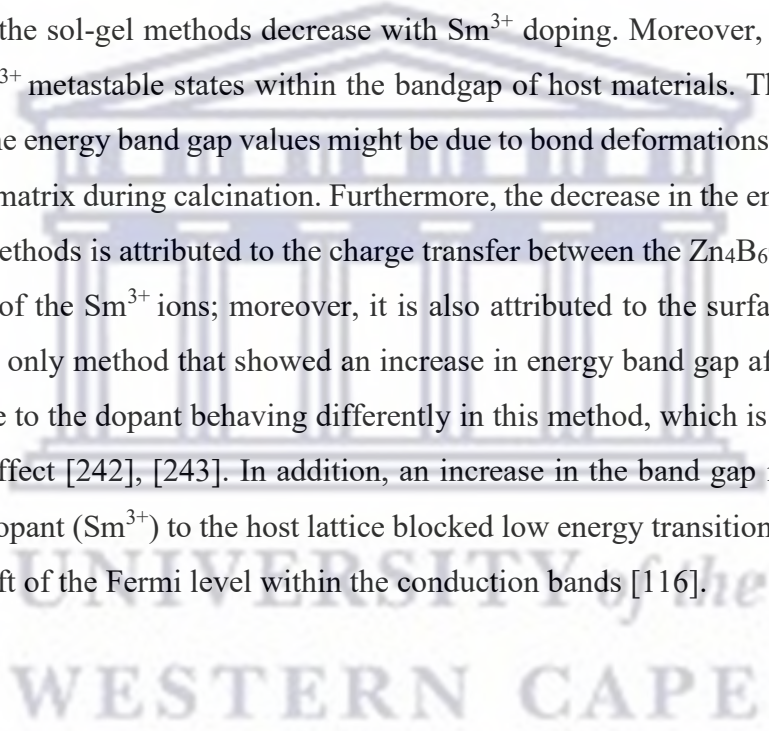


Table 4.2. Optical bandgap values of the $Zn_4B_6O_{13}:xSm^{3+}$ (where $x = 0, 1\%$) nanophosphors prepared by various chemical techniques: (1,2) Sol-Gel (3,4) Combustion (5,6) Solid-state reaction method.

S.No	Sample ID	Energy bandgap (eV)
1	$Zn_4B_6O_{13}$ (Sol-gel)	5.899
2	$Zn_4B_6O_{13}:Sm^{3+}$ (Sol-gel)	5.854
3	$Zn_4B_6O_{13}$ (Combustion)	5.948
4	$Zn_4B_6O_{13}:Sm^{3+}$ (Combustion)	5.747
5	$Zn_4B_6O_{13}$ (Solid state)	5.865
6	$Zn_4B_6O_{13}:Sm^{3+}$ (Solid state)	5.901

UNIVERSITY of the
WESTERN CAPE

4.2.5 Photoluminescence excitation and emission spectra measurements

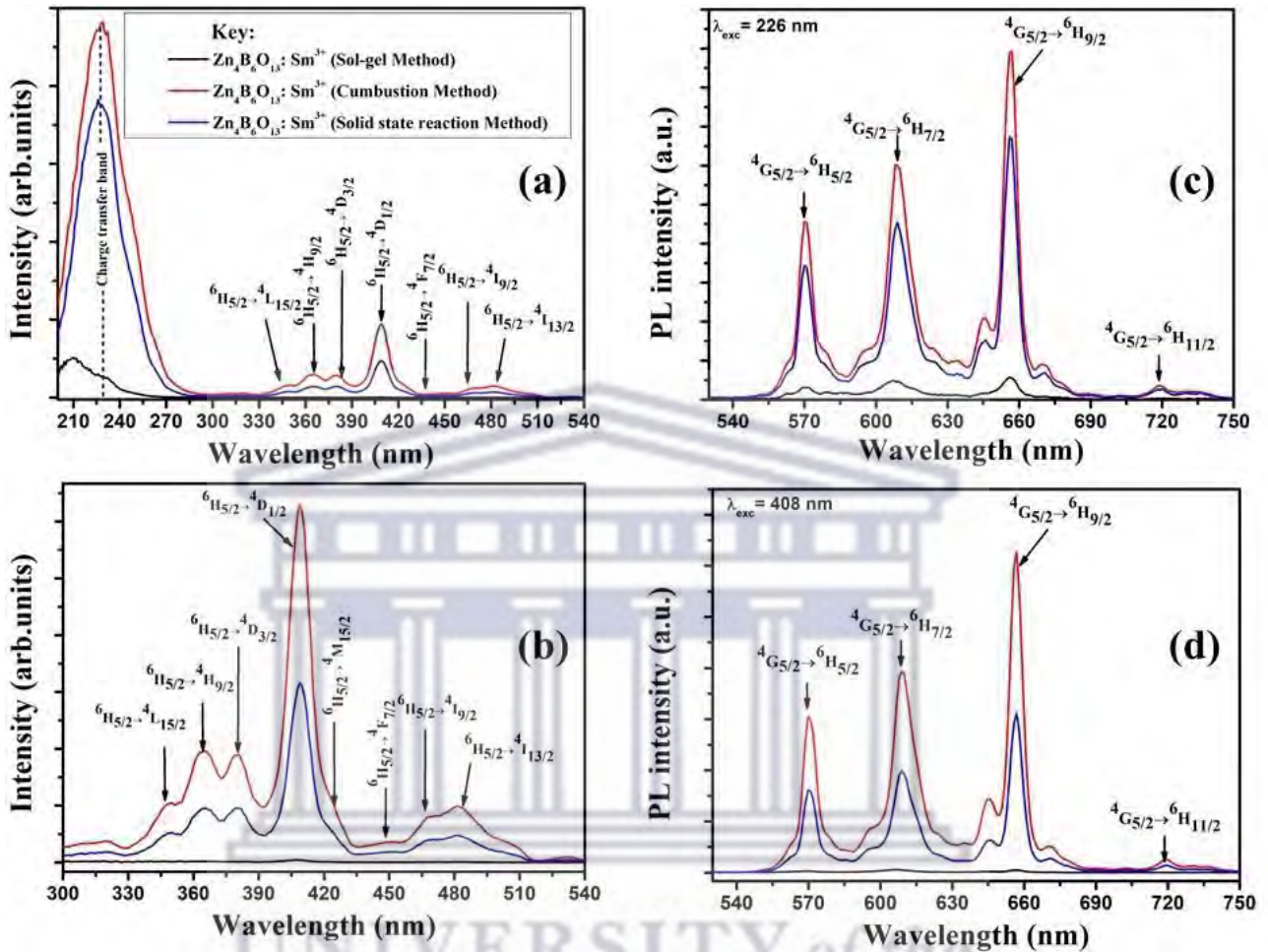


Figure 4.7 (a), (b) Photoluminescence excitation and (c), (d) emission spectra of $Zn_4B_6O_{13}:xSm^{3+}$ (where $x = 0, 1\%$) nanophosphors prepared by various chemical techniques: (1) Sol-Gel (2) Combustion (3) Solid-state reaction method using the parameters of $\lambda_{emi} = 657$ nm and $\lambda_{exc} = 226, 408$ nm wavelengths.

Figure 4.7 (a) and (b) show the photoluminescence excitation spectra of the $Zn_4B_6O_{13}:Sm^{3+}$ doped samples, prepared via sol-gel, solid-state, and combustion synthesis methods. The excitation spectra in (a) and (b) were measured within the range of 210 – 540 nm and 300 – 540 nm, respectively, while monitoring an intense emission peak at the 657 nm wavelength. These samples were excited using a monochromatic light of 226 and 408 nm wavelengths for (a) and (b), respectively. The intense absorption band found around 226 nm wavelength is due to the charge transfer band of $Sm^{3+} \rightarrow O^{2-}$. The intensity of the excitation peak at 226 nm is the charge transfer band (CTB), it is stronger than that of 4f-4f transitions, which indicates efficient

energy transfer from host to dopant, called the inter-band transition. Moreover, the excitation spectrum consists of less intense 4f – 4f excitonic transitions of Sm^{3+} at 345, 370, 380, 408, 437, 465, and 482 nm. These wavelengths are associated with the transitions of Sm^{3+} ions: ${}^6\text{H}_{5/2} \rightarrow {}^4\text{L}_{15/2}$, ${}^6\text{H}_{5/2} \rightarrow {}^4\text{H}_{9/2}$, ${}^6\text{H}_{5/2} \rightarrow {}^4\text{D}_{3/2}$, ${}^6\text{H}_{5/2} \rightarrow {}^4\text{D}_{1/2}$, ${}^6\text{H}_{5/2} \rightarrow {}^4\text{F}_{7/2}$, ${}^6\text{H}_{5/2} \rightarrow {}^4\text{I}_{9/2}$, and ${}^6\text{H}_{5/2} \rightarrow {}^4\text{I}_{13/2}$ [244], respectively. The strongest 4f-4f excitation peak occurs at 408 nm wavelength, which corresponds to the ${}^6\text{H}_{5/2} \rightarrow {}^4\text{D}_{1/2}$ electronic state transition.

Figure 4.7 (c) and (d) show the photoluminescence emission spectra for $\text{Zn}_4\text{B}_6\text{O}_{13}:x\text{Sm}^{3+}$ (where $x = 1\%$ mol) phosphors measured in the range of 540 nm to 750 nm, with the use of 226 nm and 408 nm as excitation wavelengths, respectively. From the spectra, it is noticed that there are four emission peaks at the wavelengths: 572 nm, 615 nm, 660 nm, and 718 nm, which correspond to ${}^4\text{G}_{5/2} \rightarrow {}^6\text{H}_{5/2}$, ${}^4\text{G}_{5/2} \rightarrow {}^6\text{H}_{7/2}$, ${}^4\text{G}_{5/2} \rightarrow {}^6\text{H}_{9/2}$, and ${}^4\text{G}_{5/2} \rightarrow {}^6\text{H}_{11/2}$ magnetic dipole transitions of Sm^{3+} ions, respectively. There is a strong orange-red emission band located at 660 nm, which corresponds to the ${}^4\text{G}_{5/2} \rightarrow {}^6\text{H}_{7/2}$ transition. The ${}^4\text{G}_{5/2} \rightarrow {}^6\text{H}_{7/2}$ absorption peak is associated with the electric dipole transition, which is higher than the magnetic dipole transitions. This implies the phosphor prepared by the combustion method is more suitable for red-colour LED applications [244], [245]. The $\text{Zn}_4\text{B}_6\text{O}_{13}:\text{Sm}^{3+}$ material prepared by the combustion method produced the highest emission peak compared to those prepared by the solid-state and sol-gel methods. In addition to this, it is also noticed that there is a very low emission peak for the sol-gel method at 408 nm excitation, as depicted in **Figure 4.7 (b)**. Consequently, in the sol-gel method, the Sm^{3+} recombination caused a delay in photo-generated charges, which act as effective luminescence trapping sites for charge carriers [116]. Therefore, according to the obtained results, the $\text{Zn}_4\text{B}_6\text{O}_{13}:\text{Sm}^{3+}$ phosphors synthesized with the combustion and solid-state reaction methods are only potential candidates for white LED applications.

4.2.6 Lifetime decay measurements

Figure 4.8 shows the lifetime decay curves for the emission of the Sm^{3+} ion in $\text{Zn}_4\text{B}_6\text{O}_{13}:\text{Sm}^{3+}$ phosphors prepared by sol-gel, combustion, and solid-state reaction methods. These phosphors are excited at 408 nm wavelength, while monitoring the emission peak at 657 nm. The photoluminescence decay curves for the prepared phosphors are fitted with a second-order exponential equation [246], [247], as shown below:

$$I(t) = I_0 + A_f \exp\left(-\frac{t}{\tau_f}\right) + A_s \exp\left(-\frac{t}{\tau_s}\right) \dots \dots \dots (4.4)$$

where $I(t)$ and I_0 are the luminescence intensities at time t and at $t = 0$, respectively. The fast and slow decay times are denoted by τ_f and τ_s , where their weights factors are A_f and A_s , respectively. The equation (4.6.2) below was used to calculate the average decay time (τ_{avg}) from $^4\text{D}_{5/2}$ to the ground state levels.

$$\tau_{avg} = \frac{(A_f \tau_f^2 A_s \tau_s^2)}{A_f \tau_f A_s \tau_s} \dots \dots \dots (4.5)$$

The calculated average decay time is 173 milliseconds (ms) for the $\text{Zn}_4\text{B}_6\text{O}_{13}:\text{Sm}^{3+}$ prepared with the solid-state method, 913 ms for the combustion method, and 1007 ms for the sol-gel method, as shown in **Table 4.3**. The table describes that the highest decay profile was noticed for $\text{Zn}_4\text{B}_6\text{O}_{13}:\text{Sm}^{3+}$ phosphor, which is prepared by the solid-state reaction method. This may be due to the high interaction between the host and Sm^{3+} dopant compared to the other two methods [248], [249]. These fastest-decaying phosphors could be used for LED fabrication [248], [250]. The average decay time of the phosphor material is dependent on the energy transfer between the host and the dopant [224], [251]. The longest decay time is due to fast electron-hole recombination effects, and the slow decay time is due to enhanced luminescence [49].

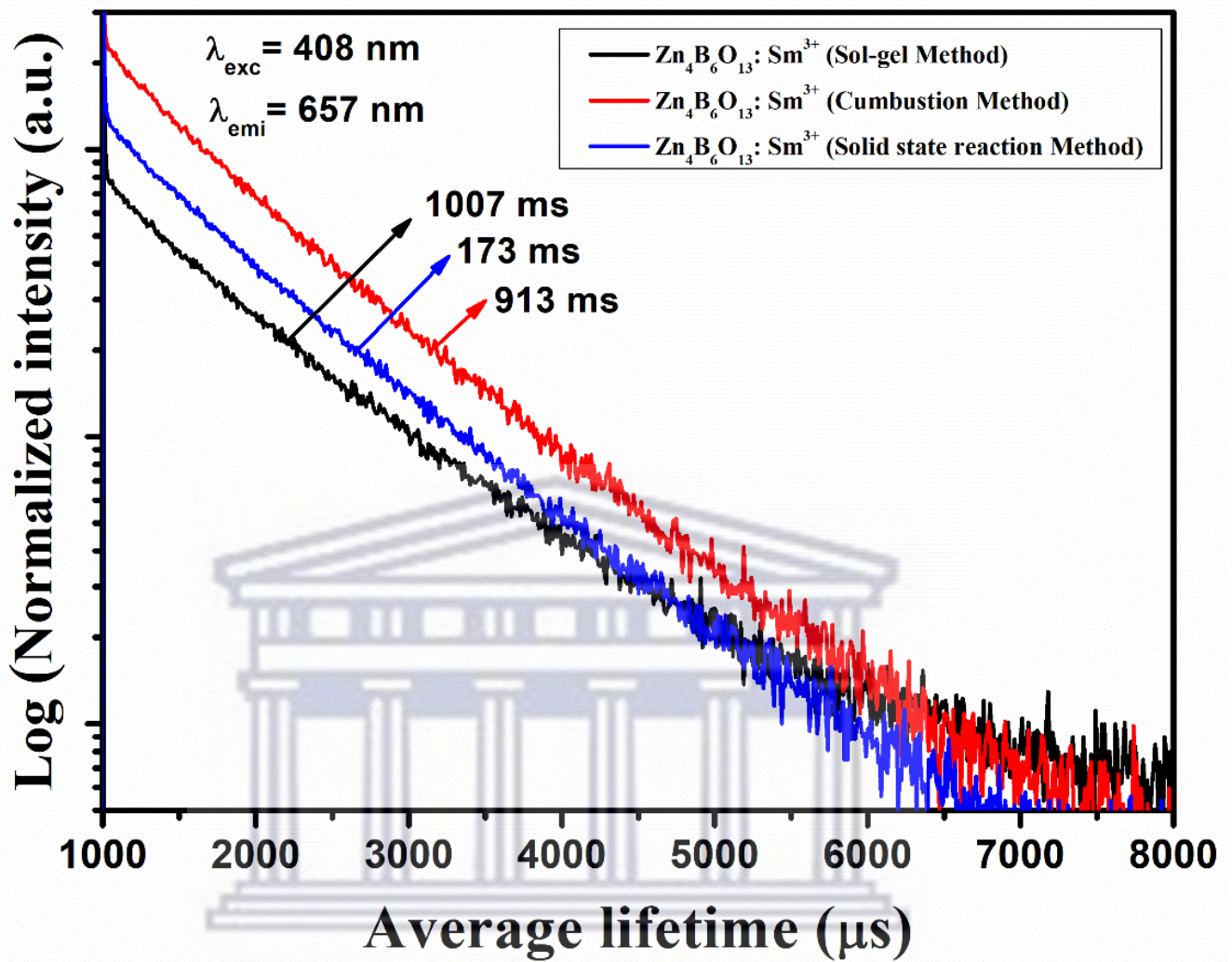


Figure 4.8 Lifetime decay profiles of $\text{Zn}_4\text{B}_6\text{O}_{13}:\text{xSm}^{3+}$ (where $x = 0, 1\%$) nanophosphors prepared by various chemical techniques: (a) Sol-Gel (b) Combustion (c) Solid-state reaction method.

Table 4.3. Average lifetime decay values of $Zn_4B_6O_{13}:xSm^{3+}$ (where $x = 0, 1\%$) nanophosphors prepared by various chemical techniques: (1) Sol-Gel (2) Combustion and (3) Solid-state reaction method.

S.No.	Sample ID	Average life-time (ms)
1	$Zn_4B_6O_{13}:Sm^{3+}$ (Sol-gel)	1007
2	$Zn_4B_6O_{13}:Sm^{3+}$ (Combustion)	913
3	$Zn_4B_6O_{13}:Sm^{3+}$ (Solid state)	173

4.2.7 CIE colour coordinates

Figure 4.9 shows the Commission Internationale de l'Eclairage chromaticity (CIE) colour diagram of $Zn_4B_6O_{13}:xSm^{3+}$ (where x is 1 mol%) nanophosphor prepared with three synthesis methods: sol-gel, combustion, and solid-state. This diagram is for the evaluation of the emission properties of Sm^{3+} ions in the prepared sample; it depicts significant CIE coordinate values and describes the nature of photoluminescence emissions [252]. The prepared samples were analyzed using an excitation wavelength of 226 nm, while monitoring an intense emission peak at the wavelength of 657 nm. The obtained CIE colour coordinates for the applied synthesis methods are as follows: solid-state (0.58, 0.43), combustion (0.59, 0.43), and sol-gel (0.47, 0.38) as depicted in **Figure 4.9**. The obtained colour coordinates were found to lie within the orange-reddish region for all synthesis methods. The sample prepared with the sol-gel method produced a low intensity orange-red emission, while other methods such as solid-state and combustion methods produced a high intensity orange-red emission. From the investigations, it is noticed that the prepared phosphors synthesized by the solid-state and combustion methods are suitable for near ultra-violet light-emitting diodes (near UV-LEDs) and solid-state lighting applications [252].

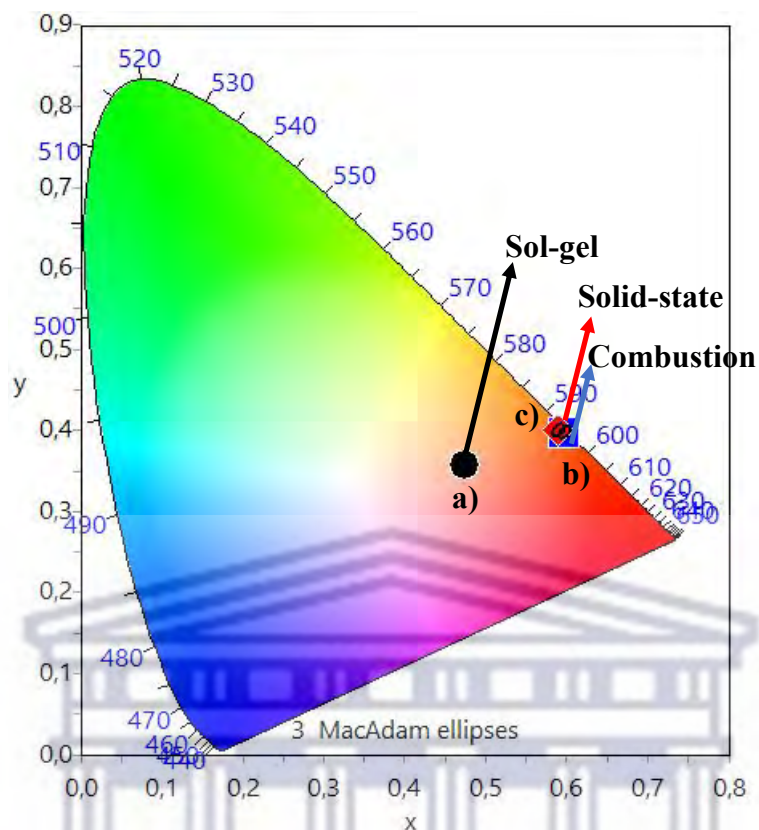


Figure 4.9 CIE colour diagram of $Zn_4B_6O_{13}:xSm^{3+}$ (where $x = 0, 1\%$) nanophosphors prepared by various chemical techniques: (a) Sol-Gel (b) Combustion (c) Solid-state reaction method.

Table 4.4. CIE colour co-ordinates of $Zn_4B_6O_{13}:xEu^{3+}$ (where $x = 0, 1\%$) nanophosphors prepared by various chemical techniques: (1) Sol-Gel (2) Combustion and (3) Solid-state reaction method.

S.No.	Sample ID	CIE-coordinates
1	$Zn_4B_6O_{13}:Eu^{3+}$ (Sol-gel)	(0.47, 0.38)
2	$Zn_4B_6O_{13}:Eu^{3+}$ (Combustion)	(0.59, 0.43)
3	$Zn_4B_6O_{13}:Eu^{3+}$ (Solid state)	(0.58, 0.43)

4.3 Conclusion

The $\text{Zn}_4\text{B}_6\text{O}_{13}$ and $\text{Zn}_4\text{B}_6\text{O}_{13}:\text{Sm}^{3+}$ phosphors were successfully synthesized with different reaction methods: sol-gel, combustion, and solid-state. The aim of the study is to determine which synthesis method yields the best phosphor materials with high luminescence. The XRD results confirmed the cubic structure of host $\text{Zn}_4\text{B}_6\text{O}_{13}$ materials and doped $\text{Zn}_4\text{B}_6\text{O}_{13}:\text{Sm}^{3+}$ phosphors prepared by the mentioned different synthesis techniques. The XRD patterns of doped $\text{Zn}_4\text{B}_6\text{O}_{13}:\text{Sm}^{3+}$ phosphors were not affected by the Sm^{3+} ions, except for shifts in the diffraction peak positions. FE-SEM was used to study the morphology of the prepared phosphors; smooth-like surfaces and hexagonal-shaped particles with agglomeration were observed. The average particle sizes of the prepared samples showed that the particles were formed in the range of 1000 to 1350 nm. Optical studies indicate that the doping of Sm^{3+} caused a decrease in energy bandgaps in samples prepared by sol-gel and combustion methods, while it increased in the solid-state method. Analysis of the PL emission spectra reveals that the sample prepared by the combustion method exhibited high intensity emissions, whereas the sol-gel method produced low intensity emissions at the 657 nm wavelength. The solid-state method produced $\text{Zn}_4\text{B}_6\text{O}_{13}:\text{Sm}^{3+}$ phosphor with the fastest average decay time compared to other synthesis methods. From the CIE diagram, it is observed that the combustion and solid-state methods produced phosphors with high purity orange red colour emissions, whereas the sol-gel method produced phosphors with high purity orange emission. The $\text{Zn}_4\text{B}_6\text{O}_{13}:\text{Sm}^{3+}$ prepared by combustion and sol-gel methods are potential candidates for producing orange-red light-emitting diodes.

Chapter V

Impact of different various chemical techniques on the structural and photoluminescence properties of $Zn_4B_6O_{13}: Eu^{3+}$ nanophosphors

5.1 Introduction

The research based on luminescent materials that are cost effective, energy-saving, have a long-life span, and are environmentally friendly is still ongoing. Luminescent materials play an important role in the manufacturing of solid-state lamps and light-emitting diodes. Solid-state lighting is regarded as energy-efficient, environmentally friendly, have longer lifetime, and have low power consumption [223].

The type of synthesis method used is significant for the quality of the phosphor material produced. Single or co-doping a host with rare earth ions enhances its luminescence efficiencies. Generally, rare earth ions are significant for enhancing colour emissions when doped in various host materials [253]. There are two methods used to produce commercial white light-emitting diodes (wLEDs): The blue LED chip Gallium Nitride (GaN) is incorporated into yellow Yttrium aluminium garnet doped with cerium (YAG: Ce^{3+}), and the second method involves the mixing of tri-phosphor materials (red-green-blue: RGB) excited by the ultraviolet light. These commercial wLEDs have a low colour rendering index (CRI < 70) and a higher correlated colour temperature (CTT > 327 °C) due to the lack of a red phosphor [90], [254]. To overcome this drawback, Eu^{3+} is used as a dopant. Due to their $^5D_0 \rightarrow ^7F_j$ ($j = 0, 1, 2, 3, 4$) transitions, Eu^{3+} doped phosphors are known for their red emissions. Doping with Eu^{3+} has numerous advantages; it reduces the bandgap of the host material, improves the conductivity of the host material, and repositions the conduction and valence bands of the host material [229], [231], [255].

Zinc borate material has been used as a host by many researchers. For instance, Liang Pan et al. [229] reported on the synthesis of $Zn_4B_6O_{13}: Eu/Tb$ materials using the conventional solid-state method to study their spectroscopic behaviour. Meijerink et al. [88] reported on the synthesis of $Zn_4B_6O_{13}$ using the solid-state method for their photoluminescence and thermoluminescence properties. Zhao et al. [89] reported on the synthesis of $Zn_4B_6O_{13}: Tb^{3+}, Yb^{3+}$ using the solid-state reaction method to study its multimodal emission for information encryption and anti-counterfeiting. This chapter focuses on the investigation of the synthesis

methods that will produce the best red emission luminescence characteristics of the nanophosphors. $Zn_4B_6O_{13}$ material is chosen as a host and Eu^{3+} as a dopant. The preparation methods involved in this work are sol-gel, solid-state, and combustion techniques. Their photoluminescence properties were studied at monochromatic light excitations of 245 and 395 nm wavelengths. At an excitation wavelength of 395 nm, all samples showed the fastest average decay time. The CIE chromaticity diagram indicated that the synthesized phosphors produced strong red emissions.

5.2 Results and discussion

5.2.1 X-ray diffraction studies

Figure 5.1 (a-d) shows the X-ray diffraction (XRD) patterns for the $Zn_4B_6O_{13}:xEu^{3+}$ (where x is 1 mol%) phosphor synthesized with three different techniques such as the combustion, sol-gel, and solid-state method, respectively, along with the standard background XRD patterns of the $Zn_4B_6O_{13}$ structure (JCPDS No: 01-076-0917), with a space group of I-43. **Figure 5.1 (a-d)** shows the X-ray diffraction (XRD) patterns for $Zn_4B_6O_{13}:xEu^{3+}$ (where x is 1 mol%) phosphor synthesized with three different techniques such as combustion, sol-gel, and solid-state method respectively, along with the standard background XRD patterns of the $Zn_4B_6O_{13}$ structure (JCPDS No: 01-076-0917), with a space group of I-43. The diffraction peaks were found around 2θ angles of 24° , 29° , 38° , 45° , 49° , 52° , 58° , 61° , 63° , 69° , 71° , 74° , 76° , and 79° , corresponding to miller planes as indexed by (200), (211), (310), (321), (400), (330), (420), (422), (510), (521), (440), (433), (600), and (532), respectively. The calculated lattice parameters are $a = 7.47407 \text{ \AA}$, $b = 7.47407 \text{ \AA}$, and $c = 7.47407 \text{ \AA}$, with a cell volume of 417.51 \AA^3 . The calculated angles are $\alpha = \beta = \gamma = 90^\circ$, which confirms the cubic structure [89], [90].

Figure 5.1 (b) and **(c)** show the XRD spectra of $Zn_4B_6O_{13}:xEu^{3+}$ (where x is 1 mol%) phosphor material prepared by the sol-gel and solid-state reaction methods. Both diffraction peaks were similar to the combustion method reported in **Figure 5.1 (a)**, except for changes in lattice parameters, viz., sol-gel: $a = 7.47547 \text{ \AA}$, $b = 7.47547 \text{ \AA}$, and $c = 7.47547 \text{ \AA}$, $\alpha = \beta = \gamma = 90^\circ$, with a cell volume of 417.75 \AA^3 . For the solid-state reaction method, the following lattice parameters were obtained: $a = 7.47148 \text{ \AA}$, $b = 7.47148 \text{ \AA}$, and $c = 7.47148 \text{ \AA}$, $\alpha = \beta = \gamma = 90^\circ$ with a lattice volume of 417.51 \AA^3 . The weak XRD intensity peak is also due to the low

crystallite size, and it is shown in **Table 5.1** that the combustion method produced the $\text{Zn}_4\text{B}_6\text{O}_{13}:\text{Eu}^{3+}$ phosphor with the lowest crystallite size.

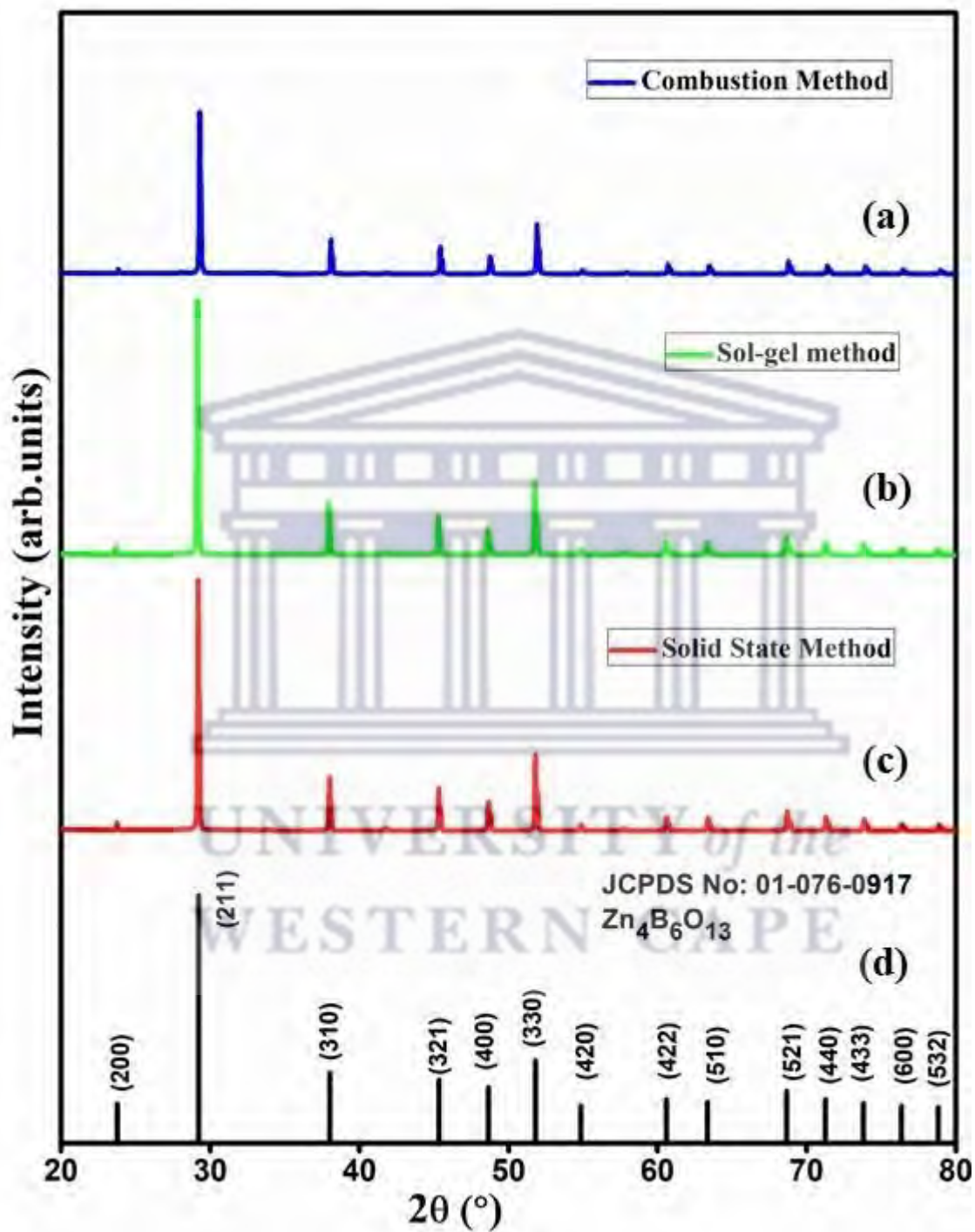


Figure 5.1. The full XRD patterns of $\text{Zn}_4\text{B}_6\text{O}_{13}:\text{xEu}^{3+}$ (where $x = 0, 1\%$) nanophosphors prepared by various chemical techniques: (a) Sol-Gel (b) Combustion (c) Solid-state reaction methods.

The crystallite sizes of the prepared $Zn_4B_6O_{13}:Eu^{3+}$ samples were calculated using the Debye-Scherrer equation (4.1) presented in Chapter IV. The dominant/intense peak (211) was used for the calculation of the crystallite sizes. **Table 5.1** shows the calculated crystallite sizes of $Zn_4B_6O_{13}:xEu^{3+}$ prepared with (1) sol-gel, (2) combustion, and (3) the solid-state reaction method. The calculated crystallite sizes are within the range of 95 – 99 nm. The average crystallite sizes were found to follow the trend below: sol-gel (98.05 nm) > solid-state (96.81 nm) > combustion (95.93 nm) produced for $Zn_4B_6O_{13}:Eu^{3+}$ phosphor materials.

Table 5.1. Crystallite size of $Zn_4B_6O_{13}:xEu^{3+}$ (where $x = 0, 1\%$) nanophosphors prepared by various chemical techniques: (1) Sol-Gel (2) Combustion and (3) Solid-state reaction method.

S.No	Sample	Crystallite size (nm)
1	$Zn_4B_6O_{13}:Eu^{3+}$ (Sol-gel)	98.05
2	$Zn_4B_6O_{13}:Eu^{3+}$ (Combustion)	95.93
3	$Zn_4B_6O_{13}:Eu^{3+}$ (Solid state)	96.81

5.2.2. Surface morphology studies and elemental analysis

Figure 5.2 shows the SEM micrographs and EDS spectra of $\text{Zn}_4\text{B}_6\text{O}_{13}:1\text{mol}\%\text{Eu}^{3+}$, prepared by different techniques: sol-gel **Fig (a) & (d)**, combustion **Fig (b) & (e)**, and solid-state **Fig (c) & (f)**, respectively. The inserted images in **Fig 5.2 (a – c)** show the magnified FE-SEM images, whereas **Fig 5.2 (d – f)** depicts the elemental mapping of the prepared materials, respectively.

Figure 5.2 (a) shows particles prepared by the sol-gel method with irregular morphologies; a cubic and polyhedron-like structures with flat face surfaces with varying sizes is clearly visible in the insert image. There are smooth particles with sharp edges that are more adherent and agglomerated, with little to no pores. The calculated average particle size using the Image J software is 890 nm, as depicted in **Figure 5.3 (a)**. The large spaces denoted by the blue arrows are due to the glass slide of the microscope that was used to hold the specimen during analysis.

Figure 5.2 (b) shows SEM images displaying rough particles that are prepared with the combustion method. Moreover, these particles have a heterogeneous morphology, being spherical and hexagonal-like. There are particles, which are agglomerated into distinct groups and are scatteredly arranged. The large particles are surrounded by smaller particles, which are uniformly distributed throughout the specimen substrate, as depicted by green arrows.

Figure 5.2 (c) shows the SEM images displaying rough particles, which are prepared with the solid-state reaction method. In addition, these particles are largely agglomerated into distinct groups and are randomly distributed in the specimen holder, as depicted by the red circles. Moreover, these particles have hexagonal-like morphology, as clearly visible in the inserted image; they are adherent, with little to no porosity. The large gaps denoted by the red arrows are due to the specimen holder and not the sample.

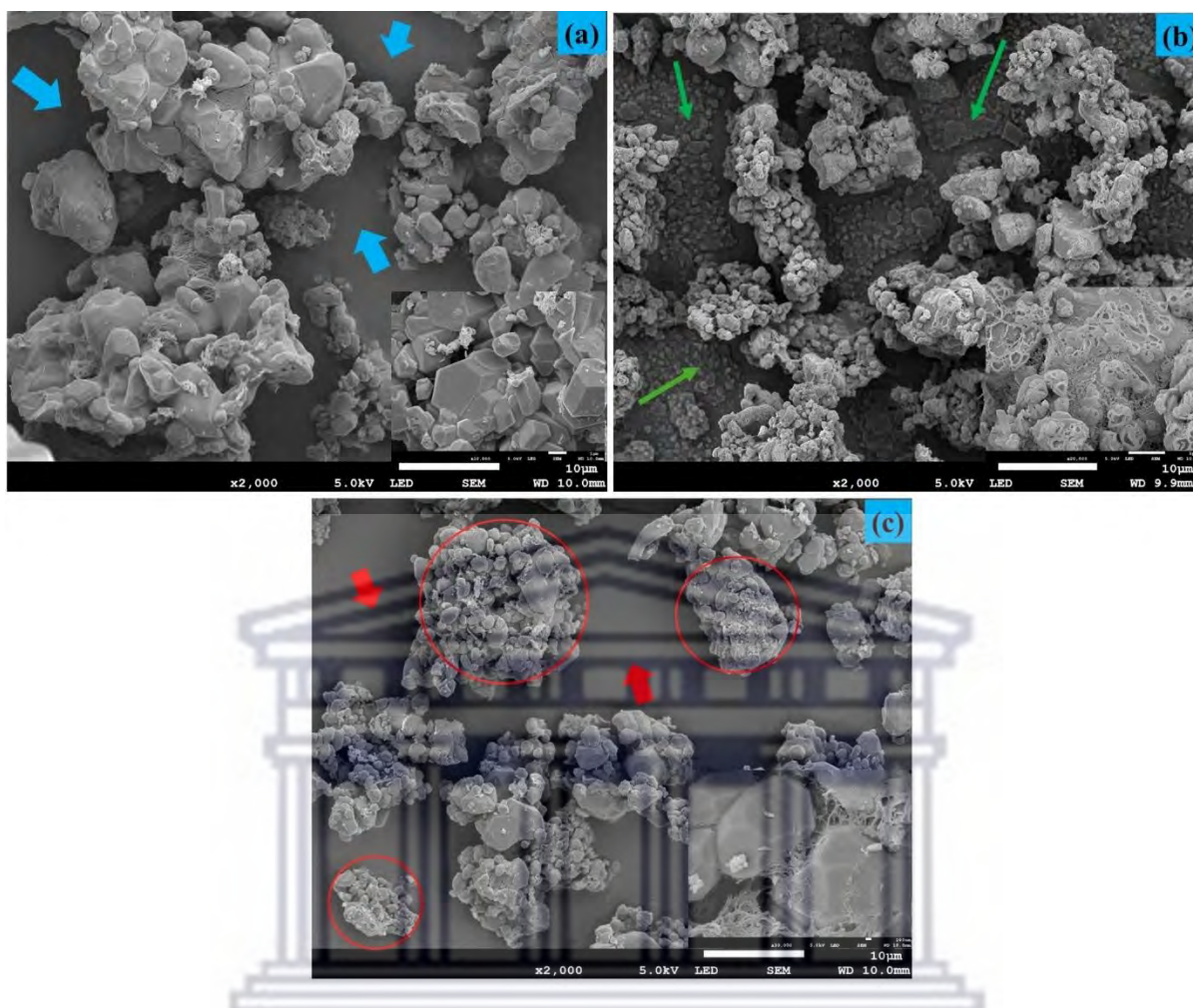


Figure 5.2: Field-emission scanning electron microscopy (FE-SEM) images of $Zn_4B_6O_{13}:xEu^{3+}$ (where $x = 0, 1\%$) nanophosphors prepared by various chemical techniques: (a) Sol-Gel, (b) Combustion, and (c) Solid-state reaction methods.

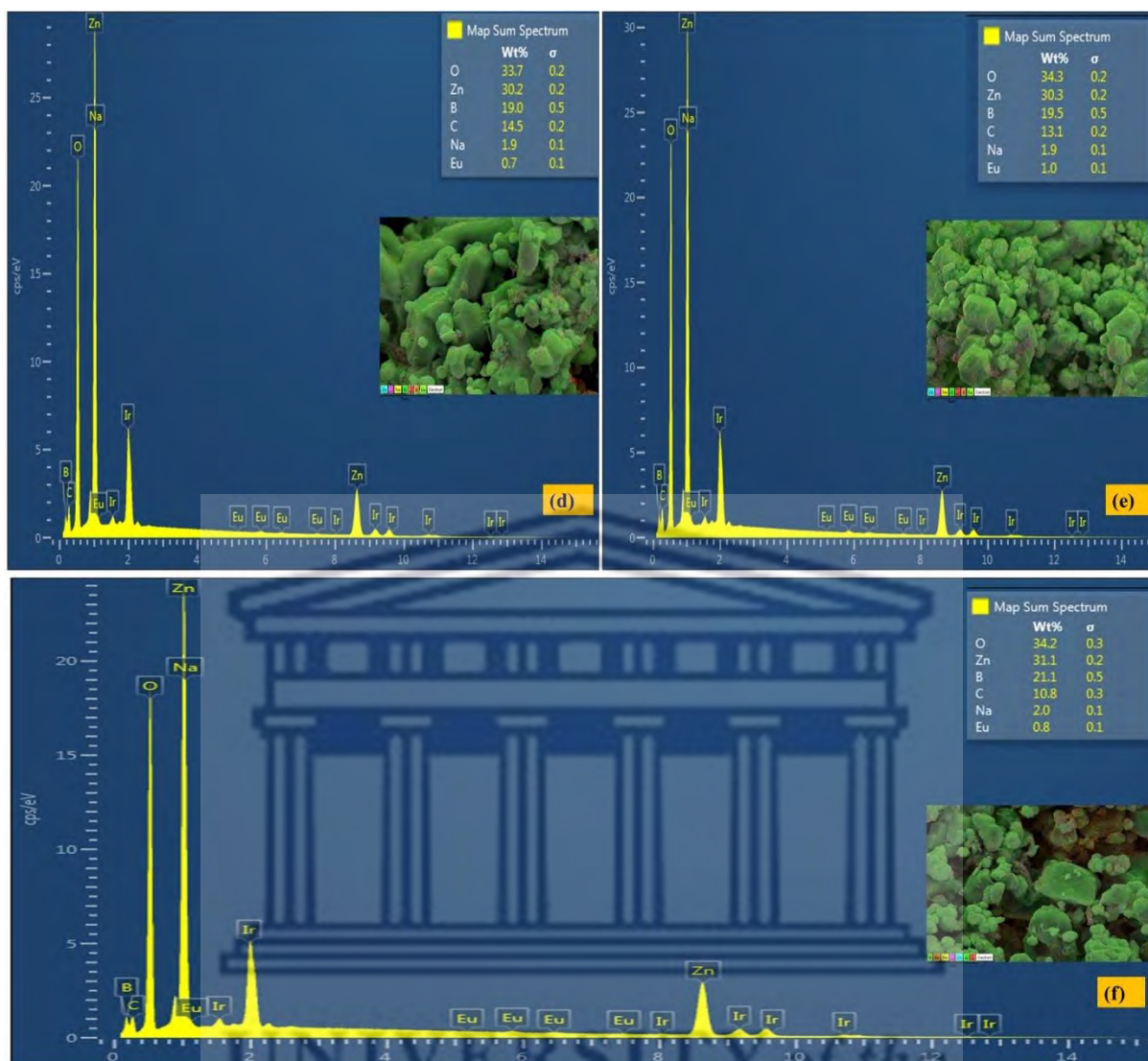


Figure 5.2: Elemental Dispersive Spectroscopy (EDS) images of Zn₄B₆O₁₃:xEu³⁺ (where x = 0, 1%) nanophosphors prepared by various chemical techniques: (d) Sol-Gel, (e) Combustion, and (f) Solid-state reaction methods.

The EDS images in **Figure 5.2 (d – f)** confirm all the elements present in the prepared materials, such as europium (Eu), zinc (Zn), oxygen (O), boron (B), sodium (Na), and carbon (C). The detection of (C) was due to the carbon tape that was used as a conductive support for the sample. The sample was coated with iridium (Ir) to rectify its conductivity and charging during characterization. The elemental mapping images (inserts) in **Figure 5.2 (d – f)** show the dominant uniform distribution of Eu and O throughout the prepared Zn₄B₆O₁₃:Eu³⁺ samples, with a higher number of counts than other elements. The average particle sizes of the prepared samples are shown in **Figure 5.3** were obtained in the following manner: 890 nm for the sol-

gel method, > 750 nm for the solid-state method, and > 500 nm for the combustion method. The adopted preparation techniques have different impacts on the morphology and the average particle sizes of $Zn_4B_6O_{13}:Eu^{3+}$ materials.

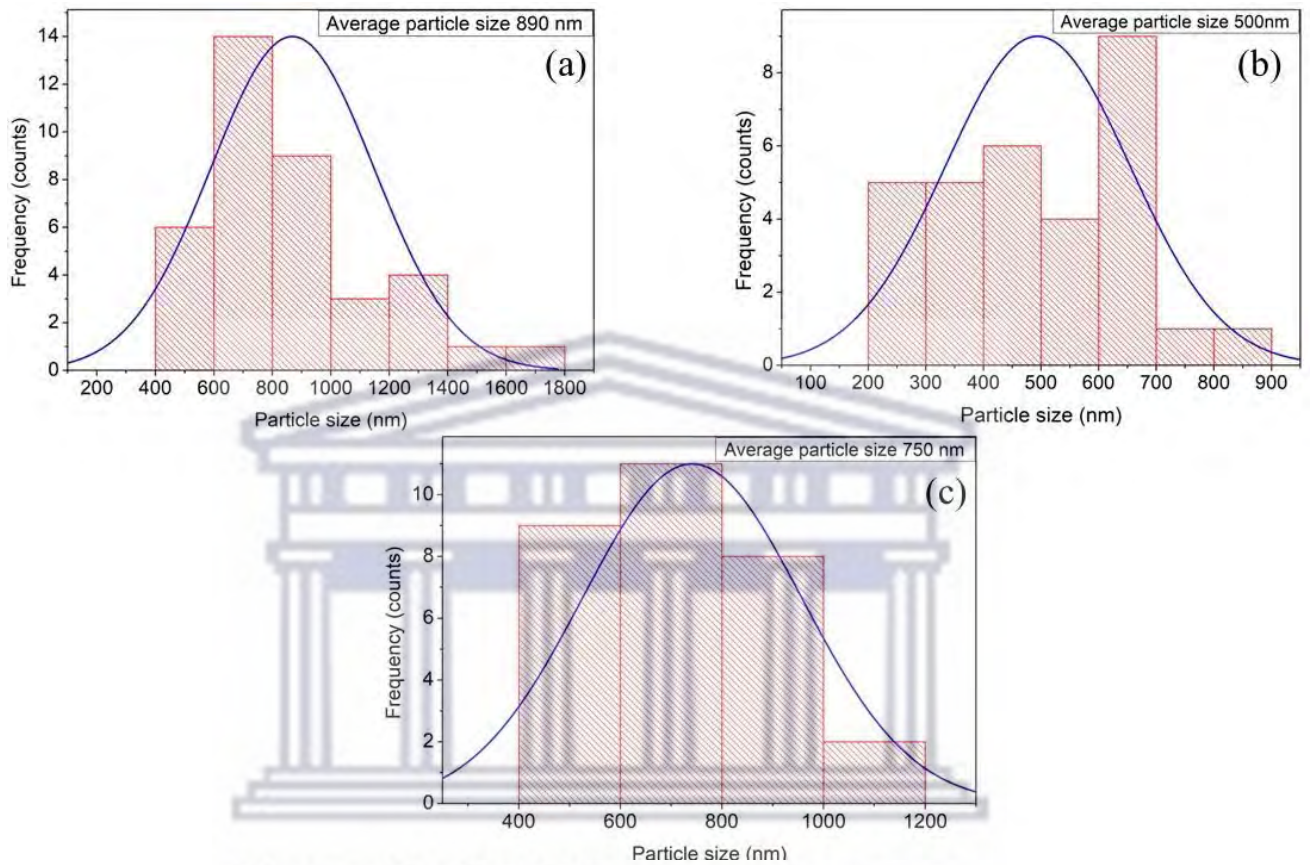


Figure 5.3 Histograms displaying the average particle size distribution of $Zn_4B_6O_{13}:xEu^{3+}$ nanophosphors prepared with (a) sol-gel, (b) combustion, and (c) solid-state methods.

5.2.3 Fourier Transform Infrared (FT-IR) analysis.

Figure 5.4 shows the FTIR spectra for the $Zn_4B_6O_{13}$ host and of the $Zn_4B_6O_{13}:xEu^{3+}$ sample prepared with sol-gel, combustion, and solid-state methods. The samples were characterized at room temperature within the wave number range of $400 - 4000\text{ cm}^{-1}$. There are sharp absorption bands at 450 cm^{-1} which are attributed to the Zn-O vibration stretching mode [256]. However, the absorption band varies with the synthesis routes followed. The broad absorption bands at 800 cm^{-1} are attributed to the vibrational bands of BO_3^{3-} groups, which are found in the $Zn_4B_6O_{13}$ structure [257], [258], [259]. The sharp peaks at around 600 cm^{-1} are signatures of BO_4 . Furthermore, the absorption bands at 1100 cm^{-1} and 3200 cm^{-1} are attributed to the O-H bonds of the water (H_2O) molecules during sample preparation [258], [259]. The $Zn_4B_6O_{13}:Eu^{3+}$ prepared with the sol-gel method showed the weakest O-H bands compared to other methods.

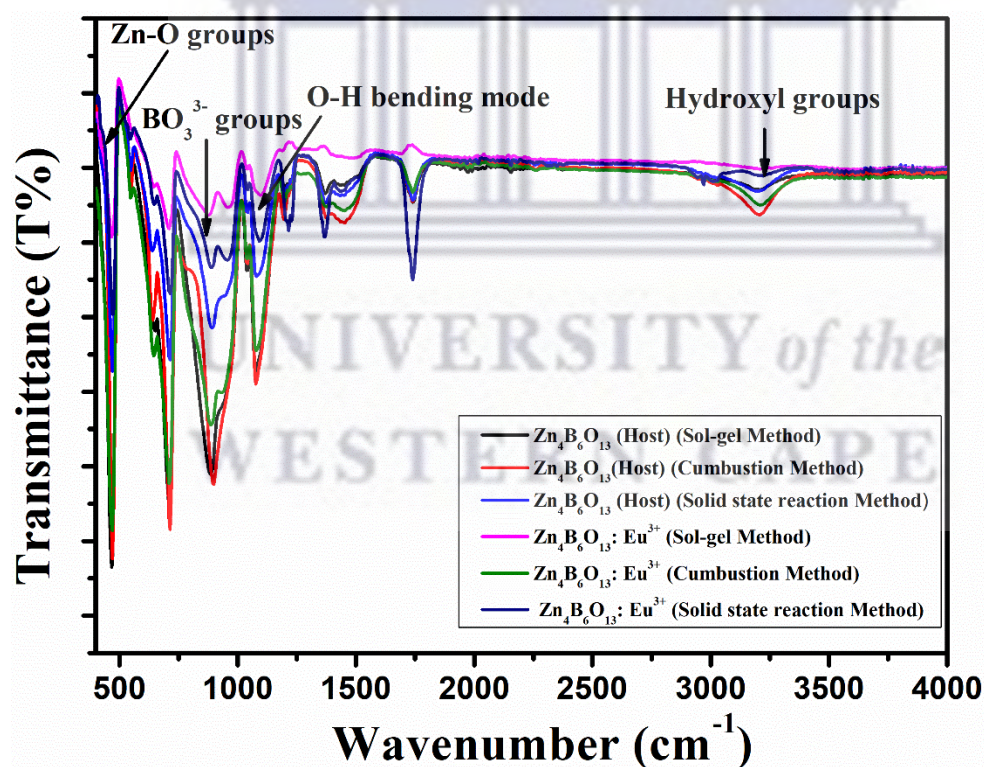


Figure 5.4: FT-IR spectra of $Zn_4B_6O_{13}:xEu^{3+}$ (where $x = 0, 1\%$) nanophosphors prepared by various chemical techniques: (a) Sol-Gel (b) Combustion (c) Solid-state reaction method.

5.2.4 UV-VIS and band gap measurements

Figure 5.5 shows the diffuse reflectance spectra (DRS) of UV – Vis for the $\text{Zn}_4\text{B}_6\text{O}_{13}$ host and $\text{Zn}_4\text{B}_6\text{O}_{13}:1\text{mol}\%\text{Eu}^{3+}$ doped nanophosphors prepared by different techniques such as sol-gel, combustion, and solid-state reaction methods, measured in the range of 200 – 2000 nm. There is a presence of Eu^{3+} absorption bands for the $\text{Zn}_4\text{B}_6\text{O}_{13}:x\text{Eu}^{3+}$ phosphor around 300, 400, and 510 nm, which are due to the parity forbidden $f \rightarrow f$ transitions i.e., ${}^7\text{F}_0 \rightarrow {}^5\text{D}_3$, ${}^7\text{F}_0 \rightarrow {}^5\text{D}_2$, and ${}^7\text{F}_0 \rightarrow {}^5\text{D}_1$, respectively, from the ground state to the higher excited state. The peaks within the region of 200 – 450 nm are attributed to the Eu – O charge transfer band. The shoulder peaks within the 600 nm region are attributed to ${}^7\text{F}_0 \rightarrow {}^7\text{F}_6$ transitions; these transitions are observed in the host and the Eu^{3+} doped samples prepared [260]. The different optical behaviour observed in sol-gel compared to other methods is due to the high agglomeration of large particles, low annealing temperature which resulted in not removing all impurities, and low photo luminescence emission compared to other methods [238]. The mentioned factors result in inability to react to light compared to other methods in the ultraviolet and visible regions. The absorption bands due to Eu^{3+} are barely visible, which implies that the dopant molecules were successfully incorporated into the host and resulted in a homogeneous distribution [90].

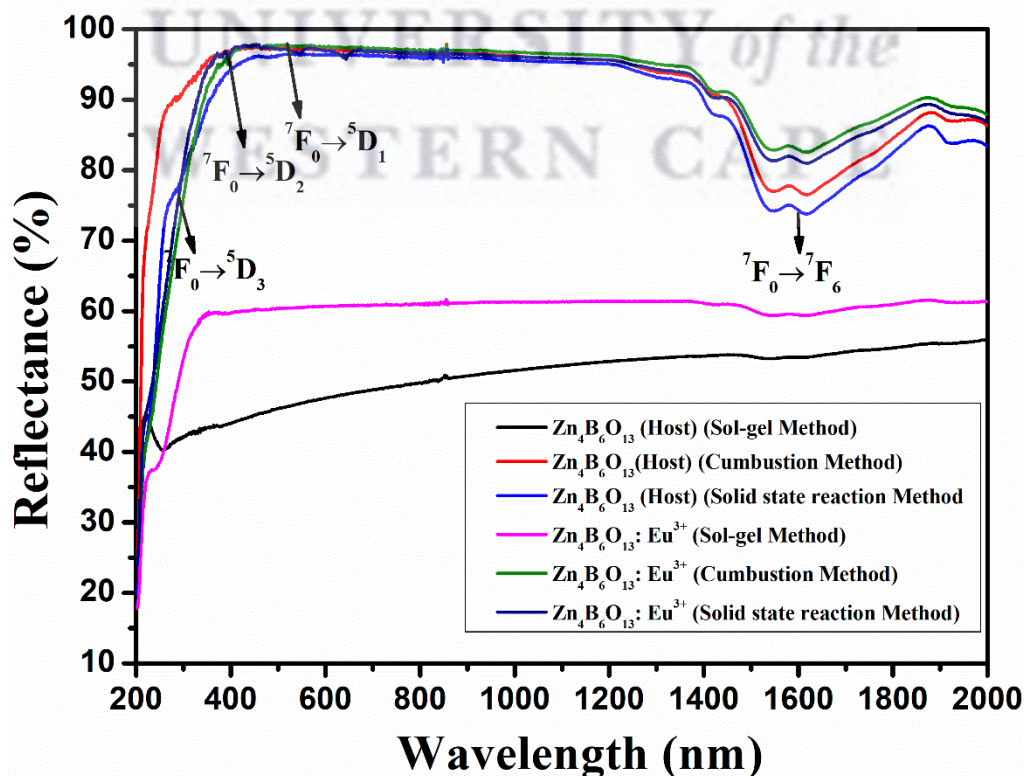


Figure 5.5. *UV-Vis DRS spectra of $Zn_4B_6O_{13}:xEu^{3+}$ (where $x = 0, 1\%$) nanophosphors prepared by various chemical techniques: Sol-Gel, Combustion, and Solid-state reaction method.*

The band gaps of the synthesized samples are estimated from the optical data in **Figure 5.6** for samples prepared with **(a)** sol-gel, **(b)** combustion, and **(c)** solid-state reaction methods. These band gaps were obtained using the Kubelka-Munk (M-K) function theory [240], [241], which is reported in Chapter IV (**equation 4.2**) and is used accordingly. The bandgap for $Zn_4B_6O_{13}$ decreased after doping with Eu^{3+} in sol-gel and combustion synthesis methods from 5.899 to 5.789 eV and from 5.948 to 5.846 eV, respectively, as shown in **Table 5.2**. When the bandgap decreases, the conduction re-aligns to a new position [261]. The decrease in band gap is also attributed to bond deformations and local defects in the $Zn_4B_6O_{13}$ matrix due to doping with Eu^{3+} during calcination. There is an increase in the optical band gap after doping with Eu^{3+} in the solid-state method from 5.865 to 5.885 eV, which can be explained by the Burstein – Moss effect [262], [263]. The increase in bandgap is attributed to the successful incorporation of the dopant into the host material, which blocks the low-energy transitions and causes an upward shift of the Fermi level within the conduction bands [262].



UNIVERSITY of the
WESTERN CAPE

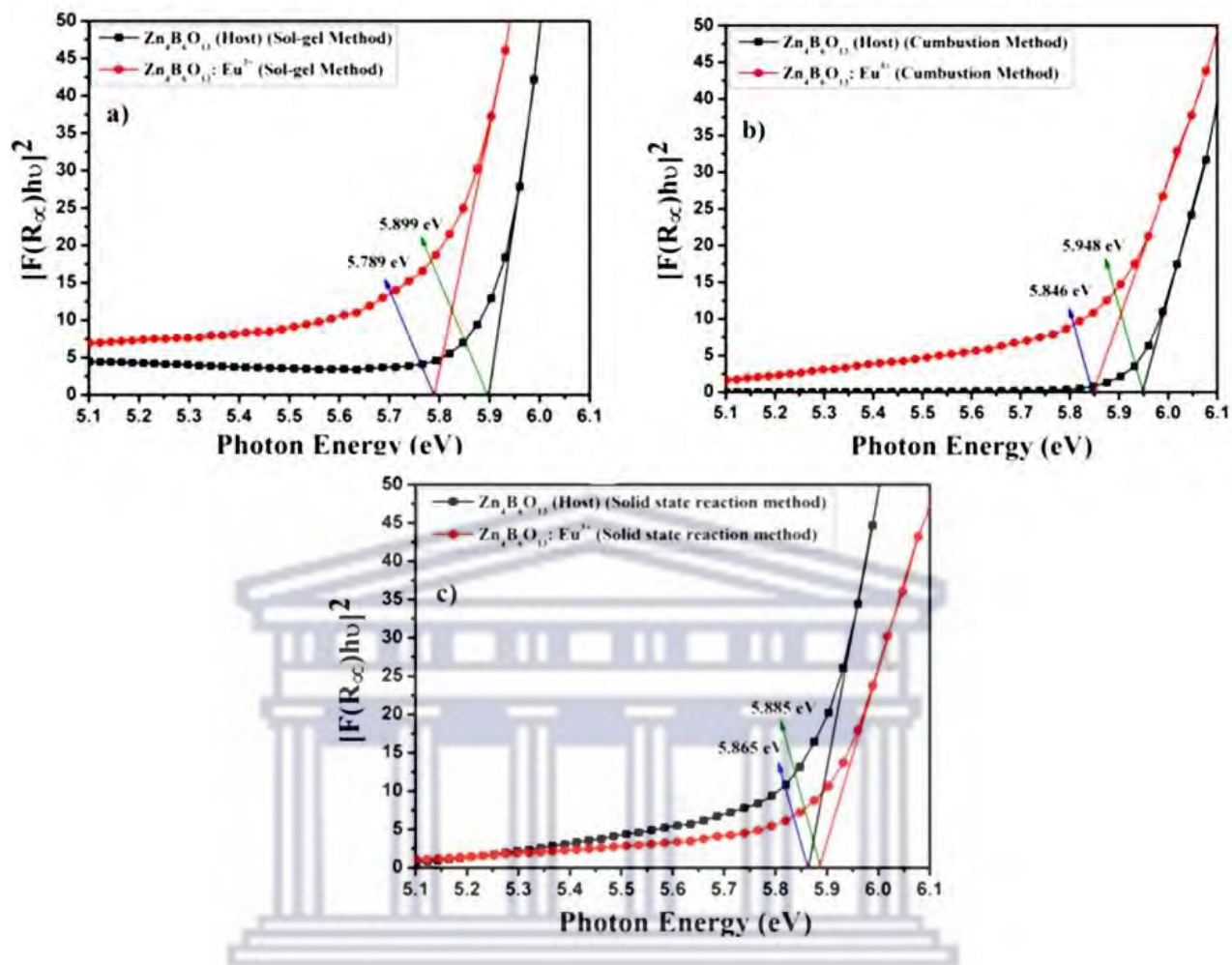


Figure 5.6. Optical bandgap calculations of $Zn_4B_6O_{13}:xEu^{3+}$ (where $x = 0, 1\%$) nanophosphors prepared by various chemical techniques: (a) Sol-Gel (b) Combustion (c) Solid-state reaction method. The line represents the best linear fit to determine the energy band gap.

Table 5.2. Optical bandgap values of the $Zn_4B_6O_{13}:xEu^{3+}$ (where $x = 0, 1\%$) nanophosphors prepared by various chemical techniques: (1,2) Sol-Gel (3,4) Combustion (5,6) Solid-state reaction method.

S.No	Sample ID	Energy bandgap (eV)
1	$Zn_4B_6O_{13}$ (Sol-gel)	5.899
2	$Zn_4B_6O_{13}:Eu^{3+}$ (Sol-gel)	5.789
3	$Zn_4B_6O_{13}$ (Combustion)	5.948
4	$Zn_4B_6O_{13}:Eu^{3+}$ (Combustion)	5.846
5	$Zn_4B_6O_{13}$ (Solid state)	5.865
6	$Zn_4B_6O_{13}:Eu^{3+}$ (Solid state)	5.885

5.2.5 Photoluminescence excitation and emission spectra measurements

Figure 5.7 (a) and **(b)** show the photoluminescence excitation spectra for $Zn_4B_6O_{13}:Eu^{3+}$ samples prepared with sol-gel, combustion, and solid-state methods, measured within 200 – 550 nm and 300 – 500 nm ranges, respectively, while monitoring the emission peak at 614 nm wavelength. This excitation spectra for combustion and solid-state methods show the excitation peaks at 320, 360, 385, 396, 470, 525, and 530 nm, which are attributed to the ${}^7F_0 \rightarrow {}^5H_6$, ${}^7F_0 \rightarrow {}^5H_3$, ${}^7F_0 \rightarrow {}^5D_4$, ${}^7F_0 \rightarrow {}^5G_j$, ${}^7F_0 \rightarrow {}^5L_6$, ${}^7F_0 \rightarrow {}^5D_2$, ${}^7F_0 \rightarrow {}^5D_1$, ${}^7F_0 \rightarrow {}^5D_1$, and ${}^7F_1 \rightarrow {}^5D_1$ transitions of Eu^{3+} ions, respectively. The wide bands within the 250 nm region are associated with the charge transfer band between the 2p orbital of O^{2-} and the 4f orbital of Eu^{3+} [254]. The excitation peaks with the highest intensity are at 246 and 395 nm wavelengths, which are more dominant in the excitation spectra [264]. **Figure 5.7 (c)** shows the emission spectrum of the prepared samples using an excitation of 246 nm wavelength. There are ${}^5D_0 \rightarrow {}^7F_j$ (where $j=1, 2, 3,$ and 4) transitions of $Zn_4B_6O_{13}:Eu^{3+}$ phosphors at 570, 583, 615, 652, and 704 nm, respectively. The peaks from 580 to 600 nm are due to the magnetic dipole transition of Eu^{3+} ions. The emission peak at 615 nm wavelength is assigned to the electric dipole transition

${}^7D_0 \rightarrow {}^7F_2$ [265]. The sol-gel method produced the most dominant emission peak, compared to other methods. This emission peak implies that there was efficient energy transfer from the host to the dopant in the sol-gel method. **Figure 5.7 (d)** shows the emission spectra at an excitation wavelength of 395 nm. The emission peaks observed in this spectrum are similar to the emission peaks that occurred through 246 nm excitation wavelength in **Figure 5.7 (c)**. The solid-state method shows the most dominant peak at 615 nm wavelength is attributed to the ${}^5D_0 \rightarrow {}^7F_2$ transition of the dopant.

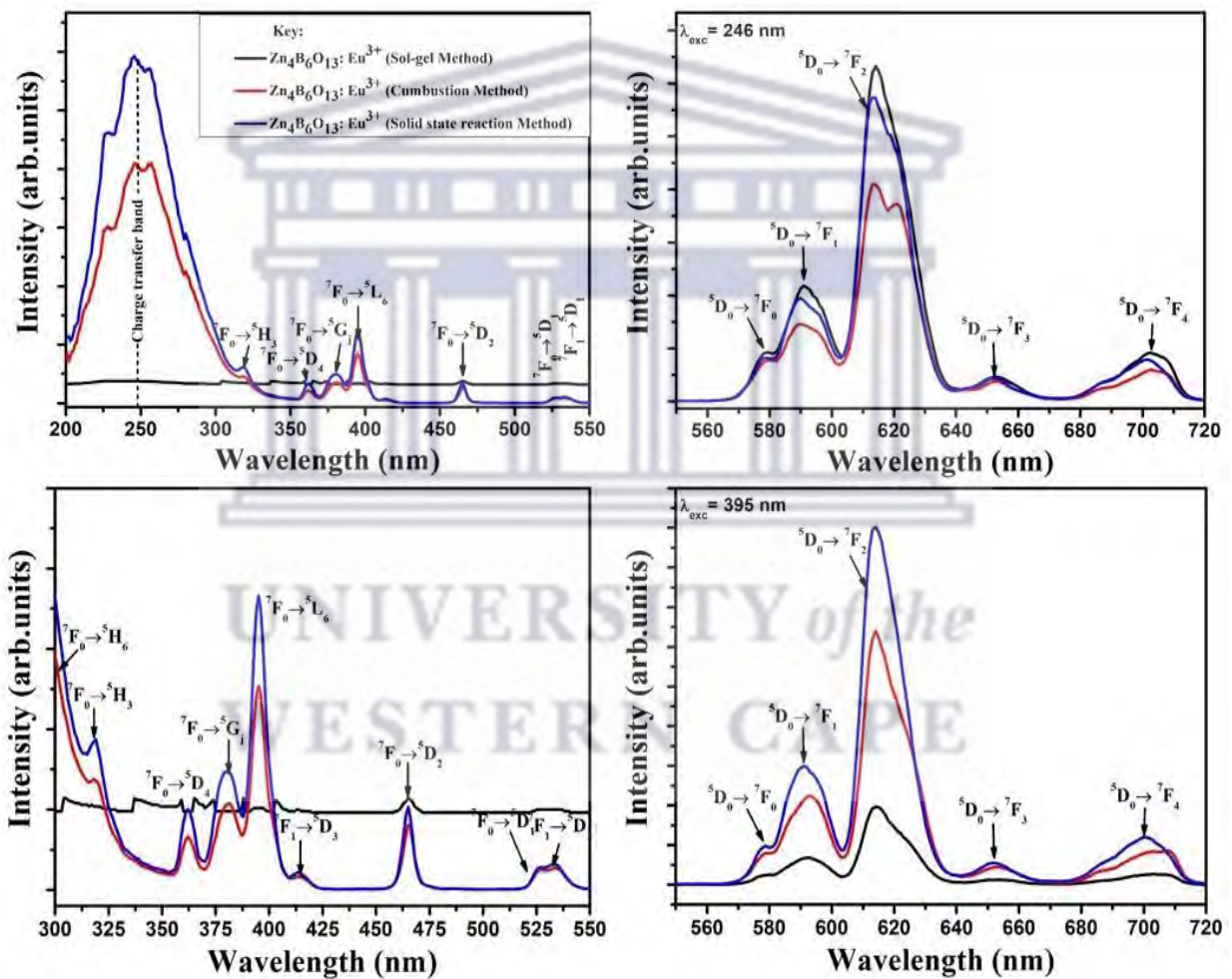


Figure 5.7. (a), (b) Photoluminescence excitation and (c), (d) emission spectra of $Zn_4B_6O_{13}:xEu^{3+}$ (where $x = 0, 1\%$) nanophosphors prepared by various chemical techniques: (1) Sol-Gel (2) Combustion (3) Solid-state reaction method using the parameters of $\lambda_{emi} = 614$ nm and $\lambda_{exc} = 246, 395$ nm wavelengths.

5.2.6 Lifetime decay measurements

Figure 5.8 shows the lifetime decay curves of $\text{Zn}_4\text{B}_6\text{O}_{13}:1 \text{ mol\%Eu}^{3+}$ nanophosphor prepared by the sol-gel, combustion, and solid-state reaction methods. These samples were excited with a 246 nm wavelength of light source while monitored at an intense emission peak of 614 nm wavelength. All decay curves are fitted with a second-order exponential equation (4.4) as described in Chapter IV [41]. The $\text{Zn}_4\text{B}_6\text{O}_{13}: \text{Eu}^{3+}$ average lifetime decay values are tabulated in **Table 5.3**. The average lifetime decay for $\text{Zn}_4\text{B}_6\text{O}_{13}: \text{Eu}^{3+}$ prepared with sol-gel, combustion, and solid-state methods was found to be 323, 244, and 463 milliseconds (ms) respectively. The sample prepared by the solid-state method showed the longest lifetime decay (463 ms), while the shortest lifetime (244 ms) value was found in the sample prepared by the combustion method. Phosphors with the fastest decay time are potential candidates for LED applications [248], [250].

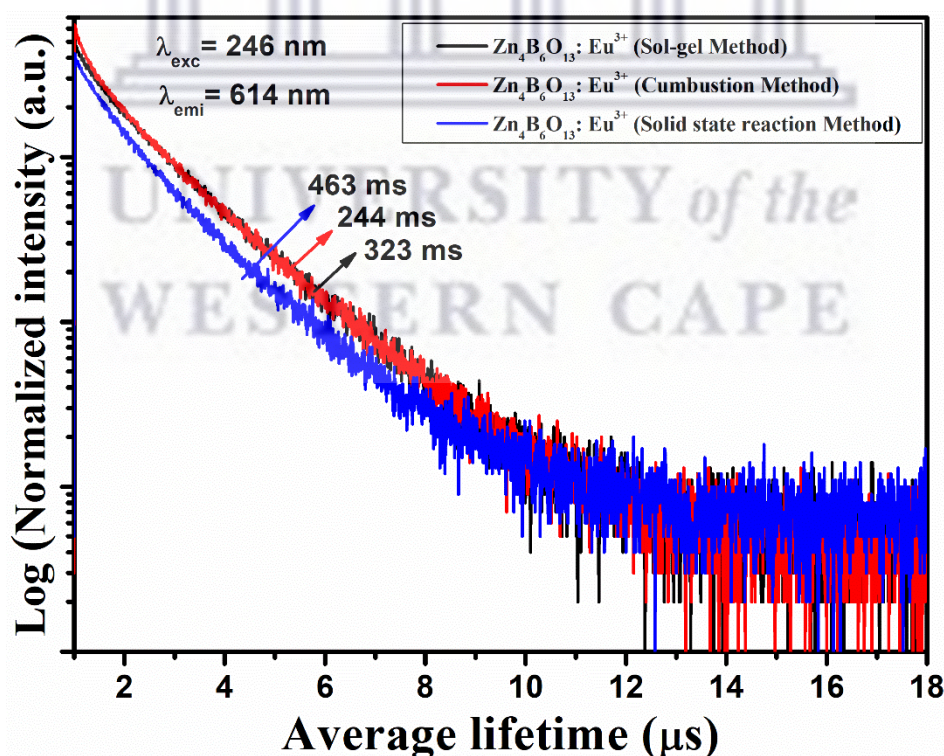


Figure 5.8. Lifetime decay profiles of $\text{Zn}_4\text{B}_6\text{O}_{13}:x\text{Eu}^{3+}$ (where $x = 0, 1\%$) nanophosphors prepared by various chemical techniques: (a) Sol-Gel (b) Combustion (c) Solid-state reaction method using the parameters of $\lambda_{\text{emi}} = 614 \text{ nm}$ and $\lambda_{\text{exc}} = 246 \text{ nm}$ wavelengths.

Figure 5.9 shows the average decay lifetime for $\text{Zn}_4\text{B}_6\text{O}_{13}:\text{Eu}^{3+}$ phosphor at an excitation wavelength of 395 nm while monitoring the emission at the 614 nm wavelength. The estimated lifetime decays at this 395 nm excitation wavelength were 2.94, 3.16, and 5.47 ms for the sol-gel, solid-state, and combustion methods, respectively. The decay lifetimes for the 395 nm excitation wavelength were also recorded in **Table 5.3**.

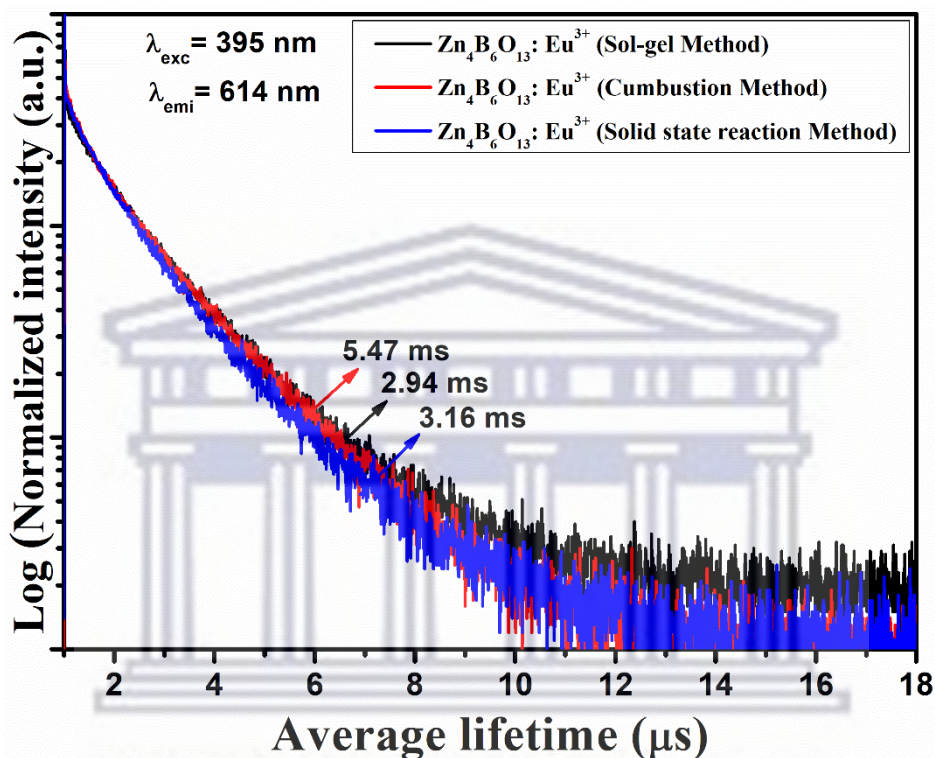


Figure 5.9. Lifetime decay profiles of $\text{Zn}_4\text{B}_6\text{O}_{13}:x\text{Eu}^{3+}$ (where $x = 0, 1\%$) nanophosphors prepared by various chemical techniques: (a) Sol-Gel (b) Combustion (c) Solid-state reaction method using the parameters of $\lambda_{\text{emi}} = 614 \text{ nm}$ and $\lambda_{\text{exc}} = 395 \text{ nm}$ wavelengths.

Table 5.3. Average lifetime decay values of $\text{Zn}_4\text{B}_6\text{O}_{13}:1\%\text{Eu}^{3+}$ nanophosphors prepared by various chemical techniques: (1) Sol-Gel (2) Combustion and (3) Solid-state reaction method

S.No.	Sample ID	Average life-time (ms)
1	$\text{Zn}_4\text{B}_6\text{O}_{13}:\text{Sm}^{3+}$ (Sol-gel)	323
2	$\text{Zn}_4\text{B}_6\text{O}_{13}:\text{Sm}^{3+}$ (Combustion)	244
3	$\text{Zn}_4\text{B}_6\text{O}_{13}:\text{Sm}^{3+}$ (Solid state)	463

5.2.7 CIE color coordinates

The Commission Internationale de l'Eclairage (CIE) chromaticity diagram for $\text{Zn}_4\text{B}_6\text{O}_{13}:1 \text{ mol}\% \text{Eu}^{3+}$ phosphors prepared by three methods are shown in **Figure 5.10**. The CIE chromaticity coordinates are in the form of (x, y) and were used for the analysis of the emission colours. The estimated CIE colour coordinates for $\text{Zn}_4\text{B}_6\text{O}_{13}:\text{Eu}^{3+}$ are as follows: (0.642, 0.353) sol-gel method, (0.641, 0.352) combustion method, and (0.644, 0.354) solid state method. All the obtained emissions fall within the red region of the CIE chromaticity diagram, which indicates efficient incorporation of Eu^{3+} ions into the host as it is known for its red emissions. The energy transitions shown in **Figure 5.7 (c) and (d)** are responsible for the red colour emission. This implies that these $\text{Zn}_4\text{B}_6\text{O}_{13}:\text{Eu}^{3+}$ phosphors are potential candidates for application in tuneable red light-emitting diodes [252]. The prepared samples were analysed under an excitation wavelength of 395 nm.

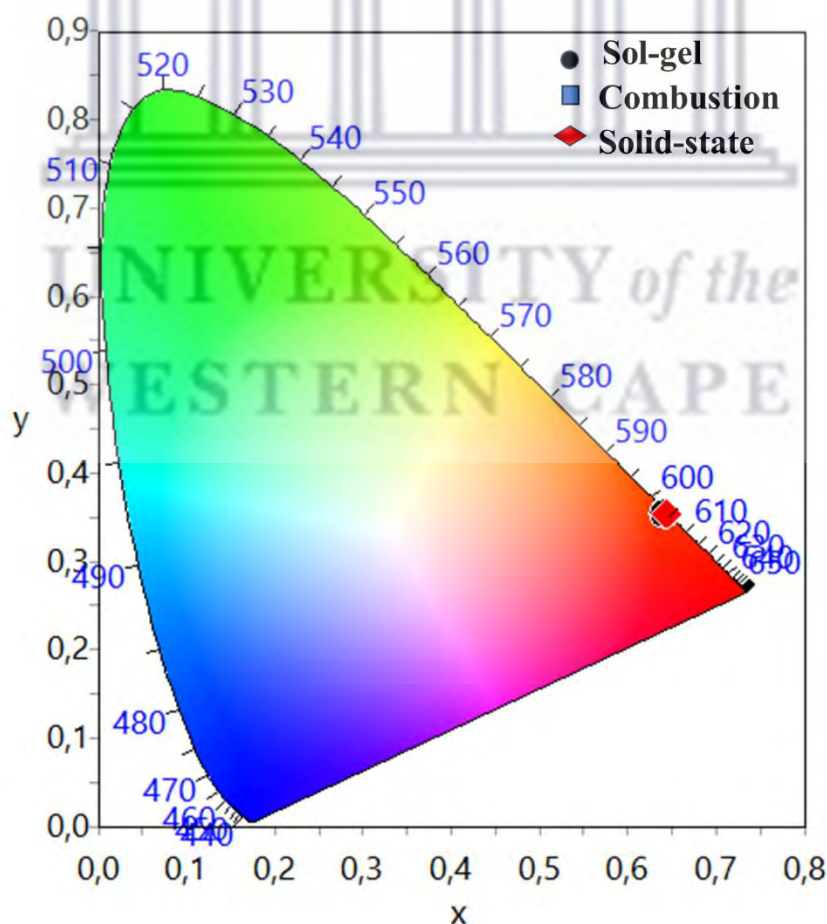


Figure 5.10. CIE colour diagram of $Zn_4B_6O_{13}:xEu^{3+}$ (where $x = 0, 1\%$) nanophosphors prepared by various chemical techniques: Sol-Gel, Combustion, and Solid-state reaction method.

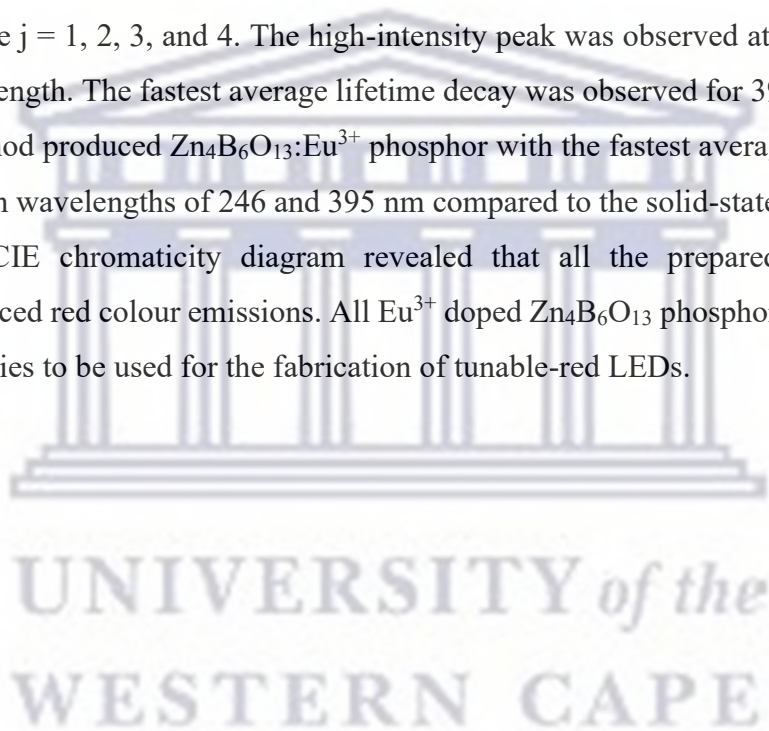
Table 5.4. CIE colour co-ordinates of $Zn_4B_6O_{13}:xEu^{3+}$ (where $x = 0, 1\%$) nanophosphors prepared by various chemical techniques: (1) Sol-Gel (2) Combustion and (3) Solid-state reaction method.

S.No.	Sample ID	CIE-coordinates
1	$Zn_4B_6O_{13}:Eu^{3+}$ (Sol-gel)	(0.642, 0.353)
2	$Zn_4B_6O_{13}:Eu^{3+}$ (Combustion)	(0.641, 0.352)
3	$Zn_4B_6O_{13}:Eu^{3+}$ (Solid state)	(0.644, 0.354)

UNIVERSITY of the
WESTERN CAPE

5.3 Conclusion

Eu^{3+} doped $\text{Zn}_4\text{B}_6\text{O}_{13}$ phosphors were successfully prepared by the sol-gel, combustion, and solid-state synthesis methods. The XRD results confirm the cubic structure of $\text{Zn}_4\text{B}_6\text{O}_{13}:\text{Eu}^{3+}$ in all synthesis methods. The incorporation of Eu^{3+} into $\text{Zn}_4\text{B}_6\text{O}_{13}$ phosphors did not affect the crystal structure of the sample. Hexagonal, cubic, and some irregular agglomerated morphologies were observed in SEM images. At 900 °C annealing temperature caused some particles to be more adherent. The prepared samples were excited at different wavelengths of 246 and 395 nm. The PL emissions spectra show characteristic emissions of Eu^{3+} from its $^5\text{D}_0$ level to $^7\text{F}_j$ where $j = 1, 2, 3,$ and 4 . The high-intensity peak was observed at 615 nm for both excitation wavelength. The fastest average lifetime decay was observed for 395 nm excitation. The sol-gel method produced $\text{Zn}_4\text{B}_6\text{O}_{13}:\text{Eu}^{3+}$ phosphor with the fastest average lifetime decay in both excitation wavelengths of 246 and 395 nm compared to the solid-state and combustion methods. The CIE chromaticity diagram revealed that all the prepared $\text{Zn}_4\text{B}_6\text{O}_{13}:\text{Eu}^{3+}$ phosphors produced red colour emissions. All Eu^{3+} doped $\text{Zn}_4\text{B}_6\text{O}_{13}$ phosphors show excellent emission properties to be used for the fabrication of tunable-red LEDs.



Chapter VI

Impact of different various chemical techniques on the structural and photoluminescence properties of $\text{Zn}_4\text{B}_6\text{O}_{13}:\text{Dy}^{3+}$ nanophosphors

6.1 Introduction

Luminescence is an optical phenomenon for the emission of light [266]. The current trend for producing luminescence phosphors with high efficiency and with lower power consumption that are long-lasting is still an ongoing research process [267], [268]. Moreover, luminescent phosphors play an important role in the manufacturing of solid-state lamps, mostly in the form of light-emitting diodes (LEDs). Zinc borate ($\text{Zn}_4\text{B}_6\text{O}_{13}$) is of great interest in this study as a host due to its photoluminescence properties, afterglow effects, and high chemical and thermal stability. Furthermore, these materials have caught the attention of researchers in fabricating luminescent materials [254], [269]. Numerous studies have been reported on the synthesis of $\text{Zn}_4\text{B}_6\text{O}_{13}$ doped with various rare earth ions for solid-state lighting. Meijerink et al. [270] reported on the synthesis of $\text{Zn}_4\text{B}_6\text{O}_{13}$ using the solid-state method for the investigation of photoluminescence and thermoluminescence properties. Chen et al. [224] studied the luminescence characteristics of $\text{Zn}_4\text{B}_6\text{O}_{13}:\text{Mn}^{2+}$ phosphor materials. This research focuses on the investigation of the synthesis methods that will produce the best photoluminescent phosphors that will contribute to solid-state lighting applications. The combustion, solid-state, and sol-gel methods are used for the preparation of $\text{Zn}_4\text{B}_6\text{O}_{13}$ compounds. The research on Dy^{3+} dopants is significant, as it is known for enhancing photoluminescence emission characteristics in the white colour light region. Moreover, this dopant is responsible for producing colour emissions within the regions blue (470→500 nm), yellow (570→600 nm), and red (650→680 nm), which are ascribed to the fundamental transitions $^4\text{F}_{9/2}\rightarrow^6\text{H}_{15/2}$, $^4\text{F}_{9/2}\rightarrow^6\text{H}_{13/2}$, and $^4\text{F}_{9/2}\rightarrow^6\text{H}_{11/2}$, respectively [105], [224], [271]. The Dy^{3+} ions have 4f electron abundance, which is capable of absorbing light within the ultra-violet region. Furthermore, its 5d – 4f transitions are responsible for the fluorescence properties of Dy^{3+} ions [168], such as the intense emission peak at the $^4\text{F}_{9/2}\rightarrow^6\text{H}_{13/2}$ position, which corresponds to an electric dipole transition of Dy^{3+} ions.

6.2 Results and discussion

6.2.1 X-ray diffraction studies

Figure 6.1 (a) – (d) shows the X-ray diffraction patterns of the $\text{Zn}_4\text{B}_6\text{O}_{13}: 1 \text{ mol}\% \text{Dy}^{3+}$ phosphors prepared by the following methods: combustion, sol-gel, and solid-state, along with the standard background data (JCPDS No: 01-076-0917) of the $\text{Zn}_4\text{B}_6\text{O}_{13}$, respectively. The XRD patterns show that the diffraction peaks for all samples were detected around 2θ angles of 25° , 30° , 39° , 46° , 49° , 53° , 59° , 62° , 65° , 69° , 72° , 75° , 77° , and 79° . Furthermore, their crystal phases are indexed as follows: (200), (211), (310), (321), (400), (330), (420), (422), (510), (521), (440), (433), (600), and (532), respectively. The obtained results are well matched with the standard PDF data file JCPDS No: 01-076-0917, which confirms a cubic crystal structure with the space group of I-43m. The calculated lattice parameters for **Figure 6.1 (a)** are $a = b = c = 7.47730 \text{ \AA}$ and $\alpha = \beta = \gamma = 90^\circ$, resulting in a cell volume of 418.06 \AA^3 .

Figure 6.1 (b) shows the XRD spectrum of the $\text{Zn}_4\text{B}_6\text{O}_{13}: \text{Dy}^{3+}$ phosphor material, prepared by the sol-gel method. The diffraction peaks obtained for this method were similar to those of the combustion method reported in **Figure 6.1 (a)**, except for the changes in the lattice parameters, which are as follows: $a = b = c = 7.47773 \text{ \AA}$ and $\alpha = \beta = \gamma = 90^\circ$, with a lattice volume of 418.13 \AA^3 . The diffraction peaks for the solid-state method in **Figure 6.1 (c)** were also determined in similar way as was previously reported for the combustion and solid-state methods, except for the changes in the lattice parameters, calculated as follows $a = b = c = 7.47773 \text{ \AA}$ and $\alpha = \beta = \gamma = 90^\circ$ with a lattice volume of 417.80 \AA^3 .

The diffraction peaks for $\text{Zn}_4\text{B}_6\text{O}_{13}:\text{Dy}^{3+}$ phosphors prepared in **Figure 6.1 (a – c)** are consistent with the cubic structure of $\text{Zn}_4\text{B}_6\text{O}_{13}$ (JCPDS No: 01-076-0917). However, there is a slight deviation of the XRD peaks to higher values of 2θ , which are associated with the presence of the dopant. Moreover, the shift is attributed to the successful substitution of Zn^{2+} ions by Dy^{3+} in the host lattice [272], [273]. The overall slight decrease in the intensity of the diffraction peaks is associated with the addition of Dy^{3+} ions to the host [135], [256], [272], [273], [274], [275]. The combustion and sol-gel methods showed weak XRD intensity peaks compared to the solid-state method; this is due to their low crystallite sizes, as depicted in

Table 6.1. In conclusion, doping with Dy^{3+} did not change the cubic structure, which confirms the well-distribution of the Dy^{3+} ions into the $\text{Zn}_4\text{B}_6\text{O}_{13}$ host lattice.

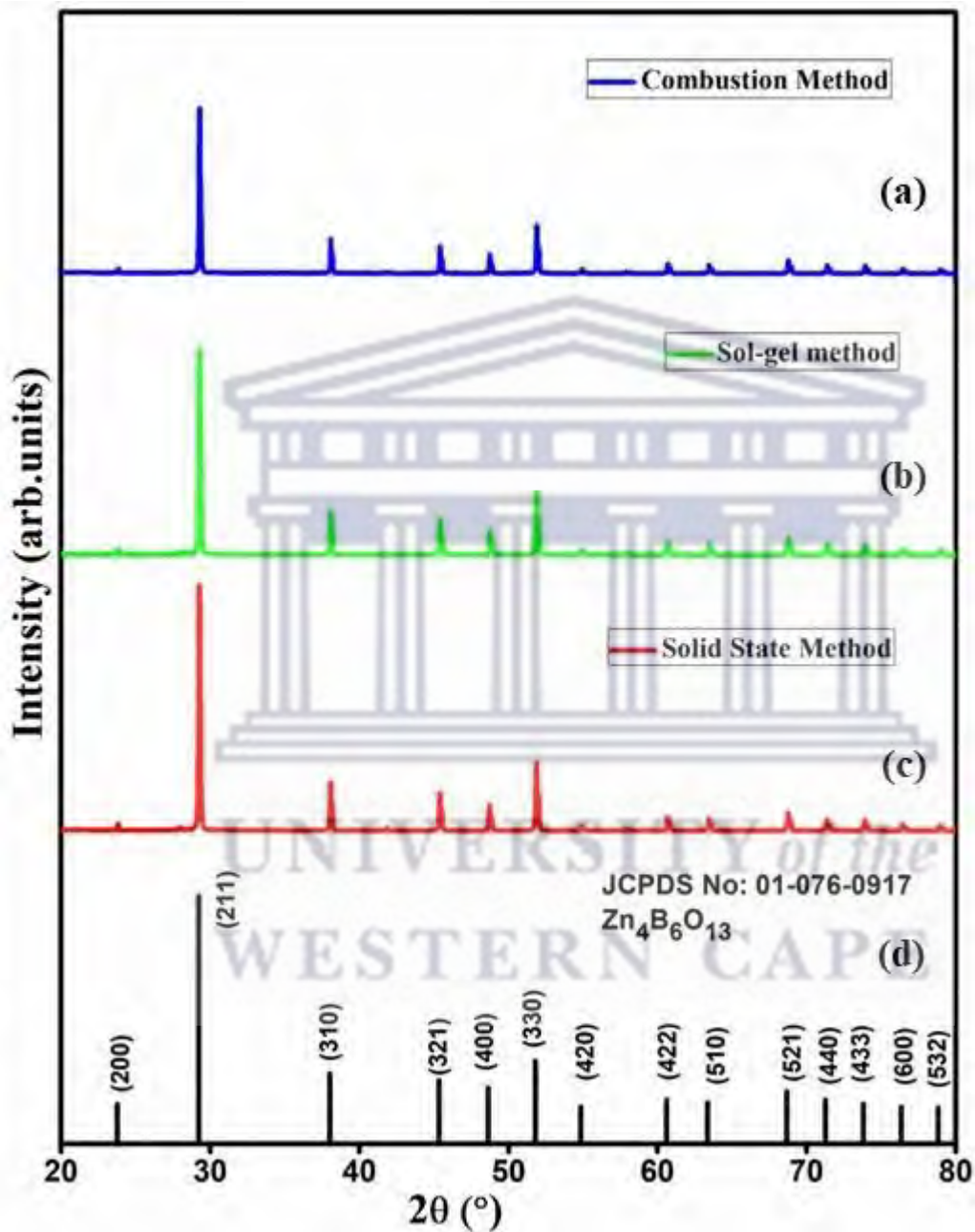


Figure 6.1. The full XRD patterns of $\text{Zn}_4\text{B}_6\text{O}_{13}:x\text{Dy}^{3+}$ (where $x = 0, 1\%$) nanophosphors prepared by various chemical techniques: (a) Sol-Gel (b) Combustion (c) Solid-state reaction method.

The crystallite sizes of the prepared $Zn_4B_6O_{13}:Dy^{3+}$ phosphors were calculated using the Debye-Scherrer equation (4.1) presented in Chapter IV. **Table 6.1 (1 – 3)** shows the calculated crystallite sizes for $Zn_4B_6O_{13}:Dy^{3+}$ prepared with sol-gel, combustion, and solid-state methods, respectively. The calculated crystallite sizes were found to follow the following trend: solid-state (99 nm) > sol-gel (89 nm) > combustion (80 nm).

Table 6.1. Crystallite size of $Zn_4B_6O_{13}:xDy^{3+}$ (where $x = 0, 1\%$) nanophosphors prepared by various chemical techniques: (1) Sol-Gel (2) Combustion and (3) Solid-state reaction method.

S.No	Sample	Crystallite size (nm)
1	$Zn_4B_6O_{13}:Dy^{3+}$ (Sol-gel)	89
2	$Zn_4B_6O_{13}:Dy^{3+}$ (Combustion)	80
3	$Zn_4B_6O_{13}:Dy^{3+}$ (Solid state)	99

6.2.2 Surface morphology studies and elemental analysis

The morphology and elemental analysis of the prepared sample were examined through scanning electron microscopy (SEM) and energy dispersive X-ray spectroscopy (EDS), respectively. **Figure 6.2** depicts the SEM and EDS micrographs for the $Zn_4B_6O_{13}:Dy^{3+}$ synthesized with (a) and (d) sol-gel, (b) and (e) combustion, and (c) and (f) solid-state methods, respectively. The inserts in (d-f) depict the elemental mapping for the used precursors. **Figure 6.2 (a)** shows a combination of crystalline and smooth-like particles with heterogeneous morphologies. The calculated average particle size from Image J software is 2200 nm, and it is shown in histogram **Figure 6.3 (b)**.

Figure 6.2 (b) depicts particles with heterogeneous morphologies, such as cubic, spherical, and hexagonal, prepared by the combustion method. The heterogeneous morphology shows

that the Dy^{3+} ions had an impact on the morphological properties of $\text{Zn}_4\text{B}_6\text{O}_{13}$ phosphor. The calculated average particle size is 790 nm, as depicted in **Figure 6.3 (a)**.

The $\text{Zn}_4\text{B}_6\text{O}_{13}:\text{Dy}^{3+}$ phosphors depicted in **Figure 6.2 (c)** were synthesized by the solid-state reaction method. There are large agglomerated and adhered particles with an average size of 2100 nm, are depicted in **Figure 6.3 (c)**, reflecting a hexagonal and cubic morphological structure. These images show that doping with Dy^{3+} affected the morphology of the host material.

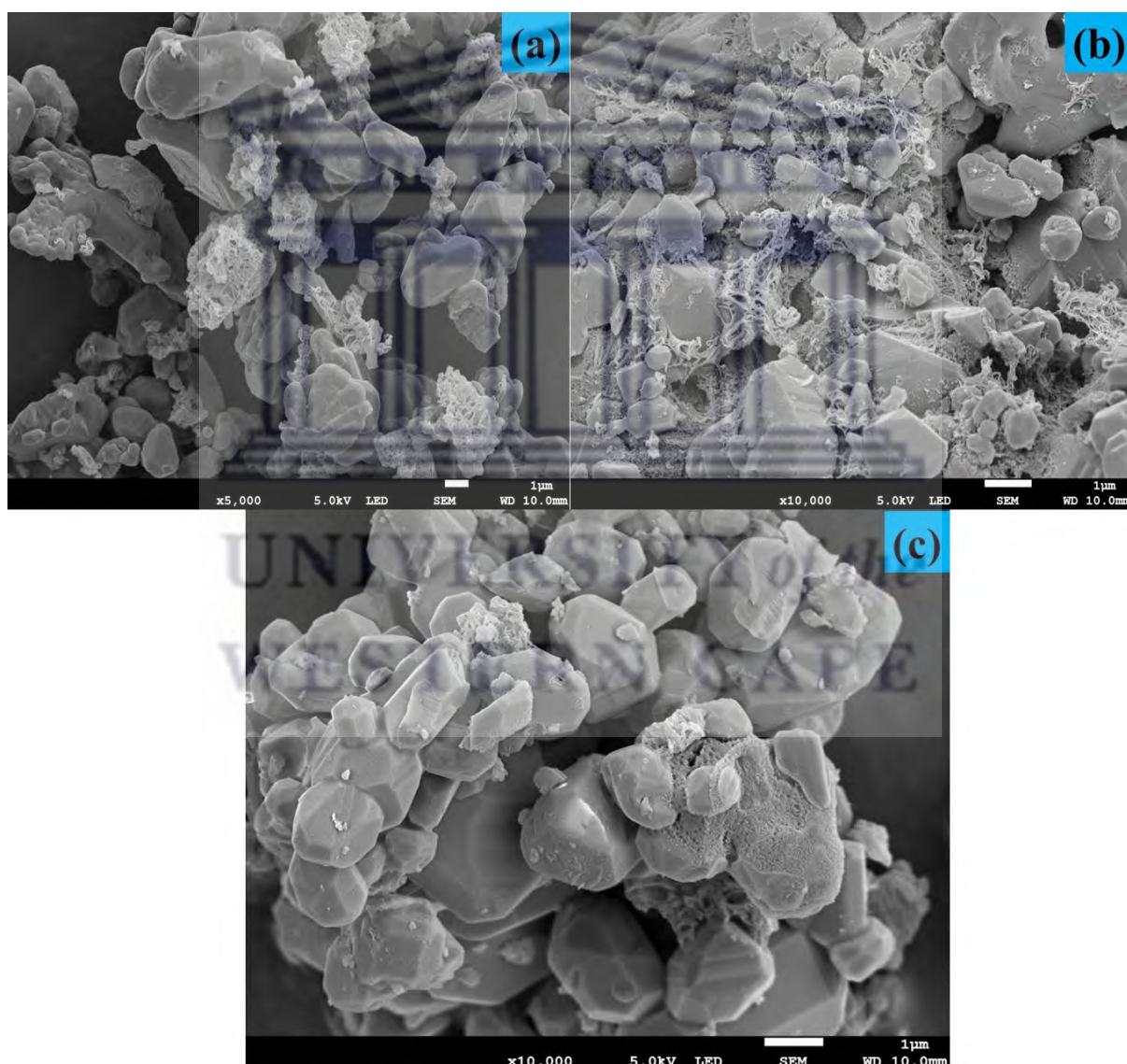


Figure 6.2: Field-emission scanning electron microscopy (FE-SEM) images of $\text{Zn}_4\text{B}_6\text{O}_{13}:\text{x}\text{Dy}^{3+}$ (where $x = 0, 1\%$) nanophosphors prepared by various chemical techniques: (a) Sol-Gel (b), Combustion, and (c) Solid-state reaction methods.

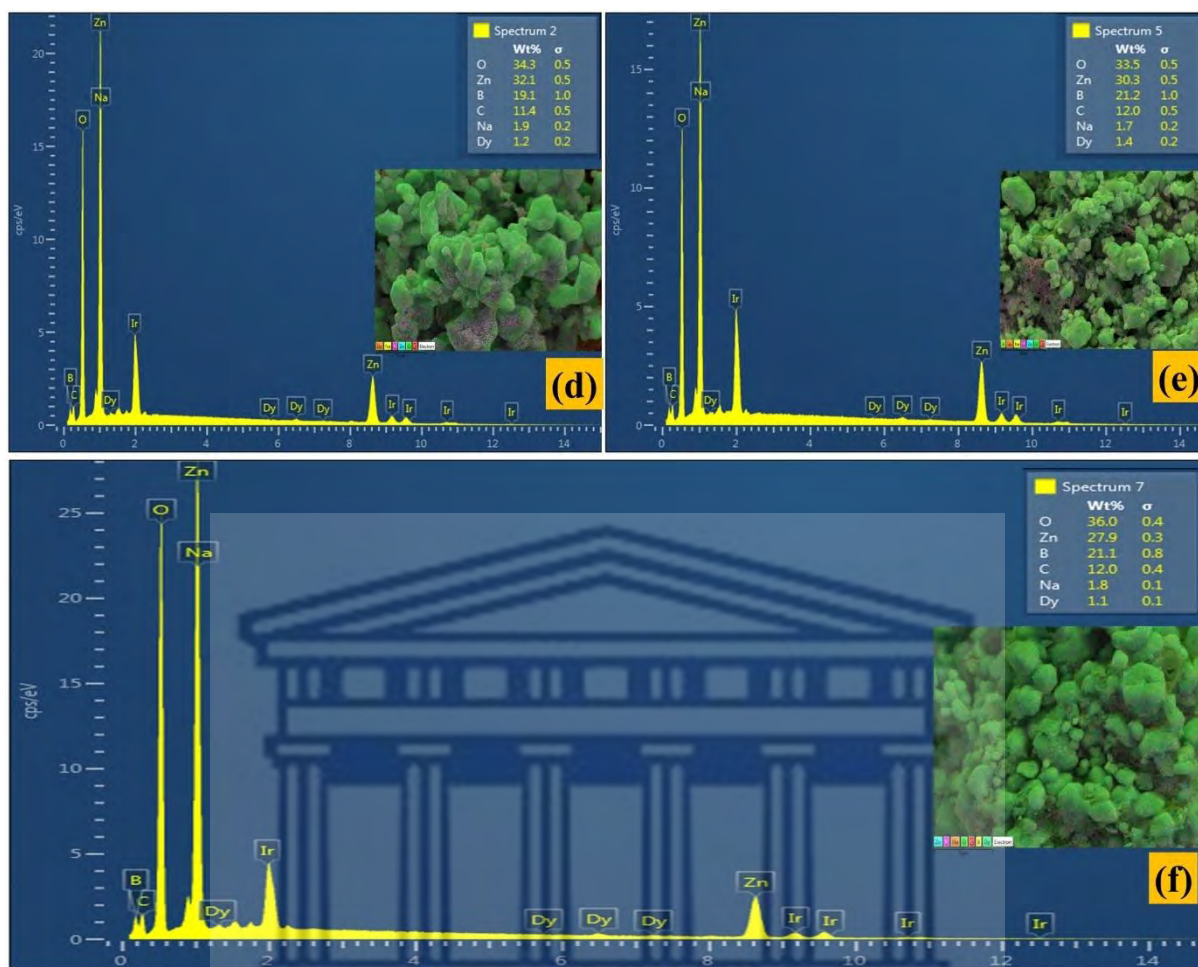


Figure 6.2: Elemental Dispersive Spectroscopy (EDS) and elemental mapping images of Zn₄B₆O₁₃:xDy³⁺ (where x = 0, 1%) nanophosphors prepared by various chemical techniques: (d) Sol-Gel, (e) Combustion, and (f) Solid-state reaction method.

The EDS spectra in **Figure 6.2** (e – f) confirm all the elements that were used for the preparation of Zn₄B₆O₁₃:Dy³⁺. These elements are dysprosium (Dy), zinc (Zn), oxygen (O), boron (B), sodium (Na), and carbon (C). The detection of carbon impurities is due to the carbon tape that was used to mount the sample during analysis. In addition to this, iridium was used as a coating agent before characterization; thereby, iridium spikes are present in the EDS spectra. The elemental images (inserts) show a uniform distribution of the precursors used. The average particle sizes of the Zn₄B₆O₁₃:Dy³⁺ phosphor were obtained in the following manner: combustion method (2200 nm) > solid-state method (2100 nm) > sol-gel (790 nm).

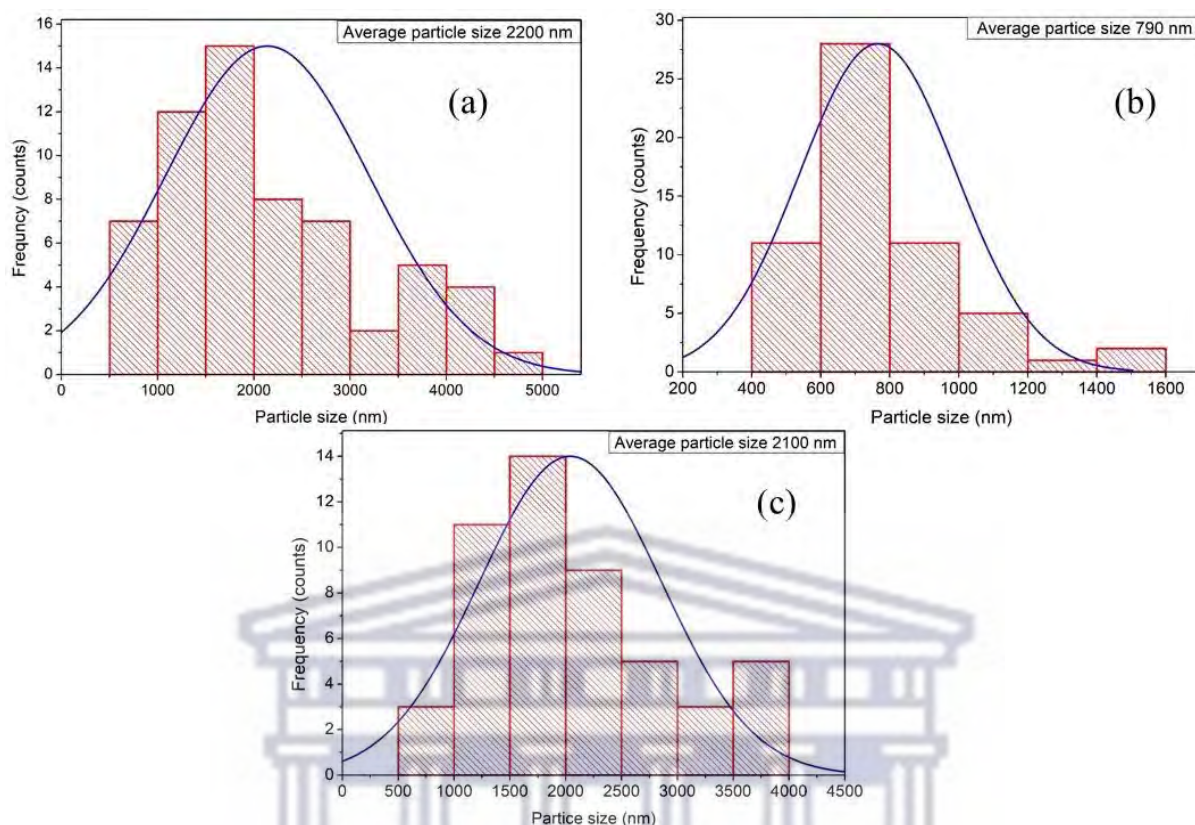


Figure 6.3 Histograms displaying the average particle size distribution of $Zn_4B_6O_{13}:Dy^{3+}$ nanophosphors prepared with (a) combustion, (b) sol-gel, and (c) solid-state methods.

6.2.3 Fourier Transform Infrared (FT-IR) analysis.

The FTIR spectra for the $Zn_4B_6O_{13}$ host and $Zn_4B_6O_{13}:xDy^{3+}$ (where $x = 1$ mol%) phosphor prepared with different techniques such as sol-gel, combustion, and solid-state methods are shown in **Figure 6.4**. The samples were characterized at room temperature, and their spectra were recorded within the wave number range of $400 - 4000\text{ cm}^{-1}$. In all spectra, the sharp absorption band within the 480 cm^{-1} regions for all phosphors are due to the stretching modes of Zn-O vibrations. The intense and broad absorption bands within $600 - 900\text{ cm}^{-1}$ regions confirm the BO_3 and BO_4 vibrational bands, respectively; these are due to the meta-borate transition within the host [257], [258]. The additional IR bands within $600 - 1000\text{ cm}^{-1}$ region are due to BO_3 symmetric modes. The structural vibration bands observed in the 1100 cm^{-1} region are ascribed to the fundamental bending modes of water molecules that were used during sample preparation. Similarly, weak vibrational bands are observed within 3250 cm^{-1} regions, which are attributed to the stretching modes of water molecules as well as the atmospheric

hydroxyl groups [276]. Doped $Zn_4B_6O_{13}:Dy^{3+}$ materials show an increase in the absorption bands, clearly observed for the combustion and solid-state methods. Doping with Dy^{3+} resulted in strong absorption bands in the phosphors prepared with the combustion and solid-state methods, whereas there was a weakening of absorption bands in the sol-gel method.

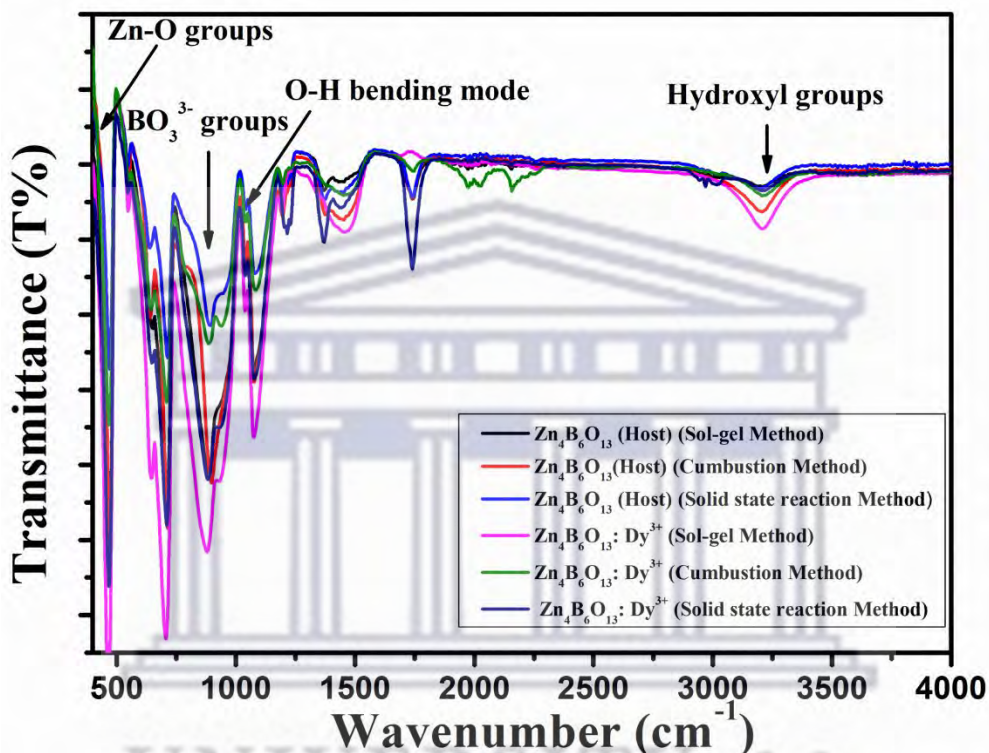


Figure 6.4: FT-IR spectra of $Zn_4B_6O_{13}:xDy^{3+}$ (where $x = 0, 1\%$) nanophosphors prepared by various chemical techniques: (a) Sol-Gel (b) Combustion (c) Solid-state reaction method.

6.2.4 UV-VIS and band gap measurements

Figure 6.5 shows the ultra-violet visible (UV-Vis) spectra of the $\text{Zn}_4\text{B}_6\text{O}_{13}$ host and $\text{Zn}_4\text{B}_6\text{O}_{13}:\text{Dy}^{3+}$ phosphors prepared with different synthesis techniques such as sol-gel, combustion, and solid-state methods, recorded within 200 – 2000 nm spectral range. Compared to the host, doped materials showed an overall increase in reflectance for all the prepared phosphors. However, there are weak absorption bands related to $4f^9 - 4f^9$ intra-configurational transitions of Dy^{3+} ions. There is an intense absorption band within the 200 nm region, which is ascribed to the electron transition within the Zn-O bonds [277], [278]. The different optical behaviour observed in sol-gel compared to other methods is due to the high agglomeration of large particles, low annealing temperature which resulted in not removing all impurities, and low photo luminescence emission compared to other methods [238]. The mentioned factors result in inability to react to light compared to other methods in the ultraviolet and visible regions. The obtained absorption peaks were observed at the following wavelengths: 300, 390, 800, 900, 1100, 1300, 1420, and 1610 nm are associated with the fundamental transition modes from the ground state to higher excited states, viz., ${}^6\text{H}_{15/2} \rightarrow {}^4\text{K}_{13/2}$, ${}^6\text{H}_{15/2} \rightarrow {}^6\text{P}_{7/2}$, ${}^6\text{H}_{15/2} \rightarrow {}^5\text{F}_{5/2}$, ${}^6\text{H}_{15/2} \rightarrow {}^6\text{F}_{7/2}$, ${}^6\text{H}_{15/2} \rightarrow {}^6\text{F}_{9/2}$, ${}^6\text{H}_{15/2} \rightarrow {}^6\text{F}_{11/2}$, ${}^6\text{H}_{15/2} \rightarrow {}^6\text{H}_{9/2}$, and ${}^6\text{H}_{15/2} \rightarrow {}^6\text{H}_{11/2}$, respectively. These bands are the characteristic $4f - 4f$ fundamental transitions of Dy^{3+} ions [279].

UNIVERSITY of the
WESTERN CAPE

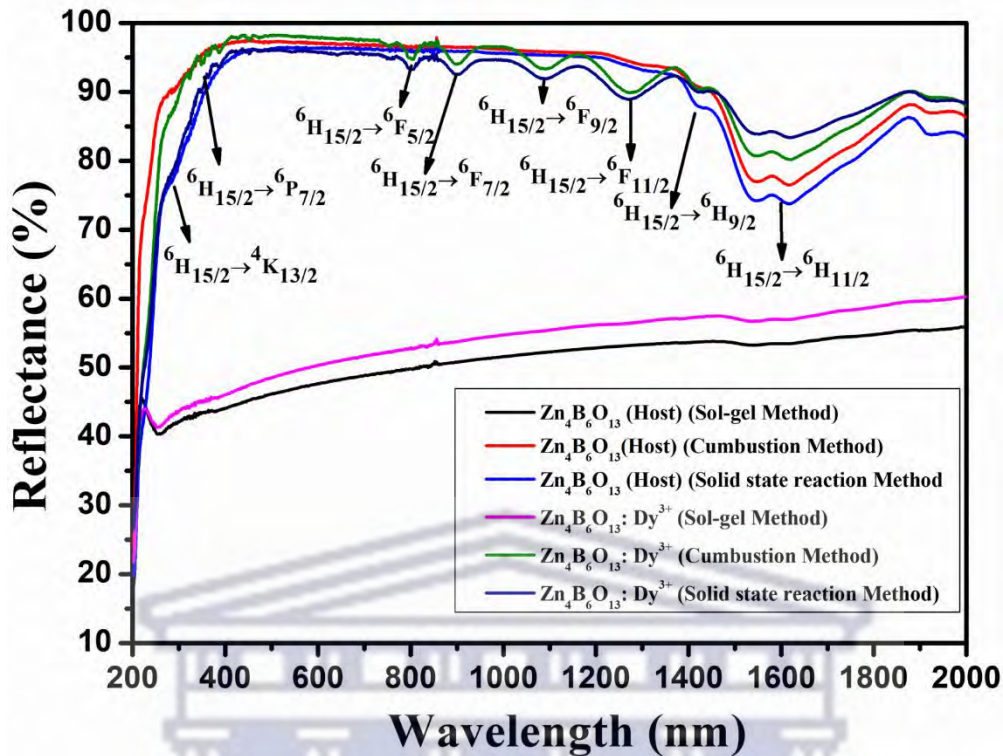


Figure 6.5. UV-Vis DRS spectra of $Zn_4B_6O_{13}:xDy^{3+}$ (where $x = 0, 1\%$) nanophosphors prepared by various chemical techniques: (a) Sol-Gel (b) Combustion (c) Solid-state reaction method.

The diffuse reflectance (DRS) data of the prepared phosphors were used for the estimation of the optical bandgap through the Kubelka-Munk (K-M) (equation 4.2) [168], [244]. Using the optical data, the Tauc's graphs were plotted with the $[F(R_{\infty})hv]^2$ function vs photon energy, (equation 4.3) presented in chapter IV, respectively. Figure 6.6 shows the band-gap values obtained through the sol-gel, combustion, and solid-state reaction methods. Table 6.2 shows the extrapolated optical band-gap values obtained from Figure 6.6 for $Zn_4B_6O_{13}$ and $Zn_4B_6O_{13}:Dy^{3+}$ phosphors. The bandgap is very close to the one reported in the literature (5.73 eV). There is a decrease in the energy band gap after doping with Dy^{3+} in all samples. The profile shows the following decreases: sol-gel (5.899 \rightarrow 5.882 eV), combustion (5.948 \rightarrow 5.834 eV), and solid-state methods (5.865 \rightarrow 5.846 eV). The decrease in the bandgap is attributed to the defect's formation of $Zn_4B_6O_{13}$ phosphors after Dy^{3+} is incorporated within the host bandgap.

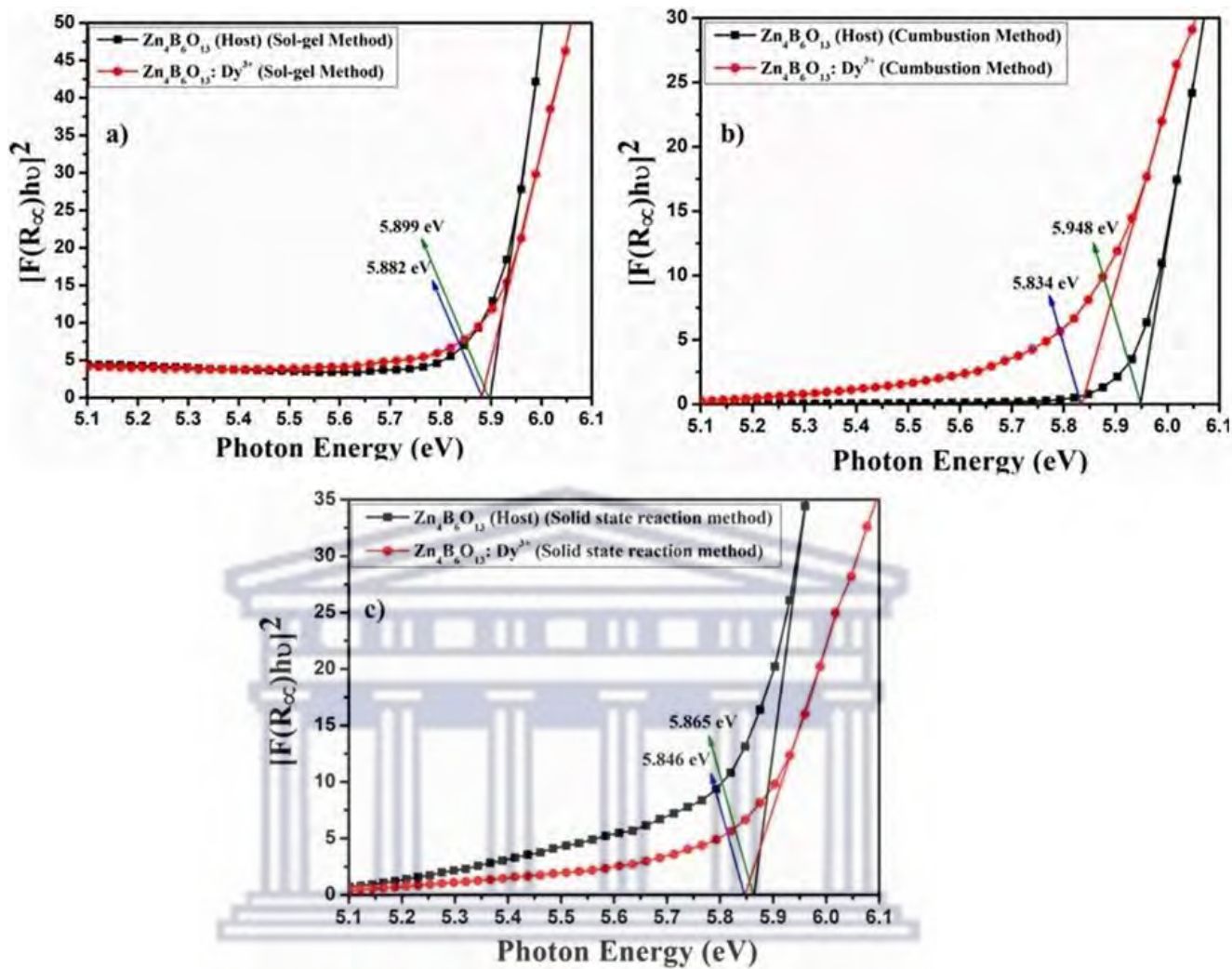


Figure. 6.6. Optical bandgap calculations of $Zn_4B_6O_{13}:xDy^{3+}$ (where $x = 0, 1\%$) nanophosphors prepared by various chemical techniques: (a) Sol-Gel (b) Combustion (c) Solid-state reaction method. The line represents the best linear fit to determine the energy band gap.

Table 6.2. Optical bandgap values of the $Zn_4B_6O_{13}:xDy^{3+}$ (where $x = 0, 1\%$) nanophosphors prepared by various chemical techniques: (1,2) Sol-Gel (3,4) Combustion (5,6) Solid-state reaction method.

S.No	Sample ID	Energy bandgap (eV)
1	$Zn_4B_6O_{13}$ (Sol-gel)	5.899
2	$Zn_4B_6O_{13}:Dy^{3+}$ (Sol-gel)	5.882
3	$Zn_4B_6O_{13}$ (Combustion)	5.948
4	$Zn_4B_6O_{13}:Dy^{3+}$ (Combustion)	5.834
5	$Zn_4B_6O_{13}$ (Solid state)	5.865
6	$Zn_4B_6O_{13}:Dy^{3+}$ (Solid state)	5.846

6.2.5 Photoluminescence excitation and emission spectra measurements

Figure 6.7 (a) and **(b)** show the photoluminescence excitation (PLE) spectra of the $Zn_4B_6O_{13}:Dy^{3+}$ phosphors synthesized with various techniques such as sol-gel, combustion, and solid-state methods. These PLE spectra were recorded within the full length-range of 200 – 500 nm and highlighted in the range of 280 -500 nm, while monitoring the high-intensity emission peak of ${}^7F_{9/2} \rightarrow {}^6H_{13/2}$ at a wavelength of 586 nm. The prepared samples comprised different excitation peaks at 348, 352, 385, 448, and 460 nm, which are attributed to the following Dy^{3+} f-f transitions: ${}^6H_{15/2} \rightarrow {}^6F_{7/2}$, ${}^6H_{15/2} \rightarrow {}^4I_{11/2}$, ${}^6H_{15/2} \rightarrow {}^4I_{13/2}$, ${}^6H_{15/2} \rightarrow {}^4I_{5/2}$, and ${}^6H_{15/2} \rightarrow {}^4F_{9/2}$, respectively. The solid-state method possesses the highest intensity peaks compared to sol-gel and combustion methods. The intense charge transfer band (CTB) peak located at 228 nm is ascribed to the oxygen (O^{2-}) and Dy^{3+} interactions, which are associated with electron transfer from the 2p orbit to the 4f shell in $Zn_4B_6O_{13}$ phosphors [168].

Figure 6.7 (c) shows the emission spectra of the $Zn_4B_6O_{13}:Dy^{3+}$ phosphors recorded using an excitation source at a 228 nm wavelength. The emission spectra consist of four sharp, distinct

emission bands at 586, 490, 670, and 760 nm. The emission band detected at 490 nm is ascribed to the blue emission, which is due to the ${}^4F_{9/2} \rightarrow {}^6H_{15/2}$ magnetic dipole transition. Moreover, the discrepancy among the intensity peaks from different methods is due to the crystal field strength around the Dy^{3+} ion [146], [244]. The highest emission peak detected at 586 nm wavelength is due to the electric dipole transition ${}^4F_{9/2} \rightarrow {}^6H_{13/2}$ which corresponds to a yellow emission. Furthermore, this emission peak is acknowledged at low symmetries without inversion centres. The low-intensity broad band at the 670 nm wavelength confirms a red emission due to the fundamental characteristics of the ${}^4F_{9/2} \rightarrow {}^6H_{11/2}$ transition of Dy^{3+} ions. The low-intensity emission peak detected at 760 nm wavelength is ascribed to the ${}^4F_{9/2} \rightarrow {}^6H_{9/2}$ transition [280].

Figure 6.7 (d) shows the emission spectra of the prepared samples using another excitation wavelength of 352 nm. Similar emission peaks were detected at the wavelengths of 490, 586, 675, and 715 nm, which are due to the following transitions: ${}^6H_{15/2} \rightarrow {}^6H_j$ (where $j = 15/2, 13/2, 11/2,$ and $9/2$), respectively. The solid-state method produced the highest emission properties, followed by the sol-gel method, and lastly, the combustion method. This trend is similar to the one reported in **Figure 6.7 (c)**. The solid-state reaction method showed the highest PL intensity peaks in both emission spectra **Figure 6.7 (c)** and **(d)**, which implies effective energy transfer from the host to the dopant. The poor emission peaks in the combustion method might be due to poor dipole-dipole interactions within the host and a dopant [168].

UNIVERSITY of the
WESTERN CAPE

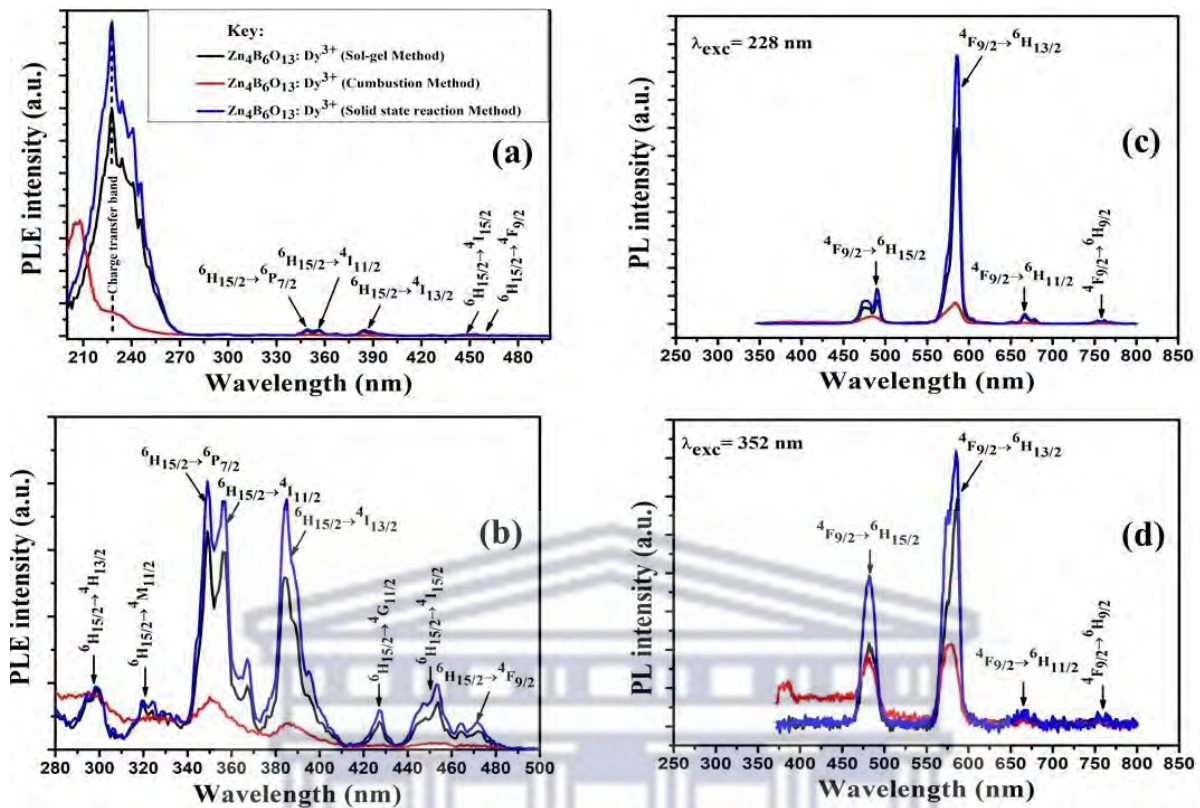


Figure 6.7. (a), (b) Photoluminescence excitation and (c), (d) emission spectra of $Zn_4B_6O_{13}:xDy^{3+}$ (where $x = 0, 1\%$) nanophosphors prepared by various chemical techniques: (1) Sol-Gel (2) Combustion (3) Solid-state reaction method using the parameters of $\lambda_{emi} = 534$ nm and $\lambda_{exc} = 228, 356$ nm wavelengths.

6.2.6 Lifetime decay measurements

The lifetime decay curves of $Zn_4B_6O_{13}:xDy^{3+}$ (where $x = 1$ mol%) phosphor were measured using different synthesis techniques such as sol-gel, combustion, and solid-state methods, as shown in **Figure 6.8**. These samples were excited using the 228 nm wavelength, while monitoring the emission peak at the 558 nm wavelength. These curves were fitted to a second order exponential equation [246], [281], as explained in chapters 4 and 5.

The average decay time measurements for the prepared $Zn_4B_6O_{13}:Dy^{3+}$ phosphor materials fall within 247 – 347 milliseconds (ms) range, as tabulated in **Table 6.3**. The $Zn_4B_6O_{13}:Dy^{3+}$

phosphor prepared by the sol-gel method showed the shortest lifetime of 347 ms, compared to the other methods, namely, combustion (347 ms) and solid-state (353 ms) methods.

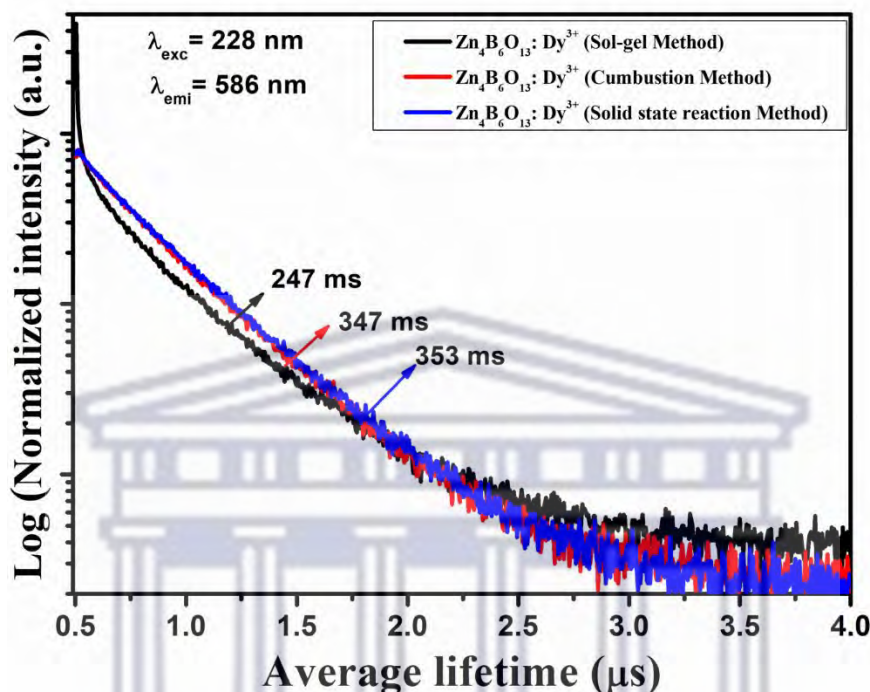


Figure 6.8. Lifetime decay profiles of $Zn_4B_6O_{13}:xDy^{3+}$ (where $x = 0, 1\%$) nanophosphors prepared by various chemical techniques: (a) Sol-Gel (b) Combustion (c) Solid-state reaction method using the parameters of $\lambda_{emi} = 536 \text{ nm}$ and $\lambda_{exc} = 228 \text{ nm}$ wavelengths.

Similarly, the extended lifetime decay measurements of $Zn_4B_6O_{13}:Dy^{3+}$ were followed up with another excitation source of 352 nm wavelength for the same emission peak monitored in earlier plots, as shown in **Figure 6.9**. The lifetime decay values for these prepared samples, namely, sol-gel, solid-state, and combustion methods, were calculated using the double exponential function and found to be 195, 314, and 352 ms, respectively. The lifetime decay values for sol-gel and solid-state methods obtained at an excitation wavelength of 353 nm are lower than those obtained at an excitation wavelength of 228 nm. However, it is vice versa for the combustion method.

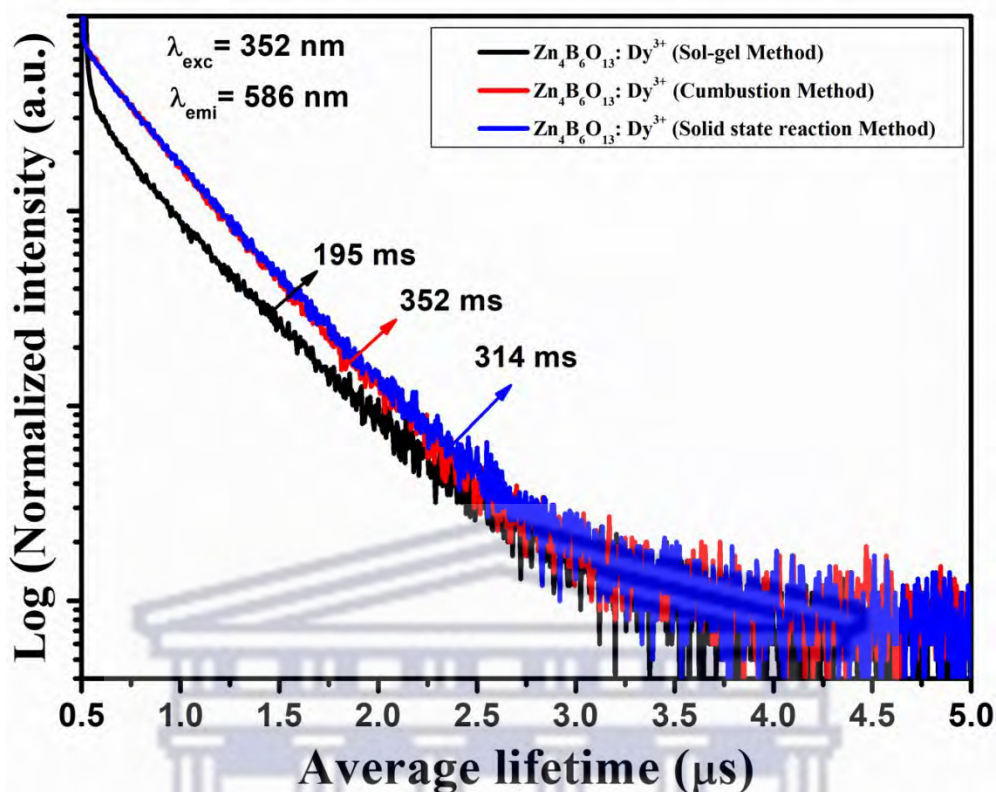


Figure 6.9. Lifetime decay profiles of $Zn_4B_6O_{13}:xEu^{3+}$ (where $x = 0, 1\%$) nanophosphors prepared by various chemical techniques: (a) Sol-Gel (b) Combustion (c) Solid-state reaction method using the parameters of $\lambda_{emi} = 614\text{ nm}$ and $\lambda_{exc} = 395\text{ nm}$ wavelengths.

Table 6.3. Average lifetime decay values of $Zn_4B_6O_{13}:1\%Dy^{3+}$ nanophosphors prepared by various chemical techniques: (1) Sol-Gel (2) Combustion and (3) Solid-state reaction method.

S.No.	Sample ID	Average lifetime (ms)
1	$Zn_4B_6O_{13}:Dy^{3+}$ (Sol-gel)	195
2	$Zn_4B_6O_{13}:Dy^{3+}$ (Combustion)	352
3	$Zn_4B_6O_{13}:Dy^{3+}$ (Solid state)	314

6.2.7 CIE color coordinates

The Commission Internationale de l'Eclairage chromaticity (CIE) colour diagram for the $\text{Zn}_4\text{B}_6\text{O}_{13}:\text{Dy}^{3+}$ ($x = 1$ mol%) phosphor prepared using sol-gel, combustion, and solid-state methods are shown in **Figure 6.10**. The CIE coordinates (x, y) are calculated by using the PL data measured with the 352 nm excitation wavelength, while monitoring its emission peak at the 586 nm wavelength. The obtained CIE colour coordinates are as follows: (0.432, 0.410), (0.296, 0.291), and (0.406, 0.404) for the sol-gel method, combustion method, and solid-state method, respectively, as tabulated in **Table 6.4**. Amongst all synthesis methods, the combustion method falls within the blue-white region (a combination of blue and yellow light), whereas the sol-gel and solid-state methods produced phosphors with orange-yellow emissions, respectively. From the results, it is noticed that the $\text{Zn}_4\text{B}_6\text{O}_{13}:\text{Dy}^{3+}$ phosphor prepared by the sol-gel method has potential for blue light-emitting diode applications, while those prepared with solid-state and combustion methods has potential for orange-yellow light-emitting diode applications.

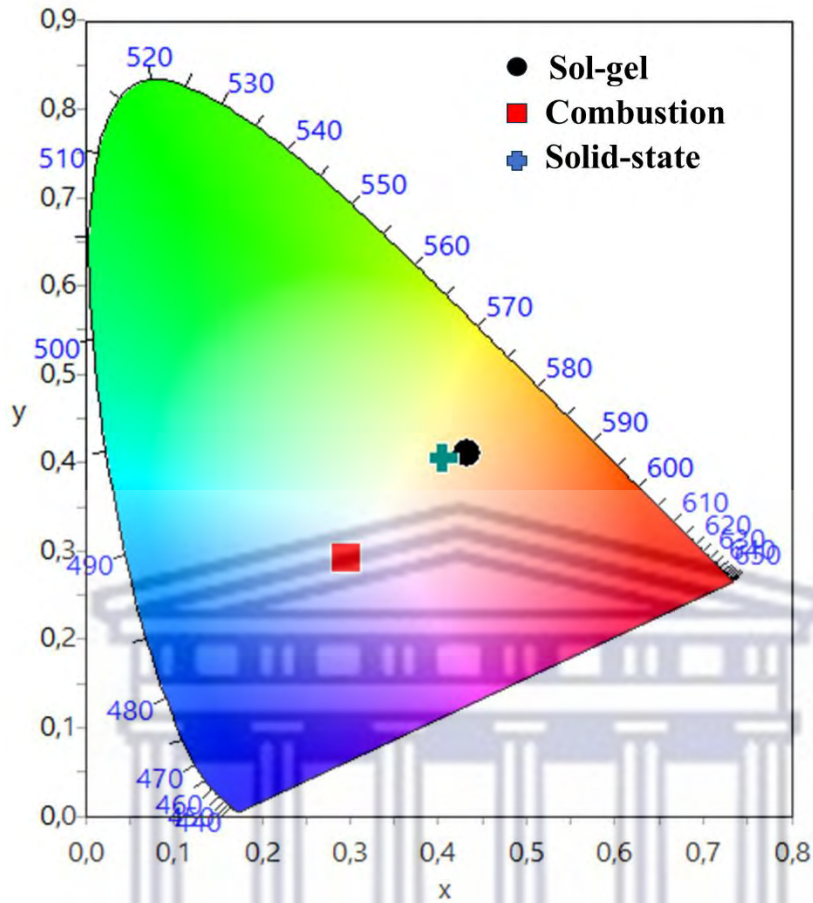


Figure 6.10. CIE colour diagram of $Zn_4B_6O_{13}:xDy^{3+}$ (where $x = 0, 1\%$) nanophosphors prepared by various chemical techniques: (a) Sol-Gel (b) Combustion (c) Solid-state reaction method.

UNIVERSITY of the
WESTERN CAPE

Table 6.4. CIE color co-ordinates of $Zn_4B_6O_{13}:xDy^{3+}$ (where $x = 0, 1\%$) nanophosphors prepared by various chemical techniques: (1) Sol-Gel (2) Combustion and (3) Solid-state reaction method.

S.No.	Sample ID	CIE-coordinates
1	$Zn_4B_6O_{13}:Dy^{3+}$ (Sol-gel)	(0.432, 0.410)
2	$Zn_4B_6O_{13}:Dy^{3+}$ (Combustion)	(0.296, 0.291)
3	$Zn_4B_6O_{13}:Dy^{3+}$ (Solid state)	(0.406, 0.404)

6.3 Conclusion

The $\text{Zn}_4\text{B}_6\text{O}_{13}:\text{Dy}^{3+}$ phosphors were successfully prepared with different synthesis techniques, such as sol-gel, combustion, and solid-state methods. The aim of this study was to find the best methods that will produce high-luminescence properties via structural, morphological, and photoluminescence measurements. XRD results confirm a cubic structure formation with an average crystallite size of 80 nm. The SEM images reveal that the particles were agglomerated by all methods. The histogram plots confirmed that the sol-gel method produced average particle sizes of 2200 nm. Tauc's plot reveals that the band gap energy values decreased for Dy^{3+} doped samples compared to the $\text{Zn}_4\text{B}_6\text{O}_{13}$ host materials. The photoluminescence characteristic emissions of the Dy^{3+} ions were studied at 228 and 352 nm excitation wavelengths. The highest emission bands were detected at 586 nm wavelength in all methods, which are ascribed to the ${}^4\text{F}_{9/2} \rightarrow {}^6\text{H}_{13/2}$ Dy^{3+} ion transition. The solid-state method showed higher photoluminescence emission properties compared to the other methods at both excitation wavelengths. The fastest-decaying phosphor (195 ms) was obtained through the sol-gel method at an excitation wavelength of 352 nm. The calculated CIE chromaticity colour coordinates indicate that the $\text{Zn}_4\text{B}_6\text{O}_{13}:\text{Dy}^{3+}$ phosphors prepared with the combustion methods were associated with blue-white emissions. The sol-gel and solid-state methods are responsible for the orange-yellow colour emissions, respectively. Based on the results obtained, all the prepared phosphors are potential candidates for white light-emitting diode applications.

Chapter VII

Conclusion

This chapter is divided into three sections: the investigation of the impact of three different techniques such as sol-gel, combustion, and solid-state reaction methods on the structural, morphological, and photoluminescence properties of undoped and doped (i) $\text{Zn}_4\text{B}_6\text{O}_{13}:\text{xSm}^{3+}$, (ii) $\text{Zn}_4\text{B}_6\text{O}_{13}:\text{xEu}^{3+}$, and (iii) $\text{Zn}_4\text{B}_6\text{O}_{13}:\text{xDy}^{3+}$ (where $x = 0$ and 1,0 mol%) phosphor materials. These prepared samples were successfully synthesized at an annealing temperature of 900 °C for two hours. The following discussion is a comparative study of the three different $\text{Zn}_4\text{B}_6\text{O}_{13}:\text{RE}^{3+}$ phosphors (where RE = Sm^{3+} , Eu^{3+} , and Dy^{3+}) materials, using different techniques.

Chapter 4 presents the impacts of the above synthesis methods on the structural, morphological, and photoluminescence properties of $\text{Zn}_4\text{B}_6\text{O}_{13}:\text{Sm}^{3+}$ phosphors. The XRD results indicate that all the $\text{Zn}_4\text{B}_6\text{O}_{13}:\text{Sm}^{3+}$ phosphor materials crystallized into a standard cubic structure of the host without any influence from the Sm^{3+} dopant. The calculated crystallite sizes using the Scherrer method were 61.42, 68.93, and 99.51 nm for sol-gel, combustion, and solid-state methods, respectively. On the SEM analysis, hexagonal-like morphologies were observed in the combustion and solid-state methods, respectively, while the sol-gel methods produced spherical and some irregular morphologies with agglomeration. The photoluminescence emission spectra of $\text{Zn}_4\text{B}_6\text{O}_{13}:\text{Sm}^{3+}$ phosphors were obtained using excitation wavelengths of 226 and 408 nm. The emission spectra show f–f transitions of Sm^{3+} ions in the host materials, with a high intensity emission at 657 nm and a low intensity emission at 619 nm wavelength in all synthesis methods. The emission profiles for all three methods are as follows: combustion method > solid-state method > sol-gel method. However, when Sm^{3+} is excited at a 408 nm wavelength, the sol-gel method produces no emission signals. The CIE chromaticity diagram shows that Sm^{3+} emissions produce orange-coloured emission for the sol-gel method and orange-red emission for both solid-state and combustion methods.

Chapter 5: represent the influence of different synthesis methods such as sol-gel, combustion, and solid-state reaction methods on the structural, morphological, and photoluminescence properties of $\text{Zn}_4\text{B}_6\text{O}_{13}:\text{Eu}^{3+}$ phosphors. The XRD patterns of all the prepared phosphors were perfectly matched with the standard background JCPDS No: 01-076-0917 data, confirming a

cubic structure, which confirms a successful incorporation of the Eu^{3+} ions into the $\text{Zn}_4\text{B}_6\text{O}_{13}$ host material. The SEM results showed a cubic and irregular morphology in the sol-gel method, while spherical and hexagonal structures were observed in the combustion and solid-state reaction methods. The photoluminescence behaviour of Eu^{3+} was studied at excitation wavelengths of 246 and 395 nm, while monitoring the highest emission peak at the 614 nm wavelength. Using the 246 nm excitation wavelength, the sol-gel method produced a high intensity emission peak compared to the other two methods, while for the 395 nm excitation wavelength, the solid-state synthesis method produced the highest intensity emission peak. The CIE chromaticity colour diagram was plotted using PL data, and it was found that the prepared $\text{Zn}_4\text{B}_6\text{O}_{13}:\text{Eu}^{3+}$ phosphors produced red colour emissions in all synthesis techniques.

Chapter 6 represents the effect of sol-gel, combustion, and solid-state methods on the structural, morphological, and photoluminescence properties of $\text{Zn}_4\text{B}_6\text{O}_{13}:\text{Dy}^{3+}$ phosphor materials. The XRD results confirmed that the prepared samples are well matched with the standard background JCPDS No: 01-076-0917 data, confirming a cubic structure in all synthesis methods. It also indicates that the Dy^{3+} ions were successfully incorporated into the host lattice. The calculated crystallite sizes from the Scherrer method were found to be 80.00, 89.00, and 99.00 nm for the combustion, sol-gel, and solid-state reaction methods, respectively. The SEM studies showed that the particles were formed into irregular shapes for samples prepared with the sol-gel method, while the cubic structures were formed for the combustion and solid-state methods, respectively. The photoluminescence properties of $\text{Zn}_4\text{B}_6\text{O}_{13}:\text{Dy}^{3+}$ phosphors were studied using UV excitation wavelengths of 228 and 352 nm while monitoring its intensity emission peak at the 586 nm wavelength. The $\text{Zn}_4\text{B}_6\text{O}_{13}:\text{Dy}^{3+}$ prepared by the solid-state method showed the highest emission peaks compared to the other two methods at both excitation wavelengths, whereas low intensity peaks were observed for the samples prepared by the combustion method. The CIE chromaticity colour diagram showed orange-yellow colour emissions produced by $\text{Zn}_4\text{B}_6\text{O}_{13}:\text{Dy}^{3+}$ phosphors prepared by the sol-gel and solid-state reaction methods. The $\text{Zn}_4\text{B}_6\text{O}_{13}:\text{Dy}^{3+}$ phosphors prepared by the combustion method produced blue-white colour emissions. From all the results, it is evident that the prepared phosphors could be potential candidates for white LED applications.

Bibliography

- [1] W. M. Yen and M. J. Weber, *Inorganic Phosphors: Compositions, Preparation and Optical Properties*. CRC Press, 2004.
- [2] B. Xu *et al.*, ‘Effect of Y:Zn ratio on microstructure and emission of Er³⁺/Yb³⁺ codoped Y₂O₃–ZnO ceramic phosphors’, *J. Rare Earths*, vol. 41, no. 12, pp. 1883–1894, Dec. 2023, doi: 10.1016/j.jre.2023.01.014.
- [3] S. H. Jaafar, M. H. Mohd Zaid, K. A. Matori, Y. Yaakob, and H. M. Mustapha, ‘Synthesis of Eu³⁺-Doped ZnO/Zn₂SiO₄ Composite Phosphor for Potent Optoelectronic Applications’, *Braz. J. Phys.*, vol. 52, no. 1, p. 6, Feb. 2022, doi: 10.1007/s13538-021-01017-z.
- [4] P. Kaur *et al.*, ‘Temperature-dependent characteristics of ZnO phosphors from synchrotron-based vacuum ultraviolet photoluminescence spectroscopy’, *Eur. Phys. J. Plus*, vol. 137, no. 1, p. 142, Jan. 2022, doi: 10.1140/epjp/s13360-022-02356-9.
- [5] G. Rajkumar, V. Ponnusamy, G. V. Kanmani, and M. T. Jose, ‘Ternary type BaY₂ZnO₅: Eu³⁺ deep-red phosphor for possible latent fingerprint, security ink and WLED applications’, *Ceram. Int.*, vol. 48, no. 1, pp. 10–21, Jan. 2022, doi: 10.1016/j.ceramint.2021.07.185.
- [6] J. Wu, H. Jia, M. Li, H. Jia, and Z. Liu, ‘Influence of pH on nano-phosphor YPO₄:2%Sm³⁺ and luminescent properties’, *Appl. Phys. A*, vol. 126, no. 2, p. 87, Jan. 2020, doi: 10.1007/s00339-019-3257-6.
- [7] S. U. Islam, U. Latief, I. Ahmad, Z. Khan, J. Ali, and Mohd. S. Khan, ‘Novel NiO/ZnO/Fe₂O₃ white light-emitting phosphor: facile synthesis, color-tunable photoluminescence and robust photocatalytic activity’, *J. Mater. Sci. Mater. Electron.*, vol. 33, no. 29, pp. 23137–23152, Oct. 2022, doi: 10.1007/s10854-022-09079-8.
- [8] J. Song *et al.*, ‘Luminescence properties and thermometric performance of Bi³⁺/Sm³⁺-codoped BaLa₂ZnO₅ phosphors’, *Ceram. Int.*, vol. 49, no. 10, pp. 15229–15236, May 2023, doi: 10.1016/j.ceramint.2023.01.105.
- [9] M. Fox and G. F. Bertsch, ‘Optical Properties of Solids’, *Am. J. Phys.*, vol. 70, no. 12, pp. 1269–1270, Dec. 2002, doi: 10.1119/1.1691372.
- [10] M. Fox, *Optical properties of solids*, 2 ed., (With corr.). in Oxford master series in physics Condensed matter physics, no. 3. Oxford: Oxford Univ. Press, 2012.
- [11] ‘W2015CHM2311 Part 1a Notes - CHM2311 Introduction to Structure & Bonding Part 1 Atomic Structure and Quantum Theory Fundamental | Course Hero’. Accessed: Mar. 06, 2024. [Online]. Available: <https://www.coursehero.com/file/13194871/W2015CHM2311-Part-1a-Notes/>
- [12] S. Tang *et al.*, ‘Temperature Dependence of the Phase Transformation and Photoluminescence Properties of Metastable ZnWO₄ Nano-Phosphors with High UV Absorption and VIS Reflectance’, *Russ. J. Phys. Chem. A*, vol. 96, no. 3, pp. 515–526, Mar. 2022, doi: 10.1134/S0036024422030220.
- [13] X. Wang *et al.*, ‘Achieving dynamic multicolor luminescence in ZnS:KBr,Mn²⁺ phosphor for anti-counterfeiting’, *Chem. Eng. J.*, vol. 429, p. 132537, Feb. 2022, doi: 10.1016/j.cej.2021.132537.
- [14] S. Das, S. Thomas, and P. P. Das, Eds., *Organic and Inorganic Materials Based Sensors*, 1st ed. Wiley, 2024. doi: 10.1002/9783527834266.
- [15] Y. Li and Y. Wang, ‘Photoluminescence properties and energy transfer of Dy³⁺ and Tm³⁺ co-activated CaZrO₃ phosphor for white LEDs’, *J. Inf. Disp.*, vol. 12, no. 2, Art. no. 2, Jun. 2011, doi: 10.1080/15980316.2011.567822.

- [16] K. Upadhyay, S. Thomas, and R. K. Tamrakar, Eds., *Hybrid Phosphor Materials: Synthesis, Characterization and Applications*. in Engineering Materials. Cham: Springer International Publishing, 2022. doi: 10.1007/978-3-030-90506-4.
- [17] V. Kumar, V. Sharma, and H. C. Swart, Eds., *Advanced Materials for Solid State Lighting*, vol. 25. in Progress in Optical Science and Photonics, vol. 25. Singapore: Springer Nature, 2023. doi: 10.1007/978-981-99-4145-2.
- [18] G. Cao, *Nanostructures & Nanomaterials: Synthesis, Properties & Applications*. Imperial College Press, 2004.
- [19] C. De Mello Donegá, Ed., *Nanoparticles: Workhorses of Nanoscience*. Berlin, Heidelberg: Springer Berlin Heidelberg, 2014. doi: 10.1007/978-3-662-44823-6.
- [20] E. Martis, R. Badve, and M. Degwekar, 'Nanotechnology based devices and applications in medicine: An overview', *Chron. Young Sci.*, vol. 3, no. 1, pp. 68–68, Jan. 2012.
- [21] 'Investigation of the photoluminescence studies of ZnO: RE³⁺ (where RE= Dy, Sm and Sm/Dy) nanophosphors via different anionic group (BO₃³⁻, PO₄²⁻ and SO₄²⁻) substitutions - University of Johannesburg'. Accessed: Feb. 20, 2024. [Online]. Available: <https://ujcontent.uj.ac.za/esploro/outputs/graduate/Investigation-of-the-photoluminescence-studies-of/9926503507691>
- [22] J. S. Sefadi and M. J. Mochane, 'Multifunctional 3D Hybrid Nanomaterials for Clean Energy Technologies', in *Handbook of Polymer and Ceramic Nanotechnology*, C. M. Hussain and S. Thomas, Eds., Cham: Springer International Publishing, 2021, pp. 1463–1492. doi: 10.1007/978-3-030-40513-7_43.
- [23] A. P. Nikalje, 'Nanotechnology and its Applications in Medicine', *Medicinal Chemistry*. Accessed: Feb. 20, 2024. [Online]. Available: http://ndl.ethernet.edu.et/bitstream/123456789/87730/1/1_MEMS_GMK.pdf
- [24] M. Seredych, M. Alhabeab, B. Anasori, and Y. Gogotsi, '(Invited) High-Temperature Behaviors of MXenes', *ECS Meet. Abstr.*, vol. MA2018-01, no. 15, p. 1136, Apr. 2018, doi: 10.1149/MA2018-01/15/1136.
- [25] H. Morkoç, S. Strite, G. B. Gao, M. E. Lin, B. Sverdlov, and M. Burns, 'Large-band-gap SiC, III-V nitride, and II-VI ZnSe-based semiconductor device technologies', *J. Appl. Phys.*, vol. 76, no. 3, pp. 1363–1398, Aug. 1994, doi: 10.1063/1.358463.
- [26] Carter, D.B.W.C.B., 2009. *Transmission Electron Microscopy A Textbook for Materials Science*. springer publication.
- [27] M. H. Huang *et al.*, 'Room-Temperature Ultraviolet Nanowire Nanolasers', *Science*, vol. 292, no. 5523, pp. 1897–1899, Jun. 2001, doi: 10.1126/science.1060367.
- [28] A. Jana *et al.*, 'Perovskite: Scintillators, direct detectors, and X-ray imagers', *Mater. Today*, vol. 55, pp. 110–136, May 2022, doi: 10.1016/j.mattod.2022.04.009.
- [29] N. T. Kalyani, H. C. Swart, and S. J. Dhoble, *Principles and Applications of Organic Light Emitting Diodes (OLEDs)*. Woodhead Publishing, 2017.
- [30] 'Principles and Applications of Organic Light Emitting Diodes (OLEDs) - N. Thejo Kalyani, Hendrik C. Swart, Sanjay J. Dhoble - Google Books'. Accessed: Feb. 20, 2024. [Online]. Available: [https://books.google.co.za/books?hl=en&lr=&id=OLgxDQAAQBAJ&oi=fnd&pg=PP1&dq=20.%09N.+Thejo+Kalyani,+H.+Swart,+and+S.+J.+Dhoble,+Principles+and+applications+of+organic+light+emitting+diodes+\(OLEDs\).+Elsevier,+2017.+&ots=bQHq6a6IL9&sig=Xde8bFoHLUbrIDVP5hcAfqES_QQ&redir_esc=y#v=onepage&q&f=false](https://books.google.co.za/books?hl=en&lr=&id=OLgxDQAAQBAJ&oi=fnd&pg=PP1&dq=20.%09N.+Thejo+Kalyani,+H.+Swart,+and+S.+J.+Dhoble,+Principles+and+applications+of+organic+light+emitting+diodes+(OLEDs).+Elsevier,+2017.+&ots=bQHq6a6IL9&sig=Xde8bFoHLUbrIDVP5hcAfqES_QQ&redir_esc=y#v=onepage&q&f=false)
- [31] V. G. Kessler, 'Sol–Gel Precursors', in *The Sol-Gel Handbook*, John Wiley & Sons, Ltd, 2015, pp. 195–224. doi: 10.1002/9783527670819.ch06.

- [32] R.-S. Liu, Ed., *Phosphors, Up Conversion Nano Particles, Quantum Dots and Their Applications*. Berlin, Heidelberg: Springer Berlin Heidelberg, 2017. doi: 10.1007/978-3-662-52771-9.
- [33] ‘Synthesis and luminescence investigations of Europium (Eu³⁺) and Samarium (Sm³⁺) doped sodium alkaline-earth sulphate phosphors (Na₆Mg(SO₄)₄ and Na₂Ca(SO₄)₂) via combustion method - University of Johannesburg’. Accessed: Mar. 06, 2024. [Online]. Available: <https://ujcontent.uj.ac.za/esploro/outputs/graduate/Synthesis-and-luminescence-investigations-of-Europium/9912903607691>
- [34] P. Botella *et al.*, ‘Investigation on the Luminescence Properties of InMO₄ (M = V⁵⁺, Nb⁵⁺, Ta⁵⁺) Crystals Doped with Tb³⁺ or Yb³⁺ Rare Earth Ions’, *ACS Omega*, vol. 5, no. 5, pp. 2148–2158, Feb. 2020, doi: 10.1021/acsomega.9b02862.
- [35] H. Widdel and D. L. Post, Eds., *Color in Electronic Displays*. Boston, MA: Springer US, 1992. doi: 10.1007/978-1-4757-9754-1.
- [36] Y. You *et al.*, ‘Hydrophilic Ultralong Organic Nanophosphors’, *Small*, vol. 16, no. 8, p. 1906733, 2020, doi: 10.1002/sml.201906733.
- [37] ‘Hydrophilic Ultralong Organic Nanophosphors - You - 2020 - Small - Wiley Online Library’. Accessed: Feb. 20, 2024. [Online]. Available: <https://onlinelibrary.wiley.com/doi/full/10.1002/sml.201906733>
- [38] T. Jüstel, H. Nikol, and C. Ronda, ‘New Developments in the Field of Luminescent Materials for Lighting and Displays’, *Angew. Chem. Int. Ed.*, vol. 37, no. 22, pp. 3084–3103, 1998, doi: 10.1002/(SICI)1521-3773(19981204)37:22<3084::AID-ANIE3084>3.0.CO;2-W.
- [39] H. A. Höppe, ‘Recent Developments in the Field of Inorganic Phosphors’, *Angew. Chem. Int. Ed.*, vol. 48, no. 20, pp. 3572–3582, 2009, doi: 10.1002/anie.200804005.
- [40] A. Birkel *et al.*, ‘Rapid Microwave Preparation of Highly Efficient Ce³⁺-Substituted Garnet Phosphors for Solid State White Lighting’, *Chem. Mater.*, vol. 24, no. 6, pp. 1198–1204, Mar. 2012, doi: 10.1021/cm3000238.
- [41] A. Balakrishna, L. Reddy, O. M. Ntwaeaborwa, and H. C. Swart, ‘Remarkable influence of alkaline earth ions on the enhancement of fluorescence from Eu³⁺ ion doped in sodium ortho-phosphate phosphors’, *J. Mol. Struct.*, vol. 1203, p. 127375, Mar. 2020, doi: 10.1016/j.molstruc.2019.127375.
- [42] L. Chen, C.-C. Lin, C.-W. Yeh, and R.-S. Liu, ‘Light Converting Inorganic Phosphors for White Light-Emitting Diodes’, *Materials*, vol. 3, no. 3, Art. no. 3, Mar. 2010, doi: 10.3390/ma3032172.
- [43] A. Balakrishna, V. Kumar, A. Kumar, and O. M. Ntwaeaborwa, ‘Structural and photoluminescence features of Pr³⁺-activated different alkaline sodium-phosphate-phosphors’, *J. Alloys Compd.*, vol. 686, pp. 533–539, Nov. 2016, doi: 10.1016/j.jallcom.2016.06.064.
- [44] P. K. Vishwakarma, S. B. Rai, and A. Bahadur, ‘Structural and optical properties of composite phosphor Th_x(MoO₄)₂/Bi₂(1-x)Mo₂O₉; (1≥x≥0) doped with Ho³⁺/Yb³⁺ as a multifunctional materials’, *Mater. Today Commun.*, vol. 35, p. 105746, Jun. 2023, doi: 10.1016/j.mtcomm.2023.105746.
- [45] L. da Conceição, A. M. Silva, N. F. P. Ribeiro, and M. M. V. M. Souza, ‘Combustion synthesis of La_{0.7}Sr_{0.3}Co_{0.5}Fe_{0.5}O₃ (LSCF) porous materials for application as cathode

- in IT-SOFC', *Mater. Res. Bull.*, vol. 46, no. 2, pp. 308–314, Feb. 2011, doi: 10.1016/j.materresbull.2010.10.009.
- [46] Y. R. Parauha, V. Sahu, and S. J. Dhoble, 'Prospective of combustion method for preparation of nanomaterials: A challenge', *Mater. Sci. Eng. B*, vol. 267, p. 115054, May 2021, doi: 10.1016/j.mseb.2021.115054.
- [47] R. Priya, O. P. Pandey, and S. J. Dhoble, 'Review on the synthesis, structural and photo-physical properties of Gd₂O₃ phosphors for various luminescent applications', *Opt. Laser Technol.*, vol. 135, p. 106663, Mar. 2021, doi: 10.1016/j.optlastec.2020.106663.
- [48] D. Bokov *et al.*, 'Nanomaterial by Sol-Gel Method: Synthesis and Application', *Adv. Mater. Sci. Eng.*, vol. 2021, p. e5102014, Dec. 2021, doi: 10.1155/2021/5102014.
- [49] M. Huang, S. Wang, Y. Zhang, G. Wan, K. Ou, and L. Yi, 'Intense red electroluminescence from ZnO: Sm³⁺/Tb³⁺ LED by efficient energy transfer from Tb³⁺ to Sm³⁺', *J. Lumin.*, vol. 205, pp. 243–247, Jan. 2019, doi: 10.1016/j.jlumin.2018.09.026.
- [50] Y.-P. Fang *et al.*, 'Systematic Synthesis and Characterization of Single-Crystal Lanthanide Orthophosphate Nanowires', *J. Am. Chem. Soc.*, vol. 125, no. 51, pp. 16025–16034, Dec. 2003, doi: 10.1021/ja037280d.
- [51] M. D. Mehare, C. M. Mehare, H. C. Swart, and S. J. Dhoble, 'Recent development in color tunable phosphors: A review', *Prog. Mater. Sci.*, vol. 133, p. 101067, Mar. 2023, doi: 10.1016/j.pmatsci.2022.101067.
- [52] S. S. Mahato *et al.*, 'Perspective Chapter: Sol-Gel Science and Technology in Context of Nanomaterials – Recent Advances', in *Sol-Gel Method - Recent Advances*, IntechOpen, 2023. doi: 10.5772/intechopen.111378.
- [53] A. Varma, A. S. Mukasyan, A. S. Rogachev, and K. V. Manukyan, 'Solution Combustion Synthesis of Nanoscale Materials', *Chem. Rev.*, vol. 116, no. 23, pp. 14493–14586, Dec. 2016, doi: 10.1021/acs.chemrev.6b00279.
- [54] A. Saffar, H. A. Ahangar, S. Salehi, M. H. Fekri, and A. Rabbani, 'Synthesis of novel ZnAl₂O₄/Al₂O₃ nanocomposite by sol-gel method and its application as adsorbent', *J. Sol-Gel Sci. Technol.*, vol. 99, no. 1, pp. 158–168, Jul. 2021, doi: 10.1007/s10971-021-05559-1.
- [55] 'Advanced Nanomaterials and Nanocomposites for Bioelectrochemical Systems 0323904041, 9780323904049', ebin.pub. Accessed: Mar. 06, 2024. [Online]. Available: <https://ebin.pub/advanced-nanomaterials-and-nanocomposites-for-bioelectrochemical-systems-0323904041-9780323904049.html>
- [56] A. O. Ijaola, P. K. Farayibi, and E. Asmatulu, 'Superhydrophobic coatings for steel pipeline protection in oil and gas industries: A comprehensive review', *J. Nat. Gas Sci. Eng.*, vol. 83, p. 103544, Nov. 2020, doi: 10.1016/j.jngse.2020.103544.
- [57] A. Dwivedi, E. Rai, D. Kumar, and S. B. Rai, 'Effect of Synthesis Techniques on the Optical Properties of Ho³⁺/Yb³⁺ Co-doped YVO₄ Phosphor: A Comparative Study', *ACS Omega*, vol. 4, no. 4, pp. 6903–6913, Apr. 2019, doi: 10.1021/acsomega.8b03606.
- [58] B. Liu, J. Li, G. Duan, Q. Li, and Z. Liu, 'The synthesis and luminescent properties of morphology-controlled Gd₂O₃:Dy³⁺/Eu³⁺ phosphors with enhanced red emission via energy transfer', *J. Lumin.*, vol. 206, pp. 348–358, Feb. 2019, doi: 10.1016/j.jlumin.2018.10.035.
- [59] S. Sakka, 'History of the Sol-Gel Chemistry and Technology', in *Handbook of Sol-Gel Science and Technology: Processing, Characterization and Applications*, L. Klein, M. Aparicio, and A. Jitianu, Eds., Cham: Springer International Publishing, 2018, pp. 3–29. doi: 10.1007/978-3-319-32101-1_87.
- [60] X. Li, M. Wang, Y. Ye, P. Che, and Y. Zhao, 'Design, synthesis and mechanism of green afterglow phosphors Zn₄B₆O₁₃:Mn²⁺ doped with Ln³⁺ (Ln = Sm, Yb, Eu) guided

- by VRBE', *J. Alloys Compd.*, vol. 906, p. 164268, Jun. 2022, doi: 10.1016/j.jallcom.2022.164268.
- [61] R. S. Perala, B. P. Singh, V. N. K. Putta, R. Acharya, and R. S. Ningthoujam, 'Enrichment of Crystal Field Modification via Incorporation of Alkali K⁺ Ions in YVO₄:Ho³⁺/Yb³⁺ Nanophosphor and Its Hybrid with Superparamagnetic Iron Oxide Nanoparticles for Optical, Advanced Anticounterfeiting, Uranyl Detection, and Hyperthermia Applications', *ACS Omega*, vol. 6, no. 30, pp. 19517–19528, Aug. 2021, doi: 10.1021/acsomega.1c01813.
- [62] 'Hydrophilic Ultralong Organic Nanophosphors - You - 2020 - Small - Wiley Online Library'. Accessed: Feb. 20, 2024. [Online]. Available: <https://onlinelibrary.wiley.com/doi/full/10.1002/sml.201906733>
- [63] P. Głuchowski and K. Rajfur, 'Impact of the Synthesis Method on the Conventional and Persistent Luminescence in Gd_{3-x}Ce_xGa₃Al₂O₁₂', *Inorg. Chem.*, vol. 60, no. 24, pp. 18777–18788, Dec. 2021, doi: 10.1021/acs.inorgchem.1c02239.
- [64] A. Abdollahi, H. Roghani-Mamaqani, B. Razavi, and M. Salami-Kalajahi, 'Photoluminescent and Chromic Nanomaterials for Anticounterfeiting Technologies: Recent Advances and Future Challenges', *ACS Nano*, vol. 14, no. 11, pp. 14417–14492, Nov. 2020, doi: 10.1021/acsnano.0c07289.
- [65] C. Chomyn and J. Plank, 'Impact of different synthesis methods on the dispersing effectiveness of isoprenol ether-based zwitterionic and anionic polycarboxylate (PCE) superplasticizers', *Cem. Concr. Res.*, vol. 119, pp. 113–125, May 2019, doi: 10.1016/j.cemconres.2019.02.001.
- [66] K. N. Shinde, S. J. Dhoble, and K. Park, 'Effect of Synthesis Method on Photoluminescence Properties of Na₂Sr₂Al₂PO₄C₁₉:Ce³⁺ Nanophosphor', *Nano-Micro Lett.*, vol. 4, no. 2, pp. 78–82, Jun. 2012, doi: 10.1007/BF03353696.
- [67] K. Upadhyay, S. Thomas, and R. K. Tamrakar, Eds., *Hybrid Phosphor Materials: Synthesis, Characterization and Applications*. in Engineering Materials. Cham: Springer International Publishing, 2022. doi: 10.1007/978-3-030-90506-4.
- [68] X. Qin, X. Liu, W. Huang, M. Bettinelli, and X. Liu, 'Lanthanide-Activated Phosphors Based on 4f-5d Optical Transitions: Theoretical and Experimental Aspects', *Chem. Rev.*, vol. 117, no. 5, pp. 4488–4527, Mar. 2017, doi: 10.1021/acs.chemrev.6b00691.
- [69] S. K. Omanwar, R. P. Sonekar, and N. S. Bajaj, *Borate Phosphors: Processing to Applications*. CRC Press, 2022.
- [70] A. AlkhayattOmran and M. R. Ahmed, 'Impact of reaction temperature on the structural, surface morphology and antibacterial activity of hydrothermally synthesized CdS nanoparticles', *J. Phys. Conf. Ser.*, vol. 1879, no. 3, p. 032091, May 2021, doi: 10.1088/1742-6596/1879/3/032091.
- [71] D. S. Bohle and C. J. Spina, 'Cationic and Anionic Surface Binding Sites on Nanocrystalline Zinc Oxide: Surface Influence on Photoluminescence and Photocatalysis', *J. Am. Chem. Soc.*, vol. 131, no. 12, pp. 4397–4404, Apr. 2009, doi: 10.1021/ja808663b.
- [72] K. Booker, M. C. Bowyer, C. J. Lennard, C. I. Holdsworth, and A. McCluskey, 'Molecularly Imprinted Polymers and Room Temperature Ionic Liquids: Impact of Template on Polymer Morphology', *Aust. J. Chem.*, vol. 60, no. 1, pp. 51–56, Jan. 2007, doi: 10.1071/CH06284.
- [73] L. E. Shea, J. McKittrick, O. A. Lopez, and E. Sluzky, 'Synthesis of Red-Emitting, Small Particle Size Luminescent Oxides Using an Optimized Combustion Process', *J. Am. Ceram. Soc.*, vol. 79, no. 12, pp. 3257–3265, 1996, doi: 10.1111/j.1151-2916.1996.tb08103.x.

- [74] M. Zahedi, S. A. Hassanzadeh-Tabrizi, and A. Saffar-Teluri, 'Sol-gel synthesis and luminescence properties of Ba₂SiO₄:Sm³⁺ nanostructured phosphors', *Ceram. Int.*, vol. 44, no. 9, pp. 10169–10174, Jun. 2018, doi: 10.1016/j.ceramint.2018.03.006.
- [75] Y. Shen, S. Zhao, and J. Luo, 'The role of cations in second-order nonlinear optical materials based on π -conjugated [BO₃]³⁻ groups', *Coord. Chem. Rev.*, vol. 366, pp. 1–28, Jul. 2018, doi: 10.1016/j.ccr.2018.03.012.
- [76] D. K. Basu, M. Das, and S. Kundu, 'A Review of the Application of Nanotechnology in Different Spheres of Life Sciences', *Int. J. Res. Publ. Rev.*, vol. 4, no. 9, pp. 2128–2143, Sep. 2023, doi: 10.55248/gengpi.4.923.92463.
- [77] S. Brahadeeswaran *et al.*, 'Influence of dopants on photo-induced damage in GdxY_{1-x}Ca₄O(BO₃)₃ crystal', *J. Cryst. Growth*, vol. 275, no. 1, pp. e881–e886, Feb. 2005, doi: 10.1016/j.jcrysgro.2004.11.029.
- [78] A. Boukerika and L. Guerbous, 'Annealing effects on structural and luminescence properties of red Eu³⁺-doped Y₂O₃ nanophosphors prepared by sol-gel method', *J. Lumin.*, vol. 145, pp. 148–153, Jan. 2014, doi: 10.1016/j.jlumin.2013.07.037.
- [79] S. G. Motke, S. P. Yawale, and S. S. Yawale, 'Infrared spectra of zinc doped lead borate glasses', *Bull. Mater. Sci.*, vol. 25, no. 1, pp. 75–78, Feb. 2002, doi: 10.1007/BF02704599.
- [80] S. R. Holmes-Farley, R. H. Reamey, T. J. McCarthy, J. Deutch, and G. M. Whitesides, 'Acid-base behavior of carboxylic acid groups covalently attached at the surface of polyethylene: The usefulness of contact angle in following the ionization of surface functionality', *Langmuir*, vol. 1, no. 6, pp. 725–740, Nov. 1985, doi: 10.1021/la00066a016.
- [81] E. S. Stoyanov, K.-C. Kim, and C. A. Reed, 'An Infrared ν NH Scale for Weakly Basic Anions. Implications for Single-Molecule Acidity and Superacidity', *J. Am. Chem. Soc.*, vol. 128, no. 26, pp. 8500–8508, Jul. 2006, doi: 10.1021/ja060714v.
- [82] Jack. Simons and K. D. Jordan, 'Ab initio electronic structure of anions', *Chem. Rev.*, vol. 87, no. 3, pp. 535–555, Jun. 1987, doi: 10.1021/cr00079a004.
- [83] D. M. P. Mingos, 'Comprehensive organometallic chemistry III', *No Title*, Accessed: Feb. 20, 2024. [Online]. Available: <https://cir.nii.ac.jp/crid/1130000796905572352>
- [84] J. Simons, 'Molecular Anions', *J. Phys. Chem. A*, vol. 112, no. 29, pp. 6401–6511, Jul. 2008, doi: 10.1021/jp711490b.
- [85] D. F. Shriver, 'Transition metal basicity', *Acc. Chem. Res.*, vol. 3, no. 7, pp. 231–238, Jul. 1970, doi: 10.1021/ar50031a004.
- [86] M. Letswalo, 'Influence of anionic SO₄²⁻-substitution in luminescence properties of Ce³⁺, Eu³⁺ and Eu²⁺ doped ZnO and Ce³⁺ co-doped ZnO: RE (RE= Eu³⁺ and Eu²⁺) phosphors for enhanced visible emission'.
- [87] W. Zhang, J. Li, Y. Wang, J. Long, and K. Qiu, 'Synthesis and luminescence properties of NaLa(MoO₄)_{2-x}AG_x:Eu³⁺ (AG = SO₄²⁻, BO₃³⁻) red phosphors for white light emitting diodes', *J. Alloys Compd.*, vol. 635, pp. 16–20, Jun. 2015, doi: 10.1016/j.jallcom.2015.02.106.
- [88] A. Meijerink, G. Blasse, and M. Glasbeek, 'Photoluminescence, thermoluminescence and EPR studies on Zn₄B₆O₁₃', *J. Phys. Condens. Matter*, vol. 2, no. 29, p. 6303, Jul. 1990, doi: 10.1088/0953-8984/2/29/008.
- [89] S. Zhao, Z. Wang, Z. Ma, F. Fan, and W. Liu, 'Achieving Multimodal Emission in Zn₄B₆O₁₃:Tb³⁺,Yb³⁺ for Information Encryption and Anti-counterfeiting', *Inorg. Chem.*, vol. 59, no. 21, pp. 15681–15689, Nov. 2020, doi: 10.1021/acs.inorgchem.0c02019.
- [90] W.-L. Lian, P. Liang, and Z.-H. Liu, 'Controllable hydrothermal synthesis and morphology evolution of Zn₄B₆O₁₃:Tb/Eu phosphors with tunable luminescent properties', *Adv. Powder Technol.*, vol. 31, no. 4, pp. 1633–1642, Apr. 2020, doi: 10.1016/j.apt.2020.02.004.

- [91] Y. Li *et al.*, ‘Zn₄B₆O₁₃: Efficient Borate Photocatalyst with Fast Carrier Separation for Photodegradation of Tetracycline’, *Inorg. Chem.*, vol. 59, no. 18, pp. 13136–13143, Sep. 2020, doi: 10.1021/acs.inorgchem.0c01425.
- [92] C. J. Bosson, ‘Understanding Cu₂ZnSnS₄ as a Photovoltaic Absorber for the Future of Solar Electricity’.
- [93] *Encyclopedia of Geology*. Academic Press, 2020.
- [94] M. Balestrieri, ‘Transparent conductive oxides with photon converting properties in view of photovoltaic applications: the cases of rare earth-doped zinc oxide and cerium oxide’.
- [95] Z. N. Urgessa, ‘Growth and characterization of ZnO nanorods using chemical bath deposition’, 2012, Accessed: Feb. 20, 2024. [Online]. Available: http://vital.seals.ac.za:8080/vital/access/manager/Repository/vital:10559?site_name=GlobalView
- [96] B. Fan, J. Liu, W. Zhao, and L. Han, ‘Luminescence properties of Sm³⁺ and Dy³⁺ co-doped BaY₂ZnO₅ phosphor for white LED’, *J. Lumin.*, vol. 219, p. 116887, Mar. 2020, doi: 10.1016/j.jlumin.2019.116887.
- [97] R. Pöttgen, T. Jüstel, and C. A. Strassert, *Rare Earth Chemistry*. Walter de Gruyter GmbH & Co KG, 2020.
- [98] and and and, ‘Preparation and characterization of nanosized GdxBi_{0.95-x}VO₄:0.05Eu³⁺ solid solution as red phosphor’, *Chin. Phys. B*, vol. 23, no. 10, p. 104224, Aug. 2014, doi: 10.1088/1674-1056/23/10/104224.
- [99] *Encyclopedia of Spectroscopy and Spectrometry*. Academic Press, 2016.
- [100] Z. Zheng and J. E. Greedan, ‘Rare Earth Elements and Materials’, in *Encyclopedia of Physical Science and Technology (Third Edition)*, R. A. Meyers, Ed., New York: Academic Press, 2003, pp. 1–22. doi: 10.1016/B0-12-227410-5/00653-0.
- [101] B. J. Ainslie, ‘A review of the fabrication and properties of erbium-doped fibers for optical amplifiers’, *J. Light. Technol.*, vol. 9, no. 2, pp. 220–227, Feb. 1991, doi: 10.1109/50.65880.
- [102] S. Neeraj, N. Kijima, and A. K. Cheetham, ‘Novel red phosphors for solid-state lighting: the system NaM(WO₄)_{2-x}(MoO₄)_x:Eu³⁺ (M□Gd, Y, Bi)’, *Chem. Phys. Lett.*, vol. 387, no. 1, pp. 2–6, Mar. 2004, doi: 10.1016/j.cplett.2003.12.130.
- [103] Y. Liu, B. Lei, and C. Shi, ‘Luminescent Properties of a White Afterglow Phosphor CdSiO₃:Dy³⁺’, *Chem. Mater.*, vol. 17, no. 8, pp. 2108–2113, Apr. 2005, doi: 10.1021/cm0496422.
- [104] B. v. Ratnam, M. Jayasimhadri, K. Jang, H. Sueb Lee, S.-S. Yi, and J.-H. Jeong, ‘White Light Emission from NaCaPO₄:Dy³⁺ Phosphor for Ultraviolet-Based White Light-Emitting Diodes’, *J. Am. Ceram. Soc.*, vol. 93, no. 11, pp. 3857–3861, 2010, doi: 10.1111/j.1551-2916.2010.03963.x.
- [105] J. Kuang, Y. Liu, and J. Zhang, ‘White-light-emitting long-lasting phosphorescence in Dy³⁺-doped SrSiO₃’, *J. Solid State Chem.*, vol. 179, no. 1, pp. 266–269, Jan. 2006, doi: 10.1016/j.jssc.2005.10.025.
- [106] R. Cao *et al.*, ‘Synthesise, energy transfer and tunable emission properties of Ba₂La₂ZnW₂O₁₂:Sm³⁺ phosphors’, *J. Lumin.*, vol. 235, p. 118054, Jul. 2021, doi: 10.1016/j.jlumin.2021.118054.
- [107] Z. Xia and D. Chen, ‘Synthesis and Luminescence Properties of BaMoO₄:Sm³⁺ Phosphors’, *J. Am. Ceram. Soc.*, vol. 93, no. 5, pp. 1397–1401, 2010, doi: 10.1111/j.1551-2916.2009.03574.x.
- [108] K. Selvaraju and K. Marimuthu, ‘Structural and spectroscopic studies on concentration dependent Sm³⁺ doped boro-tellurite glasses’, *J. Alloys Compd.*, vol. 553, pp. 273–281, Mar. 2013, doi: 10.1016/j.jallcom.2012.11.150.

- [109] S. Wu, Z. Pan, R. Chen, and X. Liu, ‘Applications of Inorganic Afterglow Phosphors’, in *Long Afterglow Phosphorescent Materials*, S. Wu, Z. Pan, R. Chen, and X. Liu, Eds., in SpringerBriefs in Materials. , Cham: Springer International Publishing, 2017, pp. 101–116. doi: 10.1007/978-3-319-60421-3_4.
- [110] Y.-C. Li, Y.-H. Chang, Y.-F. Lin, Y.-S. Chang, and Y.-J. Lin, ‘Synthesis and luminescent properties of Ln³⁺ (Eu³⁺, Sm³⁺, Dy³⁺)-doped lanthanum aluminum germanate LaAlGe₂O₇ phosphors’, *J. Alloys Compd.*, vol. 439, no. 1, pp. 367–375, Jul. 2007, doi: 10.1016/j.jallcom.2006.08.269.
- [111] A. Kumawat, K. P. Misra, and S. Chattopadhyay, ‘Band Gap Engineering and Relationship with Luminescence in Rare-Earth Elements Doped ZnO: An Overview’, *Mater. Technol.*, vol. 37, no. 11, pp. 1595–1610, Sep. 2022, doi: 10.1080/10667857.2022.2082351.
- [112] S. H. Jaafar, M. H. Mohd Zaid, K. A. Matori, Y. Yaakob, and H. M. Mustapha, ‘Synthesis of Eu³⁺-Doped ZnO/Zn₂SiO₄ Composite Phosphor for Potent Optoelectronic Applications’, *Braz. J. Phys.*, vol. 52, no. 1, p. 6, Nov. 2021, doi: 10.1007/s13538-021-01017-z.
- [113] Y. Zheng *et al.*, ‘Ba₃(ZnB₅O₁₀)PO₄:Tb³⁺ green phosphor: Microwave-assisted sintering synthesis and thermally stable photoluminescence’, *J. Alloys Compd.*, vol. 911, p. 165087, Aug. 2022, doi: 10.1016/j.jallcom.2022.165087.
- [114] R. Zhou, X.-Y. Wu, Q. Zhao, K.-K. Liu, L. Dong, and C.-X. Shan, ‘One-step synthesis of multi-colored ZnO nanoparticles for white light-emitting diodes’, *J. Lumin.*, vol. 252, p. 119425, Dec. 2022, doi: 10.1016/j.jlumin.2022.119425.
- [115] R. Bekkari, L. laânab, D. Boyer, R. Mahiou, and B. Jaber, ‘Influence of the sol gel synthesis parameters on the photoluminescence properties of ZnO nanoparticles’, *Mater. Sci. Semicond. Process.*, vol. 71, pp. 181–187, Nov. 2017, doi: 10.1016/j.mssp.2017.07.027.
- [116] W. Ben Haj Othmen, M. Ben Ali, W. Bouslama, and H. Elhouichet, ‘Solar driven photocatalytic properties of Sm³⁺ doped ZnO nanocrystals’, *Ceram. Int.*, vol. 46, no. 11, Part B, pp. 18878–18887, Aug. 2020, doi: 10.1016/j.ceramint.2020.04.208.
- [117] N. L. Tarwal *et al.*, ‘Photoluminescence of zinc oxide nanopowder synthesized by a combustion method’, *Powder Technol.*, vol. 208, no. 1, pp. 185–188, Mar. 2011, doi: 10.1016/j.powtec.2010.12.017.
- [118] J. Zhao, Z. Han, H. Lu, X. Wang, and J. Chen, ‘Synthesis and photoluminescence properties of ZnO powder by solution combustion method’, *J. Mater. Sci. Mater. Electron.*, vol. 22, no. 9, pp. 1361–1365, Sep. 2011, doi: 10.1007/s10854-011-0314-0.
- [119] C.-C. Hwang and T.-Y. Wu, ‘Synthesis and characterization of nanocrystalline ZnO powders by a novel combustion synthesis method’, *Mater. Sci. Eng. B*, vol. 111, no. 2, pp. 197–206, Aug. 2004, doi: 10.1016/j.mseb.2004.04.021.
- [120] C.-S. Lin, C.-C. Hwang, W.-H. Lee, and W.-Y. Tong, ‘Preparation of zinc oxide (ZnO) powders with different types of morphology by a combustion synthesis method’, *Mater. Sci. Eng. B*, vol. 140, no. 1, pp. 31–37, May 2007, doi: 10.1016/j.mseb.2007.03.023.
- [121] Z. Kalantari Bolaghi, M. Hasheminiyasi, and S. M. Masoudpanah, ‘Solution combustion synthesis of ZnO powders using mixture of fuels in closed system’, *Ceram. Int.*, vol. 44, no. 11, pp. 12684–12690, Aug. 2018, doi: 10.1016/j.ceramint.2018.04.069.
- [122] K. A. Adegoke, M. Iqbal, H. Louis, S. U. Jan, A. Mateen, and O. S. Bello, ‘Photocatalytic conversion of CO₂ using ZnO semiconductor by hydrothermal method’, 2018, doi: 10.21743/pjaec/2018.06.01.
- [123] P. Sagar, P. K. Shishodia, R. M. Mehra, H. Okada, A. Wakahara, and A. Yoshida, ‘Photoluminescence and absorption in sol–gel-derived ZnO films’, *J. Lumin.*, vol. 126, no. 2, pp. 800–806, Oct. 2007, doi: 10.1016/j.jlumin.2006.12.003.

- [124] D. Bera, L. Qian, S. Sabui, S. Santra, and P. H. Holloway, 'Photoluminescence of ZnO quantum dots produced by a sol-gel process', *Opt. Mater.*, vol. 30, no. 8, pp. 1233–1239, Apr. 2008, doi: 10.1016/j.optmat.2007.06.001.
- [125] S. Suwanboon, 'Structural and Optical Properties of Nanocrystalline ZnO Powder from Sol-Gel Method', *ScienceAsia*, vol. 34, no. 1, p. 031, 2008, doi: 10.2306/scienceasia1513-1874.2008.34.031.
- [126] N. Kumar, R. Kaur, and R. M. Mehra, 'Photoluminescence studies in sol-gel derived ZnO films', *J. Lumin.*, vol. 126, no. 2, pp. 784–788, Oct. 2007, doi: 10.1016/j.jlumin.2006.11.012.
- [127] M. Pudukudy and Z. Yaakob, 'Facile solid state synthesis of ZnO hexagonal nanogranules with excellent photocatalytic activity', *Appl. Surf. Sci.*, vol. 292, pp. 520–530, Feb. 2014, doi: 10.1016/j.apsusc.2013.12.004.
- [128] C. H. Lin, B.-S. Chiou, C. H. Chang, and J. D. Lin, 'Preparation and cathodoluminescence of ZnO phosphor', *Mater. Chem. Phys.*, vol. 77, no. 3, pp. 647–654, Jan. 2003, doi: 10.1016/S0254-0584(02)00120-7.
- [129] S. K. Lathika Devi and K. Sudarsanakumar, 'Photoluminescent properties of Sm³⁺-doped zinc oxide nanostructures', *J. Lumin.*, vol. 130, no. 7, pp. 1221–1224, Jul. 2010, doi: 10.1016/j.jlumin.2010.02.028.
- [130] D. Dash, N. R. Panda, and D. Sahu, 'Sm³⁺ driven enhancement in photocatalytic degradation of hazardous dyes and photoluminescence properties of hexagonal-ZnO nanocolumns', *Nano Express*, vol. 2, no. 1, p. 010007, Jan. 2021, doi: 10.1088/2632-959X/abd90b.
- [131] Y. Liu, R. Li, W. Luo, H. Zhu, and X. Chen, 'Optical Spectroscopy of Sm³⁺ and Dy³⁺ Doped ZnO Nanocrystals', *Spectrosc. Lett.*, vol. 43, no. 5, pp. 343–349, Jul. 2010, doi: 10.1080/00387010.2010.486717.
- [132] S. A. Ayon, S. Hasan, M. M. Billah, S. S. Nishat, and A. Kabir, 'Improved luminescence and photocatalytic properties of Sm³⁺-doped ZnO nanoparticles via modified sol-gel route: A unified experimental and DFT+U approach', *J. Rare Earths*, vol. 41, no. 4, pp. 550–560, Apr. 2023, doi: 10.1016/j.jre.2022.03.004.
- [133] M. R. A. Kumar, H. P. Nagaswarupa, C. R. Ravikumar, S. C. Prashantha, H. Nagabhushana, and A. S. Bhatt, 'Green engineered nano MgO and ZnO doped with Sm³⁺: Synthesis and a comparison study on their characterization, PC activity and electrochemical properties', *J. Phys. Chem. Solids*, vol. 127, pp. 127–139, Apr. 2019, doi: 10.1016/j.jpcs.2018.12.012.
- [134] O. M. Ntwaeaborwa, S. J. Mofokeng, V. Kumar, and R. E. Kroon, 'Structural, optical and photoluminescence properties of Eu³⁺ doped ZnO nanoparticles', *Spectrochim. Acta. A. Mol. Biomol. Spectrosc.*, vol. 182, pp. 42–49, Jul. 2017, doi: 10.1016/j.saa.2017.03.067.
- [135] L. Machaba, 'Effect of anionic partial substitution on structural and luminescence properties of CaMoO₄: Eu³⁺ color tunable phosphor compounds for white-light-emitting diode applications - University of Johannesburg'. Accessed: Feb. 25, 2024. [Online]. Available: https://ujcontent.uj.ac.za/esploro/outputs/graduate/Effect-of-anionic-partial-substitution-on/9910907407691?skipUsageReporting=true&skipUsageReporting=true&recordUsage=false&recordUsage=false&institution=27UOJ_INST
- [136] Y. Zhang, Y. Liu, L. Wu, E. Xie, and J. Chen, 'Photoluminescence and ZnO → Eu³⁺ energy transfer in Eu³⁺-doped ZnO nanospheres', *J. Phys. Appl. Phys.*, vol. 42, no. 8, p. 085106, Mar. 2009, doi: 10.1088/0022-3727/42/8/085106.
- [137] T.-H. Fang *et al.*, 'Photoluminescence characteristics of ZnO doped with Eu³⁺ powders', *J. Phys. Chem. Solids*, vol. 70, no. 6, pp. 1015–1018, Jun. 2009, doi: 10.1016/j.jpcs.2009.05.012.

- [138] P. A. Tanner and L. Yu, 'Photoluminescence of ZnO:Eu³⁺ Nanoflowers', *J. Nanosci. Nanotechnol.*, vol. 8, no. 3, pp. 1307–1311, Mar. 2008, doi: 10.1166/jnn.2008.18187.
- [139] M. Zhong, G. Shan, Y. Li, G. Wang, and Y. Liu, 'Synthesis and luminescence properties of Eu³⁺-doped ZnO nanocrystals by a hydrothermal process', *Mater. Chem. Phys.*, vol. 106, no. 2, pp. 305–309, Dec. 2007, doi: 10.1016/j.matchemphys.2007.06.007.
- [140] P. P. Pal and J. Manam, 'Structural and photoluminescence studies of Eu³⁺ doped zinc oxide nanorods prepared by precipitation method', *J. Rare Earths*, vol. 31, no. 1, pp. 37–43, Jan. 2013, doi: 10.1016/S1002-0721(12)60231-2.
- [141] K. Ebisawa, T. Okuno, and K. Abe, 'Photoluminescence Properties of Eu³⁺-Doped ZnO Nanoneedles', *Jpn. J. Appl. Phys.*, vol. 47, no. 9R, p. 7236, Sep. 2008, doi: 10.1143/JJAP.47.7236.
- [142] G. Amira, B. Chaker, and E. Habib, 'Spectroscopic properties of Dy³⁺ + doped ZnO for white luminescence applications', *Spectrochim. Acta. A. Mol. Biomol. Spectrosc.*, vol. 177, pp. 164–169, Apr. 2017, doi: 10.1016/j.saa.2017.01.039.
- [143] R. Kumar and S. K. Mishra, 'Enhancement in the luminescence of green-emission from emissive surface defects of Dy³⁺-doped ZnO nanoluminophores: A simple, mass-scale productive approach for optoelectronic devices', *Appl. Surf. Sci. Adv.*, vol. 9, p. 100256, Jun. 2022, doi: 10.1016/j.apsadv.2022.100256.
- [144] R. Sreeja Sreedharan *et al.*, 'Bright visible luminescence from highly textured, transparent Dy³⁺ doped RF sputtered zinc oxide films', *J. Alloys Compd.*, vol. 721, pp. 661–673, Oct. 2017, doi: 10.1016/j.jallcom.2017.06.010.
- [145] C. N. Pangul, S. W. Anwane, and S. B. Kondawar, 'Enhanced photoluminescence properties of electrospun Dy³⁺-doped ZnO nanofibres for white lighting devices', *Luminescence*, vol. 33, no. 6, pp. 1087–1093, 2018, doi: 10.1002/bio.3513.
- [146] F. Gu, S. F. Wang, M. K. Lü, G. J. Zhou, D. Xu, and D. R. Yuan, 'Structure Evaluation and Highly Enhanced Luminescence of Dy³⁺-Doped ZnO Nanocrystals by Li⁺ Doping via Combustion Method', *Langmuir*, vol. 20, no. 9, pp. 3528–3531, Apr. 2004, doi: 10.1021/la049874f.
- [147] V. Uma, K. Marimuthu, and G. Muralidharan, 'Effect of ZnO on the spectroscopic properties of Dy³⁺ doped zinc telluroborate glasses for white light generation', *J. Non-Cryst. Solids*, vol. 498, pp. 386–394, Oct. 2018, doi: 10.1016/j.jnoncrysol.2018.03.022.
- [148] A. M. Ismail, A. A. Menazea, H. A. Kabary, A. E. El-Sherbiny, and A. Samy, 'The influence of calcination temperature on structural and antimicrobial characteristics of zinc oxide nanoparticles synthesized by Sol–Gel method', *J. Mol. Struct.*, vol. 1196, pp. 332–337, Nov. 2019, doi: 10.1016/j.molstruc.2019.06.084.
- [149] U. G. Akpan and B. H. Hameed, 'The advancements in sol–gel method of doped-TiO₂ photocatalysts', *Appl. Catal. Gen.*, vol. 375, no. 1, pp. 1–11, Feb. 2010, doi: 10.1016/j.apcata.2009.12.023.
- [150] X. Yuan, X. Wu, Y. Wu, and T. van Ree, '15 - Metal oxides for emission control', in *Metal Oxides in Energy Technologies*, Y. Wu, Ed., in Metal Oxides. , Elsevier, 2018, pp. 391–414. doi: 10.1016/B978-0-12-811167-3.00015-8.
- [151] A. M. Kierzkowska, C. D. Bohn, S. A. Scott, J. P. Cleeton, J. S. Dennis, and C. R. Müller, 'Development of Iron Oxide Carriers for Chemical Looping Combustion Using Sol–Gel', *Ind. Eng. Chem. Res.*, vol. 49, no. 11, pp. 5383–5391, Jun. 2010, doi: 10.1021/ie100046f.
- [152] C. Cannas, A. Musinu, D. Peddis, and G. Piccaluga, 'Synthesis and Characterization of CoFe₂O₄ Nanoparticles Dispersed in a Silica Matrix by a Sol–Gel Autocombustion Method', *Chem. Mater.*, vol. 18, no. 16, pp. 3835–3842, Aug. 2006, doi: 10.1021/cm060650n.

- [153] R. M. Thankachan and R. Balakrishnan, ‘Chapter 8 - Synthesis Strategies of Single-Phase and Composite Multiferroic Nanostructures’, in *Synthesis of Inorganic Nanomaterials*, S. Mohan Bhagyaraj, O. S. Oluwafemi, N. Kalarikkal, and S. Thomas, Eds., in *Micro and Nano Technologies.*, Woodhead Publishing, 2018, pp. 185–211. doi: 10.1016/B978-0-08-101975-7.00008-7.
- [154] B. Stojanovic, *Magnetic, Ferroelectric, and Multiferroic Metal Oxides*. Elsevier, 2018.
- [155] H. Lv, Z. Pan, and Y. Wang, ‘Synthesis and mechanoluminescent property of (Eu²⁺, Dy³⁺)-co-doped strontium aluminate phosphor by soft mechanochemistry-assisted solid-state method’, *J. Lumin.*, vol. 209, pp. 129–140, May 2019, doi: 10.1016/j.jlumin.2019.01.026.
- [156] J. Epp, ‘4 - X-ray diffraction (XRD) techniques for materials characterization’, in *Materials Characterization Using Nondestructive Evaluation (NDE) Methods*, G. Hübschen, I. Altpeter, R. Tschuncky, and H.-G. Herrmann, Eds., Woodhead Publishing, 2016, pp. 81–124. doi: 10.1016/B978-0-08-100040-3.00004-3.
- [157] A. Chauhan, ‘Powder XRD Technique and its Applications in Science and Technology’, *J. Anal. Bioanal. Tech.*, vol. 5, no. 6, 2014, doi: 10.4172/2155-9872.1000212.
- [158] K. Mongkolsuttirat and J. Buajarern, ‘Uncertainty evaluation of crystallite size measurements of nanoparticle using X-Ray Diffraction analysis (XRD)’, *J. Phys. Conf. Ser.*, vol. 1719, no. 1, p. 012054, Jan. 2021, doi: 10.1088/1742-6596/1719/1/012054.
- [159] H. Khan, A. S. Yerramilli, A. D’Oliveira, T. L. Alford, D. C. Boffito, and G. S. Patience, ‘Experimental methods in chemical engineering: X-ray diffraction spectroscopy—XRD’, *Can. J. Chem. Eng.*, vol. 98, no. 6, pp. 1255–1266, 2020, doi: 10.1002/cjce.23747.
- [160] ‘The Effect of Ce³⁺ on the Luminescence Properties of the ABPO₄ (A= Na, B = Mg, Ca, Sr, And Ba) Using the Solid-state Reaction Method - ProQuest’. Accessed: Feb. 26, 2024. [Online]. Available: <https://www.proquest.com/openview/24b44968e8d3dfc85154dbca47072b41/1?cbl=2026366&diss=y&pq-origsite=gscholar&parentSessionId=7314yisW15w2v5UEM2KrtP9ogdgwQu%2B2JCW6QkwCtXw%3D>
- [161] M. O. Krause and J. H. Oliver, ‘Natural widths of atomic K and L levels, K α X-ray lines and several KLL Auger lines’, *J. Phys. Chem. Ref. Data*, vol. 8, no. 2, pp. 329–338, Apr. 1979, doi: 10.1063/1.555595.
- [162] P. P. Urone and R. Hinrichs, ‘30.4 X Rays: Atomic Origins and Applications’, Aug. 2016, Accessed: Feb. 26, 2024. [Online]. Available: <https://pressbooks.online.ucf.edu/algphysics/chapter/x-rays-atomic-origins-and-applications/>
- [163] A. Ul-Hamid, *A Beginners’ Guide to Scanning Electron Microscopy*. Cham: Springer International Publishing, 2018. doi: 10.1007/978-3-319-98482-7.
- [164] J. N. Cruz, Ed., *Drug Discovery and Design Using Natural Products*. Cham: Springer Nature Switzerland, 2023. doi: 10.1007/978-3-031-35205-8.
- [165] G. F. Harrington and J. Santiso, ‘Back-to-Basics tutorial: X-ray diffraction of thin films’, *J. Electroceramics*, vol. 47, no. 4, pp. 141–163, Dec. 2021, doi: 10.1007/s10832-021-00263-6.
- [166] C. Kittel, *Introduction to solid state physics*. 2005.
- [167] ‘SAINS MALAYSIANA’. Accessed: Mar. 06, 2024. [Online]. Available: http://www.ukm.my/jsm/malay_journals/jilid42bil11_2013/Jilid42Bil11_2013ms1663-1670.html

- [168] E. T. Maleho, ‘Investigation of the photoluminescence studies of ZnO: RE³⁺ (where RE= Dy, Sm and Sm/Dy) nanophosphors via different anionic group (BO₃³⁻, PO₄²⁻ and SO₄²⁻) substitutions’, University of Johannesburg, 2022. Accessed: Feb. 26, 2024. [Online]. Available: <https://ujcontent.uj.ac.za/esploro/outputs/graduate/Investigation-of-the-photoluminescence-studies-of/9926503507691>
- [169] G. Busch, H. Schade, and J. L. Birman, ‘Lectures on Solid State Physics’, *Phys. Today*, vol. 32, no. 3, p. 74, Mar. 1979, doi: 10.1063/1.2995461.
- [170] P. M. Kibasomba *et al.*, ‘Strain and grain size of TiO₂ nanoparticles from TEM, Raman spectroscopy and XRD: The revisiting of the Williamson-Hall plot method’, *Results Phys.*, vol. 9, pp. 628–635, Jun. 2018, doi: 10.1016/j.rinp.2018.03.008.
- [171] M. Sen, *Nanotechnology and the Environment*. BoD – Books on Demand, 2020.
- [172] J. I. Goldstein, D. E. Newbury, J. R. Michael, N. W. M. Ritchie, J. H. J. Scott, and D. C. Joy, *Scanning Electron Microscopy and X-Ray Microanalysis*. Springer, 2017.
- [173] A. Ul-Hamid, *A Beginners’ Guide to Scanning Electron Microscopy*. Cham: Springer International Publishing, 2018. doi: 10.1007/978-3-319-98482-7.
- [174] P. Echlin, *Handbook of Sample Preparation for Scanning Electron Microscopy and X-Ray Microanalysis*. Springer Science & Business Media, 2011.
- [175] P. Westgate, ‘Lime-based construction materials: effect of novel additives on physical and chemical properties’.
- [176] S. K. Sharma, Ed., *Handbook of Materials Characterization*. Cham: Springer International Publishing, 2018. doi: 10.1007/978-3-319-92955-2.
- [177] B. Hafner, ‘Scanning Electron Microscopy Primer’.
- [178] S. M. Ahmed and H. Imam, ‘Characterization and photocatalytic activity of Eu:ZnO & Au/Eu:ZnO nanoparticles prepared by laser ablation in water’, *Mater. Sci. Semicond. Process.*, vol. 115, p. 105128, Aug. 2020, doi: 10.1016/j.mssp.2020.105128.
- [179] A. Barhoum, R. Rasouli, M. Yousefzadeh, H. Rahier, and M. Bechelany, ‘Nanofiber Technologies: History and Development’, in *Handbook of Nanofibers*, A. Barhoum, M. Bechelany, and A. S. H. Makhlof, Eds., Cham: Springer International Publishing, 2019, pp. 3–43. doi: 10.1007/978-3-319-53655-2_54.
- [180] ‘6. microwave –assisted hydrothermal synthesis - PDF Free Download’, pdffox.com. Accessed: Mar. 06, 2024. [Online]. Available: <https://pdffox.com/6-microwave-assisted-hydrothermal-synthesis-pdf-free.html>
- [181] K. Al-Naimi *et al.*, ‘Micro-scale wettability of carbonate rocks via high-resolution ESEM imaging’, *Results Phys.*, vol. 52, p. 106871, Sep. 2023, doi: 10.1016/j.rinp.2023.106871.
- [182] W. Zhou, R. Apkarian, Z. L. Wang, and D. Joy, ‘Fundamentals of Scanning Electron Microscopy (SEM)’, in *Scanning Microscopy for Nanotechnology: Techniques and Applications*, W. Zhou and Z. L. Wang, Eds., New York, NY: Springer, 2007, pp. 1–40. doi: 10.1007/978-0-387-39620-0_1.
- [183] J. Singh *et al.*, ‘Probing structural, optical and magnetic properties of Sm-doped ZnO nanomaterials via experimental and DFT approach: Enhanced photocatalytic degradation and antibacterial performance’, *Colloids Surf. Physicochem. Eng. Asp.*, vol. 668, p. 131470, Jul. 2023, doi: 10.1016/j.colsurfa.2023.131470.
- [184] F. S. Rocha, A. J. Gomes, C. N. Lunardi, S. Kaliaguine, and G. S. Patience, ‘Experimental methods in chemical engineering: Ultraviolet visible spectroscopy—UV-Vis’, *Can. J. Chem. Eng.*, vol. 96, no. 12, pp. 2512–2517, 2018, doi: 10.1002/cjce.23344.
- [185] M. Picollo, M. Aceto, and T. Vitorino, ‘UV-Vis spectroscopy’, *Phys. Sci. Rev.*, vol. 4, no. 4, Apr. 2019, doi: 10.1515/psr-2018-0008.

- [186] A. Pirie, B. Singh, and K. Islam, ‘Ultra-violet, visible, near-infrared, and mid-infrared diffuse reflectance spectroscopic techniques to predict several soil properties’, *Soil Res.*, vol. 43, no. 6, pp. 713–721, Sep. 2005, doi: 10.1071/SR04182.
- [187] M. C. Tarun, ‘HYDROGEN AND RELATED DEFECTS IN OXIDE SEMICONDUCTORS’.
- [188] R. C. Denney, ‘Visible and ultraviolet spectroscopy’, *No Title*, Accessed: Feb. 26, 2024. [Online]. Available: <https://cir.nii.ac.jp/crid/1130282270481586304>
- [189] ‘Pavia, D.L., Lampman, G.M., Kriz, G.S. and Vyvyan, J.A., 2014. Introduction to spectroscopy. Cengage learning.’.
- [190] J. Hardesty, ‘Spectrophotometry and the Beer-Lambert Law’.
- [191] T. R. Hogness, F. P. Zscheile, and A. E. Sidwell, ‘Photoelectric Spectrophotometry. An Apparatus for the Ultra-violet and Visible Spectral Regions: Its Construction, Calibration, and Application to Chemical Problems’, *J. Phys. Chem.*, vol. 41, no. 3, pp. 379–415, Mar. 1937, doi: 10.1021/j150381a005.
- [192] S. Landi, I. R. Segundo, E. Freitas, M. Vasilevskiy, J. Carneiro, and C. J. Tavares, ‘Use and misuse of the Kubelka-Munk function to obtain the band gap energy from diffuse reflectance measurements’, *Solid State Commun.*, vol. 341, p. 114573, Jan. 2022, doi: 10.1016/j.ssc.2021.114573.
- [193] J. B. Coulter and D. P. Birnie III, ‘Assessing Tauc Plot Slope Quantification: ZnO Thin Films as a Model System’, *Phys. Status Solidi B*, vol. 255, no. 3, p. 1700393, 2018, doi: 10.1002/pssb.201700393.
- [194] B. Weckhuysen, *Ultraviolet-visible spectroscopy*. 2004.
- [195] S. Som, M. Chowdhury, and S. K. Sharma, ‘Band gap and trapping parameters of color tunable Yb³⁺/Er³⁺ codoped Y₂O₃ upconversion phosphor synthesized by combustion route’, *J. Mater. Sci.*, vol. 49, no. 2, pp. 858–867, Jan. 2014, doi: 10.1007/s10853-013-7769-8.
- [196] A. Escobedo-Morales, I. I. Ruiz-López, M. deL. Ruiz-Peralta, L. Tepech-Carrillo, M. Sánchez-Cantú, and J. E. Moreno-Orea, ‘Automated method for the determination of the band gap energy of pure and mixed powder samples using diffuse reflectance spectroscopy’, *Heliyon*, vol. 5, no. 4, p. e01505, Apr. 2019, doi: 10.1016/j.heliyon.2019.e01505.
- [197] ‘Doyle, W.M., 1992. Principles and applications of Fourier transform infrared (FTIR) process analysis. *Process Control Qual*, 2(1), pp.11-41.’.
- [198] *Introduction To Spectroscopy, 5th Edition*. 2024. Accessed: Mar. 06, 2024. [Online]. Available: <http://archive.org/details/IntroductionToSpectroscopy5thEdition>
- [199] L. Piela, ‘Computational Chemistry: From the Hydrogen Molecule to Nanostructures’, in *Handbook of Computational Chemistry*, J. Leszczynski, A. Kaczmarek-Kedziera, T. Puzyn, M. G. Papadopoulos, H. Reis, and M. K. Shukla, Eds., Cham: Springer International Publishing, 2017, pp. 3–19. doi: 10.1007/978-3-319-27282-5_1.
- [200] C. Li *et al.*, ‘Controlled Synthesis of Ln³⁺ (Ln = Tb, Eu, Dy) and V⁵⁺ Ion-Doped YPO₄ Nano-/Microstructures with Tunable Luminescent Colors’, *Chem. Mater.*, vol. 21, no. 19, pp. 4598–4607, Oct. 2009, doi: 10.1021/cm901658k.
- [201] ‘Mangabhai, R., Cave, S. and Wills, R., 2010. Application of FTIR for material identification in the construction industry. *Concrete*, 44(1), pp.37-38.’.
- [202] A. D. Gupta and S. Karthikeyan, ‘Individual and combined toxic effect of nickel and chromium on biochemical constituents in *E. coli* using FTIR spectroscopy and Principle component analysis’, *Ecotoxicol. Environ. Saf.*, vol. 130, pp. 289–294, Aug. 2016, doi: 10.1016/j.ecoenv.2016.04.025.
- [203] H. W. Siesler, Y. Ozaki, S. Kawata, and H. M. Heise, *Near-Infrared Spectroscopy: Principles, Instruments, Applications*. John Wiley & Sons, 2008.

- [204] L. P. Lekesi, 'The Influence of Metal Oxide Transport Layer and Annealing Temperature on Perovskite Solar Cells (PSCs)'.
- [205] J. Ungula, 'Growth and characterization of ZnO nanoparticles by sol-gel process', Jan. 2015, Accessed: Feb. 26, 2024. [Online]. Available: <http://hdl.handle.net/11660/1146>
- [206] G. Blasse and B. C. Grabmaier, 'A General Introduction to Luminescent Materials', in *Luminescent Materials*, G. Blasse and B. C. Grabmaier, Eds., Berlin, Heidelberg: Springer, 1994, pp. 1–9. doi: 10.1007/978-3-642-79017-1_1.
- [207] G. D. Gilliland, 'Photoluminescence spectroscopy of crystalline semiconductors', *Mater. Sci. Eng. R Rep.*, vol. 18, no. 3, pp. 99–399, Mar. 1997, doi: 10.1016/S0927-796X(97)80003-4.
- [208] H. Terraschke and C. Wickleder, 'UV, Blue, Green, Yellow, Red, and Small: Newest Developments on Eu²⁺-Doped Nanophosphors', *Chem. Rev.*, vol. 115, no. 20, Art. no. 20, Oct. 2015, doi: 10.1021/acs.chemrev.5b00223.
- [209] L. Reddy, B. Avula, A. P. Sefage, P. M. Maleka, and M. Ntwaeaborwa, 'The Effects of Synthesis Techniques on the Photoluminescent Behaviours of the Nampo $4 : \text{Ce}^{3+}$ (M=Mg, Ca, Ba, Sr) Nanophosphors', presented at the 6th International Conference on Theoretical and Applied Nanoscience and Nanotechnology (TANN'22), Jun. 2022. doi: 10.11159/tann22.125.
- [210] T. H. Gfroerer, 'Photoluminescence in Analysis of Surfaces and Interfaces', in *Encyclopedia of Analytical Chemistry*, 1st ed., R. A. Meyers, Ed., Wiley, 2000. doi: 10.1002/9780470027318.a2510.
- [211] A. Miller, D. A. B. Miller, and S. D. Smith, 'Dynamic non-linear optical processes in semiconductors', *Adv. Phys.*, vol. 30, no. 6, Art. no. 6, Dec. 1981, doi: 10.1080/00018738100101437.
- [212] B. Abdullah, D. Tahir, H. Heryanto, N. F. R. Tang, and R. Rahmat, 'Highly ordered structure and susceptibility to light absorption of ZnO/calcium phosphate (5%) to enhance the stability of charge diffusion as a methylene blue bond breaker', *Phys. Scr.*, vol. 99, no. 2, Art. no. 2, Jan. 2024, doi: 10.1088/1402-4896/ad17af.
- [213] S. Balakumar, V. Keller, and M. V. Shankar, Eds., *Nanostructured Materials for Environmental Applications*. Cham: Springer International Publishing, 2021. doi: 10.1007/978-3-030-72076-6.
- [214] 'Nonparabolic Systems with Magnetic field, Impact Ionization or under Nonuniform Condition', in *Balance Equation Approach to Electron Transport in Semiconductors*, vol. Volume 0, in Frontiers of Research with the Chinese Academy of Sciences, no. Volume 0, vol. Volume 0, , WORLD SCIENTIFIC, 2008, pp. 449–526. doi: 10.1142/9789812819031_0013.
- [215] A. M. Alshehawy, D.-E. A. Mansour, M. Ghali, M. Lehtonen, and M. M. F. Darwish, 'Photoluminescence Spectroscopy Measurements for Effective Condition Assessment of Transformer Insulating Oil', *Processes*, vol. 9, no. 5, Art. no. 5, May 2021, doi: 10.3390/pr9050732.
- [216] P. P. Mokoena, 'Narrowband Ultraviolet B emission from gadolinium and praseodymium co-activated calcium phosphate phosphors for phototherapy lamps', Jan. 2014, Accessed: Feb. 26, 2024. [Online]. Available: <http://hdl.handle.net/11660/2187>
- [217] J. Schanda, *Colorimetry: Understanding the CIE System*. John Wiley & Sons, 2007.
- [218] H. Widdel and D. L. Post, *Color in Electronic Displays*. Springer Science & Business Media, 2013.
- [219] G. B. Nair and S. J. Dhoble, 'Orange light-emitting Ca₃Mg₃(PO₄)₄:Sm³⁺ phosphors', *Luminescence*, vol. 32, no. 1, pp. 125–128, 2017, doi: 10.1002/bio.3194.

- [220] G. Balachandran, 'Extraction of Rare Earths for Advanced Applications', in *Treatise on Process Metallurgy*, Elsevier, 2014, pp. 1291–1340. doi: 10.1016/B978-0-08-096988-6.09983-1.
- [221] S. Sun *et al.*, 'Energy transfer between Ce³⁺ and Tb³⁺ and the enhanced luminescence of a green phosphor SrB₂O₄:Ce³⁺, Tb³⁺, Na⁺', *Opt. Mater. Express*, vol. 6, no. 4, pp. 1172–1185, Apr. 2016, doi: 10.1364/OME.6.001172.
- [222] A. De Almeida, B. Santos, B. Paolo, and M. Quicheron, 'Solid state lighting review – Potential and challenges in Europe', *Renew. Sustain. Energy Rev.*, vol. 34, pp. 30–48, Jun. 2014, doi: 10.1016/j.rser.2014.02.029.
- [223] N. Thejokalyani and S. J. Dhoble, 'Novel approaches for energy efficient solid state lighting by RGB organic light emitting diodes – A review', *Renew. Sustain. Energy Rev.*, vol. 32, pp. 448–467, Apr. 2014, doi: 10.1016/j.rser.2014.01.013.
- [224] C. Chen *et al.*, 'Luminescence properties of sodalite-type Zn₄B₆O₁₃:Mn²⁺', *J. Lumin.*, vol. 199, pp. 154–159, Jul. 2018, doi: 10.1016/j.jlumin.2018.03.022.
- [225] S. Arunkumar and K. Marimuthu, 'Concentration effect of Sm³⁺ ions in B₂O₃–PbO–PbF₂–Bi₂O₃–ZnO glasses – Structural and luminescence investigations', *J. Alloys Compd.*, vol. 565, pp. 104–114, Jul. 2013, doi: 10.1016/j.jallcom.2013.02.151.
- [226] A. Y. Madkhli, Ü. H. Kaynar, M. B. Coban, M. Ayvacikli, A. Canimoglu, and N. Can, 'Characterization, room and low temperature photoluminescence of yttrium aluminium borate activated with Sm³⁺ ions', *Mater. Res. Bull.*, vol. 161, p. 112167, May 2023, doi: 10.1016/j.materresbull.2023.112167.
- [227] G. Fan, X. Wang, X. Qiu, D. Fan, R. Hu, and Z. Tian, 'Luminescent properties of orange-red emitting phosphors NaGd(MoO₄)(WO₄):Sm³⁺ for white LED', *Opt. Mater.*, vol. 91, pp. 363–370, May 2019, doi: 10.1016/j.optmat.2019.02.023.
- [228] Ravita and A. S. Rao, 'Tunable photoluminescence studies of KZABS: RE³⁺ (RE³⁺ = Tm³⁺, Tb³⁺ and Sm³⁺) glasses for w-LEDs based on energy transfer', *J. Lumin.*, vol. 251, p. 119194, Nov. 2022, doi: 10.1016/j.jlumin.2022.119194.
- [229] B. Pant, M. Park, H.-Y. Kim, and S.-J. Park, 'Ag-ZnO photocatalyst anchored on carbon nanofibers: Synthesis, characterization, and photocatalytic activities', *Synth. Met.*, vol. 220, pp. 533–537, Oct. 2016, doi: 10.1016/j.synthmet.2016.07.027.
- [230] S. Qotso, P. Mbule, and B. Mothudi, 'Microwave-assisted sol-gel synthesis of P3HT-ZnO: Sm³⁺, Yb³⁺: Study of structure, morphology, optical and electrical conductivity for organic solar cells application', *Mater. Chem. Phys.*, vol. 294, p. 127023, Jan. 2023, doi: 10.1016/j.matchemphys.2022.127023.
- [231] U. Schwertmann, P. Cambier, and E. Murad, 'Properties of Goethites of Varying Crystallinity', *Clays Clay Miner.*, vol. 33, no. 5, pp. 369–378, Oct. 1985, doi: 10.1346/CCMN.1985.0330501.
- [232] I. Stavarache, A.-M. Lepadatu, T. Stoica, and M. L. Ciurea, 'Annealing temperature effect on structure and electrical properties of films formed of Ge nanoparticles in SiO₂', *Appl. Surf. Sci.*, vol. 285, pp. 175–179, Nov. 2013, doi: 10.1016/j.apsusc.2013.08.031.
- [233] X. Wu and W. Sha, 'Experimental study of the voids in the electroless copper deposits and the direct measurement of the void fraction based on the scanning electron microscopy images', *Appl. Surf. Sci.*, vol. 255, no. 7, pp. 4259–4266, Jan. 2009, doi: 10.1016/j.apsusc.2008.11.015.
- [234] S. A. Ayon, M. Jamal, Md. M. Billah, and S. Neaz, 'Augmentation of magnetic properties and antimicrobial activities of band gap modified Ho³⁺ and Sm³⁺ doped ZnO nanoparticles: A comparative experimental study', *J. Alloys Compd.*, vol. 897, p. 163179, Mar. 2022, doi: 10.1016/j.jallcom.2021.163179.

- [235] R. L. Frost and Y. Xi, ‘Vibrational spectroscopy of the borate mineral kotoite $\text{Mg}_3(\text{BO}_3)_2$ ’, *Spectrochim. Acta. A. Mol. Biomol. Spectrosc.*, vol. 103, pp. 151–155, Feb. 2013, doi: 10.1016/j.saa.2012.11.031.
- [236] P. Vasudevan, V. Vidyadharan, S. M. Simon, and U. N. V, ‘Phytochemical mediated synthesis of $\text{ZnO}:\text{Dy}^{3+}$ nanophosphors: Judd–Ofelt analysis, structural and spectroscopic properties’, *J. Sci. Adv. Mater. Devices*, vol. 5, no. 2, pp. 242–249, Jun. 2020, doi: 10.1016/j.jsamd.2020.05.001.
- [237] P.-D. Wang, Z.-Y. Jia, Y.-H. Zhong, H.-Y. Mei, C.-M. Li, and N.-P. Cheng, ‘Effect of pressure on the elastic properties and optoelectronic behavior of $\text{Zn}_4\text{B}_6\text{O}_{13}$: First-principles investigation*’, *Chin. Phys. B*, vol. 27, no. 5, p. 057101, May 2018, doi: 10.1088/1674-1056/27/5/057101.
- [238] M. N. Mphelane, M. R. Mhlongo, T. E. Motaung, L. F. Koao, T. T. Hlatshwayo, and S. V. Motloug, ‘Effects of annealing temperature on the structure and photoluminescence properties of the $\text{ZnO}/\text{ZnAl}_2\text{O}_4/\text{Ca}_5\text{Al}_6\text{O}_{14}/\text{Ca}_3\text{Al}_4\text{ZnO}_{10}:0.1\% \text{Ce}^{3+}$ mixed-phases nanophosphor prepared by citrate sol–gel process’, *Appl. Phys. A*, vol. 126, no. 10, p. 821, Oct. 2020, doi: 10.1007/s00339-020-04002-6.
- [239] Q. Ning, B. Quan, and Y. Shi, ‘Effect of alkali metal ions on the spectra of $\text{CaZn}_2(\text{PO}_4)_2:\text{Sm}^{3+}$ phosphor analyzed by J-O theory’, *J. Lumin.*, vol. 206, pp. 498–508, Feb. 2019, doi: 10.1016/j.jlumin.2018.10.101.
- [240] Y. Zhang, R. Pang, C. Li, C. Zang, and Q. Su, ‘Reddish orange long lasting phosphorescence of Sm^{3+} in $\text{Sr}_2\text{ZnSi}_2\text{O}_7:\text{Sm}^{3+}$ phosphors’, *J. Rare Earths*, vol. 28, no. 5, pp. 705–708, Oct. 2010, doi: 10.1016/S1002-0721(09)60184-8.
- [241] A. E. Morales, E. S. Mora, and U. Pal, ‘Use of diffuse reflectance spectroscopy for optical characterization of un-supported nanostructures’, 2007.
- [242] H. S. Akkera *et al.*, ‘Structural, electrical, and optical properties of rare-earth Sm^{3+} doped SnO_2 transparent conducting oxide thin films for optoelectronic device applications: Synthesized by the spin coating method’, *Opt. Mater.*, vol. 133, p. 112993, Nov. 2022, doi: 10.1016/j.optmat.2022.112993.
- [243] G. A. El-Inany, H. S. Seleem, R. Helmy, M. O. Abdel-Salam, and M. Saif, ‘Synthesis and characterization of $\text{Sm}^{3+}:\text{Bi}_4\text{Si}_3\text{O}_{12}$ and dispersed into silica nanophosphor for sensing application’, *J. Mol. Struct.*, vol. 1173, pp. 111–119, Dec. 2018, doi: 10.1016/j.molstruc.2018.06.081.
- [244] İ. Pekközlü and S. Çakar, ‘Photoluminescence properties of $\text{Li}_6\text{CaB}_3\text{O}_8.5:\text{M}^{3+}$ ($\text{M}^{3+}:\text{Dy}$ and Sm)’, *J. Lumin.*, vol. 132, no. 9, pp. 2312–2317, Sep. 2012, doi: 10.1016/j.jlumin.2012.04.025.
- [245] M. Manhas, V. Kumar, O. M. Ntwaeaborwa, and H. C. Swart, ‘Photoluminescence and thermoluminescence investigations of $\text{Ca}_3\text{B}_2\text{O}_6:\text{Sm}^{3+}$ phosphor’, *Mater. Res. Express*, vol. 2, no. 7, p. 075008, Jul. 2015, doi: 10.1088/2053-1591/2/7/075008.
- [246] T. Fujii, K. Kodaira, O. Kawauchi, N. Tanaka, H. Yamashita, and M. Anpo, ‘Photochromic Behavior in the Fluorescence Spectra of 9-Anthrol Encapsulated in Si–Al Glasses Prepared by the Sol–Gel Method’, *J. Phys. Chem. B*, vol. 101, no. 50, pp. 10631–10637, Dec. 1997, doi: 10.1021/jp971540u.
- [247] A. Balakrishna, L. Reddy, O. M. Ntwaeaborwa, and H. C. Swart, ‘Remarkable influence of alkaline earth ions on the enhancement of fluorescence from Eu^{3+} ion doped in sodium ortho-phosphate phosphors’, *J. Mol. Struct.*, vol. 1203, p. 127375, Mar. 2020, doi: 10.1016/j.molstruc.2019.127375.
- [248] J. S. Kim, K. T. Lim, Y. S. Jeong, P. E. Jeon, J. C. Choi, and H. L. Park, ‘Full-color $\text{Ba}_3\text{MgSi}_2\text{O}_8:\text{Eu}^{2+}, \text{Mn}^{2+}$ phosphors for white-light-emitting diodes’, *Solid State Commun.*, vol. 135, no. 1, pp. 21–24, Jul. 2005, doi: 10.1016/j.ssc.2005.03.068.

- [249] J. Hölsä, J. Korventausta, R.-J. Lamminmäki, E. Säilynoja, and P. Porcher, ‘Host anion effect on the energy level scheme of Sm³⁺ in SmOX (X = F, Cl and Br)’, *J. Lumin.*, vol. 72–74, pp. 204–207, Jun. 1997, doi: 10.1016/S0022-2313(96)00252-9.
- [250] P. Masson, ‘The Effect of Aging and Visual Impairments on’.
- [251] K. Korzeniowski and M. Sobczyk, ‘Anomalous red luminescence of Sm³⁺ ions in Sm³⁺:LaKNaTaO₅ single crystals’, *Solid State Commun.*, vol. 273, pp. 30–33, May 2018, doi: 10.1016/j.ssc.2018.02.003.
- [252] A. Balakrishna, H. C. Swart, R. Ramaraghavulu, A. K. Bedyal, R. E. Kroon, and O. M. Ntwaeaborwa, ‘Structural evolution induced by substitution of designated molybdate sites (MoO₄²⁻) with different anionic groups (BO₃³⁻, PO₄³⁻ and SO₄²⁻) in CaMoO₄:Sm³⁺ phosphors-A study on color tunable luminescent properties’, *J. Alloys Compd.*, vol. 727, pp. 224–237, Dec. 2017, doi: 10.1016/j.jallcom.2017.08.117.
- [253] I. Gupta, S. Singh, S. Bhagwan, and D. Singh, ‘Rare earth (RE) doped phosphors and their emerging applications: A review’, *Ceram. Int.*, vol. 47, no. 14, pp. 19282–19303, Jul. 2021, doi: 10.1016/j.ceramint.2021.03.308.
- [254] P. Liang, M. Wang, and Z. Liu, ‘Synthesis and spectroscopic studies of Zn₄B₆O₁₃ and Eu/Tb single-doped Zn₄B₆O₁₃ phosphors’, *J. Rare Earths*, vol. 35, no. 5, pp. 441–445, May 2017, doi: 10.1016/S1002-0721(17)60931-1.
- [255] X. Kang, S. Liu, Z. Dai, Y. He, X. Song, and Z. Tan, ‘Titanium Dioxide: From Engineering to Applications’, *Catalysts*, vol. 9, no. 2, Art. no. 2, Feb. 2019, doi: 10.3390/catal9020191.
- [256] L. S. Reddy Yadav, M. Raghavendra, K. H. Sudheer Kumar, N. Dhananjaya, and G. Nagaraju, ‘Biosynthesised ZnO : Dy³⁺ nanoparticles: Biodiesel properties and reusable catalyst for N-formylation of aromatic amines with formic acid’, *Eur. Phys. J. Plus*, vol. 133, no. 4, p. 153, Apr. 2018, doi: 10.1140/epjp/i2018-11963-6.
- [257] R. n. Bhargava, V. Chhabra, T. Som, A. Ekimov, and N. Taskar, ‘Quantum Confined Atoms of Doped ZnO Nanocrystals’, *Phys. Status Solidi B*, vol. 229, no. 2, pp. 897–901, 2002, doi: 10.1002/1521-3951(200201)229:2<897::AID-PSSB897>3.0.CO;2-C.
- [258] R. N. Gayen, K. Sarkar, S. Hussain, R. Bhar, and A. K. Pal, ‘ZnO films prepared by modified sol-gel technique’, *IJPAP Vol4907 July 2011*, Jul. 2011, Accessed: Feb. 26, 2024. [Online]. Available: <http://nopr.niscares.in/handle/123456789/12008>
- [259] M. Xin, ‘Effect of Eu doping on the structure, morphology and luminescence properties of ZnO submicron rod for white LED applications’, *J. Theor. Appl. Phys.*, vol. 12, no. 3, pp. 177–182, Sep. 2018, doi: 10.1007/s40094-018-0304-1.
- [260] R. Balda, J. Fernández, J. L. Adam, and M. A. Arriandiaga, ‘Time-resolved fluorescence-line narrowing and energy-transfer studies in a Eu^{3+} -doped fluorophosphate glass’, *Phys. Rev. B*, vol. 54, no. 17, pp. 12076–12086, Nov. 1996, doi: 10.1103/PhysRevB.54.12076.
- [261] A. Douayar *et al.*, ‘Investigation of the structural, optical and electrical properties of Nd-doped ZnO thin films deposited by spray pyrolysis’, *Eur. Phys. J. - Appl. Phys.*, vol. 61, no. 1, p. 10304, Jan. 2013, doi: 10.1051/epjap/2013120388.
- [262] A. K. Kunti, L. Ghosh, S. K. Sharma, and H. C. Swart, ‘Synthesis and luminescence mechanism of white light emitting Eu³⁺ doped CaZnV₂O₇ phosphors’, *J. Lumin.*, vol. 214, p. 116530, Oct. 2019, doi: 10.1016/j.jlumin.2019.116530.
- [263] J. Gao *et al.*, ‘Eu³⁺-doped CdSe nanocrystals with blueshift emission and high quantum yield’, *J. Lumin.*, vol. 255, p. 119583, Mar. 2023, doi: 10.1016/j.jlumin.2022.119583.
- [264] A. Tang, D. F. Zhang, and L. Yang, ‘Synthesis and luminescence properties of novel red-emitting phosphor InNbO₄:Eu³⁺ for white-light emitting diodes’, *Russ. Chem. Bull.*, vol. 61, no. 11, pp. 2172–2174, Nov. 2012, doi: 10.1007/s11172-012-0304-2.

- [265] Y. Yang, X. Li, W. Feng, W. Yang, W. Li, and C. Tao, 'Effect of surfactants on morphology and luminescent properties of CaMoO₄: Eu³⁺ red phosphors', *J. Alloys Compd.*, vol. 509, no. 3, pp. 845–848, Jan. 2011, doi: 10.1016/j.jallcom.2010.09.106.
- [266] D. R. Vij, *Luminescence of Solids*. Springer Science & Business Media, 2012.
- [267] J. Fan, W. Zhang, S. Dai, G. Yan, M. Deng, and K. Qiu, 'Effect of charge compensators A⁺ (A = Li, Na and K) on luminescence enhancement of Ca₃Sr₃(PO₄)₄:Sm³⁺ orange-red phosphors', *Ceram. Int.*, vol. 44, no. 16, pp. 20028–20033, Nov. 2018, doi: 10.1016/j.ceramint.2018.07.276.
- [268] X. Gao, W. Zhang, X. Wang, X. Huang, and Z. Zhao, 'Charge compensation effects of alkali metal ions M⁺ (Li⁺, Na⁺, K⁺) on luminescence enhancement in red-emitting Ca₃Si₂O₇:Eu³⁺ phosphors', *J. Alloys Compd.*, vol. 893, p. 162265, Feb. 2022, doi: 10.1016/j.jallcom.2021.162265.
- [269] K. K. Shen, S. Kochesfahani, and F. Jouffret, 'Zinc borates as multifunctional polymer additives', *Polym. Adv. Technol.*, vol. 19, no. 6, pp. 469–474, 2008, doi: 10.1002/pat.1119.
- [270] A. Meijerink, G. Blasse, and M. Glasbeek, 'Photoluminescence, thermoluminescence and EPR studies on Zn₄B₆O₁₃', *J. Phys. Condens. Matter*, vol. 2, no. 29, p. 6303, Jul. 1990, doi: 10.1088/0953-8984/2/29/008.
- [271] A. Balakrishna, D. Rajesh, and Y. C. Ratnakaram, 'Structural and photoluminescence properties of Dy³⁺ doped different modifier oxide-based lithium borate glasses', *J. Lumin.*, vol. 132, no. 11, pp. 2984–2991, Nov. 2012, doi: 10.1016/j.jlumin.2012.06.014.
- [272] M. Najafi, 'Investigation of Cu Doping, Morphology and Annealing Effects on Structural and Optical Properties of ZnO:Dy Nanostructures', *J. Fluoresc.*, vol. 26, no. 3, pp. 775–780, May 2016, doi: 10.1007/s10895-015-1756-1.
- [273] M. Akyol, A. Ekicibil, and K. Kiymaç, 'AC-magnetic susceptibility of Dy doped ZnO compounds', *J. Magn. Magn. Mater.*, vol. 385, pp. 65–69, Jul. 2015, doi: 10.1016/j.jmmm.2015.03.010.
- [274] D. Rehani, S. Bishnoi, M. Saxena, D. Haranath, V. Gupta, and S. N. Sharma, 'Efficient luminomagnetic and conductive Eu and Dy doped ZnO phosphors for multifunctional devices', *J. Phys. Chem. Solids*, vol. 143, p. 109460, Aug. 2020, doi: 10.1016/j.jpcs.2020.109460.
- [275] B. Poornaprakash, U. Chalpathi, M. Kumar, and P. T. Poojitha, 'Achieving room temperature ferromagnetism in ZnO nanoparticles via Dy doping', *J. Mater. Sci. Mater. Electron.*, vol. 29, no. 3, pp. 2316–2321, Feb. 2018, doi: 10.1007/s10854-017-8148-z.
- [276] C. Sumalatha *et al.*, 'White light emission from Dy³⁺-doped ZnO + Bi₂O₃ + BaF₂ + B₂O₃ + TeO₂ glasses: Structural and spectroscopic properties', *Spectrochim. Acta. A. Mol. Biomol. Spectrosc.*, vol. 240, p. 118568, Oct. 2020, doi: 10.1016/j.saa.2020.118568.
- [277] G. Anoop, I. H. Cho, D. W. Suh, C. K. Kim, and J. S. Yoo, 'Structural and luminescent characteristics of two-step processed BaAl_{2-x}Si_xO_{4-x}N_x:Eu²⁺ phosphors', *J. Lumin.*, vol. 134, pp. 390–395, Feb. 2013, doi: 10.1016/j.jlumin.2012.08.015.
- [278] X. Jiang *et al.*, 'Near-Zero Thermal Expansion and High Ultraviolet Transparency in a Borate Crystal of Zn₄B₆O₁₃', *Adv. Mater.*, vol. 28, no. 36, pp. 7936–7940, 2016, doi: 10.1002/adma.201601816.
- [279] S. Zhao, Z. Wang, Z. Ma, F. Fan, and W. Liu, 'Achieving Multimodal Emission in Zn₄B₆O₁₃:Tb³⁺,Yb³⁺ for Information Encryption and Anti-counterfeiting', *Inorg. Chem.*, vol. 59, no. 21, pp. 15681–15689, Nov. 2020, doi: 10.1021/acs.inorgchem.0c02019.
- [280] P. Liang, J. W. Liu, and Z. H. Liu, 'Controllable hydrothermal synthesis of Eu³⁺/Tb³⁺/Dy³⁺ activated Zn₈[(BO₃)₃O₂(OH)₃] micro/nanostructured phosphors:

energy transfer and tunable emissions', *RSC Adv.*, vol. 6, no. 92, pp. 89113–89123, Sep. 2016, doi: 10.1039/C6RA19101K.

- [281] A. Balakrishna, L. Reddy, O. M. Ntwaeaborwa, and H. C. Swart, 'Remarkable influence of alkaline earth ions on the enhancement of fluorescence from Eu^{3+} ion doped in sodium ortho-phosphate phosphors', *J. Mol. Struct.*, vol. 1203, p. 127375, Mar. 2020, doi: 10.1016/j.molstruc.2019.127375.

